



UNIVERSIDADE ESTADUAL DE CAMPINAS
Instituto de Geociências

VANESSA DE ALMEIDA PIMENTA

ALTERAÇÃO HIDROTERMAL E DEFORMAÇÃO NO DEPÓSITO DO PETECA,
PROVÍNCIA AURÍFERA DE ALTA FLORESTA (PAAF), REGIÃO DE PEIXOTO DE
AZEVEDO – MT

CAMPINAS

2018

VANESSA DE ALMEIDA PIMENTA

“ALTERAÇÃO HIDROTERMAL E DEFORMAÇÃO NO DEPÓSITO DO PETECA,
PROVÍNCIA AURÍFERA DE ALTA FLORESTA (PAAF), REGIÃO DE PEIXOTO DE
AZEVEDO – MT”

DISSERTAÇÃO APRESENTADA AO INSTITUTO DE
GEOCIÊNCIAS DA UNIVERSIDADE ESTADUAL DE
CAMPINAS PARA OBTENÇÃO DO TÍTULO DE MESTRA
EM GEOCIÊNCIAS NA ÁREA DE GEOLOGIA E
RECURSOS NATURAIS

ORIENTADORA: PROFA. DRA. MARIA JOSÉ MALUF DE MESQUITA

COORIENTADORA: PROFA. DRA. MARCIA ELISA BOSCATO GOMES

ESTE EXEMPLAR CORRESPONDE À VERSÃO FINAL
DA DISSERTAÇÃO DEFENDIDA PELA ALUNA
VANESSA DE ALMEIDA PIMENTA E ORIENTADA PELA
PROFA. DRA. MARIA JOSÉ MALUF DE MESQUITA

CAMPINAS

2018

Agência(s) de fomento e nº(s) de processo(s): Não se aplica.

ORCID: <https://orcid.org/0000-0002-0405-4343>

Ficha catalográfica
Universidade Estadual de Campinas
Biblioteca do Instituto de Geociências
Marta dos Santos - CRB 8/5892

Pimenta, Vanessa de Almeida, 1989-
P649a Alteração hidrotermal e deformação no depósito do Peteca, Província
Aurífera de Alta Floresta (PAAF), região de Peixoto de Azevedo-MT / Vanessa
de Almeida Pimenta. – Campinas, SP : [s.n.], 2018.

Orientador: Maria José Maluf de Mesquita.
Coorientador: Marcia Elisa Boscato Gomes.
Dissertação (mestrado) – Universidade Estadual de Campinas, Instituto de
Geociências.

1. Cráttons - Amazônia. 2. Mineralizações auríferas. 3. Alteração
hidrotermal. 4. Química mineralógica. 5. Geotermometria. I. Mesquita, Maria
José Maluf de, 1961-. II. Gomes, Marcia Elisa Boscato. III. Universidade
Estadual de Campinas. Instituto de Geociências. IV. Título.

Informações para Biblioteca Digital

Título em outro idioma: Hydrothermal alteration and deformation at Peteca deposit, Alta
Floresta Gold Province (AFGP), Peixoto de Azevedo-MT

Palavras-chave em inglês:

Amazon craton

Gold mineralization

Hydrothermal alteration

Mineral chemistry

Geothermometry

Área de concentração: Geologia e Recursos Naturais

Titulação: Mestra em Geociências

Banca examinadora:

Maria José Maluf de Mesquita [Orientador]

Brenda Chung da Rocha

Rafael Rodrigues de Assis

Data de defesa: 19-12-2018

Programa de Pós-Graduação: Geociências



UNIVERSIDADE ESTADUAL DE CAMPINAS
INSTITUTO DE GEOCIÊNCIAS

AUTORA: Vanessa de Almeida Pimenta

**ALTERAÇÃO HIDROTERMAL E DEFORMAÇÃO NO DEPÓSITO DO PETECA,
PROVÍNCIA AURÍFERA DE ALTA FLORESTA (PAAF), REGIÃO DE PEIXOTO DE
AZEVEDO – MT**

ORIENTADORA: Profa. Dra. Maria José Maluf de Mesquita

COORIENTADORA: Profa. Dra. Marcia Elisa Boscato Gomes

Aprovado em: 19 / 12 / 2018

EXAMINADORES:

Profa. Dra. Maria José Maluf de Mesquita - Presidente

Profa. Dra. Brenda Chung da Rocha

Prof. Dr. Rafael Rodrigues de Assis

A Ata de defesa com as respectivas assinaturas dos membros, encontra-se disponível no SIGA - Sistema de Fluxo de Dissertação e na Secretaria de Pós-graduação do IG.

Campinas, 19 de dezembro de 2018.

BIOGRAFIA

Vanessa de Almeida Pimenta

Geóloga pela Universidade Estadual Paulista Júlio de Mesquita Filho – UNESP, *campus* Rio claro (2013). Mestra em Geociências pela Universidade Estadual de Campinas – UNICAMP (2018). Durante a graduação foi monitora da disciplina de Mineralogia com ênfase em cristalografia, química mineral, descrições sistêmicas de minerais macro e microscopicamente. Também realizou estágios na empresa Yamana Gold Inc. nos projetos de exploração Fazenda Brasileiro (Teofilândia, BA) e Jacobina (BA). Foi representante discente suplente (2008-2010) do Departamento de Petrologia e Metalogenia (DPM), além de ter atuado como vice-presidente e presidente do Centro Acadêmico da Geologia (2009 e 2010, respectivamente). Tem experiência em metalogênese com ênfase em petrografia, química mineral e alterações hidrotermais em depósitos de ouro – orogênico (Fazenda Brasileiro-BA), paleoplacer com posterior remobilização aurífera (Jacobina-BA; Trabalho de Conclusão de Curso) e veio mineralizado em zonas de cisalhamento contínuas (Peixoto de Azevedo-MT, Província Aurífera de Alta Floresta, Dissertação de Mestrado).

Dedico...

À Deus.

Para Ele.

Por Ele.

E por todo sempre.

*Aos meus pais Iracema e Wanderley.
Pela paciência, compreensão, apoio, força e amor.
Por serem minha base, âncora e inspiração de batalhar.
Por acreditarem em mim.*

AGRADECIMENTOS

Primeiramente, agradeço a Deus por ter me abençoado, ter me colocado nesse caminho, ter me iluminado, dando clareza e entendimento quando me sentia perdida, por ter me sustentado até aqui, ter sido minha fortaleza. À Ele dedico cada superação, sucesso alcançado! Agradeço também a cada dificuldade ao longo destes últimos anos porque elas me fortaleceram, me fizeram crescer e permanecer grata em meio às adversidades.

Agradeço aos meus pais pelo apoio, pela infinita paciência e tolerância. Ao meu pai por sempre se preocupar com o sono e me lembrar que eu devia ir dormir rs, e à minha mãe por abraçar todo esse processo junto comigo. Sem vocês, tudo teria sido um caminho muito mais difícil, quase inimaginável p/ mim.

Agradeço a Prof. Dr^a Maria José Mesquita pela orientação, infinita paciência, pelos ensinamentos, incentivos, questionamentos e esclarecimentos de dúvidas, pelo apoio, por ter me mostrado uma grande parte do meu atual conhecimento do que é a carreira acadêmica. Ao esposo dela, Prof. Dr^o Jefferson Picanço pelas gentis conversas ao encontrá-lo junto com a Masé. Agradeço a co-orientação da Prof. Dr^a Márcia Gomes da UFRGS e a hospitalidade, delicadeza e atenção ao me receber em sua casa. A ela e a equipe do Laboratório de Microssonda Eletrônica da UFRGS, principalmente à Suzi, agradeço por todo suporte técnico nos dias em que eu frequentei o laboratório, e nos meses posteriores ao enviar resultados e esclarecer dúvidas.

Agradeço a BioGold pelos materiais e ajuda disponibilizados.

Agradeço a Érica Tonetto pelo apoio técnico, pelas ótimas conversas enquanto esperávamos as análises de MEV ficarem prontas, e confiança em mim às aulas de inglês. Agradeço ao Dailto Silva pela ajuda todas as vezes que tive alguma dificuldade com o microscópio ou com a câmera rs, pelo suporte técnico em geral. Agradeço ao Flaviano pelo preparo das lâminas e suporte quando precisei serrar amostras, polir lâminas.

Agradeço ao Pavel e ao Rafael (Boneco) por terem passado todo o material e conhecimento relacionado ao Peteca, pela disposição de esclarecer qualquer dúvida e fazer ótimas discussões. Agradeço a Poli e Verônica por sempre terem se colocado à disposição p/ eu pedir qualquer ajuda e dica, e às conversas ainda que rápidas pelos corredores. À Sammy que mal conheci e já foi assistir minha qualificação, me deu apoio e passou a ser uma das mais queridas da pós. Ao Zé Mattos agradeço pela amizade, inúmeras discussões geológicas, dicas, “zuêras”, confiança no meu trabalho como professora de inglês, pela brotheragem. Ao

Igor (Igão/Igones) e Luccho também agradeço a amizade, inúmeras discussões geológicas, ajuda e parceria, trabalho em equipe.

Aos meus primos Gustavo e Cynara, tias Maria Helena e Cacilda por todo apoio, ajuda, carinho a mim e minha família! Vocês foram essenciais! Também agradeço as tias Cássia e Valéria & famílias por me fazerem se sentir querida mesmo com tamanha distância, e por sempre entenderem minhas ausências.

Agradeço a Cremes, Malu e Érika que mesmo de longe e mesmo eu mal fazendo contato, sempre estiveram “aí”, me dando apoio e enviando palavras de força e amizade quando eu precisava. À minha querida amiga Adrielle: minha gratidão é enorme! Você esteve muito presente de alguma forma em todas as etapas e processos destes últimos anos, muitas vezes acompanhando bem de perto. À Dani Montrezor: só Deus p/ coincidir nossas etapas de vida, mais uma vez, finalizando juntas um mestrado na mesma universidade! Muito obrigada por tantos anos de amizade e por dividirmos as mesmas ansiedades desta etapa tão importante em nossas vidas. À Aline agradeço por tantas conversas, apoio, risadas; aluna querida que se tornou uma grande amiga! Agradeço a Fer Luz, Paty-Lê-Lu-Lóu, Marcus, Maria & família, Bárbara-Helô & família por todos os (poucos) momentos juntos, pela paciência por eu ter sido tão ausente, orações, apoio, e por me chamarem “pros rolês” mesmo sabendo que eu não poderia ir. Agradeço aos queridos amigos e amigas do GruPão/Grupaum, uns mais próximos ou mais distantes, que ao longo de tantos anos têm sido responsáveis por tantos momentos de alegria e do “desestressar”, por tamanho apoio, carinho, orações, parcerias.

E por fim, agradeço ao Dádis - “the last, but not the least”, aliás muito pelo contrário. Mas o último agradecimento não poderia ser melhor representativo e dedicado a ele porque foi a última pessoa que conheci durante todos os anos de mestrado. O conheci nos últimos 5 segundos do segundo tempo, já me deu apoio, leveza, tranquilidade - tão necessários nesta reta final -, além de ter me proporcionado momentos de alegria no meu dia-a-dia. Te agradeço por ter chegado (ainda que) no finalzinho, mas muito mais por estar comigo no início desta minha mais nova etapa.

*“Não te mandei eu? Esforça-te, e tem bom ânimo; não pasmes, nem te espantes:
Porque o Senhor teu Deus é contigo, por onde quer que andares”
(Josué, 1:9)*

RESUMO

A Província Aurífera de Alta Floresta (PAAF) está na porção sul do Cráton Amazônico, norte do estado de Mato Grosso. No setor leste da PAAF há depósitos de ouro concentrados no lineamento NW-SE Peru-Trairão, do tipo disseminado ou em sistemas de veios de quartzo. Na região de Peixoto de Azevedo, distrito de Flor da Serra, há quatro depósitos filonares (João Fidelis, Pedro Contim, Peteca e Queiroz), alinhados a NW-SE na Zona de Cisalhamento do Peteca. Objetivo principal foi diferenciar as alterações hidrotermais quanto à influência de processos hidrotermais de cisalhamento e hidrotermais magmáticos ocorridos. As rochas encaixantes compreendem: granitoides foliados (granada granodiorito, granada leucogranito, biotita tonalito), biotita metatonalito, diques de dacito microporfirítico e pegmatitos. Além da ocorrência do metatonalito há outras evidências de que a foliação S_n teve origem metamórfica: (a) microestruturas em feldspato e quartzo nos granitoides foliados que indicam condições metamórficas de médio a alto grau; (b) diferença composicional entre granada do granodiorito e leucogranito. Sistema de Cisalhamento-Hidrotermal produziu microestruturas de deformações em feldspato, plagioclasio e quartzo de baixo a médio grau metamórfico, e a interação entre deformação e fluido gerou biotita tonalito protomilonito, milonitos, filonitos, vênulas oblíquas a ortogonais em relação à foliação, veio de quartzo e mineralização. Estas rochas apresentam foliação S_{n+1} . Granodiorito, granada-biotita granodiorito milonito, illita granodiorito milonito e clorita-illita filonito correspondem a evolução de cisalhamento até a formação do veio de quartzo e mineralização. Clorita-illita filonito e biotita metatonalito hospedam o veio mineralizado (N70-80W/N60-90E). As foliações S_n e S_{n+1} são anastomosadas e (sub)paralelas ao filão. Vênulas de carbonato ocorreram em um primeiro evento, e as compostas por quartzo, carbonato e pirita são posteriores, pois apresentam a mesma assembleia mineral que o veio. O veio apresenta três domínios microestruturais: (1) cristais finos de quartzo com crescimento sintaxial; (2) cristais de quartzo de tamanho médio, oblíquos ao domínio 1 e paralelos à direção do veio; (3) cristais finos de quartzo e recristalizados, associados a microfraturas, microfalhas paralelas à direção do veio. No veio, pirita grossa (Py 1) deve ser contemporânea ao domínio 2. Assembleia mineral associada ao veio apresenta quartzo, pirita, esfalerita, greenockita, calcopirita, galena. Ouro ocorre em microfraturas ou microcavidades na Py 1. Assembleia de minério corresponde a: Py 1, esfalerita, ouro, calcopirita, galena. O Sistema Magmático-Hidrotermal compreende alterações hidrotermais que não constituem as foliações: albita, potássica com microclínio, propilítica, clorítica, muscovita-illita, Fe-Cu, e stockworks de carbonato-epidoto. A alteração de Fe-Cu apresenta quartzo, pirita fina (Py 2), covelita com fases de Se, Te, associada ao domínio microestrutural 3 do veio. Resultados de geotermometria mostram a temperatura de cristalização da clorita em $350^\circ \pm 20^\circ\text{C}$, embora haja um aumento, em média, de 14°C do Sistema de Cisalhamento para o Magmático. Também há aumento de temperatura entre os dois sistemas para a cristalização da mica branca. O Peteca corresponde a um depósito Au±Cu tipo-veio, resultante de três principais estágios: metamorfismo, Sistema de Cisalhamento-Hidrotermal que marca redução de temperatura e compreende a mineralização, e o Sistema Magmático-Hidrotermal que marca aumento de temperatura devido à uma fonte magmática.

Palavras chave: Cráttons – Amazônia, mineralizações auríferas, alteração hidrotermal, química mineralógica, geotermometria.

ABSTRACT

The Alta Floresta Gold Province (AFGP) occurs in the south portion of the Amazonic Craton, north of the Mato Grosso state. In the eastern sector of AFGP there are gold deposits concentrated in the NW-SE Peru-Trairão lignament, of the disseminated type or in quartz vein systems. In the region of Peixoto de Azevedo, in the Flor da Serra district, there are four deposits (João Fidelis, Pedro Contim, Peteca and Queiroz), aligned to NW-SE in the Peteca Shear Zone. The main objective of this work is to differentiate hydrothermal alterations regarding the influence of hydrothermal shear processes and magmatic hydrothermal events. The country rocks include foliated granitoids (garnet granodiorite, garnet leucogranite, biotite tonalite), biotite metatonalite, microporphyric dacite dykes and pegmatites. In addition to the occurrence of metatonalite, other evidences that the Sn foliation has a metamorphic origin base on: (a) microstructures in feldspar and quartz in foliated granitoids that indicate medium-to high-grade metamorphic conditions; (b) compositional difference between garnet of granodiorite and leucogranite. The Shear-Hydrothermal System produced microstructures of deformations in feldspar, plagioclase and quartz of low- to medium-grade metamorphic conditions, and the deformation-fluid interaction produced biotite tonalite protomylonite, mylonites and phyllonites, oblique to orthogonal veinlets in relation to the foliation, quartz vein and mineralization. These shear-rocks show S_{n+1} foliation. Granodiorite, garnet-biotite granodiorite mylonite, illite granodiorite mylonite and chlorite-illite phyllonite correspond to the shear evolution toward the quartz vein and mineralization. Chlorite-illite phyllonite and metatonalite host the mineralized vein (N70-80W / N60-90E). The foliations Sn and S_{n+1} are anastomosed and (sub) parallel to the vein. Carbonate veinlets generated in a first event of fracture formation, and those composed by quartz, carbonate and sulphide formed at a later stage, once they present the same mineral assemblage as mineralization. The quartz vein presents three microstructural domains: (1) fine-grained quartz crystals with syntax growth; (2) medium-sized quartz crystals parallel to the vein direction; (3) fine-grained quartz crystals, associated to microfractures, microfaults parallel to the vein direction. In the vein, coarse-grained pyrite (Py 1) may be contemporaneous to the domain 2. Mineral assemblage in the quartz vein comprises quartz, pyrite, sphalerite, greenockite, chalcopyrite, galena. Gold occurs in microfractures or microcavities in Py 1. Ore mineral assemblage comprises Py 1, sphalerite, gold, chalcopyrite, galena. The Magmatic-Hydrothermal System comprises hydrothermal alterations that do not constitute the foliations, such as: albite, potassic with microcline, propylitic, chloritic, muscovite-illite, Fe-Cu, and carbonate-epidote stockworks. The Fe-Cu alteration presents quartz, fine-grained pyrite (Py 2), covelite with phases of Se, Te, Ag. Geothermometry results show an average of $350^\circ \pm 20^\circ\text{C}$ for chlorite crystallization temperature, although there is an increase of 14°C on average from the Shear-Hydrothermal System to the Magmatic. Likewise, this slight temperature increase occurs for the white mica crystallization between the both of the systems. The Peteca consists of an Au \pm Cu vein-type deposit resulted from three main stages: metamorphism, Shear-Hydrothermal system that marks a temperature decrease and comprise the ore assemblage, and the Magmatic-Hydrothermal system, which mark a temperature increase due to a magmatic source.

Key words: Amazon Craton, gold mineralization, hydrothermal alteration, mineral chemistry, geothermometry.

LISTA DE FIGURAS

Figura 1 - Localização do depósito Peteca. Polígono em amarelo representa a Província Aurífera de Alta Floresta (PAAF) no MT. Círculo em vermelho indica a localização do alvo Peteca no setor Leste da PAAF. Imagem de satélite mostra os municípios de Matupá, Peixoto de Azevedo e o distrito de Flor da Serra nas proximidades do depósito.	21
Figura 2 - Infraestrutura para análise de EPMA. (A) Infraestrutura utilizada para higienização das lâminas delgadas polidas. A direita encontra-se a metalizadora. (B) Microssonda eletrônica Cameca SXFive. (C) Detalhe de processamento dos dados através do software Peak Sight 5.1.	23
Figura 3 - Compartimentação Geotectônica do Cráton Amazonas segundo Santos et al. (2000). Polígono vermelho: setor leste da PAAF (Extraído de Silva, 2014).	26
Figura 4 - Mapa geológico do Setor Leste da PAAF com principais depósitos auríferos associados ao Lineamento Peru-Trairão e destaque em vermelho para o Depósito Peteca (Assis, 2015 - Modificado de Miguel-Jr, 2011).	27
Figura 5 – Mapa Geológico da região de Peixoto de Azevedo e indicação do Depósito Peteca (Quispe, 2016).	31
Figure 6 - Map location of the Alta Floresta Gold Province. It displays the main geological domains of the eastern part of the Province (black square) (Assis, 2011 - Modified from Barros, 2007).....	44
Figure 7 - Geotectonic compartmentalization of the Amazon Craton according to Santos et al. (2000). Red polygon: eastern section of AFGP (Extracted from Silva, 2014).	48
Figure 8 - Geologic map of the eastern sector of AFGP with the main gold deposits associated with the Peru-Trairão Lineament, and highlighted in red for the Peteca deposit (Assis, 2015 - Modified from Miguel-Jr, 2011).....	49
Figure 9 – Geologic map of the region of Peixoto de Azevedo and Peteca deposit location (Quispe, 2016).	53
Figure 10 - Geologic Map with drill cores location. Image granted by Biominer Mining Company...	55
Figure 11 – Geologic section of oriented drill cores (PT-8, PT-22, PT-12, PT-15) and present lithotypes. Variations in the directions of foliation (Sn) characterize it as anastomosed. Drill cores are NE-SW and intercept the lithotypes in an average medium angle of 75°-90°.....	56
Figure 12 - Geologic section of oriented drill core (PT-30) and present lithotypes. Variations in the directions of foliation (Sn) characterize it as anastomosed. Drill core is NE-SW and intercept the lithotypes in an average medium angle of 75°-90°.....	57
Figure 13 - Core samples (A, F, J, L) and photomicrographs (B, C, D, E, G, H, I, K, M) of foliated granites and metatonalite at Peteca deposit. (A) Garnet granodiorite with weak developed foliation (Sn). (B) The minerals orientation mark Sn. Note microcline alteration of feldspar. (C) Garnet	

granodiorite with a well developed Sn. Microlithons of quartz-feldspar alternated with biotite and quartz-ribbon domains. Note elongated garnet altered to illite-muscovite. Red arrows indicate quartz aggregates. (D) Deformed bands with recrystallized grains in primary quartz. Red arrows indicate bulges at quartz boundaries. (E) Recrystallized K-feldspar. Red arrows indicate tapering edge twinning. (F) Garnet Leucogranite. (G) Photomicrograph exhibits flame perthite (red arrow) orthogonal to the Sn foliation. (H) Garnet crystal in the leucogranite. (I) Orthoclase exhibits microcline twinning formation from its boundaries (blue arrows). It also shows plagioclase inclusions. (J) Biotite tonalite weakly foliated. (K) Photomicrograph shows primary deformed matrix with the major crystals of plagioclase and quartz on the right top and a phenocryst on the left. Recrystallized matrix marked by biotite, quartz and feldspars, as narrow strip wrap primary grains. (L) Biotite metatonalite. Carbonate veinlets are (sub) parallel to Sn. (M) Recrystallized isograngular matrix. [Sn Foliation represented by yellow arrow on all pictures]..... 59

Figure 14 - Main features in core samples (A, D, E) and photomicrographs (B natural light NL, and C, F polarized light - PL) of the dykes at Peteca deposit. (A) Microporphyritic dacite dyke. (B-C) Photomicrographs show the intensely altered matrix. Note microphenocrysts of plagioclase marking Sn. (D) Leucopegmatite. (E) Reddish pegmatite with macroperthites. (F) Photomicrograph shows the quartz-feldspar composition. Red arrows indicate string and flame perthites, as well as microcline twinning irregularly distributed in grain boundary of K-feldspar. Polycrystalline quartz aggregate indicated [Sn Foliation represented by yellow arrow on all pictures]..... 61

Figure 15 - Core samples (A, D, F, H) and photomicrographs (polarized light) of the protomylonite and mylonites at Peteca. (A) Typical reddish color of the biotite tonalite protomylonite. (B) Fine-grained recrystallized bands mark Sn+1. (C) Mantle-and-core structure of porphyroblast. Blue arrows point myrmekite. Red arrows point flame perthite on the limit of Carlsbad twin. (D) Garnet-quartz mylonite. (E) Sn+1 foliation marked by alteration of augen orthoclase porphyroblast and fragments of garnet and polycrystalline quartz ribbon. Note porphyroblast with core-and-mantle structure and perthites from its boundaries (red arrows). (F) Garnet-biotite mylonite. (G) Narrow strips of chlorite mark Sn+1. Feldspar grain-size reduction by intense illite formation. (H) Yellowish illite granodiorite mylonite on the left in contact with chlorite-illite phyllonite. (I) Anastomosed Sn+1 marked by altered quartz ribbon and illite bands. Note trails of recrystallized grains on the boundaries of quartz (red arrows). (J) Red arrow indicates microfaults in plagioclase. Note sigma-type asymmetric pressure shadow of quartz in plagioclase. 65

Figure 16 - Core samples (A, C) and photomicrographs (polarized light) of the phyllonites at Peteca deposit. (A) Chlorite-illite phyllinite (above) in contact with the mineralized vein. Coarse crystal of Py 1 indicated. (B) Sn+1 foliation marked by all mineral alignments and narrow levels of chlorite and rutile. (C) Carbonate-chlorite phyllonite. Red arrows point narrow veinlets filled by chlorite and rutile as showed on the photomicrograph (D)..... 68

Figure 17 - Veinlets Infill. (A) Calcite crystals with syntax growth fills veinlet; (B) Hand specimen of illite granodiorite mylonite affect by quartz veinlet with pyrite; (C) Infill of quartz and calcite veinlet wrapped by illite halo. Note pyrite crystal is parallel to the veinlet's orientation. (D) The same pyrite on last figure. Black squares indicate location of the next two images. (E) Inclusions of sphalerite and galena on pyrite 1. Greenockite occurs as exsolutions in sphalerite. (F) Intragranular fractures filled by covellite with minor sphalerite in pyrite 1. 69

Figure 18 - Quartz Vein. (A) Photomicrograph of the quartz vein. Its hand specimen is on B. Domain 1 (white lines) represents elongated crystals resulting from syntax growth from the wall toward the center. Domains 2 and 3 are orthogonal to the 1. Blue lines indicate the boundaries of a vein. (B) Narrow white strips correspond to quartz from the domain 3. Red arrows also indicates the cavities in the vein (see. Fig. 9). Note that pyrite 1 crystals is mostly parallel to the Sn. (C) Zoom in of pyrite 1 preview indicate. It is in equilibrium with sphalerite. (D) Image obtained by EDS during SEM analysis. At left, greenockite in exsolution with sphalerite. At right, sphalerite fills fractures and boundaries of sphalerite and minor in pyrite 1..... 71

Figure 19 - Gold mineralization at Peteca Deposit. (A) Gold fills microfractures within pyrite 1 in equilibrium with sphalerite and galena. (B) Pyrite 1 in the vein. (C) Detail of the preview pyrite. It shows fracture filled by gold, chalcopyrite and sphalerite. Gold also occurs in microcavities. Red arrows without mineral label indicates exsolutions identified by SEM analyses, but with no defined composition (main elements: 73.11% O, 6.08% Al, 13.83% Cl, 0.88 Si). 72

Figure 20 – Albite, Potassic, and Propylitic hydrothermal alterations. Core samples are A, C, E, and photomicrographs (polarized light) are B, D, F, G, I, J. SEM image is H. (A) Albite alteration corresponds to the whitish portion in the biotite tonalite core sample. (B) It locally obliterates the former mineral assemblage. (C) Garnet granodiorite exhibit pinkish color due to potassic alteration. (D) Hydrothermal microcline and quartz replace plagioclase along its boundaries and fractures. (E) Garnet granodiorite exhibit orange portion that correspond to a cavity filled by potassic alteration. (F) Photomicrograph shows microcline with minor quartz. (G) Disseminated propylitic alteration in biotite tonalite. (H) SEM analyses exhibit minor phase of pentlandite and chalcopyrite as part of this alteration. (I) Massive calcite and chlorite fill veinlet with minor quartz. (J) Exsolution texture of ilmenite and rutile, besides an isolated allanite crystal in the same preview veinlet. 74

Figure 21 - Chloritic, muscovite-illitic and Fe-Cu hydrothermal alterations at Peteca deposit. (A) Chlorite fills fracture in garnet and appears as a large pseudomorph of biotite crystal. Note that chlorite alters to muscovite/illite from its boundaries and cleavage plans. (B) Reddish color on plagioclase caused by strong illite alteration with Fe hydroxide association. (C) Garnet partially replaced by chlorite. Note muscovite/illite affect garnet, chlorite, and plagioclase. (D) Coarse-grained muscovite disseminated in the quartz-feldspar matrix of the leucogranite. (E) Mineralized vein shows fractures parallel to its walls. These fractures correspond to the reddish structures of the microstructural domain 3 (Fig. 8A, B). White squares indicate the next two images. (F) Intergrowth texture of pyrite 2 and covellite. (G) Image obtained by SEM analyses. Covellite fills fractures and appears as subidiomorphic crystal on the left. Quartz (red arrows) correspond to the microstructural domain 3. The points 1, 2 and 3 correspond to a Se-Ag-Te phase associated with covellite (11-30% S, 24-47% Cu, 0.29% Fe, 5-6% Se, 0.9-2.3% Ag, \leq 1.7% Te). 76

Figure 22 – Core samples and photomicrographs of the Carbonate-Epidote Stockwork alteration at Peteca deposit. (A) Fracture filled by massive epidote, calcite and Fe hydroxide. (B) On the top, epidote fills veinlets. Veinlet with calcite in its centre and goethite on its wall. (C) Microfaults and microfractures filled by leucoxene. Kinematic sinistral indicator in yellow. (D) Red fracture found in the mineralized vein (PT-30). (E) On the centre, calcite presents syntax growth from the wall and fill the core of veinlet massively. Note the cryptocrystalline epidote. (F) Photomicrograph of image C; (G) and (H) are images obtained by SEM analysis. They correspond to the alteration that affects the albitization (see Fig. 11F). Synchysite appears as zoning in monazite. (I) and (J) correspond to the

image D. The dark portions are holes on the thin section. Reddish color observed in hand specimen on D is due to Fe hydroxide, besides siderite found in SEM analyses (J). 78

Figure 23 – Mineral chemistry of plagioclase. (A) Slight variation of Al_2O_3 content compared to Si_2O . (B) Higher content of silica for the biotite tonalite protomylonite compared to its protolith biotite tonalite. (C) Ternary diagram (Deer et al., 1992) confirms the high An content in the protomylonite. (D) Most of the perthite results are on the 9 wt% average of Na_2O 80

Figure 24 - Binary diagrams for mineral chemistry of K-feldspar in the matrix or as phenocrysts and porphyroclasts. 81

Figure 25 - Garnet crystals analysed. (A, B) From the garnet granioriorite. (B-D) From the garnet leucogranite. 82

Figure 26 - Diagrams display mineral chemical results of garnets. (A-B) Binary diagrams denote the higher content of Si_2O in the granodiorite. (C-E) Ternary diagram based on the end members..... 83

Figure 27 - AlIV vs. $\text{Fe}/(\text{Fe}+\text{Mg})$ diagram proposed by Tamizel (2014) classifies all the chemical analyses as biotite..... 84

Figure 28 - Ternary diagrams for mineral chemistry of biotite. (A) Ternary diagram proposed by Foster (1960) classifies trioctahedral micas. (B) Ternary diagram proposed by Natchi et al. (2005) classifies the primary biotite from the re-equilibrated and secondary ones. 84

Figure 29 – Binary diagrams for chemical analyses of chlorite. (A) Si to vs. $\text{Fe}^{2+}/(\text{Fe}^{2+} + \text{Mg}^{2+})$ ratio diagram proposed by Foster (1962). (B) Diagram proposed by Ciesielczuk (2012) classifies the chlorite as Fe-Al Clinochlore and Mg-Chamosite. 85

Figure 30 - Ternary diagrams for white micas applied to illite. (A) According to Deer et al. (1992), the illite corresponds to phengite. (B) Tappert (2013) ternary diagram for white micas classification. (C) Ternary diagram proposed by Velde (1985) represents the chemical composition of white micas. M: muscovite; A: magmatic micas; B: phengite; C: illite; D: illite associated to chlorite; E: illite in sandstones, in the first stages of weathering and in hydrothermal events of granitic rocks. $\text{MR3} = \text{Na} + \text{K} + \text{Ca}$; $2\text{R3} = ((\text{Al}_t) - \text{MR3}/2)$; $3\text{R2} = (\text{Fe} + \text{Mg})/3$. (D) Ternary diagram proposed by Guidotti (1987) to classify white micas. Fmu: ferri-muscovite; Mu: muscovite; Ph: phengite; Fpg: ferri-phengite; Mu: muscovite. 86

Figure 31 - Correlation diagrams for illite. (A) Correlation diagram Al^{VI} vs. $(\text{Fe} + \text{Mg})$. (B) $\text{Al}_{(t)}$ vs. $[\text{Si} + (\text{Fe} + \text{Mg})]$ for the white micas of the Peteca deposit. R = Correlation coefficient. 87

Figure 32 - Ternary diagrams for white micas applied to muscovite. (A) According to Deer et al. (1992), the illite corresponds to phengite. (B) Tappert (2013) ternary diagram for white micas classification. (C) Ternary diagram proposed by Velde (1985) represents the chemical composition of white micas. M: muscovite; A: magmatic micas; B: phengite; C: illite; D: illite associated to chlorite; E: illite in sandstones, in the first stages of weathering and in hydrothermal events of granitic rocks. $\text{MR3} = \text{Na} + \text{K} + \text{Ca}$; $2\text{R3} = ((\text{Al}_t) - \text{MR3}/2)$; $3\text{R2} = (\text{Fe} + \text{Mg})/3$. (D) Ternary diagram proposed by

Guidotti (1987) to classify white micas. Fmu: ferri-muscovite; Mu: muscovite; Ph: phengite; Fpg: ferri-phengite; Mu: muscovite.....	88
Figure 33 - Correlation diagrams for muscovite. (A) Correlation diagram Al^{VI} vs. $(\text{Fe} + \text{Mg})$. (B) $\text{Al}_{(\text{t})}$ vs. $[\text{Si} + (\text{Fe} + \text{Mg})]$ for the white micas of the Peteca deposit. R = Correlation coefficient.....	89
Figure 34 - Diagrams for mineral chemistry of Fe-Ti oxides. (A) Ternary diagram classification according to $\text{Fe}^{2+}\text{Fe}^{3+}\text{Ti}^{4+}$. (B) Ti vs. Fe_{t} diagram. (C) Mg vs. Fe_{t} diagram.	90
Figure 35 - Chlorite crystallization temperatures at the Peteca deposit according to Bourdelle et al. (2013) geothermometer.....	91
Figure 36 – Chlorite crystallization temperatures at the Peteca deposit according to Inoue et al. (2009) geothermometer.....	92
Figure 37 - Illite crystallization temperatures at the Peteca deposit according to Battaglia (2004) geothermometer.....	93
Figure 38 - Muscovite crystallization temperatures at the Peteca deposit according to Battaglia (2004) geothermometer.....	94
Figure 39 - Geologic section of oriented drill cores (PT-8, PT-22, PT-12, PT-15) display their lithotypes and both of the shear- and magmatic-hydrothermal systems distributions. The color mix in some portions indicate predominance of more than one hydrothermal alteration.	97
Figure 40 - Geologic section of oriented drill core (PT-30) displays its lithotypes and both of the shear- and magmatic-hydrothermal systems distributions. The color mix in some portions indicate predominance of more than one hydrothermal alteration.	98

LISTA DE TABELAS

Tabela 1 - Geocronologias e ambientes tectônicos das principais unidades geológicas do setor Leste da PAAF (Modificado de Assis, 2015).....	29
Table 2 – Geocronology and tectonic settings of the main geologic units at the eastern sector of AFGP (Modified from Assis, 2015).....	51
Table 3 - Main features of the foliated granitoids, metatonalite, and the microporphyrityc dacite dyke (*% constituent of the rock).	63
Tabela 4 - Distribution of the Hydrothermal Systems according to the lithotypes.	79
Tabela 5 - Shear-hydrothermal evolution at Peteca deposit.	101
Tabela 6 - Magmatic-hydrothermal evolution at Peteca deposit.	104

SUMÁRIO

1. APRESENTAÇÃO.....	19
1.1. INTRODUÇÃO	19
1.2. OBJETIVOS	20
1.3. LOCALIZAÇÃO E VIAS DE ACESSO.....	21
2. MATERIAIS E MÉTODOS	22
2.1. AMOSTRAGENS E DESCRIÇÕES MACROSCÓPICAS.....	22
2.2. DIFRAÇÃO DE RAIOS-X	22
2.3. QUÍMICA MINERAL.....	23
3. CONTEXTO GEOLÓGICO REGIONAL	25
3.1. APRESENTAÇÃO	25
3.2. SETOR LESTE DA PROVÍNCIA AURÍFERA DE ALTA FLORESTA	26
4. SÍNTSEZ DAS PRINCIPAIS CONCLUSÕES DO ARTIGO.....	32
REFERÊNCIAS	33
APPENDIX A.....	40
1. INTRODUCTION	43
2. ANALYTICAL PROCEDURES.....	45
3. REGIONAL GEOLOGICAL SETTING.....	47
3.1. INTRODUCTION	47
3.2. EASTERN SECTOR OF AFGP	48
4. RESULTS	54
4.1 COUNTRY ROCKS.....	58
4.2. HYDROTHERMAL SYSTEMS.....	64
4.2.1. <i>Shear-hydrothermal System</i>	64
4.2.2. <i>Magmatic-hydrothermal System</i>	73
4.3. MINERAL CHEMISTRY	80
4.4. GEOTHERMOMETRY	91
5. DISCUSSIONS	95
5.1. METAMORPHISM	95
5.2. HYDROTHERMAL SYSTEMS	95
5.2.1. <i>Shear-hydrothermal System</i>	99
5.2.2. <i>Magmatic-hydrothermal system</i>	103
5.3. SYNTHESIS OF DISCUSSIONS	108
6. CONCLUSIONS	110
APPENDIX B.....	118
APPENDIX C.....	121
APPENDIX D.....	123
APPENDIX E.....	126
APPENDIX F	149

1. APRESENTAÇÃO

A primeira parte da presente dissertação compreende a introdução da área de estudo e objetivos de pesquisa, materiais e métodos, contexto geológico regional e uma síntese dos resultados obtidos. A segunda parte (Appendix A) corresponde ao artigo científico que será submetido a revista Ore Geology Reviews, o qual contém os resultados em detalhe, discussões e conclusões. Os demais apêndices correspondem a localização e análises realizadas por amostras (Appendix B), composição modal das rochas encaixantes e produtos de cisalhamento (Appendix C), resultados das análises de difração de raios-X (Appendix D), resultados das análises de química mineral (Appendix E), resultados de geotermômetros aplicados (Appendix F).

1.1. INTRODUÇÃO

A Província Aurífera de Alta Floresta (PAAF) localiza-se na porção sul do Cráton Amazônico, norte do estado de Mato Grosso. Representa uma área alongada de 500 km de extensão que ocorre em um *trend* NW-SE, que é limitada ao norte pelo Gráben do Cachimbo e ao sul pelo Gráben dos Caiabis (Barros, 2007).

Os depósitos primários na PAAF podem ser subdivididos em (Assis et al., 2017):

- (1) Au ± Cu disseminado (e.g. Luizão, Serrinha, Juruena, X1 e Pé Quente) e Au ± Cu tipo-veio (e.g. Paraíba, Pezão); (2) Au ± Mo ± Cu disseminados (e.g., Ana and Jaca); e (3) Au + Zn + Pb ± Cu tipo-veio em ambiente rúptil (e.g., Franscisco, Bigode, and Luiz).

A mineralização do Peteca, principal alvo desta área, é associada a sulfetos em veio de quartzo principal (filão) com direção N70-80W/N60-90E, hospedado em filonito (Teixeira, 2015). As rochas encaixantes são granitoides foliados de composição granodiorítica a tonalítica de idade entre 2,04 a 1,98 Ga além de intrusões dacíticas de idade 2,01Ga (Quispe, 2016). Todo o arcabouço do depósito apresenta intensas zonas de alteração hidrotermal, além de vênulas extensionais de até 4 cm de espessura, compostas por quartzo, carbonato, sulfetos (Teixeira, 2015).

Zonas de cisalhamento atuam como condutos de fluidos mineralizantes ou como remobilizadores de depósitos minerais preexistentes. Isto é possível devido diversos fatores, tais como: presença de fraturas e falhas, diferenças de pressões litostática e de fluido, calor gerado durante os esforços cisalhantes que facilitam o transporte de soluções aquosas com metais. Os compostos iônicos se aglutinam entre si de acordo com as afinidades químicas e, após o resfriamento do fluido, se precipitam e têm-se veios de quartzo mineralizados a ouro e

outros metais, formados nos sítios de dilatação (Groves et al., 1998; Goldfarb et al., 2005; Bons et al., 2012).

A influência de fluidos em processos de deformação resultam em mecanismos de abrandamento que são importantes para a evolução de ZCs, tais como: enfraquecimento hidrolítico, reações de abrandamento, redução do tamanho dos grãos, desenvolvimento de grãos com orientação preferencial e menos resistentes (Griggs, 1967; Tullis and Yund, 1980; Hippert, 1998; Stünitz & Tullis, 2001; Yonkee et al., 2003; Mancktelow & Pennacchioni; Fusseis & Handy, 2008; Hartman et al., 2010; Jaquet & Schmalholz, 2018; Lee et al., 2018).

A interação fluido-rocha ocasiona desequilíbrio nos minerais devido às novas condições de temperatura, pressão e constituintes químicos do fluido. Isto gera transformações mineralógicas, químicas e texturais para fases de maior equilíbrio, que resulta em alterações hidrotermais através de metassomatismo (Barnes, 1997; Putnis & Austrheim, 2010). Características das rochas como permeabilidade e porosidade controlam a infiltração do fluido, nas quais são gerados halos ou zonas de alterações hidrotermais que são importantes guias prospectivos para exploração mineral (Zhu et al., 2011).

Depósitos filonares de Au ± Cu como Pezão e Paraíba, apresentam relações com plútôns graníticos apontados como fonte para calor, fluidos e metais em sistemas magmático-hidrotermais (Trevisan, 2015). O depósito do Pezão foi classificado como um sistema de depósito epitermal rico em Au-Cu de baixa sulfatação. E o Paraíba apresenta divergências quanto ao modelo metalogenético, uma vez que apresenta características correlacionáveis aos depósitos tipo pôrfiro (Seedorff et al., 2005; Sillitoe, 2011), IRGS (Lang & Baker, 2001) e ouro orogênico (Groves et al., 1998).

1.2. OBJETIVOS

A presente dissertação de mestrado é centrada na diferenciação das alterações hidrotermais do depósito Peteca, quanto à influência de processos hidrotermais de cisalhamento e hidrotermais-magmáticos ocorridos. Busca-se obter a evolução paragenética hidrotermal do depósito. Os objetivos específicos para atingir o objetivo geral são:

- Definição dos litotipos;
- Definição de microestruturas de deformação nos litotipos;
- Caracterização das alterações hidrotermais e da mineralização a partir de:
 - ✓ Definição de seus estilos de ocorrência e abrangências no depósito;
 - ✓ Caracterizações petrográficas;

- ✓ Caracterizações das diferenças mineralógicas e químicas das principais assembleias minerais dos litotipos hospedeiros ao minério, para os hidrotermais e do veio mineralizado;
- ✓ Definição de diferentes fases de geração de sulfetos e suas relações temporais e espaciais com a mineralização;
- ✓ Compreensão da evolução hidrotermal.

1.3. LOCALIZAÇÃO E VIAS DE ACESSO

A PAAF situa-se na porção norte do estado de Mato Grosso, a cerca de 700 km de Cuiabá, capital do estado. O setor leste da Província abrange parte das cidades de Peixoto de Azevedo, Matupá, Nova Guarita, Novo Mundo e Guarantã do Norte. O depósito do Peteca ocorre no distrito de Flor da Serra, pertencente ao município de Peixoto de Azevedo – MT (Fig.1).

O acesso se faz de avião até a cidade de Sinop, onde o acesso à cidade de Peixoto de Azevedo inicia-se pela rodovia federal BR-163. De Peixoto de Azevedo até a área de estudo, a distância de menos de 40 km é percorrida em estradas locais não pavimentadas.

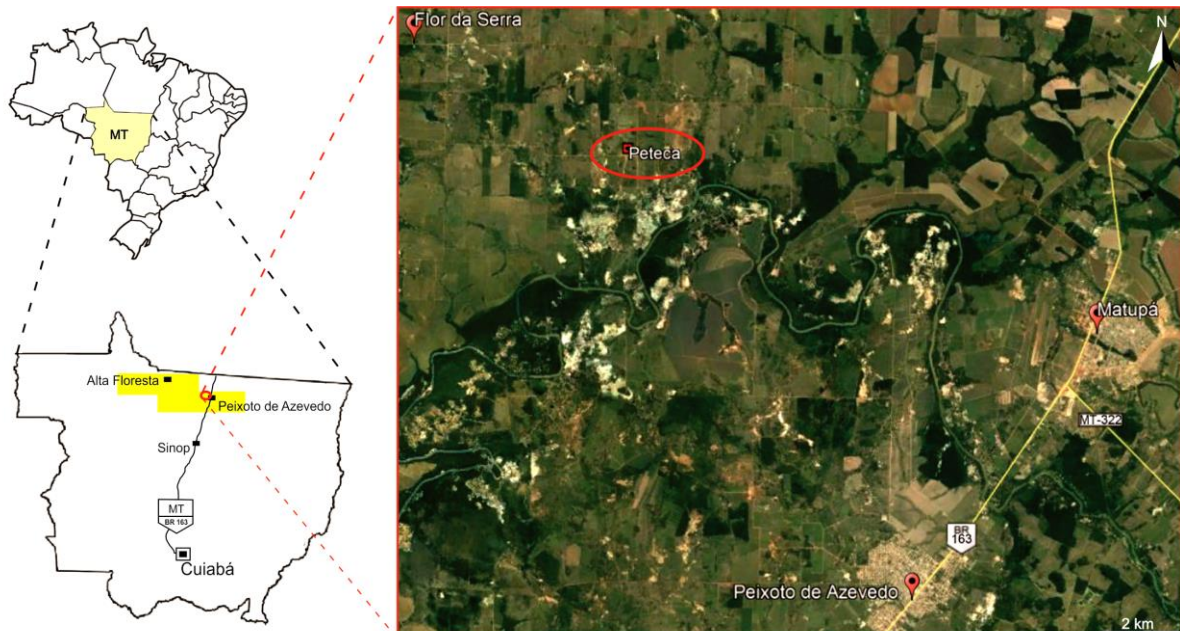


Figura 1 - Localização do depósito Peteca. Polígono em amarelo representa a Província Aurífera de Alta Floresta (PAAF) no MT. Círculo em vermelho indica a localização do alvo Peteca no setor Leste da PAAF. Imagem de satélite mostra os municípios de Matupá, Peixoto de Azevedo e o distrito de Flor da Serra nas proximidades do depósito.

2. MATERIAIS E MÉTODOS

2.1. AMOSTRAGENS E DESCRIÇÕES MACROSCÓPICAS

As descrições macroscópicas dos litotipos do depósito do Peteca se realizaram a partir de cinco testemunhos de sondagem orientados (PT-8, PT-12, PT-15, PT-22, PT-30), além de seis amostras não orientadas provenientes da pilha de concentração de minério, e três amostras orientadas da galeria da mina. O Apêndice B contém as coordenadas para localização dos furos de sondagem e respectivas profundidades máximas, além da relação de todas as análises realizadas por amostras.

Todas as descrições foram realizadas para definição das rochas encaixantes e hospedeiras, alterações hidrotermais e seus estilos, tipos de vênulas e distribuição de sulfetos e minério. Foram coletadas amostras de diversas características e 47 lâminas polidas foram analisadas a partir de microscópio óptico da marca Leica DM-EP, no Instituto de Geociências da Universidade de Campinas, Brasil.

Durante as análises microscópicas foram descritas assembleias minerais ígneas, hidrotermais e metamórficas, além de microestruturas. Maior detalhamento foi dado às transformações minerais nas alterações hidrotermais, das rochas distais à mineralização. Para as amostras menos deformadas, a composição modal final corresponde a média de composições estimadas em porcentagem de 12 partes iguais da lâmina. As abreviações dos minerais utilizadas basearam-se em Whitney & Evans (2010).

A partir das análises sob microscópio petrográfico, 14 lâminas polidas foram selecionadas e analisadas sob microscópio eletrônico de varredura (MEV) de marca LEO 430i (ZEISS), acoplado a um espectrômetro de raios-X por dispersão de energia (EDS) no Instituto de Geociências da Universidade de Campinas, Brasil. As condições operacionais padrão incluíram potencial de aceleração de 15 kV, corrente de feixe de 3 nA e distância focal de 19 mm.

2.2. DIFRAÇÃO DE RAIOS-X

Outra etapa pertinente para complementação dos estudos petrográficos foi a realização de análises de Difrações de Raios-X. O veio mineralizado apresenta cavidades de até dois centímetros de diâmetro, preenchidas por material criptocristalino. A fim de determinar a assembleia mineral nas cavidades, foram selecionadas 6 amostras diferentes de até 3g cada para análises de Difratometria de Raios X (LDRX). Foram realizadas através de difratômetro Siemens (Bruker) D-5000, no Laboratório de Difrações de Raios-X do Instituto de Geociências (IGEO) da Universidade Federal do Rio Grande do Sul (UFRGS).

2.3. QUÍMICA MINERAL

Ao todo, 11 lâminas polidas foram selecionadas (Apêndice B) a partir da etapa de petrografia para análises de química mineral através de microssonda eletrônica (EPMA - Electron Probe Microanalyzers). Estas análises foram realizadas no Laboratório de Microssonda Eletrônica do Instituto de Geociências (IGEO) da UFRGS (Fig. 2).



Figura 2 - Infraestrutura para análise de EPMA. (A) Infraestrutura utilizada para higienização das lâminas delgadas polidas. A direita encontra-se a metalizadora. (B) Microssonda eletrônica Cameca SXFive. (C) Detalhe de processamento dos dados através do software Peak Sight 5.1.

Primeiramente, as lâminas foram higienizadas, recobertas por carbono através de uma metalizadora da marca Jeol JEE 4B. A microssonda eletrônica utilizada é da marca Cameca SXFive, acoplada com WDS (Wave Dispersive X-Ray Spectrometer) e EDS. As condições operacionais padrão foram: potencial de aceleração de 15 kV ou 20 kV (sulfetos), corrente de feixe de 15 nA, 10 nA (micas e óxidos muito finos) ou 20 nA (sulfetos) e diâmetro do feixe de 5 μm . Os dados brutos adquiridos sob porcentagens de óxidos em peso foram recalculados para obter a distribuição catiônica através do software AX (<https://www.esc.cam.ac.uk/research/research-groups/holland/ax>).

2.4. GEOTERMOMETRIA

Temperatura de cristalização da clorita foi empiricamente obtida através de geotermômetros propostos por Bourdelle et al. (2013) e Inoue et al (2009). Pressão e temperaturas muito altas não são consideradas em ambos os métodos, apenas membros finais selecionados. O geotermômetro proposto por Bourdelle et al. (2013) baseia-se no diagrama Si

vs. R2+ proposto por Wiewióra & Weiss (1990). Temperatura de cristalização de mica branca foi obtidas através do geothermômetro proposto por Bataggia (2004), no qual o conteúdo de K e correlação entre Fe e Mg são considerados. O apêndice E contém os resultados de geotermometria da clorita e mica branca.

3. CONTEXTO GEOLÓGICO REGIONAL

3.1. APRESENTAÇÃO

O Cráton do Amazonas está localizado na porção setentrional da América do Sul, cercado por cinturões orogênicos neoproterozoicos (Fig. 3). Segundo Silva & Abram (2008), a evolução geotectônica do Cráton foi considerada por diversos autores (Almeida, 1977; Hasui et al., 1984) como resultado de sucessivos eventos orogênicos, formando paleocontinentes. A atual concepção mais aceita baseia-se na evolução de eventos orogênicos que formaram sucessivos arcos magmáticos (Cordani & Teixeira, 1981; Tassinari, 1981; Tassinari & Macambira, 1999; Tassinari et al., 2000; Santos et al., 2000). A formação de crosta juvenil e retrabalhamento do material mais antigo ocorreram durante o arqueano e paleoproterozoico, respectivamente representando 30% e 70% da crosta continental do Cráton Amazônico (Tassinari & Macambira, 1999).

Com base em dados geocronológicos a partir de datações U-Pb em zircões e de isótopos Sm-Nd, Santos et al. (2000) compartimentaram o Cráton Amazônico em sete províncias tectono-estruturais: (i) Carajás (3,0-2,5 Ga); (ii) Amazônia Central (Arqueano); (iii) Transamazonas (2,26-2,01 Ga); (iv) Tapajós-Parima (2,03-1,88 Ga); (v) Rio Negro (1,82-1,62 Ga); (vi) Rondônia-Juruena (1,82-1,54 Ga); (vii) Sunsás e K'Mudku (1,45-1,10 Ga) (Fig. 3).

Neste modelo, a PAAF abrange parte da Província Tapajós-Parima e Rondônia-Juruena. A PAAF é constituída por sucessivas sequências plutono-vulcânicas acrescidos a Província Amazônica Central durante o Paleoproterozoico e Mesoproterozoico (Tassinari & Macambira, 1999; Santos, 2006; Silva & Abram, 2008).

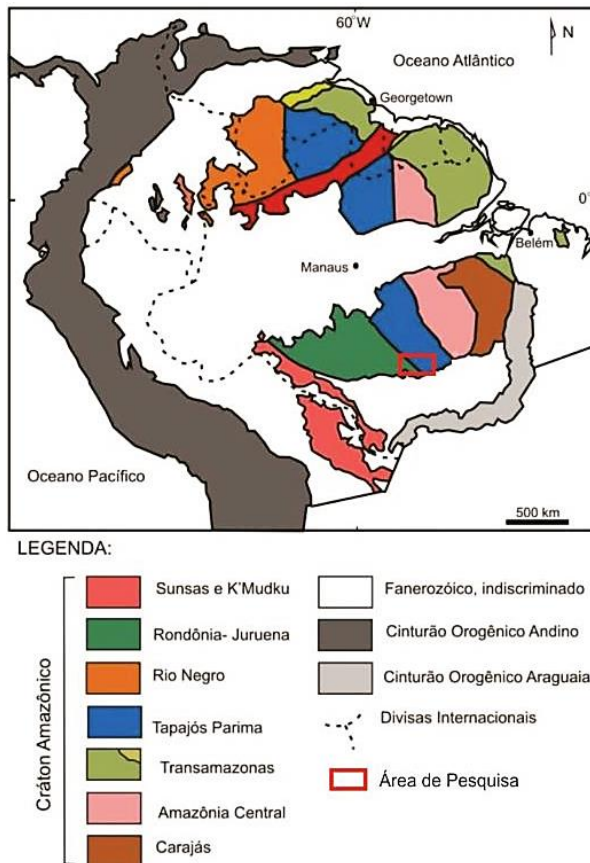


Figura 3 - Compartimentação Geotectônica do Cráton Amazonas segundo Santos et al. (2000). Polígono vermelho: setor leste da PAAF (Extraído de Silva, 2014).

3.2. SETOR LESTE DA PROVÍNCIA AURÍFERA DE ALTA FLORESTA

Na região de Peixoto de Azevedo, o Lineamento Peru-Trairão tem alinhamento NW-SE e hospeda centenas de depósitos de ouro (Barros, 2007; Fig. 4). Afeta rochas do embasamento arqueano, granitoides paleoproterozóicos, e as interceptam como zonas de cisalhamento descontínua-contínua sinistral.

Os depósitos primários associados a este Lineamento são hospedados em suítes plutônio-vulcânicas paleoproterozóicas (Barros, 2007; Miguel Jr., 2011; Assis et al., 2014), que são afetadas por diques maficos (Quispe, 2016). As interceptações de cisalhamento nos granitoides apresentam um sistema de mineralização em veios de quartzo sub-verticais e anastomosados. A mineralização aurífera em filões é a mais comum na região com teores <5g Au/t, seguida de depósitos em sistemas de veios em *stockworks* e mineralizações disseminadas.

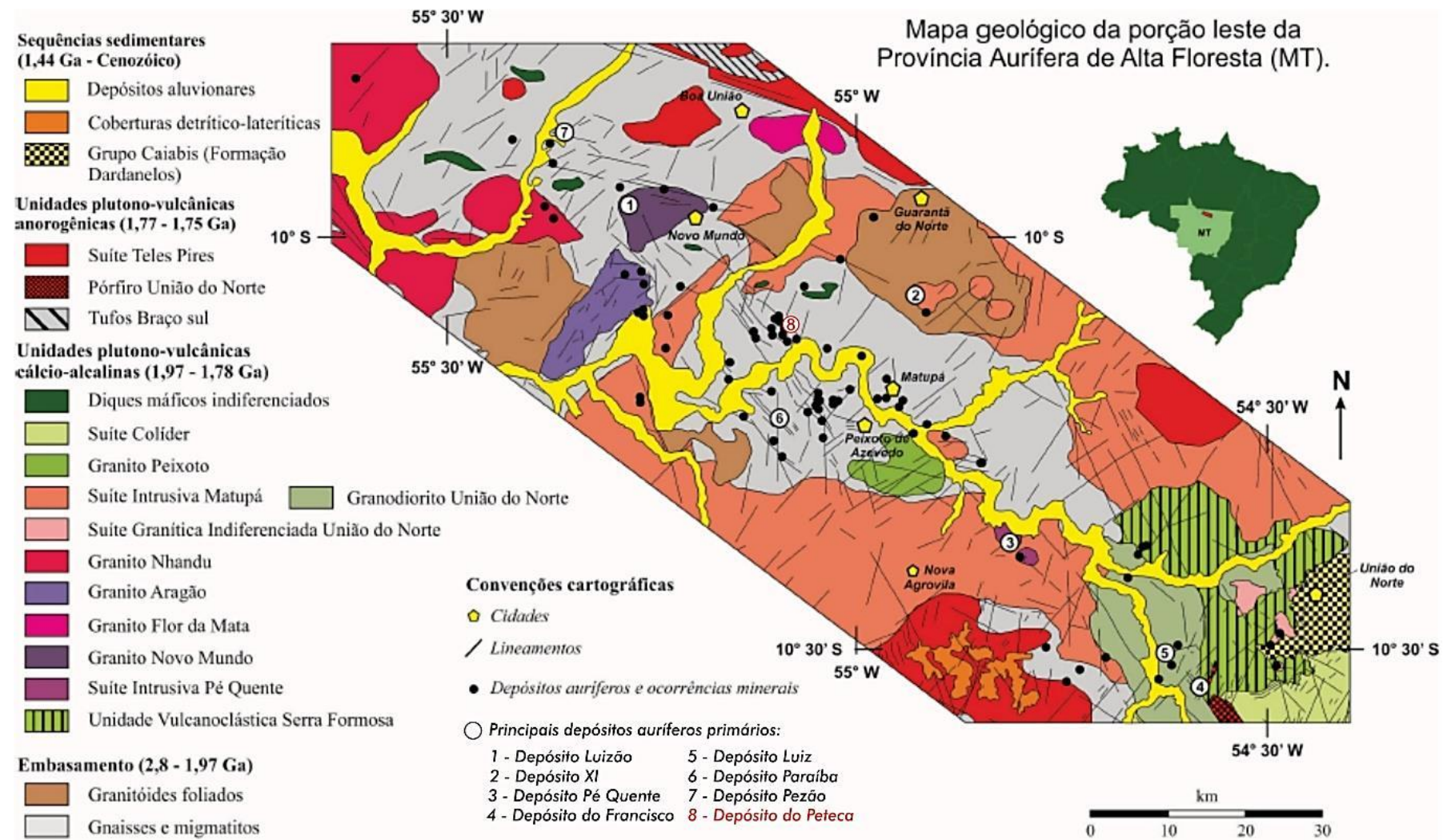


Figura 4 - Mapa geológico do Setor Leste da PAAF com principais depósitos auríferos associados ao Lineamento Peru-Trairão e destaque em vermelho para o Depósito Peteca (Assis, 2015 - Modificado de Miguel-Jr, 2011).

No setor leste da PAAF, as diferentes unidades presentes nesta área se subdividem em: (a) embasamento (2,8-1,9 Ga; Souza et al., 2005; Barros, 2007; Assis, 2015), (b) sequências plutono-vulcânicas cálcio-alcalinas (1,97-1,71 Ga; Barros, 2007; Assis, 2015; Trevisan, 2015; Quispe, 2016; Oliveira, 2017), (c) sequências pós-orogenicas e anorogênicas (1,77-1,75 Ga), e (d) sequências sedimentares (1,3 Ga-Quaternário; Leite & Saes, 2003; Souza et al., 2005) (Tab. 1).

A região do distrito de Flor da Serra, município de Peixoto de Azevedo, apresenta dobras e zonas de cisalhamento contínuas de direção NW-SE (Cunha, 1996; Phani et al., 2014; Quispe, 2016). Estas zonas de cisalhamento (ZC) denominam-se Joaquim (ZCJ), Paraíba, (ZCP), Peteca (ZCP) e Serinha (ZCS), de oeste para leste (Quispe, 2016; Fig.5). Os depósitos de ouro Paraíba e Peteca estão hospedados nas zonas de cisalhamento homônimas. Cunha (1996) definiu um segundo tipo de lineamento estrutural atribuído às drenagens da região, tais como falhas sinistrais NW, zona de cisalhamento contínua com direção aproximada de NS, e zona de cisalhamento descontínua NE.

Tabela 1 - Geocronologias e ambientes tectônicos das principais unidades geológicas do setor Leste da PAAF (Modificado de Assis, 2015).

DOMÍNIOS GEOLÓGICOS	UNIDADES GEOLÓGICAS	IDADES (Ma)	AMBIENTES TECTÔNICOS	REFERÊNCIAS
Sequências Sedimentares	Coberturas Tercio-Quaternárias Sedimentos clásticos e pelitos inconsolidados	Terciário Quaternário	Sedimentos intracratônicos inconsolidados	Souza <i>et al.</i> (2005)
	Grupo Caiabis (Formação Dardanelos) Arenito e arenito arcoseano com níveis conglomeráticos e estratificações plano-paralelas e cruzadas acanaladas	$1,987 \pm 4$ a $1,377 \pm 13$	Bacia pull-apart ou strike-slip	Saes & Leite (2003), Souza <i>et al.</i> (2005)
Unidades plutono-vulcânicas anorogênicas (Tipo A)	Grupo Batistão Riolito maciço microesferulítico, quartzo feldspato pôrfiro	Idade desconhecida	Anorogênico (dados isotópicos não disponíveis)	Quispe (2016)
	Suite Intrusiva Teles Pires Álcali-feldspato granito, granito porfírico, granófiros, riolito, riódacito, dacito, andesito, tufo, brechas e ignimbrito.	$1,782 \pm 17$ a $1,757$ (U-Pb)	Pós-colisional ($1,94 < \text{Tdm} < 2,28$; $-3,4 < \epsilon\text{Nd(t)} < +3$)	Santos (2000), Pinho <i>et al.</i> (2001), Souza <i>et al.</i> (2005), Silva & Abram (2008)
	Pôrfiro União do Norte Álcali-feldspato granito a monzogranito porfírico	$1,774 \pm 7,5$	Pós-colisional (dados isotópicos não disponíveis)	Assis (2011); Miguel-Jr (2011)
Unidade plutono-vulcânicas cálcio-alcalinas (Granitos tipo-I)	Suite Colider Rochas vulcânicas, subvulcânicas, piroclásticas e epiclásticas intermediárias a ácidas.	$1,786 \pm 17$; $1,785 \pm 6,3$; $1,781 \pm 8$	Arco vulcânico a sin-colisional ($1,94 < \text{TDM} < 2,34$; $-3,4 < \epsilon\text{Nd(t)} < +3$)	JICA/MMAJ (2000), Silva & Abram (2008), Pimentel (2001)
	Granito Peixoto Biotita granodiorito e biotita tonalito	$1,792 \pm 2$ (Pb-Pb), 1781 ± 10 (U-Pb)	Arco vulcânico sin-colisional (dados isotópicos não disponíveis)	Barros (2007), Silva <i>et al.</i> (2014)
	Suite Granodiorítica União Biotita-hornblenda granodiorito e biotita-hornblenda tonalito	$1,853 \pm 23$ (LA-ICP-MS)	Granitos de arco vulcânico (dados isotópicos não disponíveis)	Assis (2011), Miguel-Jr (2011)
	Suite Granítica Indiferenciada União do Norte Sienogranito, monzogranito, sienito e quartzo-monzonito	Idade desconhecida	Granitos de arco vulcânico (dados isotópicos não disponíveis)	Assis (2008)
	Suite Intrusiva Matupá Biotita granito, biotita monzogranito, hornblenda monzogranito, biotita hornblenda monzonito, hornblenda monzodiorito, biotita hornblenda monzogranito, biotita monzogranito porfírico, biotita monzogranito, biotita sienogranito e sienomonzogranito porfírico-rapakivi	$1,872 \pm 12$ (Pb-Pb); $1,875 \pm 13$ a $1,851 \pm 12$ (U-Pb)	Arco vulcânico sin-colisional ($2,15 < \text{TDM} < 2,34$; $-4,3 < \epsilon\text{Nd(t)} < +3,04$)	Moura (1998), Souza <i>et al.</i> (2005), Assis (2011), Silva <i>et al.</i> (2014), Rocha <i>et al.</i> (2016), Oliveira (2017)

Unidade plutono-vulcânicas cálcio-alcalinas (Granitos tipo-I)	Suite Nhandu (Dezula et al., 2018)	Granito Nhandu	$1,889 \pm 17$; $1,879 \pm 5.5$ (U-Pb) e $1,848 \pm 17$; 1969 ± 2 a 1946 ± 21 (U-Pb)	Arco vulcânico sin-colisional ($2.14 < TDM < 2.17$; $\epsilon Nd(t) = -0.91$)	Moreton & Silva (2005), Silva & Abram (2008), JICA/MMAJ (2000), Rocha et al. (2016)
		Granito Aragão	$1,931 \pm 12$ (U-Pb); $1,964 \pm 11$ (U-Pb); $1,967 \pm 2$ (U-Pb);	Arco vulcânico (dados isotópicos não disponíveis)	Vitório (2010), Miguel-Jr (2011), Ramos (2011), Dezula et al. (2018)
	Granito Flor da Mata	Álcali-feldspato granito, sienogranito e rochas monzoníticas a granodioríticas	Idade desconhecida (correlacionada ao Granito Novo Mundo)	Arco vulcânico (dados isotópicos não disponíveis)	Ramos (2011)
	Granito Novo Mundo	Sienogranito, monzogranito, granodiorito, quartzo-monzonito e monzonito	$1,970 \pm 3$ a $1,964 \pm 1$ (Pb-Pb)	Arco vulcânico sin-colisional ($2.55 < TDM < 2.76$; $-7.62 < \epsilon Nd(t) < -4.48$)	Barros (2007)
	Suite Intrusiva Pé Quente	Monzonito, quartzo-monzonito, quartzo-monzdiorito, monzdiorito, albítito fino, granodiorito aplítico e biotita tonalito	$1,979 \pm 31$ (U-Pb) a $1,901 \pm 7$ (U-Pb)	Arco vulcânico (dados isotópicos não disponíveis)	Assis (2011), Miguel-Jr (2011), Assis (2015)
	Unidade Vulcanoclástica Serra Formosa	Arenito, grauvaca, arenito-lítico e conglomerado arenoso polimítico matriz-suportado	Idade mínima: 2,009	Bacia de ante-país retro-arco em margem continental ativa (dados isotópicos não disponíveis)	Assis (2011), Miguel-Jr (2011)
Unidade plutono-vulcânicas cálcio-alcalinas (Granitos tipo-I) - Granitoides Foliados	Granitoides foliados	Biotita granito, hornblenda-quartzo diorito, hornblenda-biotita monzogranito, tonalito, biotita tonalito, dacitos, granada-muscovita leucogranito e granodiorito geralmente foliados	$1,998$ (Pb-Pb); $2,037 \pm 6$ a $1,978 \pm 8$ (U-Pb)	Arco vulcânico ($2.18 < TDM < 2.67$; $-2.14 < \epsilon Nd(t) < -3.84$)	Barros (2007), Assis (2015), Trevisan (2015), Quispe (2016), Oliveira (2017)
Embassamento	Gnaisses e migmatitos	Gnaisse gavião, anfibolito e ortognaisse de composição monzonítica, tonalítica e granítica, parcialmente migmatizados	$2,816 \pm 4$ (U-Pb) a $1,980 \pm 9$ (U-Pb)	Arco vulcânico (dados isotópicos não disponíveis)	Souza et al. (2005), Barros (2007), Assis (2015)

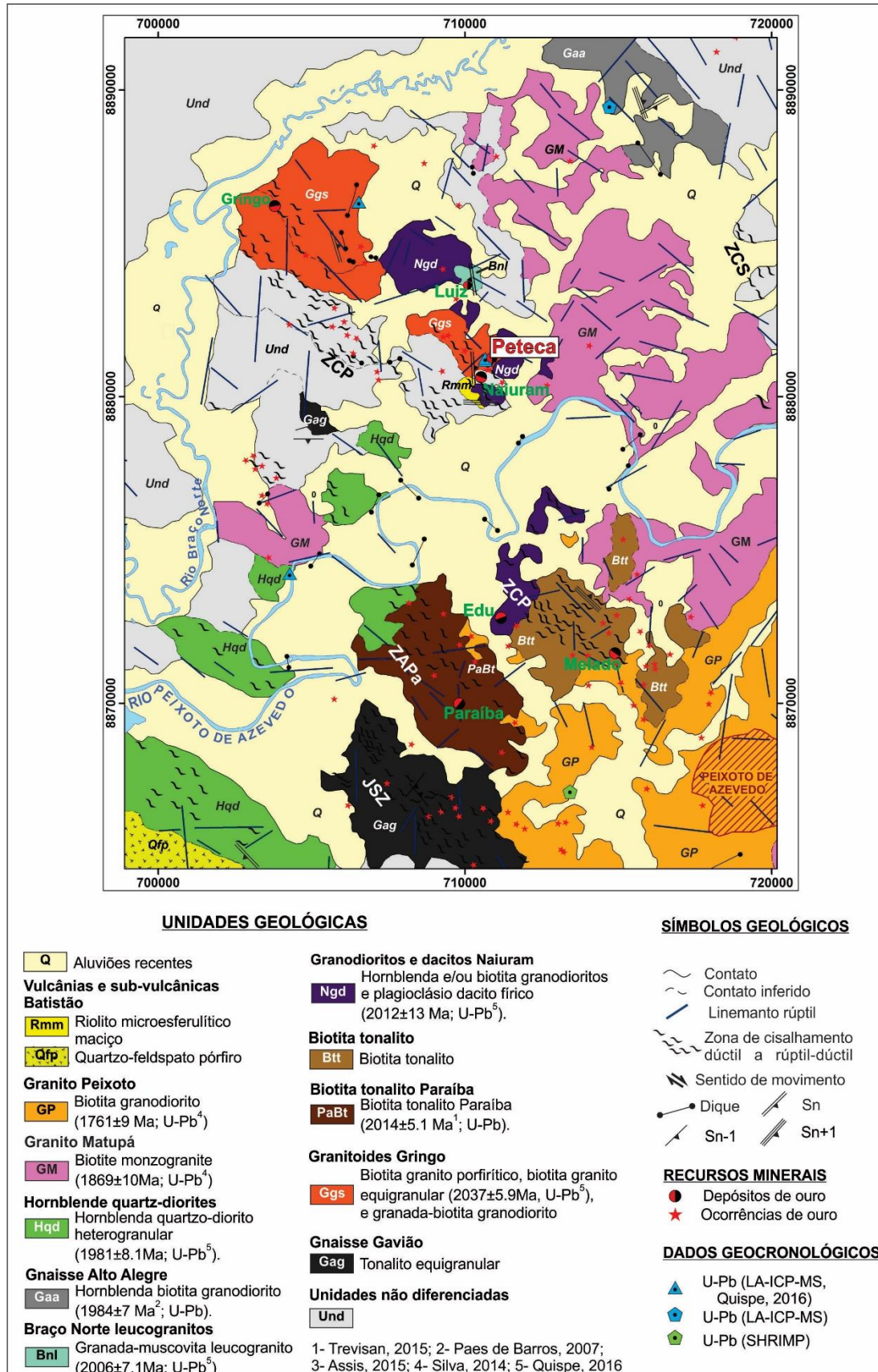


Figura 5 – Mapa Geológico da região de Peixoto de Azevedo e indicação do Depósito Peteca (Quispe, 2016).

4. SÍNTESE DAS PRINCIPAIS CONCLUSÕES DO ARTIGO

- (1) Rochas encaixantes do depósito do Peteca: granitoides foliados (granada granodiorito, granada leucogranito, biotita tonalito), biotita metatonalito, diques de dacito microporfirítico e pegmatitos.
- (2) Evento metamórfico: geração do biotita metatonalito e provável foliação S_n nos granitoides foliados.
- (3) Sistema de Cisalhamento-Hidrotermal gerou protomilonito, milonitos, filonitos, vênulas, veio de quartzo e mineralização, além da foliação S_{n+1} .
- (4) Sistema Magmático-Hidrotermal compreende alterações hidrotermais sem orientação preferencial.
- (5) As temperaturas de cristalização da clorita apresentam média de $350^\circ \pm 20^\circ\text{C}$, mas há aumento de temperatura do Sistema de Cisalhamento-Hidrotermal para o Sistema Magmático-Hidrotermal, de 369°C para $394^\circ \pm 20^\circ\text{C}$. Este aumento de temperatura também ocorre para a mica branca (illita e muscovita), variando de $288^\circ\text{-}304^\circ\text{C}$ no primeiro sistema para $275^\circ\text{-}314^\circ\text{C}$ no sistema posterior.
- (6) O Peteca corresponde à um depósito tipo-veio de $\text{Au}\pm\text{Cu}$, resultante de três estágios principais, em ordem temporal: metamorfismo, Sistema de Cisalhamento-Hidrotermal e Sistema Magmático-Hidrotermal.

REFERÊNCIAS

- Almeida F.F.M. 1977. *Tectonic map of South América*, 1:5.000.000 - Explanatory note. Trabalho elaborado em parceria com CGMW e UNESCO. Brasília: DNPM, 23 p.
- Amaral G. 1974. Geologia Pré-Cambriana da região amazônica. Tese de Livre Docência, Instituto de Geociências, Universidade de São Paulo, São Paulo, 212p.
- Antignano A. & Manning C.E. 2008. Rutile solubility in H₂O, H₂O–SiO₂, and H₂O–NaAlSi₃O₈ fluids at 0.7–2.0 GPa and 700–1000°C: Implications for mobility of nominally insoluble elements. *Chemical Geology*, **255**: 283–293.
- Assis R. R. 2008. Contexto geológico e associação paragenética das mineralizações auríferas de União do Norte, região de Peixoto de Azevedo, Província de Alta Floresta (MT). Trabalho de Conclusão de Curso, Instituto de Geociências, Universidade Estadual de Campinas, 77p.
- Assis R.R. 2011. Depósitos auríferos associados ao magmatismo granítico do setor leste da Província de Alta Floresta (MT), Craton Amazônico: tipologia das mineralizações, modelos genéticos e implicações prospectivas. Dissertação de Mestrado, Instituto de Geociências, Universidade Estadual de Campinas, 462p.
- Assis, R.R., Xavier, R.P., Trevisan, V.G., Creaser, R., Paes de Barros, A.J. 2014. Re-Os sulfide ages for the Paleoproterozoic disseminated Au-porphyry from the Alta Floresta Gold Province: Amazon Craton (Mato Grosso). In: 47º Congresso Brasileiro de Geologia, Salvador.
- Assis R.R. 2015. Depósitos auríferos associados ao magmatismo félscio da Província de Alta Floresta (MT), Cráton Amazônico: litogegeoquímica, idade das mineralizações e fonte dos fluidos. Tese de Doutorado, Instituto de Geociências, Universidade Estadual de Campinas, 363p.
- Assis R.R., Xavier R.P., Creaser R.A. 2017. Linking the Timing of Disseminated Granite-Hosted Gold-Rich Deposits to Paleoproterozoic Felsic Magmatism at Alta Floresta Gold Province, Amazon Craton, Brazil: Insights from Pyrite and Molybdenite Re-Os Geochronology. *Economic Geology*, **112**: 1937–1957.
- Baker J.H. 1985. Rare earth and other trace element mobility accompanying albitization in a Proterozoic granite, W. Bergslagen, Sweden. *Mineralogical Magazine*, **49**: 107-15.
- Barnes, H. L. 1997. *Geochemistry of Hydrothermal Ore Deposits*. John Wiley and Sons (ed.), Inc. New York., 798p.
- Barros A.J.P. 2007. Granitos da região de Peixoto de Azevedo – Novo Mundo e mineralizações auríferas relacionadas – Província Aurífera Alta Floresta (MT). Tese de Doutorado, Instituto de Geociências, Universidade Estadual de Campinas, Campinas, 154p.
- Battaglia S. 2004. Variations in the chemical composition of illite from five geothermal fields: a possible geothermometer. *Clay Minerals*, **39**: 501–510.

- Blenkinsop T.G., Oliver N.H.S., Dirks P.G.H.M., Nugus M., Tripp G., Saniskav I. (no prelo). 2018. Structural geology applied to the evaluation of hydrothermal gold deposits. (Aceito ainda sem data de publicação).
- Bourdelle F. & Cathelineau M. 2015. Low-temperature chlorite geochemistry: a graphical representation based on a T-R2 + - Si diagram. *Eur. J. Miner.*, **27**: 617- 626.
- Bons P.D., Elburg M.A., Gomez-Rivas, E. 2012. A review of the formation of tectonic veins and their microstructures. *Journal of Structural Geology*, **43**:33–62, doi:10.1016/j.jsg.2012 .07.00
- Ciesielczuk J. 2012. Chlorite of hydrothermal origin in the Strzelin and Borów granites (Fore-Sudetic Block, Poland). *Geological Quarterly*, **56(2)**: 333-344.
- Ciobanu C.L., Cook N.J., Spry P.G. 2006. Preface – Special Issue: Telluride and selenide minerals in gold deposits – how and why? *Mineralogy and Petrology*, **87**: 163–169.
- Costa J.B.S. & Hasui, Y. 1997. Evolução geológica da Amazônia. In: Costa, M. L. da; Angélica, R. S. Contribuições à geologia da Amazônia. Belém: SBG-NO, 15-90.
- Cruz Filho B.E., Conceição H., Rosa M.L.S., Rios D.C., Marinho M.M. 2005. Química mineral e condições de colocação do batólito trondhjemítico Nordestina, Núcleo Serrinha, Bahia. *Revista Brasileira de Geociências*, **35(4)**: 83-92.
- Deer W.A., Howie R.A., Zussman J. 1992. *An introduction to rock-forming minerals*. 2nd Ed., Essex. Longman Scientific & Technical. 696p.
- Dezula S.E.M., Barros M.A.S.Ab. Santos J. J.O. Rafael Rodrigues Assis R.R.. Granito Aragão — Suíte intrusiva Nhandú — um granito oxidado, tipo A2, de 1967 a 1964 Ma na Província Aurífera Alta Floresta — Cráton Amazônico. *Revista do Instituto de Geociências (USP)*, **(18)**: 3-20.
- Drake H., Tullborg E., Annersten H. 2008. Red-staining of the wall rock and its influence on the reducing capacity around water conducting fractures. *Applied Geochemistry*, **23**:1898-1920.
- Einaudi, M.T., Hedenquist, J.W., Inan, E.E. 2003. Sulfidation state of fluids in active and extinct hydrothermal systems: transitions from porphyry to epithermal environments. *Society of Economic Geologist and Geochemical Society, Special Publication 10*. In press: Guggenbach Volume.
- Engvik A. K., Putnis A., Gerald J.D.F., Austrheim H. 2008. Albitization of granitic rocks: the mechanism of replacement of oligoclase by albite. *The Canadian Mineralogist*, **46**:1401-1415.
- Fossen H. & Cavalcante G.C.G. 2017. Shear zones – A review. *Earth-Science Reviews*, **171**: 434-455.
- Foster M.D. 1960. Layer charge relations in the dioctahedral and trioctahedral micas. *The American Mineralogist*, **45**: 383-398.

- Foster M.D. (Ed.) 1962. Interpretation of the Composition of Trioctahedral Micas. In: Foster M.D. (Ed.) *Shorter contributions to general geology*. Geological Survey Professional Paper **354B**: 11-48.
- Fusseis F. & Handy M.R. 2008. Micromechanisms of shear zone propagation at the brittle–viscous transition. *Journal of Structural Geology*, **30**: 1242–1253.
- Gapais, D. 1989. Shear structures within deformed granites: mechanical and thermal indicators. *Geology*, **17**: 1144–1147.
- Goldfarb RJ, Baker T, Dube B, Groves DI, Hart CJR, Gosselin P. 2005. Distribution, character, and genesis of gold deposits in metamorphic terranes: *Econ Geol 100th Anniv*:407-450
- Groves DI, Goldfarb RJ, Gebre-Mariam M, Hagemann SG, Robert F. 1998. Orogenic gold deposits: a proposed classification in the context of their crustal distribution and relationship to other gold deposit types. *Ore Geol Rev*, **13**:7–27.
- Guidotti C.V., Cheney J.T., Henry D.J. 1988. Compositional variation of biotite as a function of metamorphic reactions and mineral assemblage in the pelitic schists of western maine. *American Journal of Science*, **288A**: 270-292.
- Guidotti C.V., Cheney J.T. 1975. Interrelationship between Mg/Fe Ratio and Octahedral Al. content in Biotite. *The American Mineralogist*, **60**: 849-853.
- Hartman S.M., Paterson S.R., Holk G.J., Kirkpatrick J.D. 2018. Structural and hydrothermal evolution of a strike-slip shear zone during a ductile-brittle transition, Sierra Nevada, CA. *Journal of Structural Geology*, **113**: 134-154.
- Hasui Y., Haralyi N.L., Schobbenhaus C. 1984. Elementos geofísicos e geológicos da região Amazônica: subsídios para o modelo geotectônico. In: Simpósio de Geologia da Amazonia, Manaus, SBG, p. 129-147.
- Hayden L.A. & Manning C.E. 2011. Rutile solubility in supercritical NaAlSi₃O₈–H₂O fluids. *Chemical Geology*, **284**: 74-81.
- Hippert J. F. 1998. Breakdown of feldspar, volume gain and lateral mass transfer during mylonitization of granitoid in a low metamorphic shear zone. *Journal of Structural Geology*, **20**:175-193.
- Hedenquist J. 2003. Sulfidation state of hydrothermal fluids: The porphyry-epithermal transition and beyond. Special publication 10, *Society of Economic Geologists and Geochemical Society*, **15**: 1-50.
- Hövelmann J., Putnis A., Geisler T., Schmidt B.C., Golla-Schindler U. 2010. The replacement of plagioclase feldspars by albite: observations from hydrothermal experiments. *Contrib. Mineral Petrol.*, **159**: 43–59.
- Ilmen S., Alansari A., Bajddi A., Maacha L. 2015. Cu-Au vein mineralization related to the Talat n'Imjjad shear zone (western High Atlas, Morocco): geological setting, ore mineralogy, and geochemical evolution. *Arab J Geosci.*, **8**:5039-5056.

- Inoue A., Meunier A., Patrier-Mas P., Rigault C., Beaufort D., Vieillard P. 2009. Application of chemical geothermometry to low-temperature trioctahedral chlorites. *Clays and Clay Minerals*, **57(3)**: 371–382.
- Jacquet Y. & Schmalholz S.M. 2018. Spontaneous ductile crustal shear zone formation by thermal softening and related stress, temperature and strain rate evolution. *Tectonophysics*, **746**: 384-397.
- Jefferies S.P., Holdsworth R.E., Wibberley C.A.J., Shimamoto T., Spiers C.J., Niemeijer A.R., Lloyd G.E. 2006. The nature and importance of phyllonite development in crustal-scale fault cores: an example from the Median Tectonic Line, Japan. *Journal of Structural Geology*, **28**: 220–235.
- JICA/MMAJ. 2000. Metal Mining Agency of Japan/Japan International Cooperation Agency. Report on the Mineral Exploration in the Alta Floresta Area, Brazil, Final Report, Projeto Alta Floresta - MT, Japan, March, 137p.
- Kreuzer O. P. 2006. Textures, paragenesis and wall-roch alteration of lode-gold deposits in the Charters Towers district, north Queensland: implications for the conditions of ore formation. *Mineralium Deposita* 40:639-663.
- Dilles J.H. & Einaudi M.T. 1992. Wall-Rock Alteration and Hydrothermal Flow Paths about the Ann-Mason Porphyry Copper Deposit, Nevada--A 6-Kin Vertical Reconstruction. *Economic Geology*, **87**: 1963-2001.
- Kruhl J.H. 1996. Prism- and basal-plane parallel subgrain boundaries in quartz: a microstructural geothermobarometer. *Journal Metamorphic Geol.*, **14**:581-589.
- Lang J.R. & Baker T. 2001. Intrusion-related gold systems: The present level of understanding. *Mineralium Deposita*, **36**: 477-489.
- Lexa J., Stohl J., Konecný V. 1999. The Banská Štiavnica ore district: relationship between metallogenetic processes and the geological evolution of a stratovolcano. *Mineralium Deposita*, **34**: 639-654.
- Lee A.L., Torvela T., Lloyd G.E., Walker A.M. 2018. Melt organisation and strain partitioning in the lower crust. *Journal of Structural Geology*, **113**: 188-199.
- Leite J.A.D. & Saes G.S. 2003. Geocronologia Pb/Pb de zircões detriticos e análise estratigráfica das coberturas sedimentares proterozóicas do Sudoeste do Cráton Amazônico. *Geologia USP: Série Científica*, **3(1)**:113-127.
- Mancktelowa N.S. & Pennacchioni G. 2004. The influence of grain boundary fluids on the microstructure of quartz-feldspar mylonites. *Journal of Structural Geology*, **26**: 47–69.
- Mancktelowa N.S. & Pennacchioni G. 2005. The control of precursor brittle fracture and fluid–rock interaction on the development of single and paired ductile shear zones. *Journal of Structural Geology*, **27**: 645–661.
- Mark G. 1998. Albite formation by selective pervasive sodic alteration of tonalite plutons in the Cloncurry district, Queensland. *Australian Journal of Earth Sciences*, **45**: 765-774.
- Meinert L.D. 1992. Skarns and Skarn Deposits. *Geoscience Canada*, **19(4)**: 145-162.
- Menegon L., Pennacchioni G., Stünitz H. 2006. Nucleation and growth of myrmekite during ductile shear deformation in metagranites. *Journal Metamorphic Geol.*, **24**:553-568.
- Mesquita, M. J., Hartmann, L. A., Fyfe, W. S., Picanço, J. L., Castro, A. B. 2006. Alteração metamórfico-hidrotermal nos depósitos de ouro tipo-veio da Província de Porto Nacional, TO, Brasil: evidências de química mineral e microestruturas. *Revista Brasileira de Geociências*, **36**:34–50.
- Mesquita, M. J.; Bitencourt, M. F. ; Picanço, J. L. ; Vasconcellos, E. M. G. ; Moretto, A. L. 2013. Evolução Microestrutural do Granito Água Comprida e formação de filonitos, Antiforme Setuva, Paraná. *Geociências (São Paulo. Online)*, **32**: 269-285.

- Mesquita M.J., Quispe P. C., Xavier R., Geraldes M., Matos J. H., Moreira I., Gaidukas G. 2017. Geology, Geochemistry and U-Pb Geochronology of Arc-Related Granitoids of the Alta Floresta Gold Province and implications to the Orosian gold metallogeny of SW Amazon craton, Brazil. In: 14th SGA Biennial Meeting, 2017, Quebec. Proceedings of the 14th SGA Biennial Meeting, Québec City, Canada, 1628p. *Quebec: Society for Geology Applied to Mineral Deposits*, 1:175-178.
- Miller C.F., Stoddard E.F., Bradfish L.J., Dollase W.A. 1981. Composition of plutonic muscovite: genetic implications. *Can. Mineral.*, **19**:25-34.
- Mikhail A. 1989. Rare Earth element systematics in hydrothermal fluids. *Geochemica et Cosmochimica Acta*, **53**:745-750.
- Middleton A.W., Förster A.J., Uysal I.T., Golding S.D., Rhede D. 2013. Accessory phases from the Soultz monzogranite, Soultz-sous-Forêts, France: Implications for titanite destabilisation and differential REE, Y and Th mobility in hydrothermal systems. *Chemical Geology*, **335**: 105-117.
- Migdisonva A., Williams-Jones A.E., Brugger J., Caporuscio F.A. 2016. Hydrothermal transport, deposition, and fractionation of the REE: Experimental data and thermodynamic calculations. *Chemical Geology*, **439**: 13-42.
- Miguel Jr E. 2011. Controle Estrutural das mineralizações auríferas e idades U-Pb das rochas encaixantes ao longo do Lineamento Peru-Trairão: Província Aurífera de Alta Floresta, Mato Grosso. Dissertação de Mestrado, Universidade Estadual de Campinas, 86p.
- Moreton L.C. & Martins E.G. 2005. Geologia e Recursos Minerais de Alta Floresta. Vila Guarita. Escala 1:250.000. Brasília, Serviço Geológico do Brasil, CPRM, 68 p.
- Morad S., El-Ghali M.A.K., Caja M.A., Sirat M., Al-Ramadan K., Mansurbeg H. 2010. Hydrothermal alteration of plagioclase in granitic rocks from Proterozoic basement of SE Sweden. *Geol. J.*, **45**: 105–116.
- Moura M.A. 1998. O Maciço Granítico Matupá e o Depósito de Ouro Serrinha (MT): Petrologia, Alteração Hidrotermal e Metalogenia. Tese de Doutorado, Instituto de Geociências, Universidade de Brasília, 238p.
- Munz I.A., Wayne D., Austrheim H. 1994. Retrograde fluid infiltration in the high-grade Modum Complex, South Norway: evidence for age, source and REE mobility. *Contrib. Mineral Petrol.*, **116**: 32-46.
- Nachit H., Ibhi A., Abia E. H., Ohoud B. 2005. Discrimination between Primary Magmatic Biotites, Reequilibrated Biotites and Neoformed Biotites. *Comptes Rendus Geoscience*, **337(16)**: 1415-1420.
- Parneix J.C., Beaufort D., Dudoignon P., Meunier A. 1985. Biotite chloritization process in hydrothermally altered granites. *Chemical Geology*, **51**:89-101.
- Passchier C.W. & Trouw R.A. 2005. *Microtectonics*. 2nd ed., Springer, Berlin, 366pp.
- Pirajno, F. 2009. *Hydrothermal processes and mineral systems*. Geological Survey of Western Australia, Perth, 1250 pp.
- Plümper O. & Putnis A. 2009. The complex hydrothermal history of granitic rocks: multiple feldspar replacement reactions under subsolidus conditions. *Journal of Petrology*, **50**:967-987.
- Poggi L. (em preparação). 2019. O depósito de Au-Cu-Mo Paraíba (MT): integração de técnicas espectrais e convencionais para a exploração mineral. Tese de Mestrado, Instituto de Geociências, Universidade Estadual de Campinas (UNICAMP), 93 p.
- Pryer L.L. 1993. Microstructures in feldspars from a major crustal thrust zone: the Grenville Front, Ontario, Canada. *J Struct Geol.*, **15**:21-36

- Pryer L.L. & Robin P.Y.F. 1996. Differential stress control on the growth and orientation of flame perthite: a paleostress-direction indicator. *Journal of Structural Geology*, **18**:1151-1166.
- Putnis A. & Putnis C.V. 2007. The mechanism of reequilibration of solids in the presence of a fluid phase. *Journal of Solid State Chemistry*, **180**:1783–1786.
- Putnis, A. & Austrheim, H. 2010. Fluid-induced processes: measomatism and metamorphism. *Geofluids*, **10**:254-269.
- Quispe, P.E. 2016. Geologia, geoquímica e geocronologia dos granitoides foliados e rochas subvulcânicas da região de Peixoto de Azevedo, setor leste da AFGP, MT, IG-Unicamp. Dissertação de Mestrado.
- Ramos G.S. 2011. Características geoquímicas de plútôns graníticos auríferos e estéreis da Província Aurífera de Alta Floresta (MT). Trabalho de Conclusão de Curso, Instituto de Geociências, Universidade Estadual de Campinas, 82p.
- Robb L. 2004. *Introduction to ore-forming processes*. Blackwell, Oxford, 386 pp.
- Rodrigues R.M. 2012. Caracterização geológica e metalogenética do Depósito X1 – Província Aurífera de Alta Floresta, Região de Matupá (MT). Dissertação de Mestrado, Instituto de Geociências, Universidade Estadual de Campinas, 70p.
- Rosenberg C.L. & Stünitz H. 2003. Deformation and recrystallisation of plagioclase along 707 a temperature gradient: an example from the Bergell tonalite. *J. Struct. Geol.*, **25**:389-408.
- Seedorff E., Dilles J.H., Proffett Jr J.M., Einaudi M.T., Zurcher L., Stavast W.J.A., Johnson D.A., Barton M.D. 2005. Porphyry deposits: characteristics and origin of hypogene features. *Economic Geology 110th Anniversary*, 251-298.
- Santos J.O.S. 2000. Os terrenos Paleoproterozóicos da Província do Tapajós e as mineralizações de ouro associadas. Tese de Doutorado, Instituto de Geociências, Universidade Federal do Rio Grande do Sul, 208p.
- Santos J.O.S., Hartmann L.A., Gaudette H.E., Groves D.I., McNaughton N.J., Fletcher I.R. 2000. A New understand of the provinces of the Amazon Craton based on integration of field mapping and U-Pb and Sm-Nd geochronology. *Gondw. Res.*, **3(4)**:453-488.
- Sibson R.H., Moore J.M., Rankin A.H. 1975. Seismic pumping: A hydrothermal fluid transport mechanism: *Journal of the Geological Society*, **131**:653–659.
- Sibson R.H. 1981. Fluid flow structure faulting: field evidence and models. *Earthquake Prediction: an international review. Maurice Ewing Series*, **4**:593-603.
- Sillitoe R.H. 2010. Porphyry Copper Systems. *Economic Geology*, **105**:3–41.
- Silva, F.R. 2014. Geoquímica e geocronologia U-Pb (SHRIMP) de granitos da região de Peixoto de Azevedo – Província Aurífera de Alta Floresta – MT. Dissertação de Mestrado, Instituto de Ciências Exatas e da Terra, Universidade Federal de Mato Grosso, 80p.
- Silva M.G. & Abram M.B. 2008. Projeto metalogenia da Província Aurífera Juruena-Teles Pires, Mato Grosso. Goiânia, Serviço Geológico Brasileiro, CPRM, 212p.
- Sinclair W.D. 2007. Porphyry deposits, in Goodfellow, W.D., ed., *Mineral Deposits of Canada: A Synthesis of Major Deposit-Types, District Metallogeny, the Evolution of Geological Provinces, and Exploration Methods: Geological Association of Canada, Mineral Deposits Division, Special Publication*, **5**:223-243.
- Souza J.P., Frasca A.A.S., Oliveira C.C. 2005. Geologia e Recursos Minerais da Província Mineral de Alta Floresta. Relatório Integrado. Brasília, Serviço Geológico Brasileiro, CPRM, 164p.

- Tamizel I., Mehmet A., Emel A.Y., Cem Y. 2014. Mineral chemistry and thermobarometry of Eocene monzogabbroic stocks from the Bafra (Samsun) area in Turkey: implications for disequilibrium crystallization and emplacement conditions. *International Geology Review*, **56(10)**:1226-1245.
- Tappert M. C., Rivard B., Giles D., Tappert R., Mauger A.J. 2013. The mineral chemistry, near-infrared, and mid-infrared reflectance spectroscopy of phengite from the Olympic Dam IOCG deposit, South Australia. *Ore Geology Reviews*, **53**:26-38.
- Tassinari C.C.G. & Macambira M.J.B. 1999. Geochronological Provinces of the Amazonian Craton. *Episodes*, **22(3)**:174-182.
- Teixeira R.V. 2015. Rochas hospedeiras e controle estrutural da mineralização aurífera do depósito Peteca, região de Flor da Serra – MT, na província Aurífera de Alta Floresta. Trabalho de Conclusão de Curso, Instituto de Geociências, Universidade Estadual de Campinas, 107p.
- Tullis J., & Yund R.A. 1980. Hydrolitic weakening of experimentally deformed Westerly granite and hale albite rock. *Journal of Structural Geology*, **2**:439-452.
- Thompson A.J.B. & Thompson J.F.H. 1996. *Atlas of alteration: a field and petrographic guide to hydrothermal alteration minerals*. Geological Association of Canada, Mineral Deposits Division, 119 pp.
- Velde B. 1985. Possible chemical control illite/smectite composition during diagenesis. *Mineral Magazine*, **49**:387-391.
- Vitório J.A. 2010. A suíte granítica Teles Pires da Província Aurífera de Alta Floresta: Características petrográficas, geoquímicas e implicações metalogenéticas. Instituto de Geociências, Universidade Estadual de Campinas, Relatório PIBIC/ CNPq, 20p.
- Whitney D.L. & Bernard W.E. 2010. Abbreviations for names of rock-forming minerals. *American Mineralogist*, **95**:185-187.
- Zhu Y., An F., Tan J. 2011. Geochemistry of hydrothermal gold deposits: A review. *Geoscience Frontiers*, **2(3)**:367–374.

APPENDIX A

ARTIGO

Artigo:

“Hydrothermal alteration and deformation at Peteca gold deposit, Alta Floresta Gold Province (AFGP), Peixoto de Azevedo region-MT”

VANESSA DE ALMEIDA PIMENTA¹

Maria José Mesquita¹

¹*Instituto de Geociências, Universidade Estadual de Campinas, Campinas, Brazil*

Artigo a ser submetido a “Ore Geology Reviews”

ABSTRACT

The Alta Floresta Gold Province (AFGP) occurs in the south portion of the Amazonic Craton, north of the Mato Grosso state. In the eastern sector of AFGP there are gold deposits concentrated in the NW-SE Peru-Trairão lignament, of the disseminated type or in quartz vein systems. In the region of Peixoto de Azevedo, in the Flor da Serra district, there are four deposits (João Fidelis, Pedro Contim, Peteca and Queiroz), aligned to NW-SE in the Peteca Shear Zone. The main objective of this work is to differentiate hydrothermal alterations regarding the influence of hydrothermal shear processes and magmatic hydrothermal events. The country rocks include foliated granitoids (garnet granodiorite, garnet leucogranite, biotite tonalite), biotite metatonalite, microporphyric dacite dykes and pegmatites. In addition to the occurrence of metatonalite, other evidences that the Sn foliation has a metamorphic origin base on: (a) microstructures in feldspar and quartz in foliated granitoids that indicate medium-to high-grade metamorphic conditions; (b) compositional difference between garnet of granodiorite and leucogranite. The Shear-Hydrothermal System produced microstructures of deformations in feldspar, plagioclase and quartz of low- to medium-grade metamorphic conditions, and the deformation-fluid interaction produced biotite tonalite protomylonite, mylonites and phyllonites, oblique to orthogonal veinlets in relation to the foliation, quartz vein and mineralization. These shear-rocks show S_{n+1} foliation. Granodiorite, garnet-biotite granodiorite mylonite, illite granodiorite mylonite and chlorite-illite phyllonite correspond to the shear evolution toward the quartz vein and mineralization. Chlorite-illite phyllonite and metatonalite host the mineralized vein (N70-80W / N60-90E). The foliations Sn and S_{n+1} are anastomosed and (sub) parallel to the vein. Carbonate veinlets generated in a first event of fracture formation, and those composed by quartz, carbonate and sulphide formed at a later stage, once they present the same mineral assemblage as mineralization. The quartz vein presents three microstructural domains: (1) fine-grained quartz crystals with syntax growth; (2) medium-sized quartz crystals parallel to the vein direction; (3) fine-grained quartz crystals, associated to microfractures, microfaults parallel to the vein direction. In the vein, coarse-grained pyrite (Py 1) may be contemporaneous to the domain 2. Mineral assemblage in the quartz vein comprises quartz, pyrite, sphalerite, greenockite, chalcopyrite, galena. Gold occurs in microfractures or microcavities in Py 1. Ore mineral assemblage comprises Py 1, sphalerite, gold, chalcopyrite, galena. The Magmatic-Hydrothermal System comprises hydrothermal alterations that do not constitute the foliations, such as: albite, potassic with microcline, propylitic, chloritic, muscovite-illite, Fe-Cu, and carbonate-epidote stockworks. The Fe-Cu alteration presents quartz, fine-grained pyrite (Py 2), covelite with phases of Se, Te, Ag. Geothermometry results show an average of $350^\circ \pm 20^\circ\text{C}$ for chlorite crystallization temperature, although there is an increase of 14°C on average from the Shear-Hydrothermal System to the Magmatic. Likewise, this slight temperature increase occurs for the white mica crystallization between the both of the systems. The Peteca consists of an Au ± Cu vein-type deposit resulted from three main stages: metamorphism, Shear-Hydrothermal system that marks a temperature decrease and comprise the ore assemblage, and the Magmatic-Hydrothermal system, which mark a temperature increase due to a magmatic source.

Key words: Amazon Craton, gold mineralization, hydrothermal alteration, mineral chemistry, geothermometry.

1. INTRODUCTION

The Alta Floresta Gold Province (AFGP) is in the southern portion of the Amazon Craton, north of the state of Mato Grosso, Brazil (Barros, 2007). It occurs along a NW-SE trend of 500 km extent between the Cachimbo Graben and the Caiabis Graben (Barros, 2007; Fig. 6).

The primary gold deposits at AFGP split into: (Assis et al., 2017): (1) disseminated Au ± Cu (e.g. Luizão, Serrinha, Juruena, X1 e Pé Quente), and vein-type Au ± Cu (e.g. Paraíba, Pezão); (2) disseminated Au ± Mo ± Cu (e.g., Ana and Jaca); and (3) vein-type Au + Zn + Pb ± Cu deposits (e.g., Francisco, Bigode, and Luiz).

Peteca mineralization associates to sulphides in the main quartz vein with N70-80W/N60-90E orientation (Teixeira, 2015). The country rocks presents granodioritic to tonalitic composition, besides dacite and pegmatites dykes (Teixeira, 2015; Quispe, 2016). The whole deposit present intense hydrothermal alterations, besides sheeted veinlets of up to 4 cm thick, composed of quartz, carbonate and sulphides (Teixeira, 2015).

Shear zones (SZ) act as channelways of mineralizing fluids or as remobilizers of preexisting mineral deposits. This is possible due to several factors, such as the presence of fractures and faults, differences in lithostatic and fluid pressures, heat generated during shear stresses that facilitate the transport of aqueous solutions with metals. The ionic compounds agglutinate according to their chemical affinities and, after the fluid cooling, they precipitate and mineralized quartz veins at the sites of expansion (Groves et al., 1998; Goldfarb et al., 2005; Bons et al., 2012).

Fluids influence deformation processes which result in softening reactions that are important to the SZ evolution (Griggs, 1967; Tullis & Yund, 1980; Hippert, 1998; Stünitz & Tullis, 2001; Yonkee et al., 2003; Mancktelow & Pennacchioni, 2004; Fusseis & Handy, 2008; Hartman et al., 2010; Jaquet & Schmalholz, 2018; Lee et al., 2018). Shear rocks classification into cataclasite, ultramylonite, mylonite, phyllonite depends on the fluid/rock ratio (Jefferies et al., 2006; Mesquita et al., 2006; Mesquita & Fernandes, 1991). Fluid-rock interaction provides new conditions of temperature, pressure and chemical constituents. It generates reactions called as metassomatism, which results in halos or hydrothermal alteration zones (Barnes, 1997; Putnis & Austrheim, 2010; Zhu et al., 2011).

Au ± Cu vein-type deposits as Paraíba and Pezão present relations to granite plutons pointed as heat, flow and metal source for magmatic-hydrothermal system (Trevisan, 2015). According to this author, Pezão deposit corresponds to a rich Au-Cu epithermal low

sulfidation deposit, while the Paraíba deposit present features correlated to porphyry deposit, IRGS, and orogenic gold. Hence, the accomplishment of study gaps at Peteca may also improve the comprehension evolution of gold vein-type deposits in the region.

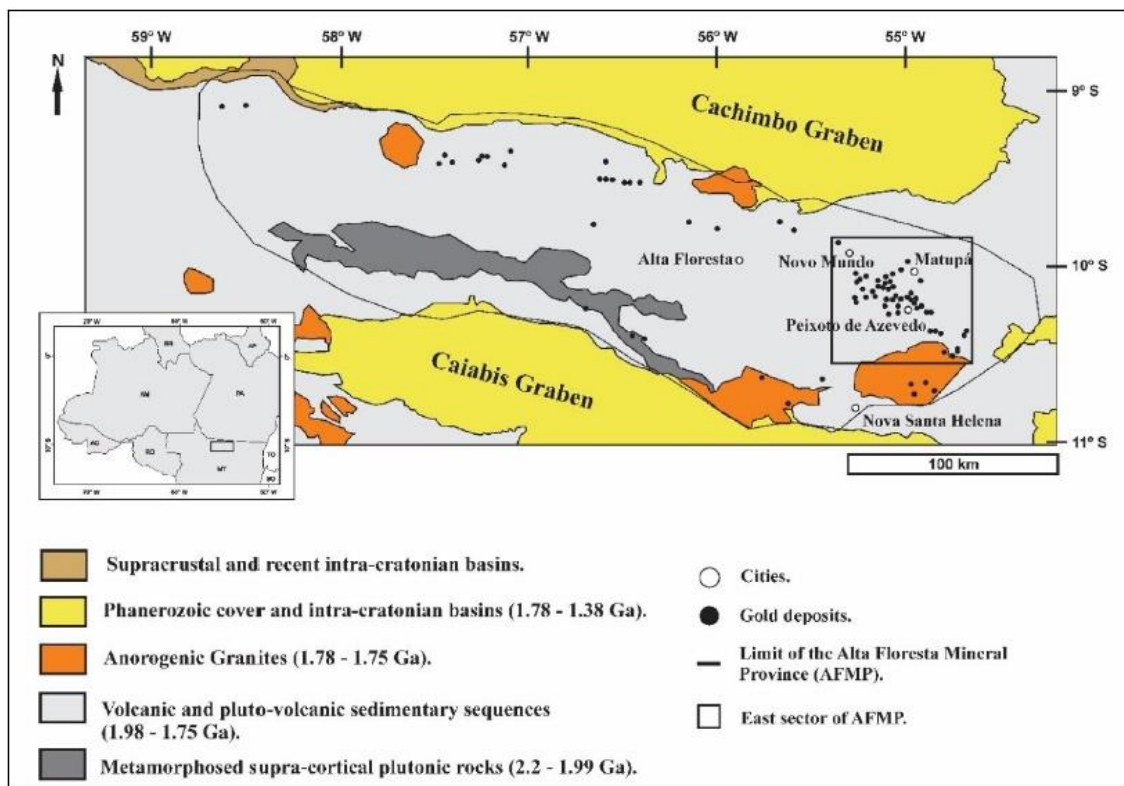


Figure 6 - Map location of the Alta Floresta Gold Province. It displays the main geological domains of the eastern part of the Province (black square) (Assis, 2011 - Modified from Barros, 2007).

2. ANALYTICAL PROCEDURES

In total, five oriented core samples from the Peteca deposit were described (PT-8, PT-12, PT-15, PT-22, PT-30), besides 6 no oriented samples from the ore concentration stack, and 3 oriented samples from the mine gallery. The Appendix B presents the coordinates for location of the drill cores and their respective maximum depth, besides the relation of all analyzed samples and the analytical methods applied on each of them.

All of those descriptions were carried out to define the country and the host rocks, hydrothermal alterations and their occurrence types, veinlet types, and gold-sulphide distribution. Afterwards, it was aimed to collect samples from the main different features found, and 47 thin-polished sections were studied using a Leica DM-EP optical microscope at the Institute of Geosciences of the University of Campinas, Brazil. During the analyses were described the igneous and hydrothermal mineral assemblages, structures in the rocks. Further detail was given to the hydrothermal mineral transformations from the distal rocks to the mineralization, as well as textural relations, associations and styles of occurrence. The modal analyses were estimated. For the least deformed samples, it was obtained through the compositional average of 12 equal parts of the thin section, in which the composition was estimated in percentage. Mineral abbreviations used according to Whitney & Evans (2010).

In order to complement the petrographic descriptions, 14 thin-polished sections were analyzed under a LEO 430i (ZEISS) scanning electron microscope (SEM) coupled with an energy dispersive X-ray spectrometer (EDS) at the Institute of Geosciences of the University of Campinas, Brazil. Standard operating conditions included an accelerating potential of 15 kV, a beam current of 3 nA, and a focal length of 19 mm.

The mineralized vein presents small cavities filled by cryptocrystalline material. In order to define its mineral assemblage, 6 samples of up to 3g each were collected and analyzed by X-ray diffraction using a SIEMENS (Bruker) D-5000 diffractometer at the Laboratory of X-ray Diffractometry of the Institute of Geosciences (IGEO) of the Federal University of Rio Grande do Sul, Brazil.

All the elemental analyses (Appendix B, D) were obtained from 11 thin-polished sections using a CAMECA SXFive coupled electron micropobe at the Electron Microprobe Laboratory of the Institute of Geosciences (IGEO) of the Federal University of Rio Grande do Sul, Brazil. It is equipped with wave dispersive X-ray spectrometer (WDS) and EDS, and the software to process the data is Peak Sight 5.1. Standard operating conditions included accelerating potential of 15 kV or 20 kV (sulphides), beam current of 15 nA, 10 nA (micas

and very fine oxides) or 20 nA (sulphides), and size diameter beam of 5 μm . The raw microprobe data in the form of oxide weight percents were recalculated using the AX software (<https://www.esc.cam.ac.uk/research/research-groups/holland/ax>), obtaining the cation distribution.

Chlorite crystallization temperatures were empirically obtained by applying geothermometers proposed by Bourdelle et al. (2013) and Inoue et al. (2009). Neither pressure nor very high temperatures are considered in both of these methods, only selected end members. The geothermometer proposed by Bourdelle et al. (2013) is according to Si *vs.* R²⁺ diagram of Wiewióra and Weiss (1990). White mica crystallization temperatures were obtained using the geothermometer proposed by Bataggia (2004), in which the K content and a correlation between Fe and Mg are considered. Geothermometry results of chlorite and white mica are on the Appendix E.

3. REGIONAL GEOLOGICAL SETTING

3.1. INTRODUCTION

The Amazon Craton is in the northern portion of South America, surrounded by neoproterozoic orogenic belts (Fig. 7). The geotectonic evolution of the Craton resulted from successive orogenic events, forming paleocontinents (Hasui et al., 1974; Almeida, 1977). Its current most accepted conception bases on the evolution of orogenic events that formed successive magmatic arcs (Cordani & Teixeira, 1981; Tassinari & Macambira, 1999; Tassinari et al., 2000; Santos et al., 2000). The juvenile crust formation and reworking of the oldest material occurred during the archean and paleoproterozoic, respectively representing 30% and 70% of the continental crust of the Amazonian Craton (Tassinari & Macambira, 1999).

Based on geochronological data from U-Pb dating in zircons and Sm-Nd isotopes, Santos et al. (2000) splitted the Amazonian Craton in seven tectono-structural provinces: (i) Carajás (3.0-2.5 Ga); (ii) Amazônia Central (Archean); (iii) Transamazonas (2.26-2.01 Ga); (iv) Tapajós-Parima (2.03-1.88 Ga); (v) Rio Negro (1.82-1.62 Ga); (vi) Rondônia-Juruena (1.82-1.54 Ga); (vii) Sunsás e K'Mudku (1.45-1.10 Ga) (Fig. 7).

According to this model, the AFGP embraces part of the Tapajós-Parima Province and Rondônia-Juruena. The AFGP is composed of successive plutono-volcanic sequences added to the Central Amazon Province during the paleoproterozoic and mesoproterozoic (Tassinari & Macambira, 1999; Santos, 2006; Silva & Abram, 2008).

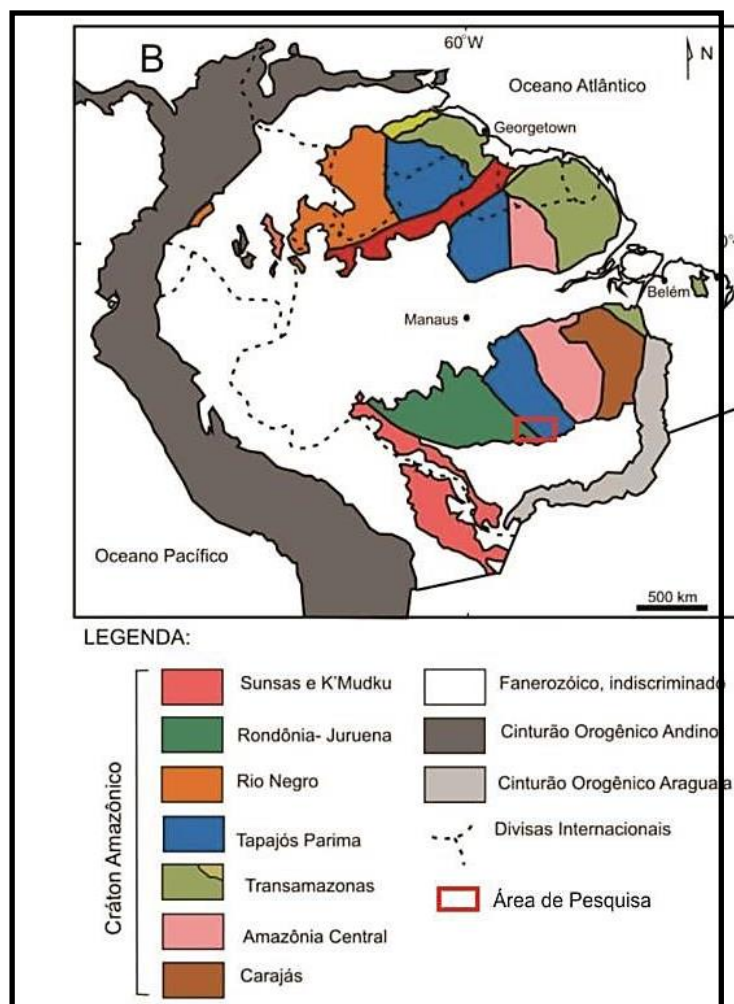


Figure 7 - Geotectonic compartmentalization of the Amazon Craton according to Santos et al. (2000). Red polygon: eastern section of AFGP (Extracted from Silva, 2014).

3.2. EASTERN SECTOR OF AFGP

In the region of Peixoto de Azevedo, the Peru-Trairão Lineament has NW-SE alignment and hosts many gold deposits (Barros, 2007; Fig. 8). It affects rocks of the arqueano basement, paleoproterozoic granitoids, and intercept them as sinistral discontinuous-continuous shear zones.

Except some gold projects in the region of Agrovila União do Norte in the southeast region of AFGP, where mineralization is associated with a sedimentary-clastic sequence (Dardanelos Formation), the primary deposits associated to this Lineament occur in plutono-volcanic paleoproterozoic suites (Barros, 2007; Miguel Jr., 2011; Assis et al.; 2014). The shear intercepts in the granitoids present a system of mineralization in sub-vertical and anastomosed quartz veins. The gold mineralization in lodes is the most common in the region with <5g Au/t, followed by deposits in stockwork veins and disseminated mineralizations.

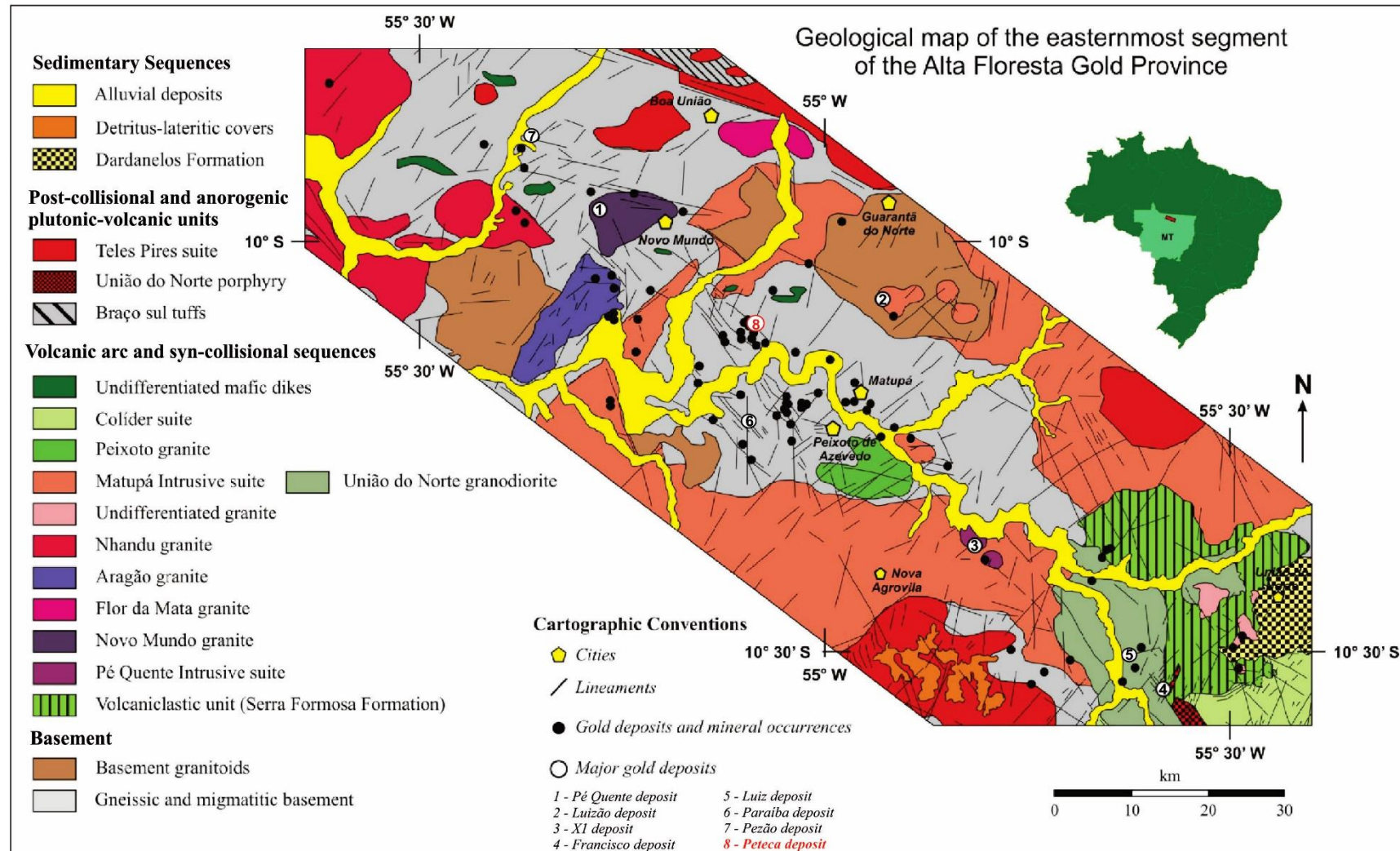


Figure 8 - Geologic map of the eastern sector of AFGP with the main gold deposits associated with the Peru-Trairão Lineament, and highlighted in red for the Peteca deposit (Assis, 2015 - Modified from Miguel-Jr, 2011).

In the eastern sector of the AFGP, the different units subdivide into: (a) basement (2,8-1,9 Ga; Souza et al., 2005; Barros, 2007; (b) plutono-volcanic calc-alkaline sequences (1.97-1.71 Ga; Barros, 2007; Assis, 2015; Trevisan, 2015; Quispe, 2016; Oliveira, 2017), (c) post-orogenic and anorogenic sequences (1.77-1.7 Ga), and (d) sedimentary sequences (1.3-Quaternary; Leite & Saes, 2003; Souza et al., 2005) (Tab. 2). The Flor da Serra district region, belonging to the Peixoto de Azevedo city, presents folds and continuous shear zones of direction NW-SE (Cunha, 1996; Phani et al., 2014; Quispe, 2016). These shear zones (SZ) are called Joaquim (SZJ), Paraíba, (SZPa), Peteca (SZP) and Serinha (Szs), from west to east (Quispe, 2016; Fig. 9). The Paraíba and Peteca gold deposits occur in the homonymous shear zones. Cunha (1996) defined a second type of structural alignment attributed to the drainages of the region, such as sinistral faults NW, continuous shear zone with approximate direction of NS, and discontinuous shear zone NE. Moreton et al. (2005) individualized mafic dykes in the region as Suite Flor da Serra. However, Quispe (2016) describes that mafic dykes affect paleoproterozoic granitoids, and does not individualize mafic rocks as a lithological unit.

Table 2 – Geocronology and tectonic settings of the main geologic units at the eastern sector of AFGP (Modified from Assis, 2015).

Calc-alkaline plutono-volcanic units (I-type granites)	Nhandu Suite (Dezula et al., 2018)	Nhandu granite	$1,889 \pm 17$; $1,879 \pm 5.5$ (U-Pb) e $1,848 \pm 17$; 1969 ± 2 a 1946 ± 21 (U-Pb)	Syn-collisional volcanic arc ($2.14 < TDM < 2.17$; $\epsilon Nd(t) = -0.91$)	Moreton & Silva (2005); Silva & Abram (2008), IICA/MMAJ (2000), Rocha et al. (2016)
		Aragão granite	$1,931 \pm 12$ (U-Pb); $1,964 \pm 11$ (U-Pb); $1,967 \pm 2$ (U-Pb)	Volcanic-arc (no isotopic data available)	Vitório (2010), Miguel-Jr (2011), Ramos (2011), Dezula et al. (2018)
		Flor da Mata granite	Unknown age (correlated to the Novo Mundo granite)	Volcanic-arc (no isotopic data available)	Ramos (2011)
		Novo Mundo granite	$1,970$ to $1,964$ (U-Pb e Pb-Pb)	Syn-collisional volcanic arc ($2.55 < TDM < 2.76$; $-7.62 < \epsilon Nd(t) < -4.48$)	Barros (2007)
		Pé Quente Intrusive suite	$1,979 \pm 31$ (U-Pb) to $1,901 \pm 6.8$ (U-Pb)	Volcanic-arc (no isotopic data available)	Assis (2011), Miguel-Jr (2011), Assis (2015)
		Serra Formosa Volcaniclastic Unit	Maximum age: 2,009	Back-arc foreland basin within na active continental margin (no isotopic data available)	Assis (2011), Miguel-Jr (2011)
Calc-alkaline plutono-volcanic units (I-type granites) - Foliated granitoids	Foliated granitoids	Biotite granite, hornblende-quartz diorite, hornblende-biotite monzogranite, tonalite, biotite tonalite, dacite, garnet-muscovite leucogranite and granodiorite commonly foliated	$1,998$ (Pb-Pb); $2,037 \pm 6$ to $1,978 \pm 8$ (U-Pb)	Volcanic-arc ($2.18 < TDM < 2.67$; $-2.14 < \epsilon Nd(t) < -3.84$)	Barros (2007), Assis (2015), Trevisan (2015), Quispe (2016), Oliveira (2017)
Basement: metamorphosed supracrustals and plutonic sequences	Gneisses and migmatites	Anfibolite and monzonitic, tonalitic and granitic orthogneiss, partly migmatite	$2,816 \pm 4$ (U-Pb) to $1,980 \pm 9$ (U-Pb)	Calc-alkaline volcanic-arc (no isotopic data available)	Souza et al. (2005), Barros (2007), Assis (2015)

Calc-alkaline plutono-volcanic units (I-type granites)	Nhandu Suite (Dezula et al., 2018)	Nhandu granite	$1,889 \pm 17$; $1,879 \pm 5.5$ (U-Pb) e $1,848 \pm 17$; 1969 ± 2 a 1946 ± 21 (U-Pb)	Syn-collisional volcanic arc ($2.14 < TDM < 2.17$; $\epsilon Nd(t) = -0.91$)	Moreton & Silva (2005), Silva & Abram (2008), JICA/MMAJ (2000), Rocha et al. (2016)
		Aragão granite	$1,931 \pm 12$ (U-Pb); $1,964 \pm 11$ (U-Pb); $1,967 \pm 2$ (U-Pb)	Volcanic-arc (no isotopic data available)	Vitório (2010), Miguel-Jr (2011), Ramos (2011), Dezula et al. (2018)
	Flor da Mata granite	Alkali-feldspar granite, syenogranite, monzonite, granodiorite	Unknown age (correlated to the Novo Mundo granite)	Volcanic-arc (no isotopic data available)	Ramos (2011)
	Novo Mundo granite	Syenogranite, monzogranite, granodiorite, quartzmonzonite and monzonite	$1,970$ to $1,964$ (U-Pb e Pb-Pb)	Syn-collisional volcanic arc ($2.55 < TDM < 2.76$; $-7.62 < \epsilon Nd(t) < -4.48$)	Barros (2007)
	Pé Quente Intrusive suite	Monzonite, quartz-monzonite, quartz-monzdiorite, monzdiorite, fine-coarse albitite, aplitic granodiorite and biotite tonalite	$1,979 \pm 31$ (U-Pb) to $1,901 \pm 6.8$ (U-Pb)	Volcanic-arc (no isotopic data available)	Assis (2011), Miguel-Jr (2011), Assis (2015)
	Serra Formosa Volcaniclastic Unit	Feldspathic-sandstone, feldspathic-wake, lithicsandstone and matrix supported sandy-polymictic conglomerate	Maximum age: 2,009	Back-arc foreland basin within na active continental margin (no isotopic data available)	Assis (2011), Miguel-Jr (2011)
Calc-alkaline plutono-volcanic units (I-type granites) - Foliated granitoids	Foliated granitoids	Biotite granite, hornblende-quartz diorite, hornblende-biotite monzogranite, tonalite, biotite tonalite, dacite, garnet-muscovite leucogranite and granodiorite commonly foliated	$1,998$ (Pb-Pb); $2,037 \pm 6$ to $1,978 \pm 8$ (U-Pb)	Volcanic-arc ($2.18 < TDM < 2.67$; $-2.14 < \epsilon Nd(t) < -3.84$)	Barros (2007), Assis (2015), Trevisan (2015), Quispe (2016), Oliveira (2017)
Basement: metamorphosed supracrustals and plutonic sequences	Gneisses and migmatites	Anfibolite and monzonitic, tonalitic and granitic orthogneiss, partly migmatite	$2,816 \pm 4$ (U-Pb) to $1,980 \pm 9$ (U-Pb)	Calc-alkaline volcanic-arc (no isotopic data available)	Souza et al. (2005), Barros (2007), Assis (2015)

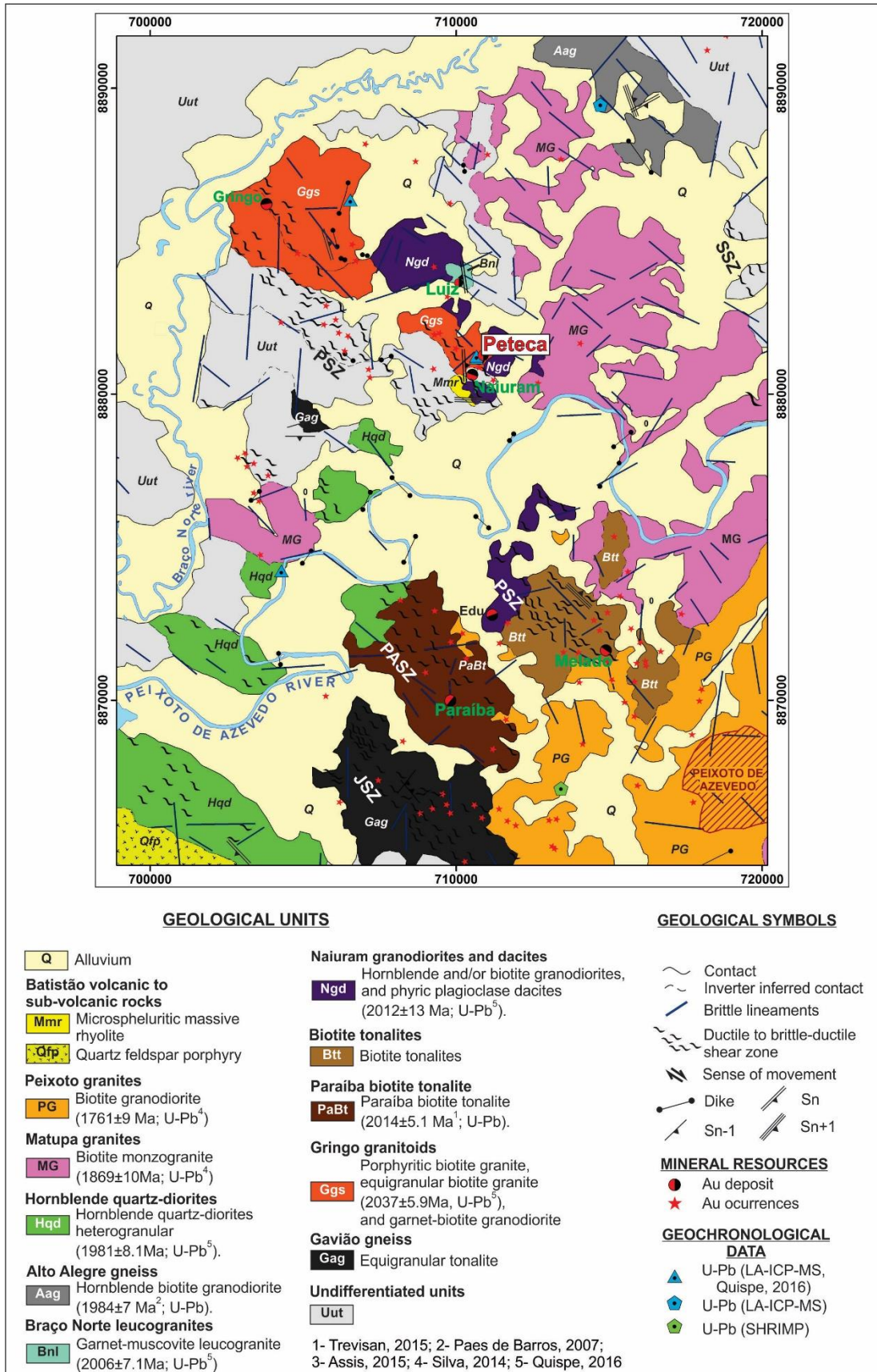


Figure 9 – Geologic map of the region of Peixoto de Azevedo and Peteca deposit location (Quispe, 2016).

4. RESULTS

The lithotypes at Peteca deposit were defined from drill cores. Their location is on the geological map granted by Biogold Mining Company (Fig. 10). The drill cores PT-8, PT-22, PT-12 and PT-15 occur on a same geologic section (Fig. 11), while the PT-30 is on another one (Fig. 12). The Peteca deposit has a regolith ranging from 40 to 70 m of thickness and the framework deposit presents intense hydrothermal alteration. The considered protholytes are those lithotypes with mineral assemblages closer to the primary ones. They correspond to three foliated granites: (i) *garnet granodiorite*, belonging to the Gringo granitoids lithological unit (Quispe, 2016), (ii) *garnet leucogranite*, belonging to the Braço Norte lithological unit (Quispe, 2016), and (iii) *biotite tonalite*. Besides them, there are the biotite metatonalite, and dykes of (i) *microporphyritic dacite* (Quispe, 2016), and (ii) *pegmatite*. The Appendix B presents their modal composition, and their main features are on Table 3.

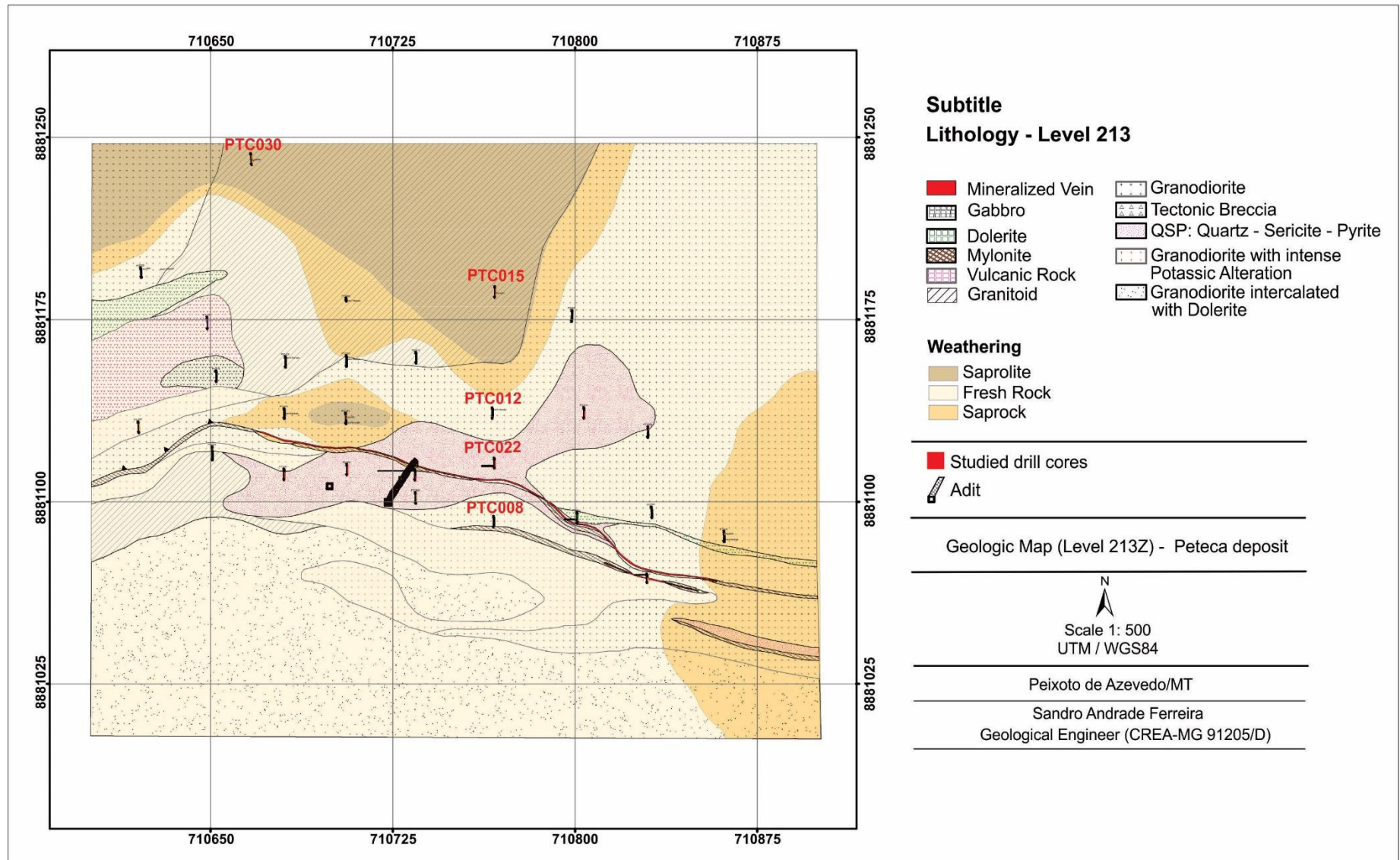


Figure 10 - Geologic Map with drill cores location. Image granted by Biominer Mining Company.

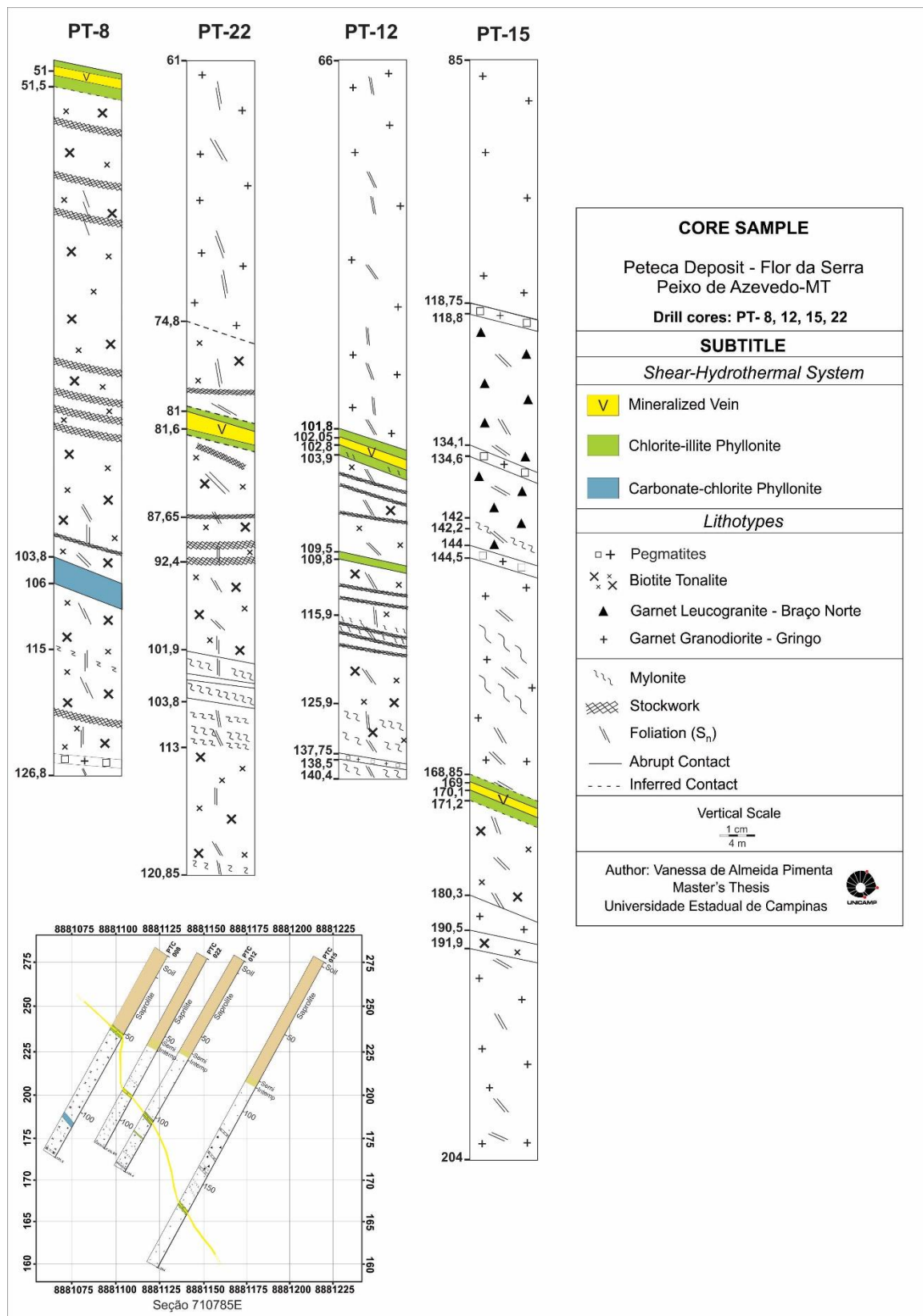


Figure 11 – Geologic section of oriented drill cores (PT-8, PT-22, PT-12, PT-15) and present lithotypes. Variations in the directions of foliation (S_n) characterize it as anastomosed. Drill cores are NE-SW and intercept the lithotypes in an average medium angle of 75°-90°.

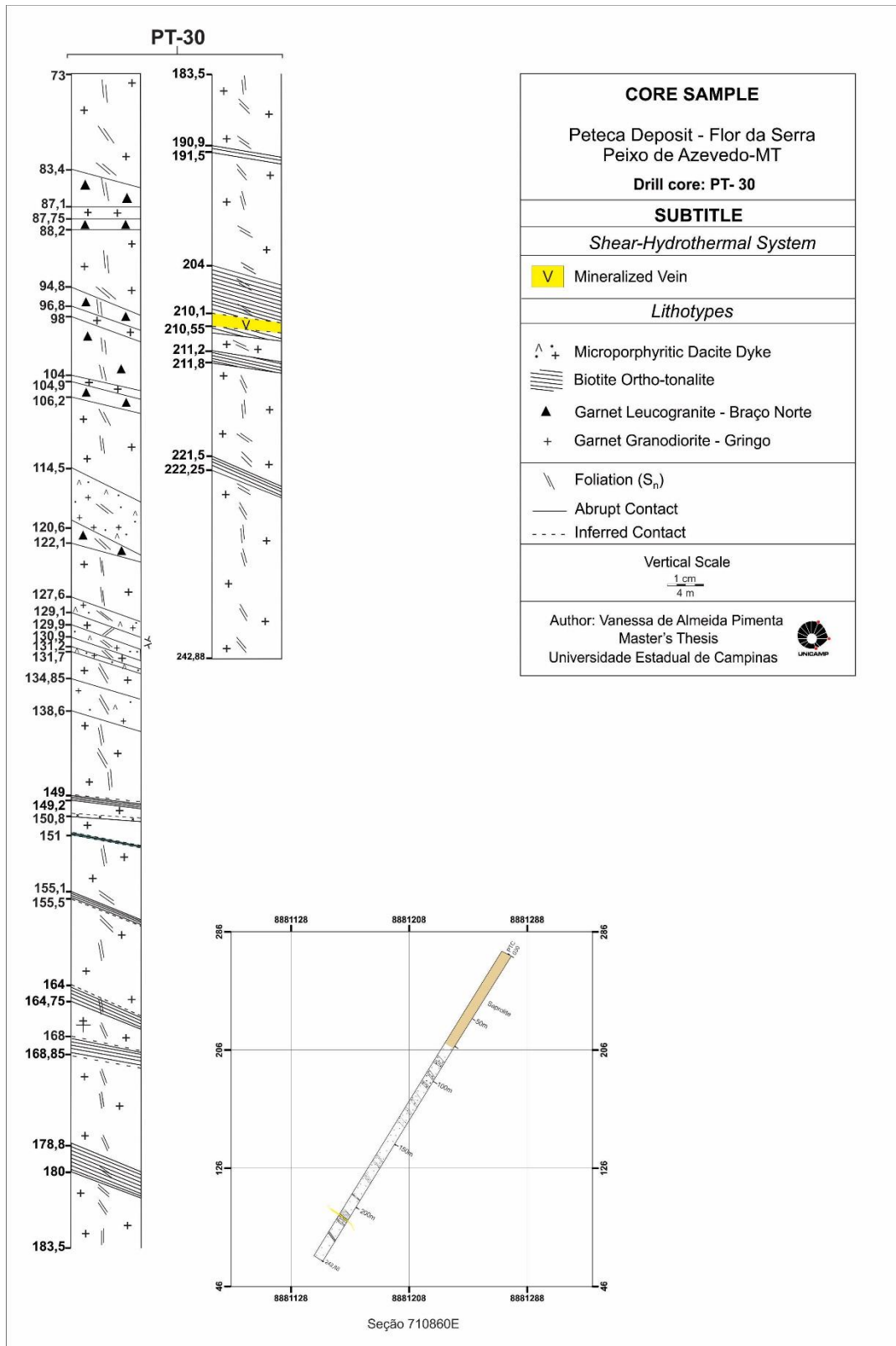


Figure 12 - Geologic section of oriented drill core (PT-30) and present lithotypes. Variations in the directions of foliation (S_n) characterize it as anastomosed. Drill core is NE-SW and intercept the lithotypes in an average medium angle of 75°-90°.

4.1 COUNTRY ROCKS

Its major lithotype corresponds to the *garnet granodiorite* that occurs in the drill cores PT-12, PT-15, PT-22, PT-30. In the PT-8 it may correspond to the regolith portion, once it is on the north of the mineralized vein in the first three drill cores (Figs. 11, 12). The granodiorite is mesocratic with porphyritic texture with plagioclase phenocrysts within a medium- to fine-grained matrix. Deformation was heterogeneous, generating a weak to well-developed foliation, marked by alignment of minerals (Fig. 13A, B) to a spaced schistosity foliation (Sn) with quartz-feldspar microlithons and biotite in schistosity domains (Fig. 13C). Primary quartz shows undulose extinction, deformation bands and subgrains. Its grain boundaries are irregular, with bulges along them (Fig 13D). Secondary quartz differs from that, mainly by occurring as polycrystalline aggregates (Fig. 13C). Plagioclase occurs (a) as phenocrysts (Fig. 13B) and (b) in the primary matrix. Both of the types crystals are subeuhedral with polysynthetic twinning, and lobate to straight boundaries. Illitic alteration is often concentrated in the center of the crystal producing a zoning observed through thin section. However, there is no different compositional patterns between its center and edge. K-feldspar appears in the primary matrix as subhedral crystals with rare illitic alteration. Its boundaries are convex and present microcline twinning, heterogeneously distributed in the phenocrysts. Garnet occurs as fragments (Fig. 13B) to elongated crystals (Fig. 13D), with intragranular fractures filled by illite and/or chlorite. It presents a straight contact with biotite relic, and both minerals alter to chlorite, illite and muscovite. Lamellae of biotite with orange-to-brown pleochroism and dark halo compose mafic aggregates (Fig. 13D). Biotite is weakly to intensely replaced from its boundaries, and cleavage planes [001].

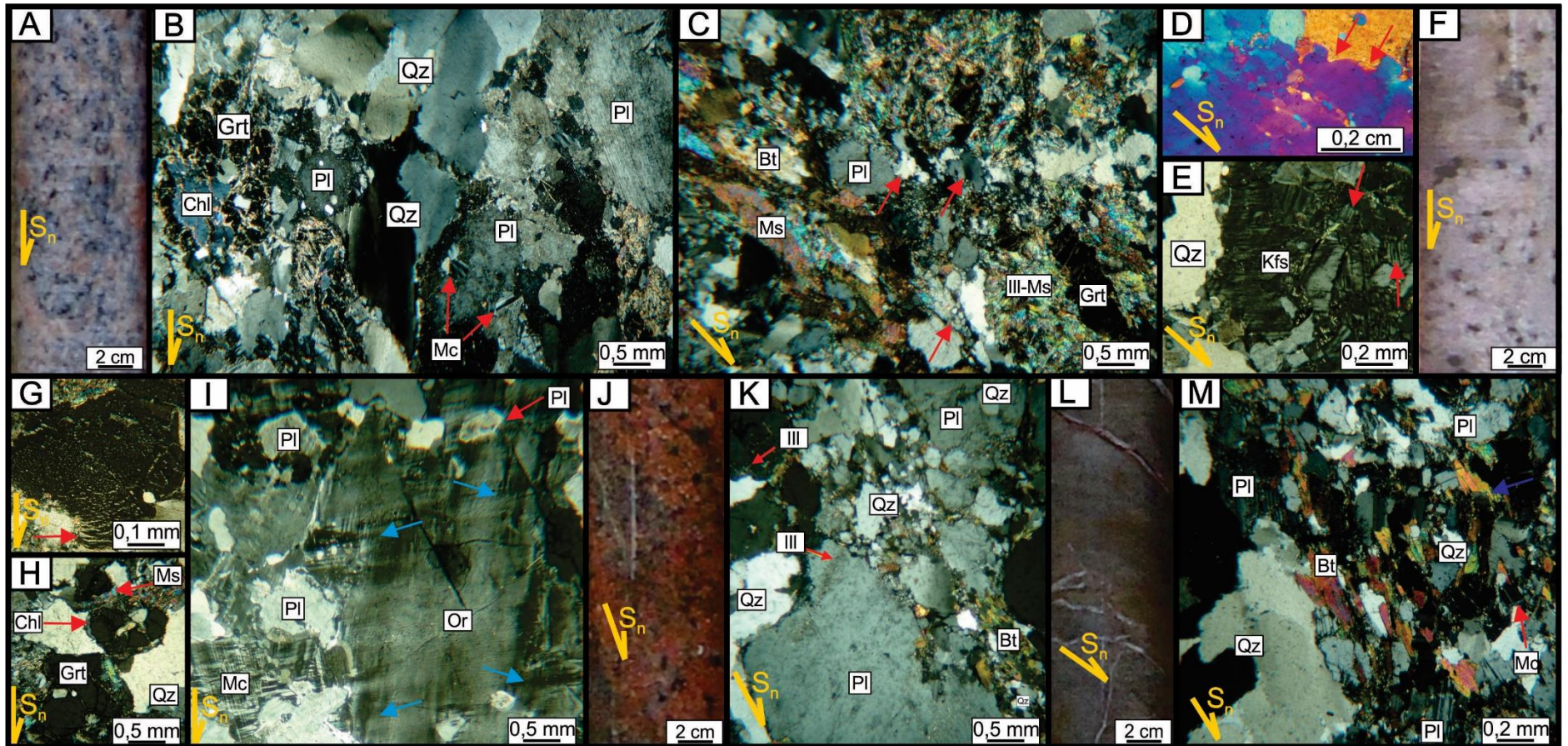


Figure 13 - Core samples (A, F, J, L) and photomicrographs (B, C, D, E, G, H, I, K, M) of foliated granites and metatonalite at Peteca deposit. (A) Garnet granodiorite with weak developed foliation (S_n). (B) The minerals orientation mark S_n . Note microcline alteration of feldspar. (C) Garnet granodiorite with a well developed S_n . Microlithons of quartz-feldspar alternated with biotite and quartz-ribbon domains. Note elongated garnet altered to illite-muscovite. Red arrows indicate quartz aggregates. (D) Deformed bands with recrystallized grains in primary quartz. Red arrows indicate bulges at quartz boundaries. (E) Recrystallized K-feldspar. Red arrows indicate tapering edge twinning. (F) Garnet Leucogranite. (G) Photomicrograph exhibits flame perthite (red arrow) orthogonal to the S_n foliation. (H) Garnet crystal in the leucogranite. (I) Orthoclase exhibits microcline twinning formation from its boundaries (blue arrows). It also shows plagioclase inclusions. (J) Biotite tonalite weakly foliated. (K) Photomicrograph shows primary deformed matrix with the major crystals of plagioclase and quartz on the right top and a phenocryst on the left. Recrystallized matrix marked by biotite, quartz and feldspars, as narrow strip wrap primary grains. (L) Biotite metatonalite. Carbonate veinlets are (sub) parallel to S_n . (M) Recrystallized isogranular matrix. [S_n Foliation represented by yellow arrow on all pictures].

The *garnet leucogranite* (Fig. 13F) occurs in the drill cores PT-15 and PT-30. It presents a monzogranitic composition, inequigranular, medium- to fine-grained texture. Oriented minerals, mainly quartz and garnet, mark Sn. K-feldspar presents string perthite spreaded in all the crystal and flame perthite (Fig. 13G), and microcline twinning (Fig. 13I). There are intragranular fractures filled by calcite. Plagioclase shows illitic alteration mostly concentrated in its center. Mafic aggregates consist of sobrounded garnet (Fig. 13H) in equilibrium with biotite relicts. Both minerals alters to chlorite, muscovite and illite. Biotite also occurs as aggregates in matrix. Globular quartz occurs in garnet crystals as a secondary origin.

The *biotite tonalite* occurs in the drill cores PT-8, PT-12, PT-22, and it is the predominant rock in the south of the *garnet granodiorite*, wherewith there is an abrupt contact (Fig. 11). It is a red rock, porphyritic with plagioclase phenocrysts within a medium- to fine-grained inequigranular matrix (Fig. 13J). Mineral alignment, rare quartz ribbons, and narrow strips showing a recrystallized matrix mark Sn (Fig. 13K). Plagioclase occurs: (a) as slight rounded phenocrysts, (b) in the matrix, and (c) as secondary crystals. Plagioclase phenocrysts tight intragranular fractures filled by illite. Their boundaries are convex to straight, and present carbonate and epidote along them. Secondary plagioclase displays straight boundaries in equilibrium with quartz. Primary crystals of K-feldspar may exhibit microcline twinning concentrated along their boundaries, unlike string perthite distributed in all the crystal. Biotite has light to dark green pleochroism, alters to chlorite, ilmenite with minor rutile and titanite. Zircon can occur as an inclusion in biotite.

The *biotite metatonalite* occurs as bands (thickness from 30 cm to 5 meters) restricted to core PT-30. It shows inferred contacts with the garnet granodiorite, marked by an increasing of rock fragmentation and of quartz veinlets toward the metamorphic rock (Fig. 12). It hosts the mineralized vein at 210 m deeping. The metatonalite is dark gray to black (Fig. 13L) with Sn marked by mineral alignments, mainly biotite. The texture is fine sub-polygonal granoblastic composed of quartz-feldspar, and core-mantle texture in grain boundaries of feldspar and quartz with polycrystalline quartz-feldspar and biotite (Fig. 13M). Plagioclase is subidioblastic to idioblastic, its boundaries are either irregular or straight with biotite, and alters to illite. Biotite occurs in aggregates ($\leq 0,75$ cm) of fine lamellae and presents a light brown to orange pleochroism. It alters to chlorite, illite, calcite, epidote, Fe-Ti oxides, pyrite and chalcopyrite.

The *microporphyritic dacite dykes* are light green rocks (Fig. 14A) cutting the garnet leucogranite and the garnet granodiorite, wherewith there is a high angle contact. They are restricted to the core PT-30 (see Fig. 12). Their texture comprises phenocrysts of plagioclase (Fig. 14B) within an intensely altered aphanitic matrix, which presents illite, carbonate, chlorite, quartz, pyrite (Fig. 14C). The phenocrysts mark Sn, exhibit a prismatic habit, and a strong alteration to illite, epidote, and carbonate.

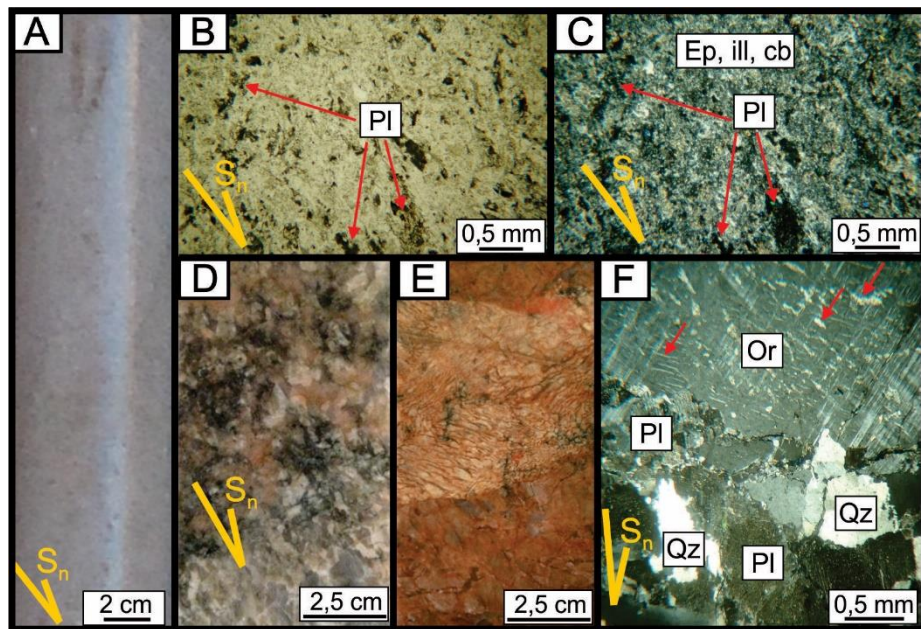


Figure 14 - Main features in core samples (A, D, E) and photomicrographs (B natural light NL, and C, F polarized light - PL) of the dykes at Peteca deposit. (A) Microporphyritic dacite dyke. (B-C) Photomicrographs show the intensely altered matrix. Note microphenocrysts of plagioclase marking Sn. (D) Leucogranite. (E) Reddish pegmatite with macroperthites. (F) Photomicrograph shows the quartz-feldspar composition. Red arrows indicate string and flame perthites, as well as microcline twinning irregularly distributed in grain boundary of K-feldspar. Polycrystalline quartz aggregate indicated [Sn Foliation represented by yellow arrow on all pictures].

Pegmatite dykes are 10-meter thick at most, and affect the garnet granodiorite and the biotite tonalite (Fig. 12). They are whitish (Fig. 14D) to reddish rocks (Fig. 14E), medium- to very coarse-grained, inequigranular, with a quartz-feldspar composition. The pegmatites present a heterogeneous deformation with oriented crystals in some portions. The igneous mineral assemblage consists of quartz, plagioclase, K-feldspar, and the secondary minerals are quartz, microcline, illite, muscovite, carbonate, chlorite, and pyrite. Primary quartz crystals exhibit undulose extinction and subgrains, lobate to irregular boundaries. Secondary quartz appears as very fine crystals among crystal boundaries or filling fractures in feldspars. Plagioclase crystal is often zoned by an illitic alteration in its center, and presents intragranular fractures filled by illite and carbonate. Primary K-feldspar crystals display

macroperthites and microcline twining observed even with naked eye (Fig. 14E, F). Interstices among grains are filled by very fine secondary quartz and K-feldspar crystals, besides fine aggregates (≤ 0.4 cm) composed of illite, carbonate, chlorite, and rare pyrite.

Table 3 - Main features of the foliated granitoids, metatonalite, and the microporphyritic dacite dyke (*% constituent of the rock).

Lithotypes	Texture	Pheno-crysts/ Porphyro-clasts*	Mafic Minerals	Primary/ Metamorphic Mineral Assemblage	Accessory Minerals	Secondary Mineral Assemblage	Foliation (Sn)	Deformational Microstructures
Grt Granodiorite	Porphyritic. Medium-to fine grained matrix	Pl (40%)	Bt, grt	Qz, pl, kfs, bt, grt	Fe-Ti oxides, zrn, ap, py	Qz, ab, mc, chl, ill, ms, ep, cb, Fe-Ti oxide, py, ccp	Heterogeneous (weak to well developed) spaced Sn: Bt schistosity domains; Qz-fd in microlithons domains	Qz: undulose extinction, subgrains, deformation bands, bulges at crystal boundaries; Pl: polysynthetic twinning; Kfs: microcline twinning, flame perthite; Bt: pseudoform (completely altered to Chl): kink band; Others: fractures in Grt
Grt Leucogranite	Inequigranular. Medium- to fine grained matrix	X	Bt, grt	Qz, kfs, pl, bt	Zrn, ap	Qz, ab, mc, chl, ill, ms, ep, Fe-Ti oxide, py	Heterogeneous Spaced Sn: Gr pressure shadow and slightly elongated	Qz: undulose extinction, bulges at crystal boundaries; Pl: polysynthetic twinning; Kfs: microcline twinning, string perthites; Others: fractures in Grt , and in Kfs phenocryst
Bt Tonalite	Porphyritic. Medium-to fine grained matrix	Pl (60-70%)	Bt	Qz, pl, kfs, bt	Fe-Ti oxide, zrn, ap, py	Qz, ab, mc, chl, ill, ep, leucoxene, cb, Fe-Ti oxide, py, gth	Heterogeneous Spaced Sn: : Bt schistosity domains qz-feldspar in microlithon domains.	Qz: undulose extinction, bulges at crystal boundaries; Pl: polysynthetic twinning; Kfs (hydrothermal?): microcline macula; Others: microfractures in Pl
Bt Metatonalite	Granolepidoblastic, fine <u>isograngular</u>	X	Bt	(Qz, pl, kfs, bt)*	X	Ill, chl, cal, ep, Fe-Ti oxide, py	Mineral alignments, mainly biotite	Recrystallized matrix
Micropor- phyritic dacite dyke	Microporphyritic. Very fine-grained equigranular matrix	Pl (20%)	X	Qz	X	Ill, chl, cal, ep, py, Fe-Ti oxide	Spaced Sn: matrix in schistosity domains, oriented Pl phenocryst in microlithon domain	Not observed.

4.1. HYDROTHERMAL SYSTEMS

Two hydrothermal systems occur at Peteca, defined as Shear-hydrothermal and Magmatic-Hydrothermal Systems. The main difference between them is the predominant absence of mineral preferential orientation in the latter system. Their belongings products and hydrothermal alterations are on the following two sections. The distribution of each system among the lithotypes are on Table 4 at the end of this section.

4.1.1. Shear-hydrothermal System

The *shear-hydrothermal system* comprises the products of hydrothermal alteration and deformation classified as protomylonite, mylonites, phyllonites, veinlets, quartz vein (lode) and mineralization. The shear rocks are absent in the core sample PT-30 (see Fig. 12). The Appendix C exhibit the modal composition of the protomylonite, mylonites and phyllonites.

Protomylonite

The *biotite tonalite protomylonite* occurs as reddish bands (10 cm to 7 m thick) in the biotite tonalite (Fig. 15A). The foliation (S_{n+1}) is marked by feldspar porphyroclasts and medium-grained quartz wrapped by recrystallized bands (up to 0.2 thick) composed of fine-to very-fine grained albite, microcline, quartz, biotite and ilmenite. The protomylonite mainly differs from its protolith biotite *tonalite* for the increasing amount of recrystallized bands (Fig. 15B).

Compared to its protolith, the plagioclase compositions of the primary matrix present higher content of calcium and lower of sodium. Illitic alteration in plagioclase causes a reddish color to it, which also contributes to the rock's appearance. Other reason for that is due to a microcline formation present in the recrystallized bands as an alteration. Microcline porphyroclasts present core-and-mantle structure composed of quartz, microcline and plagioclase (Fig. 15C). They also show tapering edge twinning, inclusions of plagioclase, intragranular fractures, and flame perthite from crystal boundaries. The biotite lamellae are fine-grained and partially altered to chlorite, ilmenite, and rutile. Pyrite appears as idiomorphic to subidiomorphic crystals disseminated or as part of fine aggregates of chlorite, carbonate and ilmenite in the matrix. They show sphalerite inclusions, which are absent in the sulphides from its protolith.

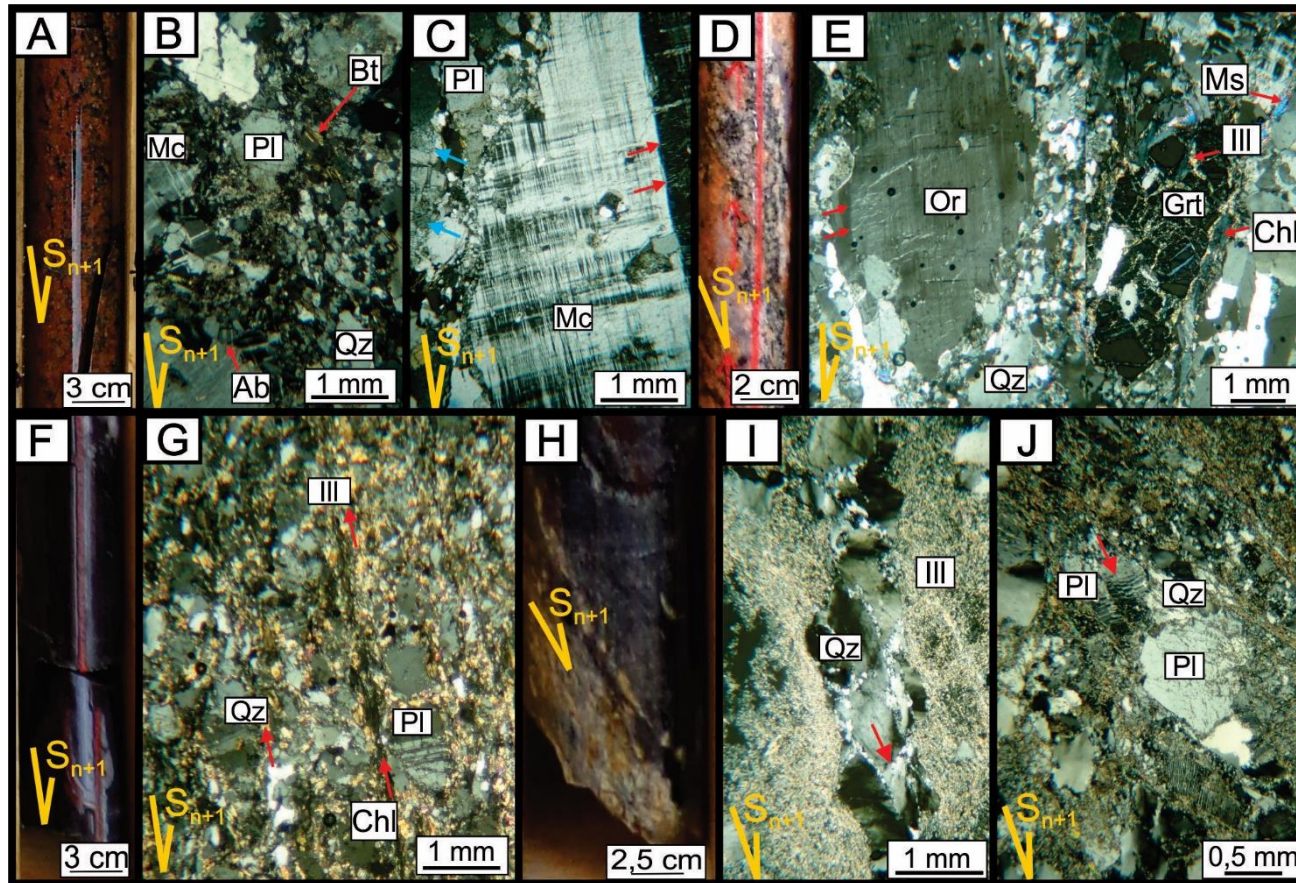


Figure 15 - Core samples (A, D, F, H) and photomicrographs (polarized light) of the protomylonite and mylonites at Peteca. (A) Typical reddish color of the biotite tonalite protomylonite. (B) Fine-grained recrystallized bands mark S_{n+1} . (C) Mantle-and-core structure of porphyroblast. Blue arrows point myrmekite. Red arrows point flame perthite on the limit of Carlsbad twin. (D) Garnet-quartz mylonite. (E) S_{n+1} foliation marked by alteration of augen orthoclase porphyroblast and fragments of garnet and polycrystalline quartz ribbon. Note porphyroblast with core-and-mantle structure and perthites from its boundaries (red arrows). (F) Garnet-biotite mylonite. (G) Narrow strips of chlorite mark S_{n+1} . Feldspar grain-size reduction by intense illite formation. (H) Yellowish illite granodiorite mylonite on the left in contact with chlorite-illite phyllonite. (I) Anastomosed S_{n+1} marked by altered quartz ribbon and illite bands. Note trails of recrystallized grains on the boundaries of quartz (red arrows). (J) Red arrow indicates microfaults in plagioclase. Note sigma-type asymmetric pressure shadow of quartz in plagioclase.

Mylonites

At Peteca, *garnet-quartz mylonite* formed as millimetric strips in both *granodiorite* and *leucogranite*. *Garnet-biotite granodiorite mylonite*, *illite granodiorite mylonite* and *chlorite-illite phyllonite* represent a deformation evolution from their *biotite granodiorite* protolith.

Garnet-quartz mylonite is light grey to pinkish with asymmetrical anastomosed spaced foliation (S_{n+1}), in which plagioclase and K-feldspar porphyroclasts altern with recrystallized bands and quartz ribbon (Fig. 15D-E). Plagioclase and K-feldspar porphyroclasts are almond shaped with core-and-mantle structures composed of quartz, plagioclase and microcline. Regarding the protolith as either the granodiorite or the leucogranite, it shows an increase of (a) illite and pyrite, (b) microcline twinning by deformation, (c) polycrystalline or monocrystalline quartz ribbons and fine-grained crystals with straight boundaries in the recrystallized bands, (d) and hydrothermal quartz polycrystalline aggregates. At Peteca, there are three mylonites: *garnet-quartz mylonite*, *garnet-biotite granodiorite mylonite* and *illite granodiorite mylonite*. The protolith of *garnet-quartz mylonite* remains undefined once it appears as milimetric strips from the *granodiorite* and the *leucogranite*.

Garnet-biotite granodiorite mylonite is blackish characterized by anastomosed foliation (S_{n+1}) marked by chlorite (Fig. 15F). The garnet appears as very fine fragments in the foliation. From the protolith, there is a significant matrix grain-size reduction (< 0,4 mm) and decreasing amount of plagioclase, K-feldspar, garnet, besides a size reduction of biotite and plagioclase due to the increasing alteration to illite (Fig. 15G).

The *illite granodiorite mylonite* is whitish to light green, characterized by anastomosed foliation (S_{n+1}), well-marked by mono- and polycrystalline quartz ribbons and illitic bands (Fig. 15H-I). Plagioclase relics show intense illitic alteration, but are still recognized, while new K-feldspar appears in the recrystallized matrix with no illitic alteration. Sense of movement indicators are shear microfaults in plagioclase and pressure shadow (Fig. 15J). Comparing to the former mylonite, the *illite mylonite* presents an increasing amount of illite, chlorite, quartz, pyrite and decreasing amount of plagioclase, and complete absence of garnet.

Phyllonites

The *chlorite-illite phyllonite* hosts the mineralized quartz vein (Fig. 11, 16A) and it is the next stage of deformation evolution from the *illite granodiorite mylonite*. Toward this phyllonite, S_{n+1} is of fine continuous cleavage type, well-marked by illite, chlorite, quartz, pyrite, rutile, ilmenite, chalcopyrite, and zircon (Fig. 16B). There are narrow strips (0,04-0,06 cm) composed of chlorite and rutile marking the S_n as well. Very fine-grained chlorite (0,02-0,1 cm) and illite (0,01-0,03 cm) lamellae occur associated and may form aggregates (< 0,2 cm). Quartz appears as isolated grains or, mainly, as fine aggregates (0,01-0,5 cm; Fig. 16B). From the last mylonite, in this phyllonite there is total absent of plagioclase and alkali feldspar, besides an increasing amount of illite, chlorite, pyrite, rutile and ilmenite. The sulphide can present sphalerite inclusions and microfractures.

The *carbonate-chlorite phyllonite* is grey to dark green (Fig. 16C), it is distal to the mineralized vein and occurs as an only strip at PT-8 (see Fig. 1). Its probable protolith is the *biotite tonalite*. Its foliation (S_{n+1}) is of fine continuous cleavage type, marked by all mineral assemblage, but mainly chlorite, illite, calcite, quartz (Fig. 16D). There are narrow veinlets filled by massive calcite that are parallel to orthogonal in relation to S_n (Fig. 16C). Quartz occur as fine polycrystalline aggregates and exhibit undulose extinction. Pyrite crystals are subhedral to euhedral with cubic habit, and very fine aggregates of rutile and ilmenite are associated to the chlorite lamellae.

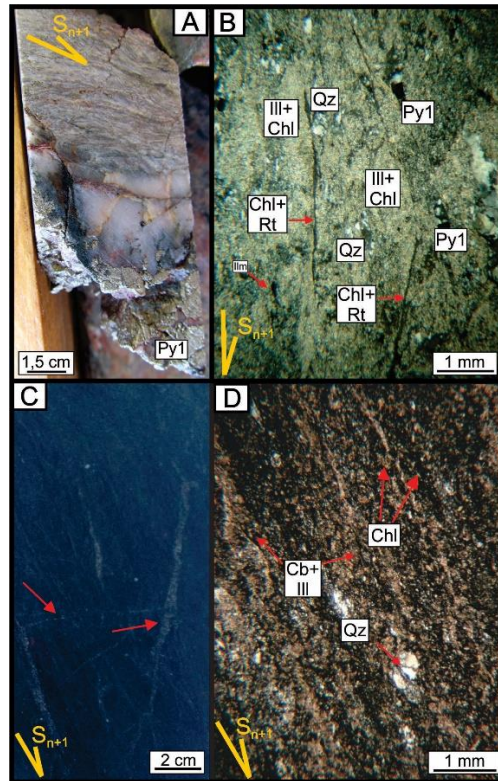


Figure 16 - Core samples (A, C) and photomicrographs (polarized light) of the phyllonites at Peteca deposit. (A) Chlorite-illite phyllonite (above) in contact with the mineralized vein. Coarse crystal of Py 1 indicated. (B) S_{n+1} foliation marked by all mineral alignments and narrow levels of chlorite and rutile. (C) Carbonate-chlorite phyllonite. Red arrows point narrow veinlets filled by chlorite and rutile as showed on the protomicrograph (D).

Fractures and Veinlets Infill

It comprises (a) intragranular microfractures in quartz and feldspar, and (b) veinlets that are oblique (30° - 75°) or orthogonal to the Sn foliation. The microfractures consists of monomineralic calcite and occur in the *leucogranite*. The veinlets present (a) polymineralic calcite and rare quartz of up to 0,75 cm thick (Fig.1 7A) or (b) quartz, sulphide, and minor calcite (Fig. 17B). The first veinlet type mainly occurs in the *illite granodiorite mylonite* and *chorite-illite phyllonite*.

Quartz veinlets are 1,0 to 2,5 cm thick, wrapped by illite halos that mark Sn (Fig. 17C). Quartz crystals have syntax growth at most and they are very fine- to fine-grained. They present undulose extinction as intracrystalline microstructure and their boundaries are straight to slight convex. Calcite appears as very fine- to fine-grained crystals with their boundaries of straight to convex type. The boundaries between calcite and quartz are often straight. Pyrite crystals are parallel to the veinlet orientation (Fig. 17D). They are euhedral to subhedral with cubic habit, and ranging from 0,04 to 2,0 cm. Pyrite presents inclusions of sphalerite, greenockite, galena, chalcopyrite and rare hessite (Fig. 17E), besides microfractures parallel to the veinlet direction with covellite (Fig. 17F).

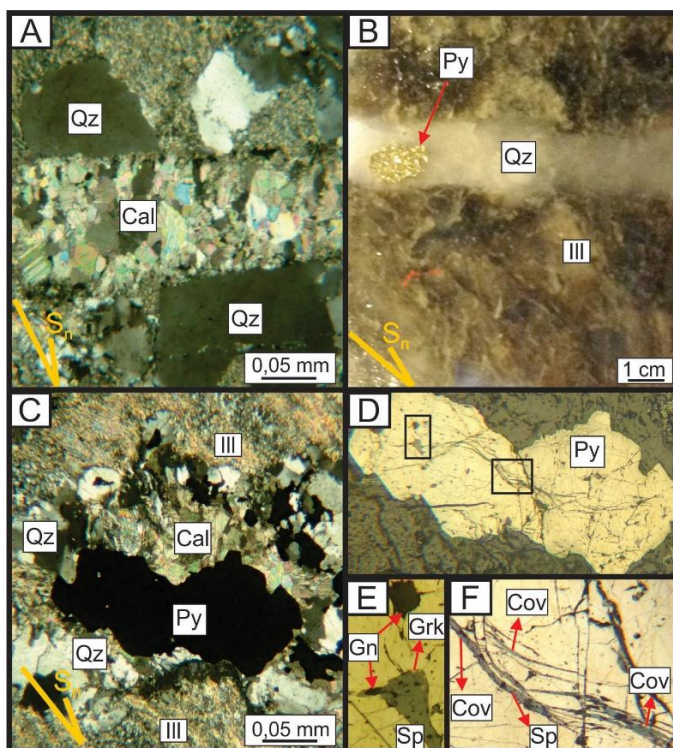


Figure 17 - Veinlets Infill. (A) Calcite crystals with syntax growth fills veinlet; (B) Hand specimen of illite granodiorite mylonite affect by quartz veinlet with pyrite; (C) Infill of quartz and calcite veinlet wrapped by illite halo. Note pyrite crystal is parallel to the veinlet's orientation. (D) The same pyrite on last figure. Black squares indicate location of the next two images. (E) Inclusions of sphalerite and galena on pyrite 1. Greenockite occurs as exsolutions in sphalerite. (F) Intragranular fractures filled by covellite with minor sphalerite in pyrite 1.

Quartz Vein

The quartz vein assemblage is composed of quartz, pyrite 1, sphalerite, greenockite, chalcopyrite and galena. The quartz vein consists of grain crystals with undulose extinction as intracrystalline microstructures and they present three microstructure domains as showed on Figure 18A.

Domain 1: crystals (0,35-0,65 cm) present syntax growth, orthogonal to oblique in relation to the wall vein. The boundaries are straight at most, but slight sinuous type is also present, and there are bulges.

Domain 2: crystals (0,4-1,2 cm) are oblique to orthogonal in relation to the domain 1, which turns out the domain 2 is subparallel to parallel to the vein orientation. Boundaries are straight to irregular with bulges.

Domain 3: consists of microfaults, anastomosed fractures and narrow polycrystalline vein. All these structures are parallel to the vein orientation. The microfaults and fractures display very fine-grained recrystallized quartz, and they are reddish due to Fe-hydroxid. Cavities (0,2-1,5 cm) are affected by these fractures.

Pyrite 1 occurs as medium- to coarse-grained crystals (0,7-3,0 cm) that are usually parallel to the vein orientation and the foliation (Sn). This orientation and size grain are similar to the quartz grains from the microstructural domain 2, which turns out they may be cogenetic. Pyrite 1 displays sphalerite, chalcopyrite and galena inclusions. Sphalerite is also found in equilibrium with pyrite 1 as medium- to coarse-grained crystals that are subhedral with cubic habit, and have a brownish-yellow color. The both of sphalerite occurrence types show microfractures and boundaries crystals with greenockite.

The cavities found in the vein are black to reddish-orange, and six samples were analyzed from X-ray diffraction. The results show they are composed mainly of sphalerite, pyrite, quartz, and subordinated amounts of illite, chorite and caolinite (Appendix D).

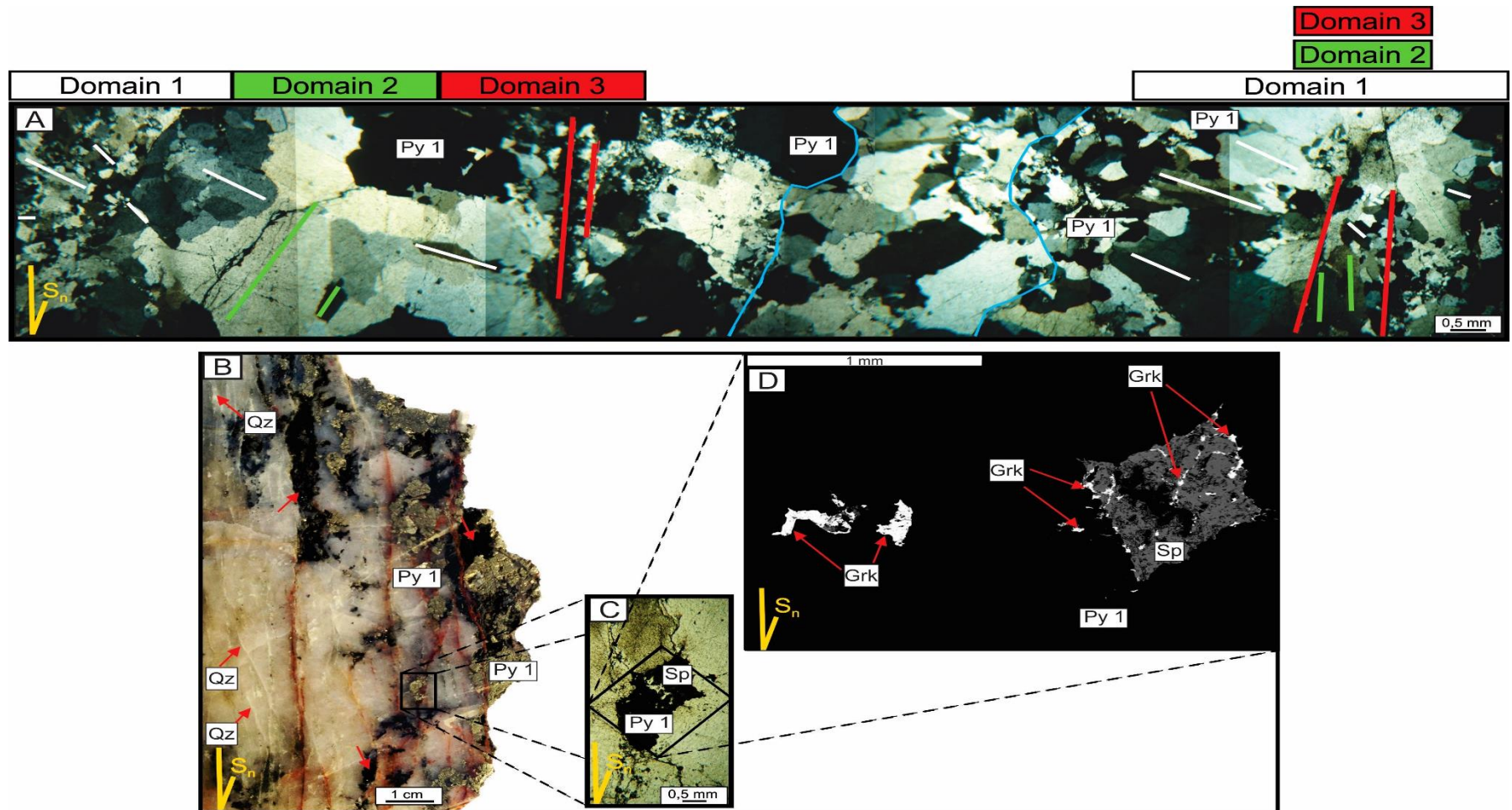


Figure 18 - Quartz Vein. (A) Photomicrograph of the quartz vein. Its hand specimen is on B. Domain 1 (white lines) represents elongated crystals resulting from syntax growth from the wall toward the center. Domains 2 and 3 are orthogonal to the 1. Blue lines indicate the boundaries of a vein. (B) Narrow white strips correspond to quartz from the domain 3. Red arrows also indicates the cavities in the vein (see. Fig. 9). Note that pyrite 1 crystals is mostly parallel to the Sn. (C) Zoom in of pyrite 1 preview indicate. It is in equilibrium with sphalerite. (D) Image obtained by EDS during SEM analysis. At left, greenockite in exsolution with sphalerite. At right, sphalerite fills fractures and boundaries of sphalerite and minor in pyrite 1.

Mineralization

The gold occurs in intragranular microfractures (Fig. 19A) or microcavities (Fig. 19C) within the pyrite 1 in crystals size ranging from 0,04 to 0,01 mm. The ore mineral assemblage consists of, in decreasing amount abundance, sphalerite, chalcopyrite, gold and galena. In the fractures, galena and sphalerite is in straight contact with gold (Fig. 19A). According to SEM analyses, gold composition presents 77-85% of Au content and 14-19% of Ag content, with a Ag:Au ratio between 0,16 and 0,25.

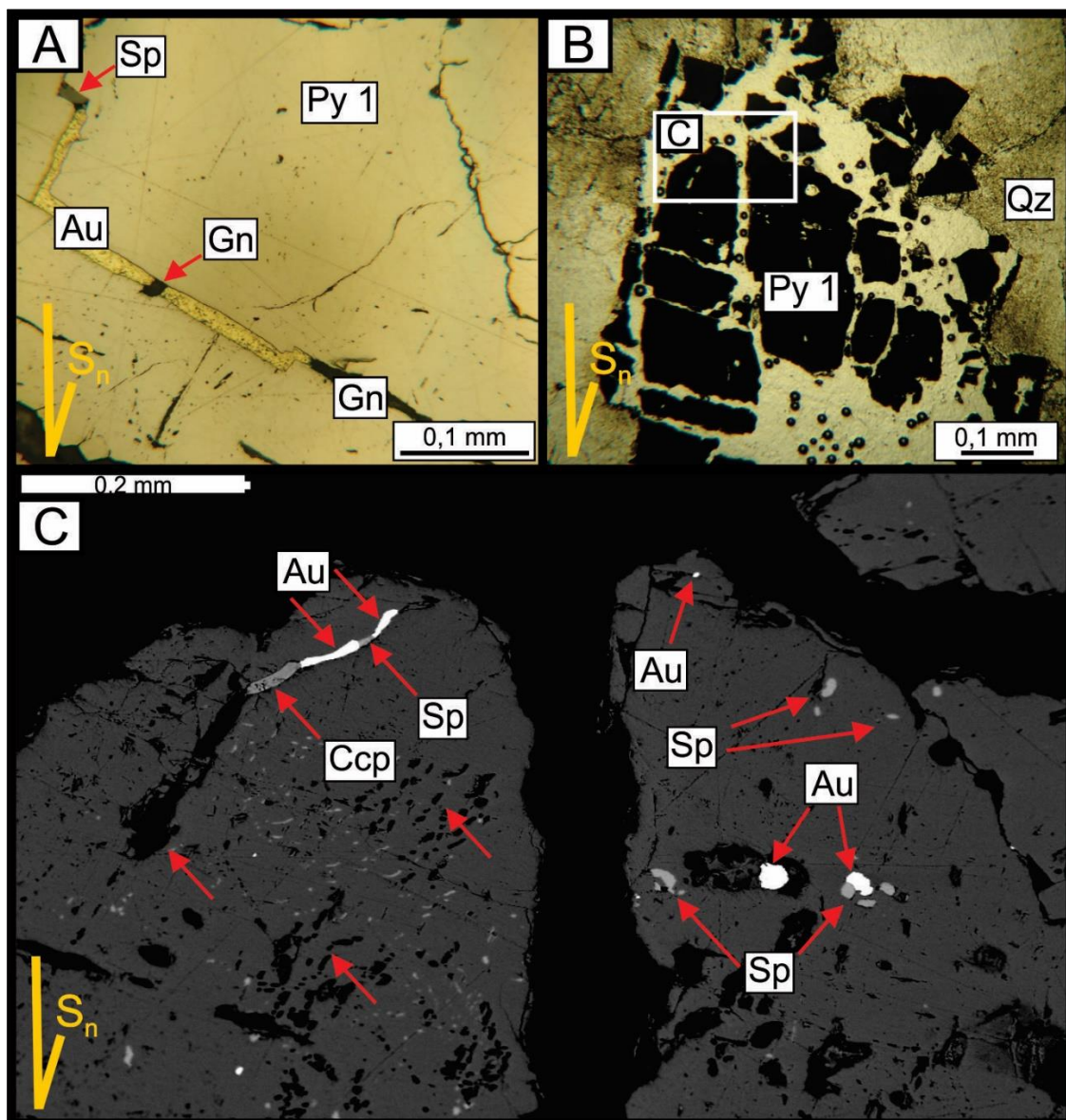


Figure 19 - Gold mineralization at Peteca Deposit. (A) Gold fills microfractures within pyrite 1 in equilibrium with sphalerite and galena. (B) Pyrite 1 in the vein. (C) Detail of the preview pyrite. It shows fracture filled by gold, chalcopyrite and sphalerite. Gold also occurs in microcavities. Red arrows without mineral label indicates exsolutions identified by SEM analyses, but with no defined composition (main elements: 73.11% O, 6.08% Al, 13.83% Cl, 0.88 Si).

4.1.2. Magmatic-hydrothermal System

The *magmatic-hydrothermal system* comprises seven hydrothermal alterations post mineralization at the Peteca deposit: (a) albite alteration, (b) potassic alteration with microcline, (c) propylitic alteration, (d) chloritic alteration, (e) muscovite-illite alteration, (f) Fe-Cu alteration, and (g) carbonate-epidote stockwork. These alterations do not comprise the foliation.

Albite alteration

Albite alteration occurs as a disseminated alteration in a strip of 5 cm in the *biotite tonalite* (Fig. 20A), and as veinlet of euhedral albite and quartz in *garnet granodiorite*. It is responsible for the whitish color on the rock, its assemblage comprises albite and quartz, and locally obliterates the igneous assemblage (Fig. 20B). Albite occurs as fine- to medium-grained crystals with straight boundaries, and alters to illite. Quartz crystals are medium-grained with straight to convex boundaries, and undulose extinction.

Potassic Alteration with Microcline

The hydrothermal microcline generation is responsible for the pinkish to light red color in the altered rocks (Fig. 20C). It occurs in the lithotypes distal to the mineralized vein. Microcline is an alteration product from plagioclase from its intracrystalline fractures and boundaries (Fig. 20D). Less common, the potassic alteration produce located orange portions composed of fine aggregates of idiomorphic microcline and hexagonal quartz subordinated (Fig. 20E, F).

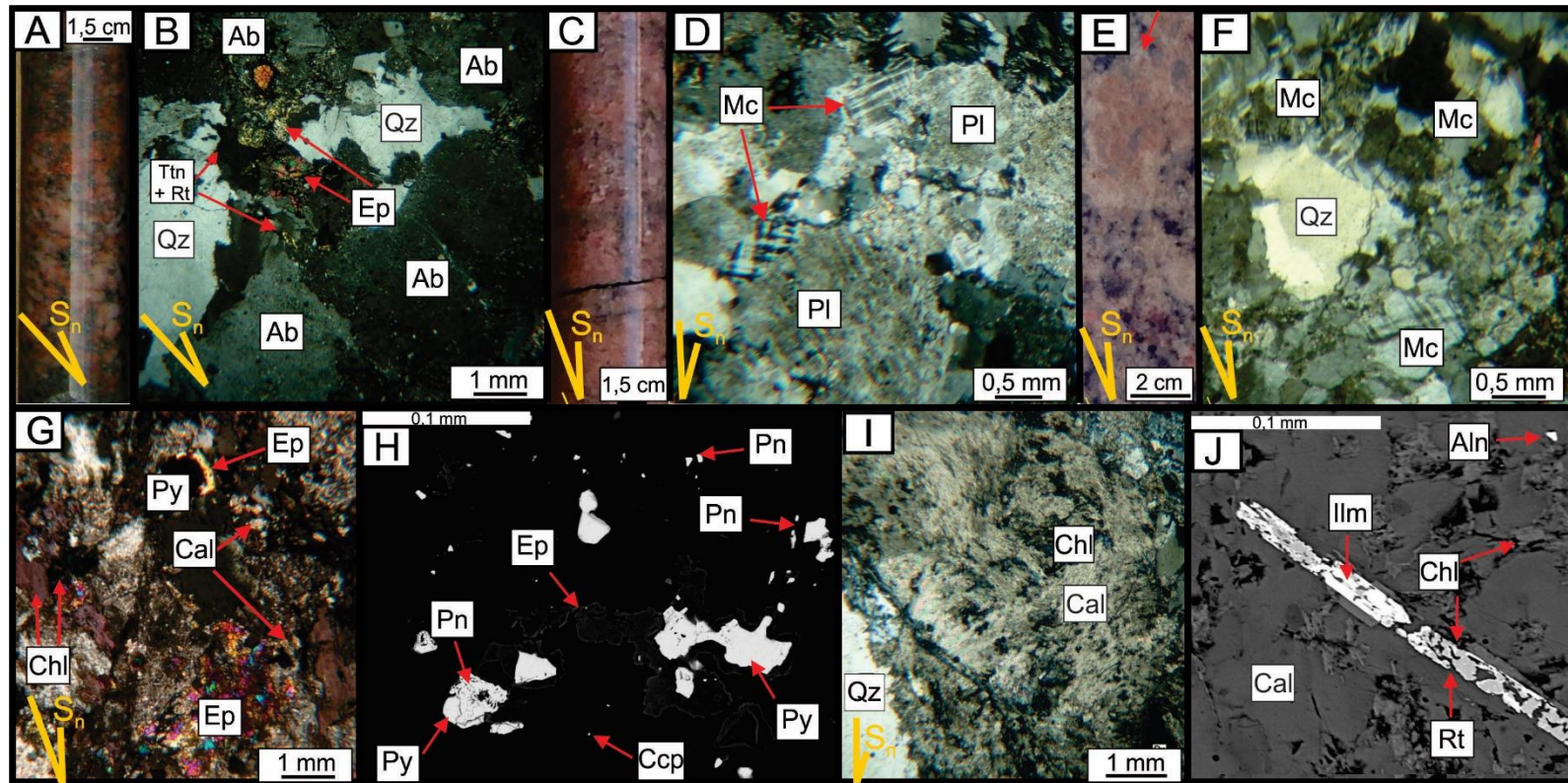


Figure 20 – Albite, Potassic, and Propylitic hydrothermal alterations. Core samples are A, C, E, and photomicrographs (polarized light) are B, D, F, G, I, J. SEM image is H. (A) Albite alteration corresponds to the whitish portion in the biotite tonalite core sample. (B) It locally obliterates the former mineral assemblage. (C) Garnet granodiorite exhibit pinkish color due to potassian alteration. (D) Hydrothermal microcline and quartz replace plagioclase along its boundaries and fractures. (E) Garnet granodiorite exhibit orange portion that correspond to a cavity filled by potassian alteration. (F) Photomicrograph shows microcline with minor quartz. (G) Disseminated propylitic alteration in biotite tonalite. (H) SEM analyses exhibit minor phase of pentlandite and chalcopyrite as part of this alteration. (I) Massive calcite and chlorite fill veinlet with minor quartz. (J) Exsolution texture of ilmenite and rutile, besides an isolated allanite crystal in the same preview veinlet.

Propylitic Alteration

Propylitic alteration is predominant in the lithotypes distal to the mineralization, although it also occurs in the *biotite metatonalite*, which hosts the mineralized vein in the PT-30 (Fig. 12). Its occurrence types and respective mineral assemblages correspond to (a) pervasive and disseminated: chlorite, calcite, epidote, pyrite, chalcopyrite (Fig. 20G, H); (b) veinlets filled by: massive Mn-calcite, chlorite, pyrite, ilmenite, rutile, pyrrhotite, galena and allanite (Fig. 20I, J); and (c) selective alteration of plagioclase. This last type is not common and occurs in granodiorite, generating carbonate with chlorite and rare epidote from plagioclase. The veinlets only appears in the *granodiorite*.

Pervasive alteration differs from the disseminated because it is more intense and can entirely obliterates the igneous assemblages, changing the color of the rock to light to dark green. Disseminated alteration occur as mineral aggregate in the matrix. Chlorite lamellae (0,03-0,5 cm) have light green pleochroism and anomalous purple to Berlin blue interference color. Epidote prismatic crystals (0,05-0,1 cm) occur in the matrix or along the boundaries and cleavage planes of chlorite. Pyrite appears as idiomorphic to subidiomorphic cubic crystals (0,1-0,2 cm) and rare sphalerite inclusions. Calcite appears as a fine anhedral mass. Pentlandite and chalcopyrite occurs as very fine-grained crystals or in exsolution with pyrite (Fig. 20H).

Chloritic Alteration

It occurs in lithotypes distal to the mineralization: *granodiorite*, *leucogranite*, *tonalite*, *garnet-quartz granodiorite mylonite*, and *biotite tonalite mylonite*. It corresponds to a selective or disseminated style alteration in which the mineral assemblage comprises chlorite, ilmenite and rutile. It is a partial or complete selective alteration of biotite and garnet from their grain boundaries, and along [001] cleavage planes or fractures (Fig. 21A). It presents a light green pleochroism and anomalous purple to Berlin blue interference color. The disseminated alteration occurs as fine aggregates of chlorite in the matrix, with no preferential orientation and it may produce a black color in some portions of the *garnet granodiorite*. Ilmenite and/or rutile occur in both of the style alteration, but absent from garnet's alteration. They appear in fine prismatic crystals or micro grains along the cleavage plans and boundaries in chlorite lamellae.

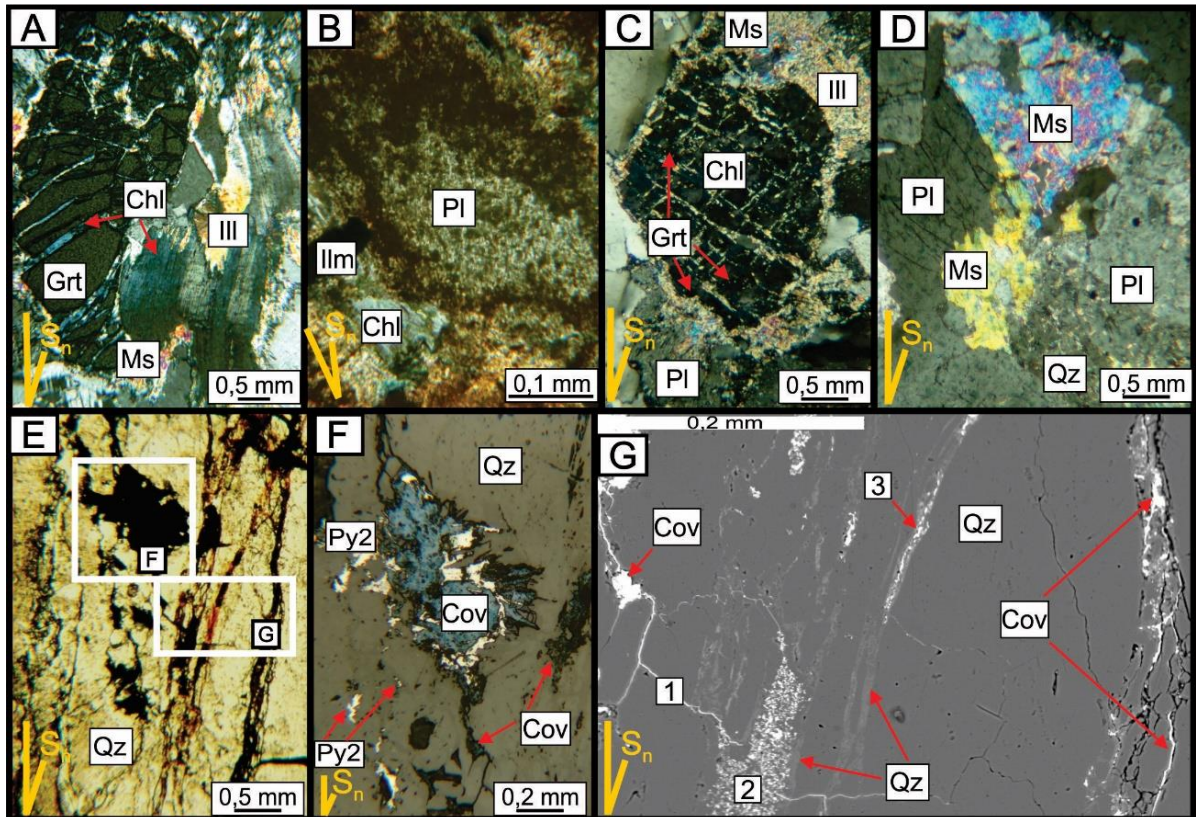


Figure 21 - Chloritic, muscovite-illitic and Fe-Cu hydrothermal alterations at Peteca deposit. (A) Chlorite fills fracture in garnet and appears as a large pseudomorph of biotite crystal. Note that chlorite alters to muscovite/illite from its boundaries and cleavage plans. (B) Reddish color on plagioclase caused by strong illite alteration with Fe hydroxide association. (C) Garnet partially replaced by chlorite. Note muscovite/illite affect garnet, chlorite, and plagioclase. (D) Coarse-grained muscovite disseminated in the quartz-feldspar matrix of the leucogranite. (E) Mineralized vein shows fractures parallel to its walls. These fractures correspond to the reddish structures of the microstructural domain 3 (Fig. 8A, B). White squares indicate the next two images. (F) Intergrowth texture of pyrite 2 and covellite. (G) Image obtained by SEM analyses. Covellite fills fractures and appears as subidiomorphic crystal on the left. Quartz (red arrows) correspond to the microstructural domain 3. The points 1, 2 and 3 correspond to a Se-Ag-Te phase associated with covellite (11-30% S, 24-47% Cu, 0.29% Fe, 5-6% Se, 0.9-2.3% Ag, \leq 1.7% Te).

Muscovite-Illite Alteration

This is the main hydrothermal alteration at Peteca, but muscovite is mainly restricted to the lithotypes with garnet as *granodiorite*, *leucogranite*, *garnet-quartz granodiorite mylonite*, and to the *leucopelmatite*. Its alteration styles do not prefer any orientation and corresponds to (a) selective, (b) disseminated, and (c) infill. The selective alteration affects plagioclase, garnet, biotite and chlorite (Fig. 21A-C). Illite is an alteration product from plagioclase, occurring as very fine lamellae (0,02-0,08 cm) in its boundaries and twinning plans, and generates a turbid aspect on the altered crystals. In the *biotite tonalite*, this alteration causes an intense reddish color in the plagioclase (Fig. 21B). This generated

color origin remains questionable, once there were not found oxides or goethite neither under conventional petrographic microscope nor under SEM analyses. It turns out there is an iron hydroxide association with the illite as long as no crystalline structure was formed to mineral identification.

Disseminated alteration correspond to medium- to coarse-grained muscovite in the matrix (Fig. 21D). The infill style alteration comprises intragranular fractures in quartz and K-feldspar, millimetric veinlets, and cavities filled by illite with minor muscovite and quartz. These cavities are restricted to the granodiorite and leucogranite.

Fe-Cu Alteration

Fe-Cu hydrothermal alteration occurs in the mineralized vein (Fig. 21E) and in rare sub-horizontal veinlets. Its mineral assemblage corresponds to pyrite 2, covellite, quartz, and mineral phase composed of Se-Ag-Te (Fig. 21F, G). In the veinlets, covellite fills intragranular fracture in pyrite 1 (see Fig. 17F). In the vein, it is associated to the faults and fractures that affect pyrite 1 and, less often, sphalerite.

These fractures exhibit fine-grained pyrite crystals (0,01-0,03 cm) herewith classified as pyrite 2. It appears as cubic idiomorphic crystals with no inclusion. Covellite (0,01-0,75 cm) either show straight contact or intergrowth texture with pyrite 2 (Fig. 21F).

Carbonate-Epidote Stockwork

It affects the biotite tonalite and the mineralized vein (PT-30; see Fig. 12). It occurs as (a) veinlets (up to 1,5 cm of thickness; Fig. 22A), (b) stockwork (Fig. 22B), (c) microfaults (Fig. 22C), and (d) fractures (Fig. 22D). Its mineral assemblage comprises calcite, epidote, rutile, leucoxene, goethite, Mn-calcite, titanite, synchysite, monazite, apatite, siderite, quartz.

Epidote (Fig. 22E) occurs as fine subhedral crystals, fine aggregates or as euhedral crystals with prismatic habit. Calcite appears in fine subhedral crystals or as an anhedral mass (Fig. 22E). Microfaults (Fig. 22F) consists of leucoxene, goethite and titanite. Rutile appears as submillimetric crystals or in an intergrowth with titanite and calcite (see Fig. 20B; Fig. 22G, H). Mn-calcite, synchysite (REE phosphate), monazite and apatite occur as very fine-grained crystals or in intergrowth texture with epidote (Fig. 22G, H). Siderite is associated to the Mn-calcite, apatite and fine recrystallized crystals of quartz in fractures and microfaults that affect the mineralized vein in the PT-30 (Fig. 22H).

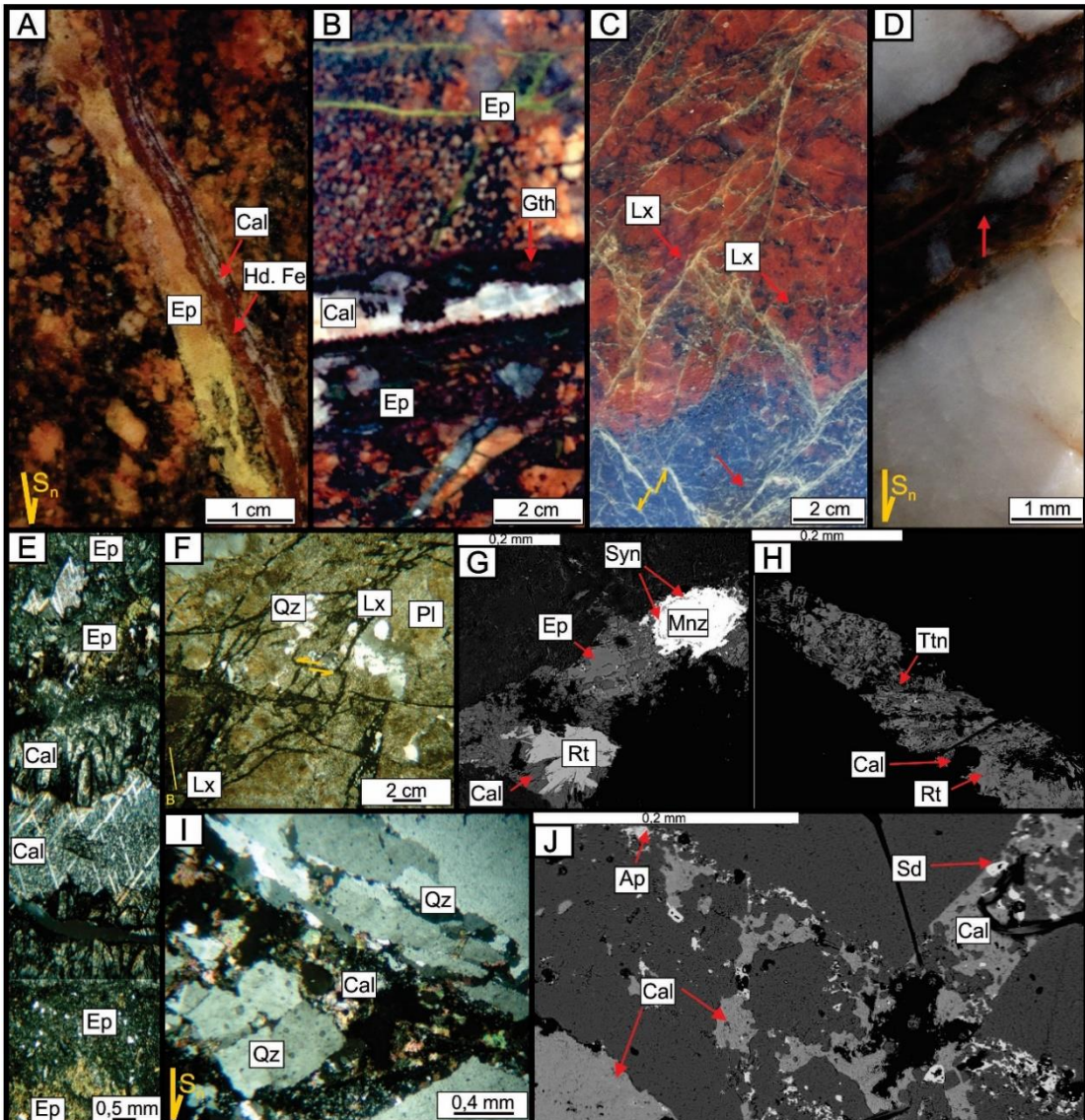


Figure 22 – Core samples and photomicrographs of the Carbonate-Epidote Stockwork alteration at Peteca deposit. (A) Fracture filled by massive epidote, calcite and Fe hydroxide. (B) On the top, epidote fills veinlets. Veinlet with calcite in its centre and goethite on its wall. (C) Microfaults and microfractures filled by leucoxene. Kinematic sinistral indicator in yellow. (D) Red fracture found in the mineralized vein (PT-30). (E) On the centre, calcite presents syntax growth from the wall and fill the core of veinlet massively. Note the cryptocrystalline epidote. (F) Photomicrograph of image C; (G) and (H) are images obtained by SEM analysis. They correspond to the alteration that affects the albitization (see Fig. 11F). Synchysite appears as zoning in monazite. (I) and (J) correspond to the image D. The dark portions are holes on the thin section. Reddish color observed in hand specimen on D is due to Fe hydroxide, besides siderite found in SEM analyses (J).

Tabela 4 - Distribution of the Hydrothermal Systems according to the lithotypes.

		Foliated Granitoids and Metamorphic Rock				Dykes		Protomylonite and Mylonites				Phyllonites		Fractures and Veinlets Infill (oblique to orthogonal in relation to Sn)	Qz Vein
		Grt granodiorite	Grt leucogranite	Bt tonalite	Bt meta- tonalite	Dacite	Pegmatites	Bt ton proto- mylonite	Grt-Qz mylonite	Gnt-Bt granodiorite mylonite	Ill granodiorite mylonite	Cb-chl	Chl-ill		
Shear-hydrothermal System	<i>Bt tonalite protomylonite</i> <i>Grt-Qz mylonite</i> <i>Grt-Bt granodiorite mylonite</i> <i>Illite granodiorite mylonite</i> <i>Cb-chl phyllonite</i> <i>Chl-ill phyllonite</i> <i>Cb infill</i> <i>Qz veinlets with sulphides</i> <i>Qz Vein</i> <i>Mineralization</i>	X		X		X		X	X	X	X	X	X	X	X
Magma-hydrothermal System	<i>Albite</i> <i>Potassic with Microcline</i> <i>Propylitic</i> <i>Chloritic</i> <i>Muscovite-Illite</i> <i>Fe-Cu</i> <i>Stockworks of Cb-Ep</i>	X	X	X	X	X	X	X	X	X	X		X	X	X

4.2. MINERAL CHEMISTRY

Plagioclase

Eighty-three plagioclase analyses are from the garnet granodiorite, garnet leucogranite, biotite tonalite and biotite tonalite protomylonite (Appendix E). They consist of matrix crystals, inclusions and phenocrysts. Cation distribution based on eight oxygens.

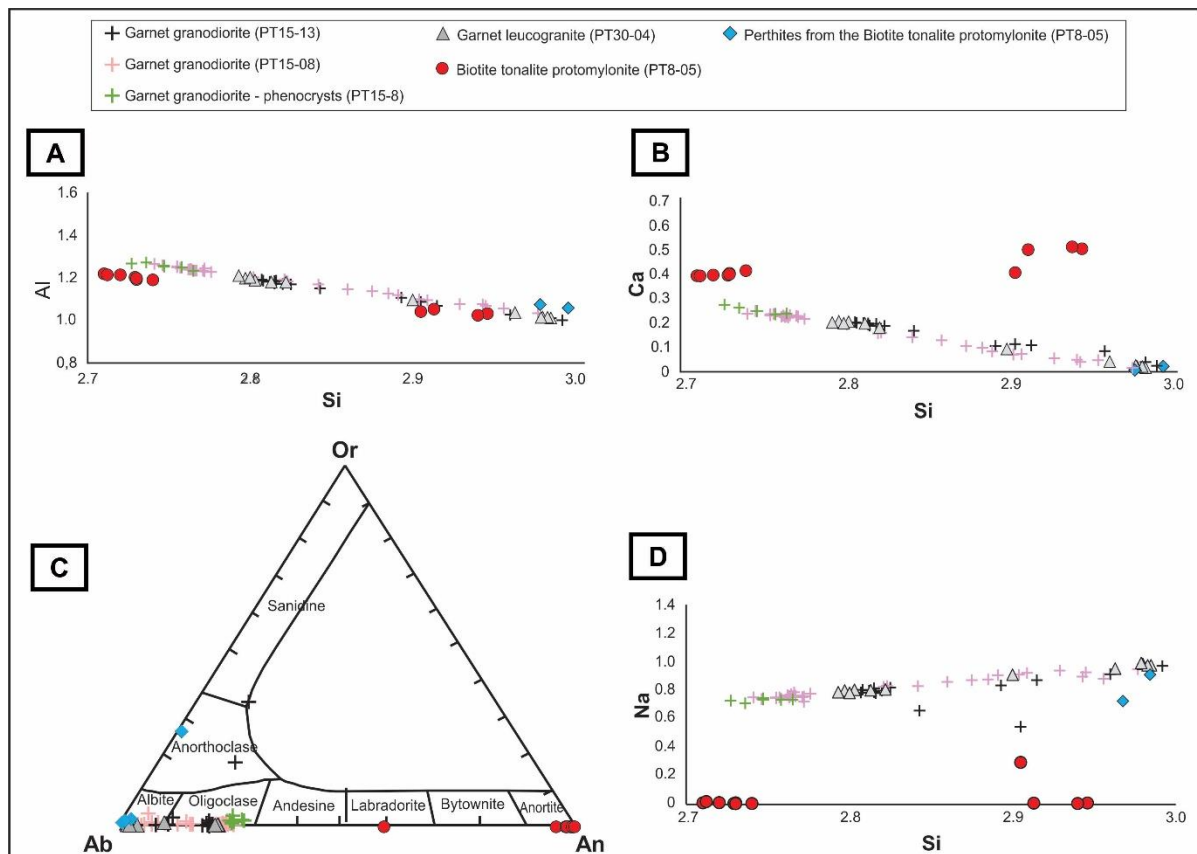


Figure 23 – Mineral chemistry of plagioclase. (A) Slight variation of Al_2O_3 content compared to Si_2O . (B) Higher content of silica for the biotite tonalite protomylonite compared to its protolith biotite tonalite. (C) Ternary diagram (Deer et al., 1992) confirms the high An content in the protomylonite. (D) Most of the perthite results are on the 9 wt% average of Na_2O .

From the granodiorite, the thin-polished section PT15-13 represents the least altered sample compared to PT15-08. Except some spots, the results from PT15-13 concentrate in the range of 64 wt% of SiO_2 whilst the spots from PT15-08 show a greater spread range of silica (Fig. 23A, B, D). The phenocrysts analyses display the lowest content of SiO_2 . Plagioclase from granodiorite and leucogranite correspond to albite and oligoclase, according to the ternary diagram Or-Ab-An proposed by Deer et al. (1992; Fig. 23C). Granodiorite presents two compositional plagioclase groups (An_{2-9} , Ab_{91-98} and An_{11-25} , Ab_{75-89}) as well as the leucogranite (An_{2-9} , Ab_{90-97}) and (An_{18-21} , Ab_{79-81}). Biotite tonalite is

composed of oligoclase (An_{12} and Ab_{86-87}) whilst the biotite tonalite protomylonite presents labradorite and mainly anorthite (An_{96-100} and Ab_{1-4}) (Fig. 23C).

Six analyses of perthite in K-feldspar from the biotite tonalite protomylonite correspond to albite (An_{1-2} and Ab_{98-99}), despite two spots with higher content of potassium (An_{0-1} and Ab_{42-73} ; Fig. 23C).

K-Feldspar

Thirty-nine feldspar analyses are from the garnet granodiorite, garnet leucogranite, biotite tonalite mylonite (Appendix E). They consist of matrix grains, phenocrysts, and porphyroclasts. Cation distribution based on eight oxygens.

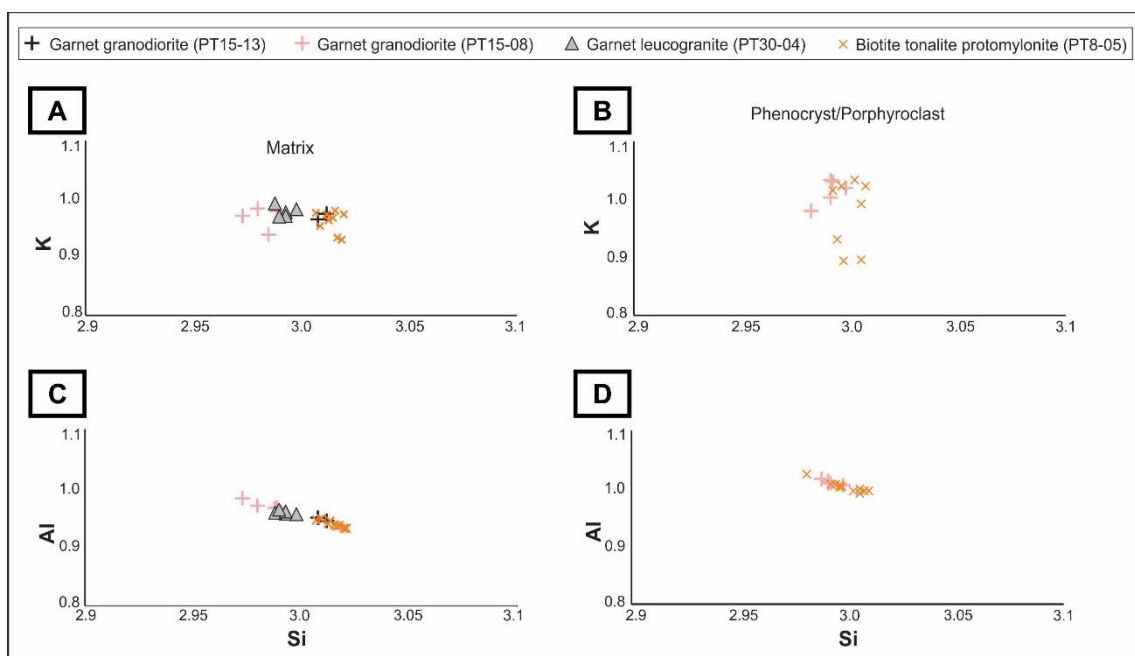


Figure 24 - Binary diagrams for mineral chemistry of K-feldspar in the matrix or as phenocrysts and porphyroclasts.

The results among the matrix grains exhibit a silica compositional variation in which the biotite tonalite protomylonite show the highest value of it (Fig. 24A-D). The more altered K-feldspar from PT 15-13 present more silica and the same content of K_2O and Al_2O_3 as the least altered ones from PT15-08 (Fig. 24A, C). The porphyroclasts present higher content of silica compared to the phenocrysts, and a K_2O compositional variation into two groups (13% and 15-17%).

Garnet

Representative two grains of garnet from the granodiorite (Fig. 25A, B) and three ones from the leucogranite (Fig. 25C, D) were analyzed (Appendix E). Cation distribution based on 12 oxygens and the end members in according to Deer et al. (1992).

Garnets from granodiorite has higher content of Si than the ones in the leucogranite (Fig. 26A, B). The content of Al is constant for garnet in leucogranite, but variable in granodiorite (Fig. 26A). The $\text{Fe}^{3+}/\text{Fe}^{2+}$ ratio decreases toward the garnet from granodiorite (Fig. 26B).

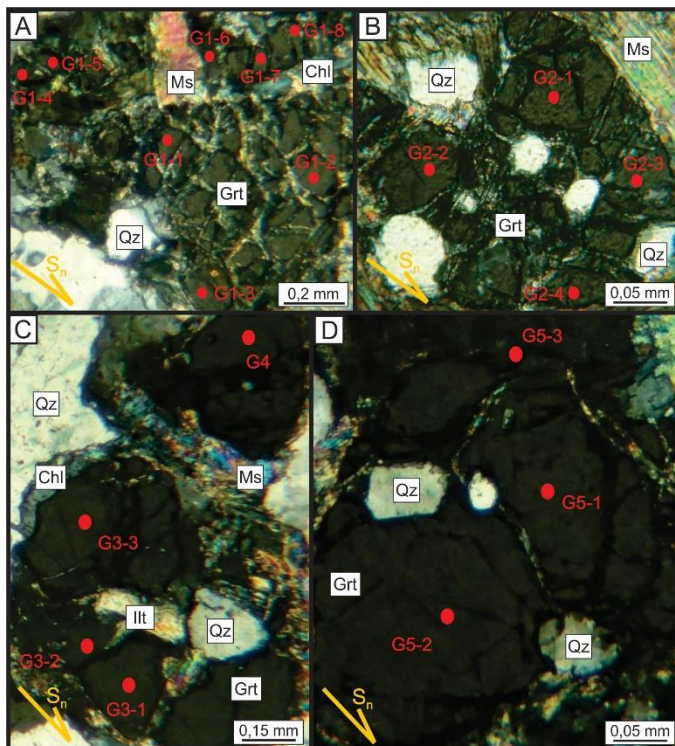


Figure 25 - Garnet crystals analysed. (A, B) From the garnet granodiorite. (B-D) From the garnet leucogranite.

Garnet in both of the lithotypes have the main variation upon pyrope-spessartine endmembers. In the granodiorite, garnet has Prp_{8-18} and Sps_{5-20} , and in the leucogranite Prp_{13-22} and Sps_{4-11} . The ternary diagrams show that the garnets from the granodiorite have higher content of spessartine (Fig. 27C-E). Almandine has a narrow compositional variation comparing the granodiorite (Alm_{70-75}) to leucogranite (Alm_{72-77}). Grossular content is constant at 2 in each analysis (Appendix E). The results of G1 and G5 indicate variational compositions inside the crystals, which it may suggest different populations of garnet, except these differences occur within the same crystals. However, the crystals do not exhibit any zoning under EDS analyses.

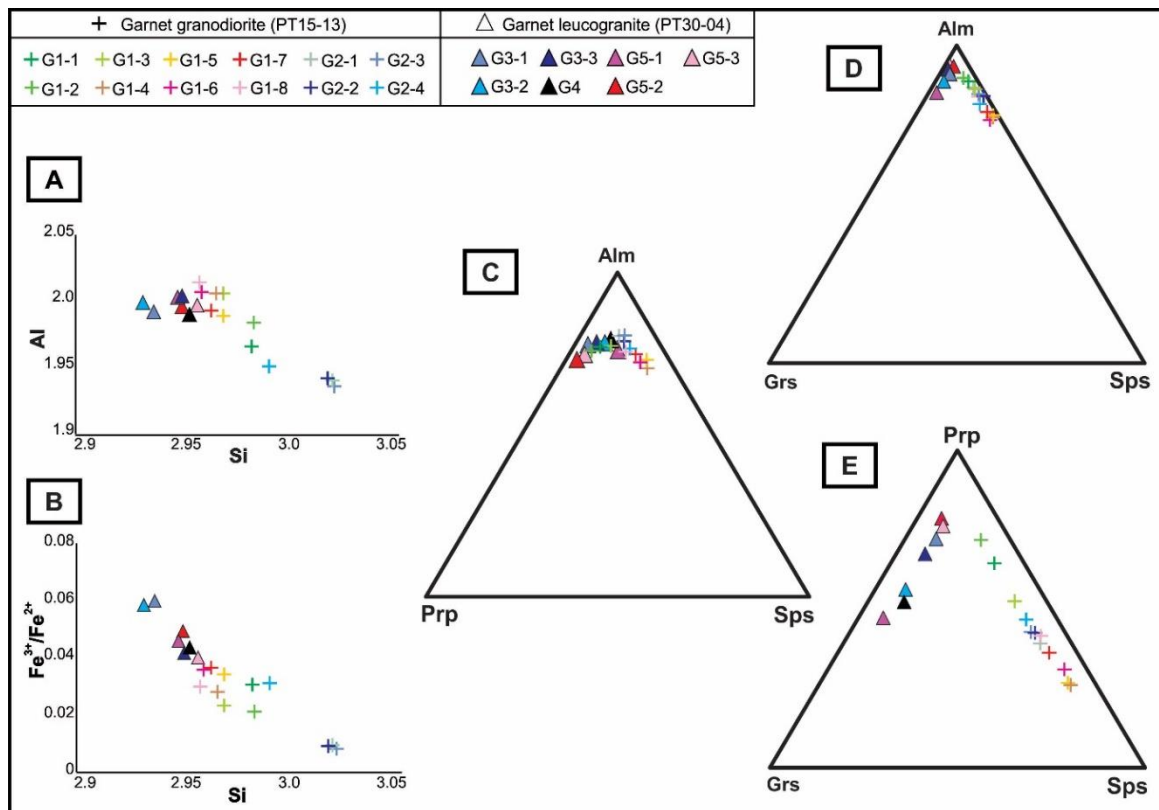


Figure 26 - Diagrams display mineral chemical results of garnets. (A-B) Binary diagrams denote the higher content of Si_2O in the granodiorite. (C-E) Ternary diagram based on the end members

Biotite

Fifty-three analyses of biotite are from the garnet granodiorite, garnet leucogranite, biotite tonalite and biotite tonalite protomylonite, and they commonly replace to chlorite and/or white mica (Appendix E). Cation distribution based on the anhydrous basis per 11 oxygens. In terms of Al^{IV} vs. $\text{Fe}/(\text{Fe}+\text{Mg})$, all the micas are classified as biotite with high siderophyllite-annite contents, and the biotite tonalite protomylonite has the higher values of $\text{Fe}/(\text{Fe}+\text{Mg})$ ratio (Fig. 27). The same diagram shows three groups for this lithotype according to the varying Al^{IV} : 1.2-1.3; 1.3-1.4; and higher than 1.4 a.p.f.u. However, these compositional variations occur within the same lamella and no pattern for these distributions appears.

The ternary diagram $\text{Mg}-(\text{AL}^{\text{VI}}+\text{Fe}^{3+}+\text{Ti})-(\text{Fe}^{2+}+\text{Mn}^{2+})$ displays the biotite data as Fe^{2+} -biotite according to the nomenclature of Foster (1960; Fig. 28A). According to the ternary diagram $10*\text{TiO}_2-(\text{FeO}_t+\text{MnO})-\text{MgO}$ proposed by Nachit et al. (2005), most of the data lie within the reequilibrated primary biotite field (Fig. 28B). Comparing the protomylonite and granodiorite (PT15-13) data, it is noticeable the decreasing of TiO_2 and

slight increase of $\text{FeO}_t + \text{MnO}$ toward the secondary biotite field (Fig. 29B). The four analyses from the PT15-13 sample classified as secondary biotite correspond to three different lamellae (bi1, bi3 and bi4; Appendix D). They exhibit lower contents of TiO_2 , SiO_2 and more of Al_2O_3 .

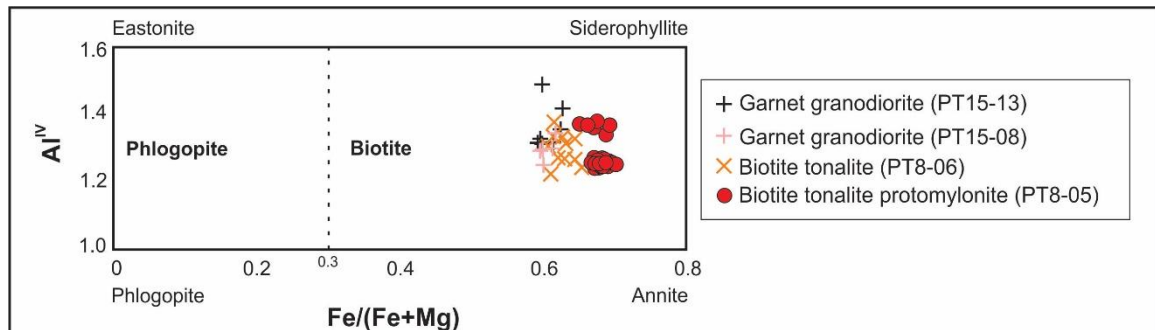


Figure 27 - Al^{IV} vs. $\text{Fe}/(\text{Fe}+\text{Mg})$ diagram proposed by Tamizel (2014) classifies all the chemical analyses as biotite.

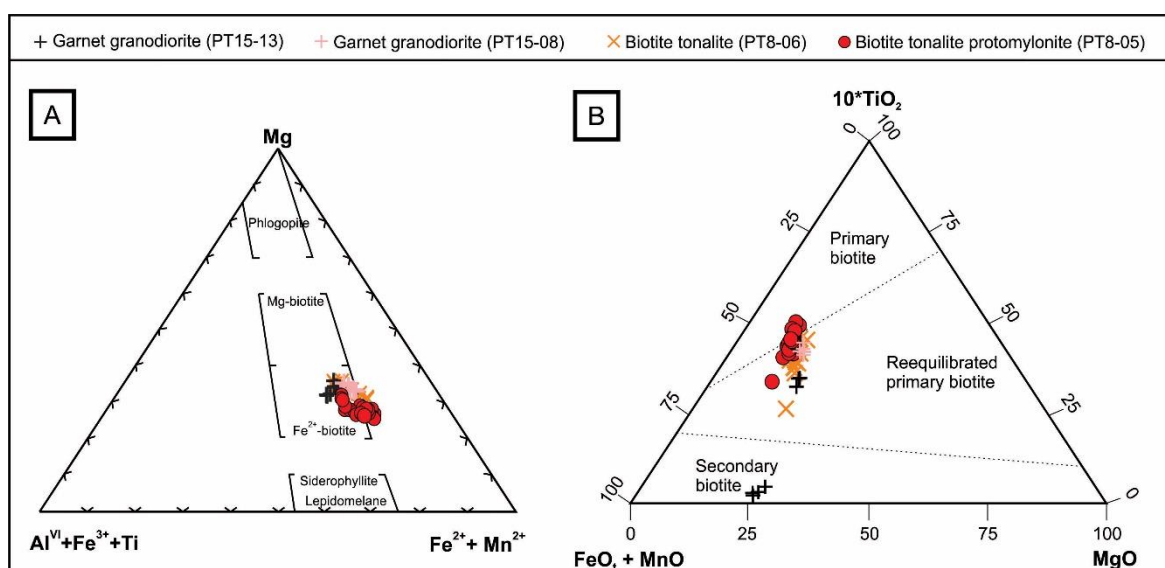


Figure 28 - Ternary diagrams for mineral chemistry of biotite. (A) Ternary diagram proposed by Foster (1960) classifies trioctahedral micas. (B) Ternary diagram proposed by Natchi et al. (2005) classifies the primary biotite from the re-equilibrated and secondary ones.

Chlorite

Thirty-nine analyses of chlorite are from the chlorite-illite phyllonite, and alterations from the magmatic-hydrothermal system as the propylitic and selective of biotite and garnet (Appendix E). Cation distribution based on the anhydrous basis per 14 oxygens. According to the diagram proposed by Foster (1962), the main variation for all groups is at Si content (Fig. 29A). The chlorite from the phyllonite and propylitic alteration are classified as ripidolite. The other results groups show variable range between ripidolite and brunsvigite. The chlorite from the biotite tonalite protomylonite has the greatest Fe/(Fe+Mg) ratio, which is confirmed through the diagram proposed by Ciesielczuk (2012; Fig. 29B). According to this graph, chlorite from the phyllonite, propylitic alteration, and selective alteration in the leucogranite and tonalite are in the Fe-Al Clinochlore field. Chlorite from selective alteration in the granodiorite and the tonalite protomylonite is within the Fe-Al Clinochlore and Mg-Chamosite fields, indicating a lower Al^{IV}/(Si+Al^{IV}) ratio.

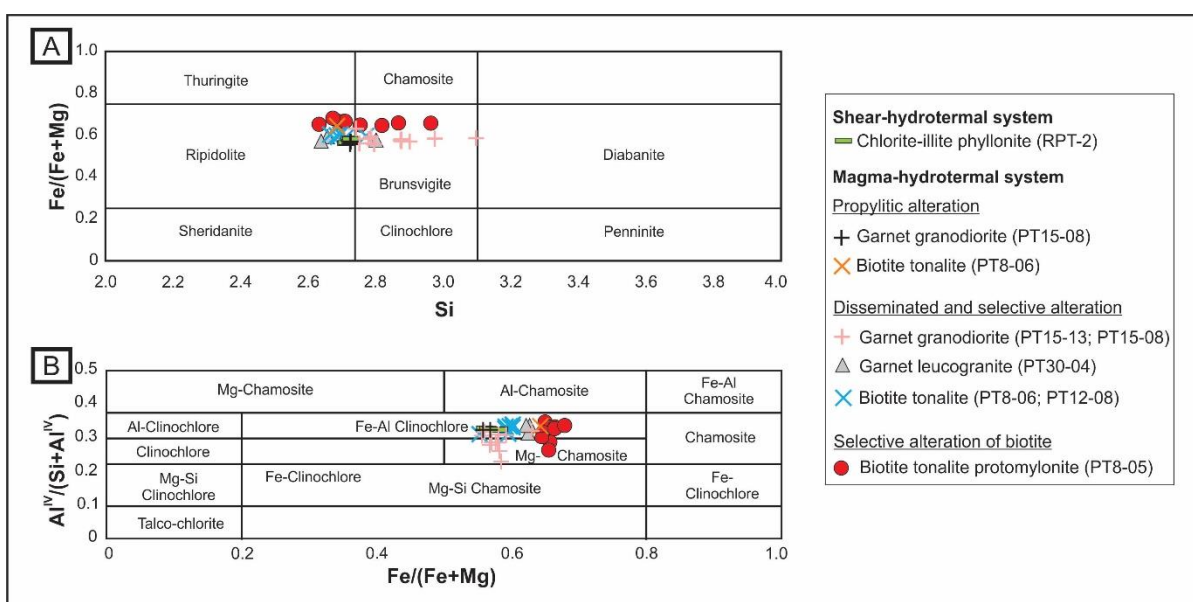


Figure 29 – Binary diagrams for chemical analyses of chlorite. (A) Si to vs. $\text{Fe}^{2+}/(\text{Fe}^{2+} + \text{Mg}^{2+})$ ratio diagram proposed by Foster (1962). (B) Diagram proposed by Ciesielczuk (2012) classifies the chlorite as Fe-Al Clinochlore and Mg-Chamosite.

White Micas

According to the petrographic stage analyses, the white micas splits into illite and muscovite mainly based on their size lamellae (Appendix E). Cation distribution based on the anhydrous basis per 11 oxygens.

Illite

The eight-four illite data obtained relates to the shear-hydrothermal system and to the magmatic-hydrothermal system (Appendix E). The selective alteration affects feldspars and micas, and this mica infill small cavities in the biotite tonalite. According to the ternary diagram proposed by Deer et al. (1992), all these mica groups correspond to phengite (Fig. 30A). The same result is confirmed through the ternary diagram proposed by Tappert (2013; Fig. 30B), which show that the phengite group has a Si:Al ratio higher than 3.1.

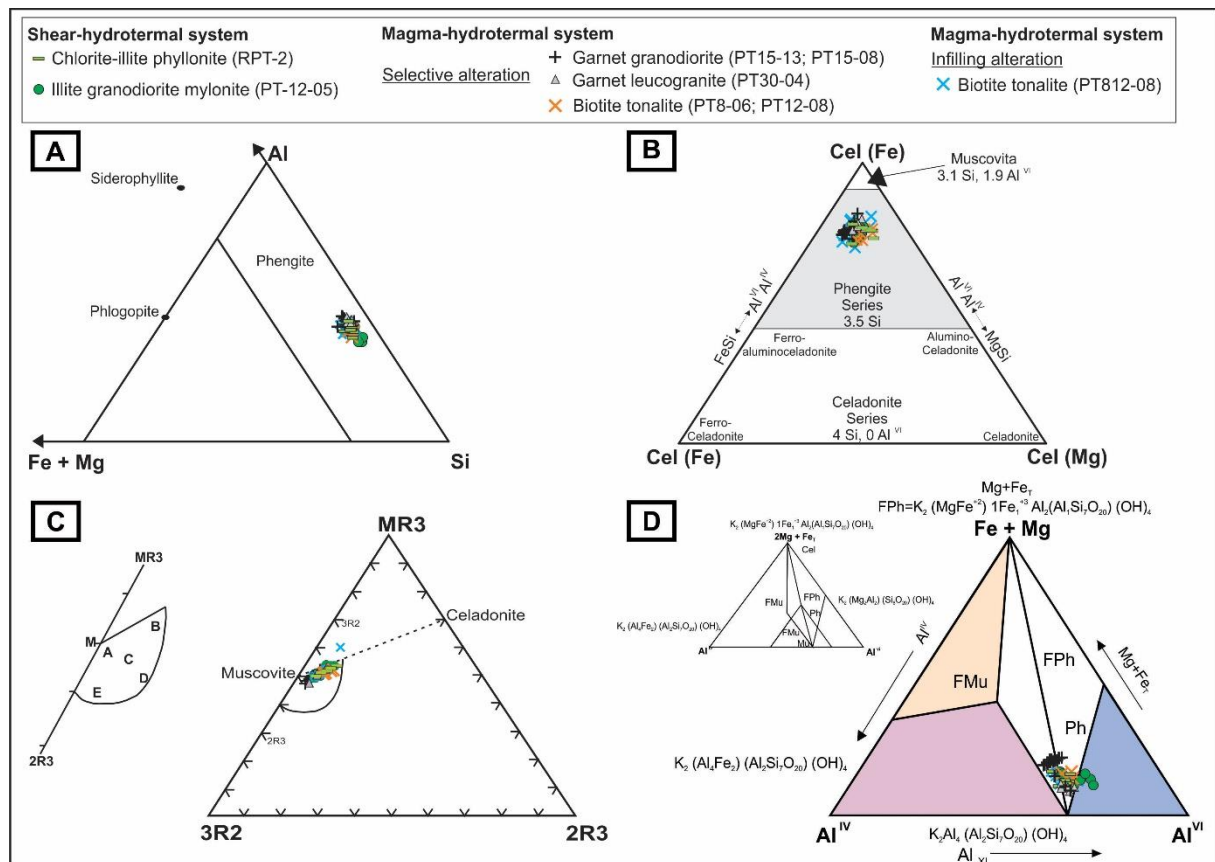


Figure 30 - Ternary diagrams for white micas applied to illite. (A) According to Deer et al. (1992), the illite corresponds to phengite. (B) Tappert (2013) ternary diagram for white micas classification. (C) Ternary diagram proposed by Velde (1985) represents the chemical composition of white micas. M: muscovite; A: magmatic micas; B: phengite; C: illite; D: illite associated to chlorite; E: illite in sandstones, in the first stages of weathering and in hydrothermal events of granitic rocks. $MR_3 = Na + K + Ca$; $2R_3 = ((Al_i) - MR_3)/2$; $3R_2 = (Fe + Mg)/3$. (D) Ternary diagram proposed by Guidotti (1987) to classify white micas. FMu: ferri-muscovite; Mu: muscovite; Ph: phengite; Fpg: ferri-phengite; Mu: muscovite.

The ternary diagram proposed by Velde (1985) comprises the solid solution Muscovite-Phengite-Illite line (Fig. 30C). The micas from the shear system show a trend phengite-illite; micas from the granodiorite and leucogranite classified as muscovite with a tendency toward the phengite; the selective alteration present in the biotite tonalite tends to be more illitic than the infilling alteration. The ternary diagram proposed by Guidotti (1987) also confirms that all these micas correspond to phengite (Fig. 30D). Furthermore, the results from the granodiorite has a tendency toward the Ferri-Phengite, meanwhile the ones from the leucogranite has lower in its content; the alteration in the biotite tonalite and the illite from the phyllonite have an intermediate composition between the other two lithotypes; and the illite mylonite show a variable trend according to the Al content.

According to Miller et al. (1981), the replacement of $\text{Al}_{(\text{t})}$ by $[\text{Si}^{4+} + (\text{Fe}^{2+} + \text{Mg}^{2+})]$ is common in the phengite group as displayed in the Fig. 31A. Replacement of Al^{VI} by $(\text{Fe}^{2+} + \text{Mg}^{2+})$ in the octahedral positions is other charge compensation (Fig. 31B). The same figure denotes two concentrated areas for the alteration in the granodiorite. However, no petrographic or textural pattern appears to distinguish of them. Both graphs also show that the infilling alteration presents the least efficient exchanging charges.

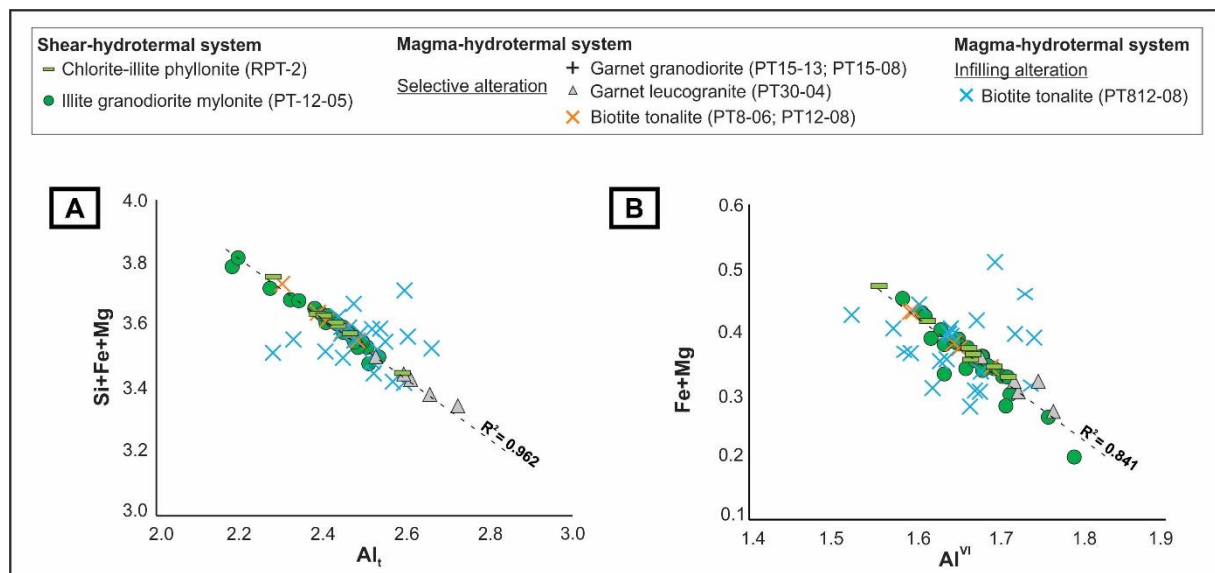


Figure 31 - Correlation diagrams for illite. (A) Correlation diagram Al^{VI} vs. $(\text{Fe} + \text{Mg})$. (B) $\text{Al}_{(\text{t})}$ vs. $[\text{Si} + (\text{Fe} + \text{Mg})]$ for the white micas of the Peteca deposit. R = Correlation coefficient.

Muscovite

The twenty-five muscovite data obtained relates to the selective alteration of garnet from the granodiorite and leucogranite, besides the coarse muscovite lamellae corresponding to the disseminated alteration in the leucogranite (Appendix E). Similar to the results from illite, all muscovite data correspond to phengite according to Deer et al. (1992; Fig. 32A). It is noticeable the results from the granodiorite present a tendency toward the celadonite, which is confirmed using the diagram proposed by Tappert (2013) , and on the solid solution Muscovite-Phengite-Illite line proposed by Velde (1985; Fig. 32B, C). The diagram proposed by Guidotti (1987) also confirms the phengite classification, but with a greater content of Al^{VI} in the results from the granodiorite. These three mica groups present great charge compensation as showed on the Fig. 33.

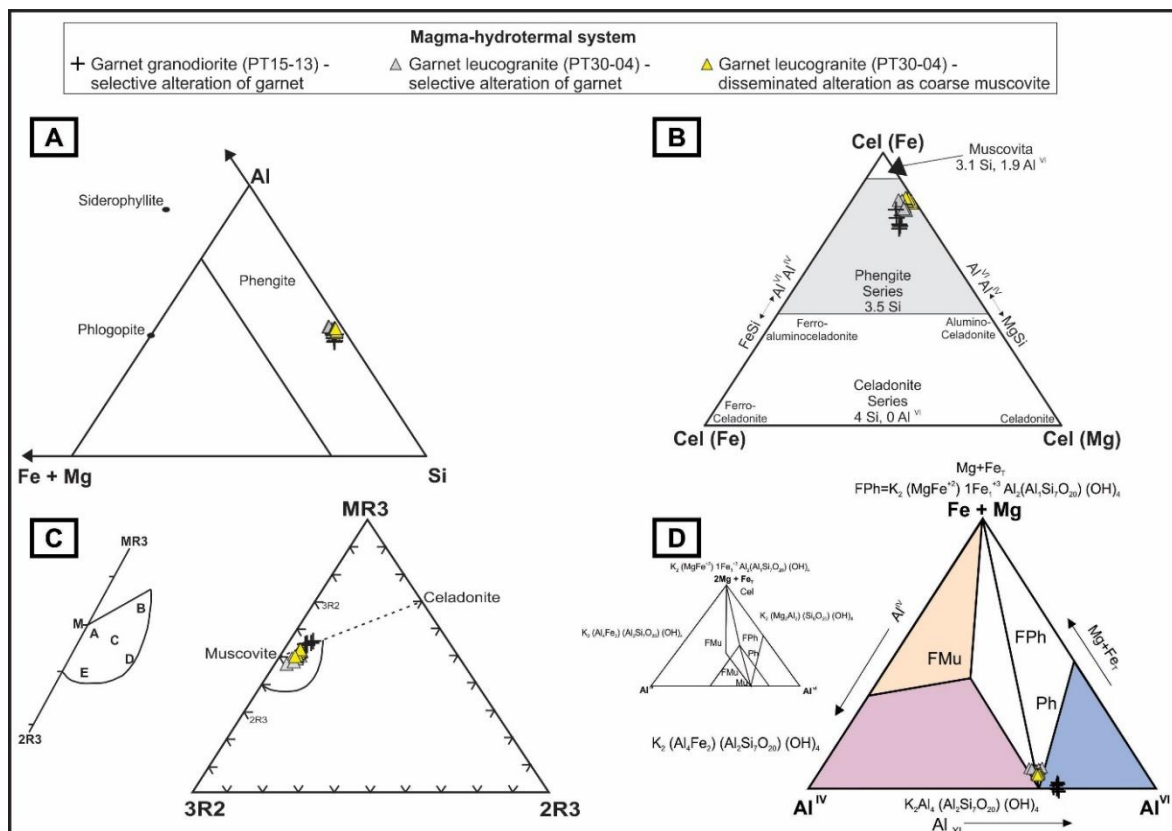


Figure 32 - Ternary diagrams for white micas applied to muscovite. (A) According to Deer et al. (1992), the illite corresponds to phengite. (B) Tappert (2013) ternary diagram for white micas classification. (C) Ternary diagram proposed by Velde (1985) represents the chemical composition of white micas. M: muscovite; A: magmatic micas; B: phengite; C: illite; D: illite associated to chlorite; E: illite in sandstones, in the first stages of weathering and in hydrothermal events of granitic rocks. $\text{MR3} = \text{Na} + \text{K} + \text{Ca}$; $2\text{R3} = ((\text{Al}_t) - \text{MR3}/2)$; $3\text{R2} = (\text{Fe} + \text{Mg})/3$. (D) Ternary diagram proposed by Guidotti (1987) to classify white micas. Fmu: ferri-muscovite; Mu: muscovite; Ph: phengite; Fpg: ferri-phengite; Mu: muscovite.

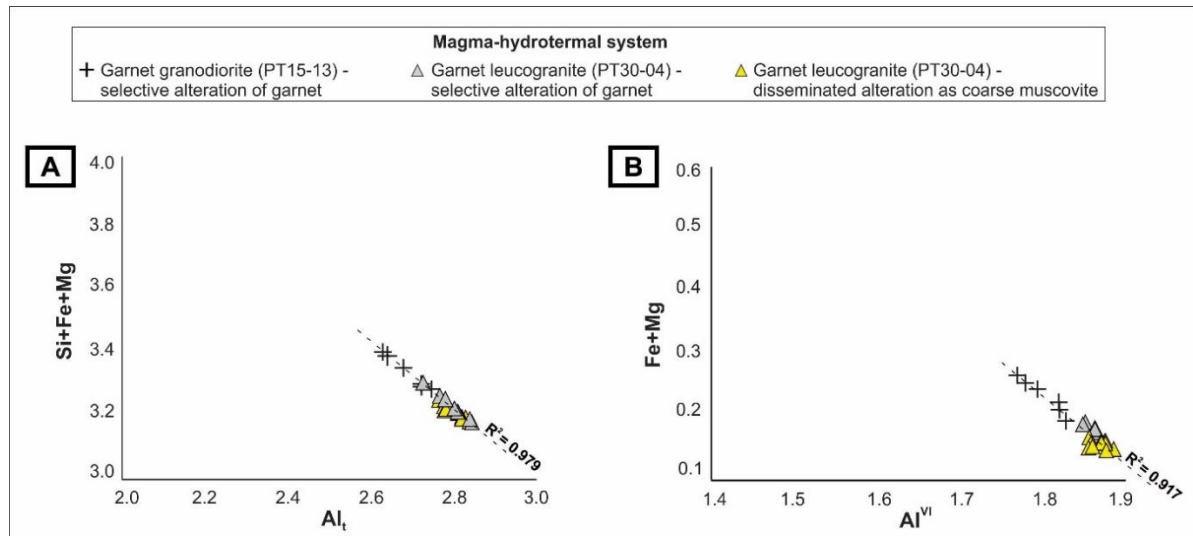


Figure 33 - Correlation diagrams for muscovite. (A) Correlation diagram Al^{VI} vs. $(\text{Fe} + \text{Mg})$. (B) $\text{Al}_{\text{(t)}}$ vs. $[\text{Si} + (\text{Fe} + \text{Mg})]$ for the white micas of the Peteca deposit. R = Correlation coefficient.

Fe-Ti Oxides

Fourty-nine analyses of Fe-Ti oxides correspond to ilmenite-hematite and rutile (Appendix E). Recalculated structural formulae for ilmenite-hematite based on the anydrous basis per 3 oxygens, while for rutile per 2 oxygens. Among the ilmenite-hematite analyses, the ternary diagram Ti^{4+} - Fe^{2+} - Fe^{3+} (Fig. 34A) shows that micas alters to ilmenite or hematite, as well as the intra-grain exsolution is composed of theses two oxides. Medium-grained crystals corresponde to ilmenite. A rare exsolution of oxides also present titanite and rutile. In the phyllonite, rutile is the only present oxide. The binary diagrams (Fig. 34B, C) shows the same grouped spots with low, intermediate and high Fe_{t} content.

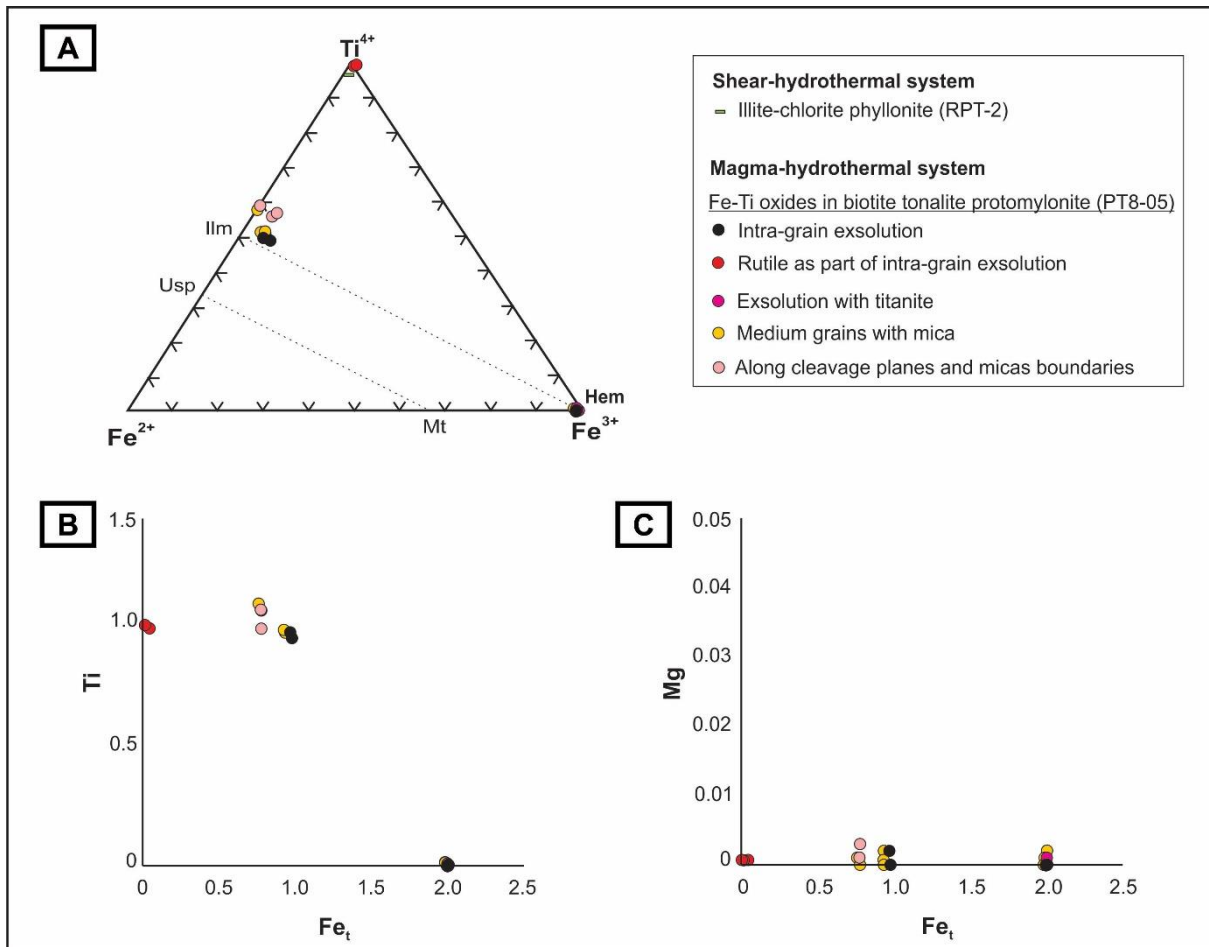


Figure 34 - Diagrams for mineral chemistry of Fe-Ti oxides. (A) Ternary diagram classification according to $\text{Fe}^{2+}\text{Fe}^{3+}\text{Ti}^{4+}$. (B) Ti vs. Fe_t diagram. (C) Mg vs. Fe_t diagram.

4.4. GEOTHERMOMETRY

After applying the geothermometer model proposed by Bourdelle et al. (2013) for chlorite, most of the results denote a minimum temperature of 350°C (Fig. 35), except the large variation of temperature related to the alteration in the granodiorite. According to these authors, this method presents an uncertainty of $\pm 20^\circ\text{C}$.

For the Inoue et al. (2009) calculations, the chloritization includes the both of disseminated and selective types. Based on this method, which there is an uncertainty of $\pm 20^\circ\text{C}$, the chloritization presents the largest range of temperatures, meanwhile the phyllonite the narrowest variation (Fig. 36). Calculated geometric means show the chlorite crystallization temperatures are higher in alterations from the magmatic-hydrothermal system, achieving more than 420°C. The chlorite geometric mean from the phyllonite is at 369°C, while the both of chlorites from the propylitic and chloritization resulted at 394°C.

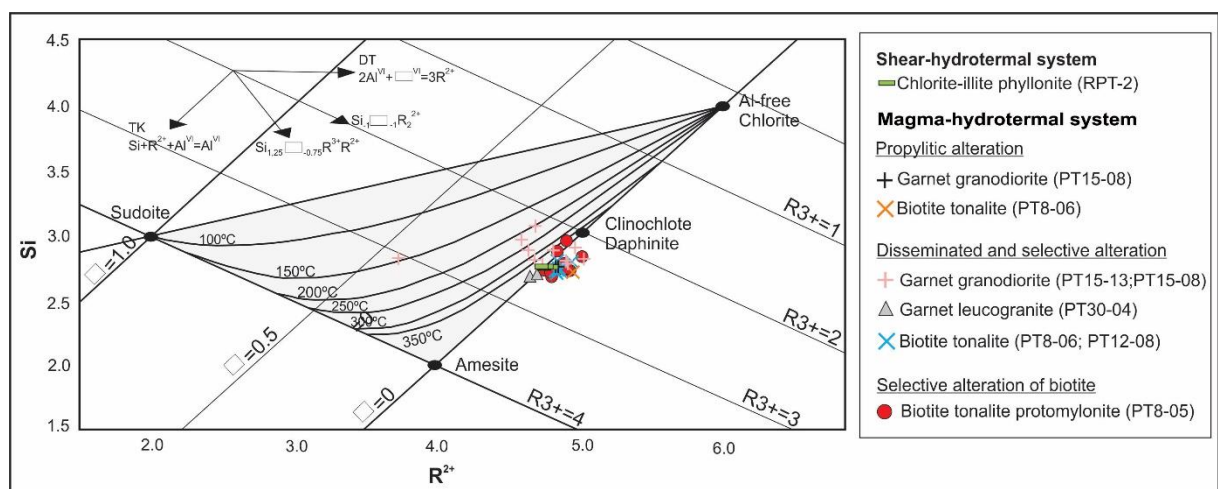


Figure 35 - Chlorite crystallization temperatures at the Peteca deposit according to Bourdelle et al. (2013) geothermometer.

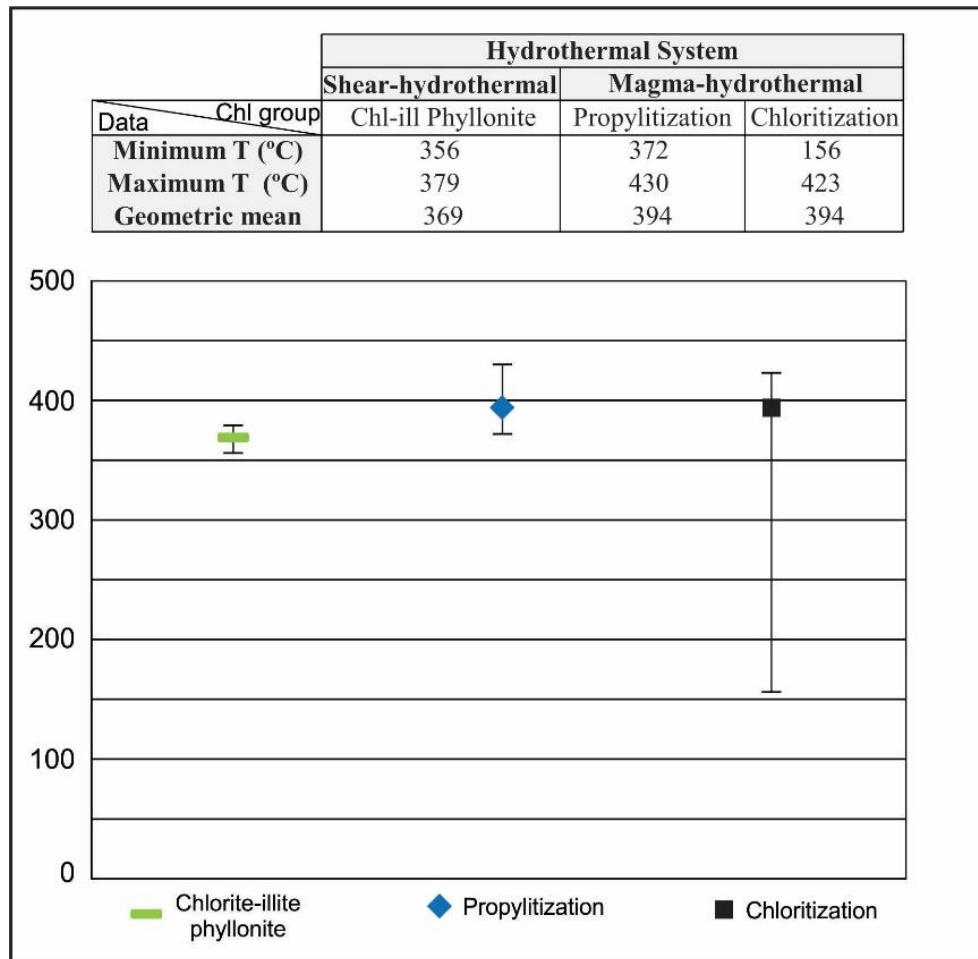


Figure 36 – Chlorite crystallization temperatures at the Peteca deposit according to Inoue et al. (2009) geothermometer.

Considering the Battaglia (2004) geothermometer for white mica, its method presents a mean error of 7%. For illite (Fig. 37), the illite granodiorite mylonite presents the greater temperature variation with a minimum at 230°C and a maximum at 310°C with a geometric mean at 288°C. Toward the chlorite-illite phyllonite, there is a slight temperature increase with a geometric mean at 304°C. The geometric mean for the magmatic-hydrothermal varies from 295 to 314 in the selective type, and at 302°C for the infilling style.

Applying the same geothermometer for muscovite (Fig. 38), the selective alteration of garnet presents temperatures ranging from 275° to 314°C, meanwhile the disseminated alteration as coarse-grained lamellae shows the geometric mean at 286°C. Comparing the selective alterations either to illite or to muscovite, the granodiorite comprises the highest crystallization temperatures of white mica.

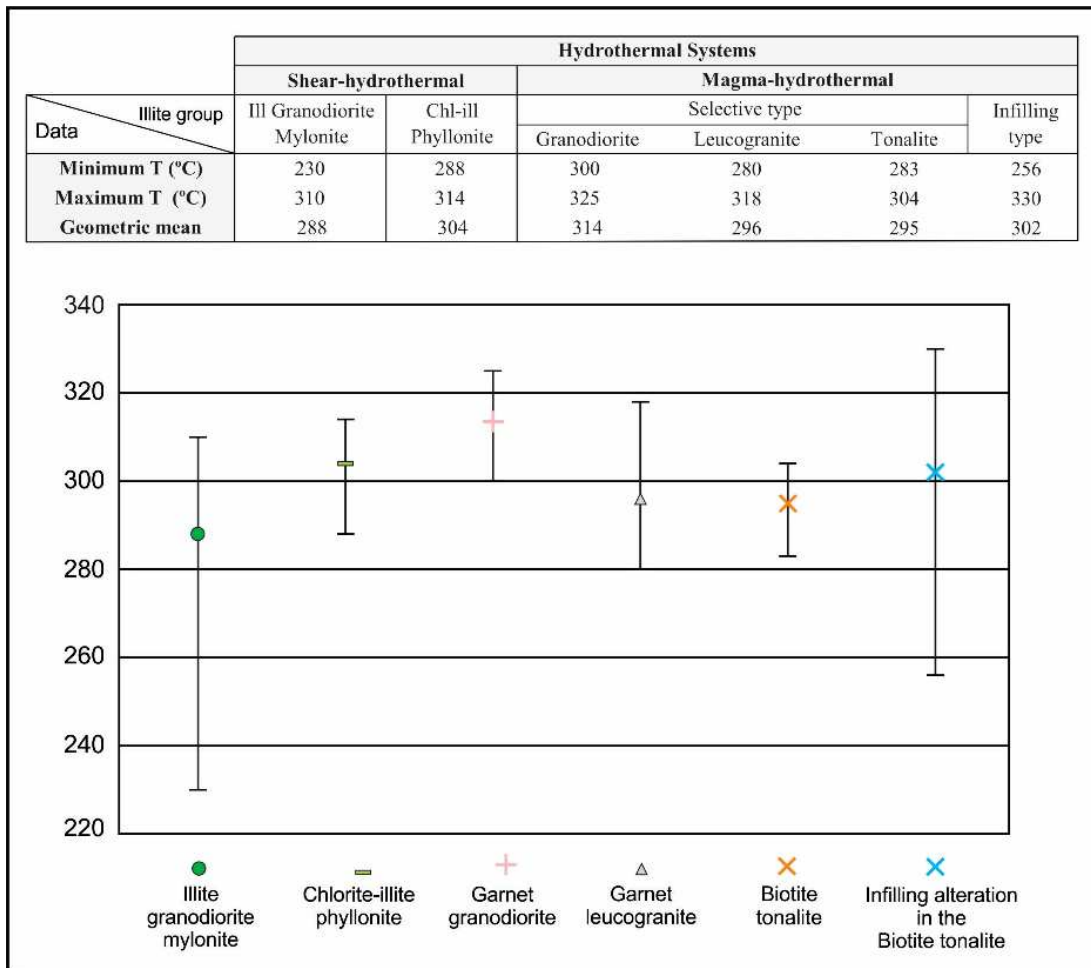


Figure 37 - Illite crystallization temperatures at the Peteca deposit according to Battaglia (2004) geothermometer.

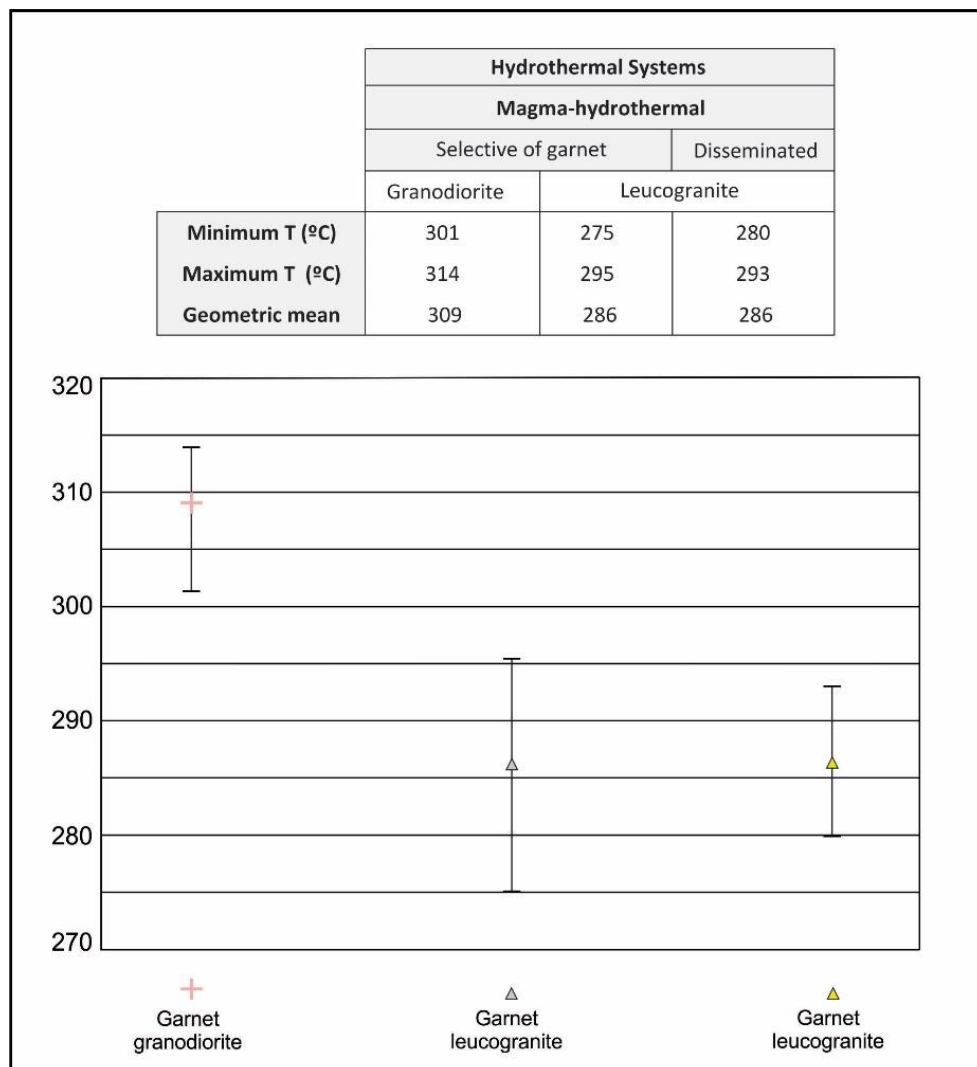


Figure 38 - Muscovite crystallization temperatures at the Peteca deposit according to Battaglia (2004) geothermometer.

5. DISCUSSIONS

5.1. METAMORPHISM

Both of the granodiorite and the leucogranite present tapering edge twinning in feldspar (Fig. 13E) that indicates deformation or mechanical twinning formed at low- to medium-grade condition with temperature range of 400°-500°C (Passchier & Trouw, 2005). In addition, the granodiorite presents recrystallized feldspar, which starts to be common in higher-grade conditions, up to 650°C (Tullis, 2002; Passchier & Trouw, 2005). Quispe (2016) relates chessboard subgrain pattern as a quartz microstructure in the same lithotype that points to temperatures above 650°C (Krul, 1996; Rosemberg & Stünitz., 2003).

The garnet leucogranite here written was former classified as garnet-muscovite leucogranite by Quispe (2016) as the correspondent of the Braço Norte granitoids unit. According to this author, the garnet play an important role as an Al-rich mineral, besides the kyanite-garnet xenolith reported by himself. This author correlates the leucogranite as an S-type granite indicating a crustal melting source for the magmatism related to the Cuiú-Cuiú magmatic arc. Regarding these considerations, the garnet in the leucogranite may have an igneous origin.

The both of the garnet from the leucogranite ($\text{Alm}_{0,72-0,77}\text{Prp}_{0,12-0,22}\text{Sps}_{0,04-0,11}\text{Grs}_{0,02}$) and granodiorite ($\text{Alm}_{0,70-0,77}\text{Prp}_{0,08-0,18}\text{Sps}_{0,05-0,20}\text{Grs}_{0,02}$) correspond to almandine, and present low content of grossular (Ca end member). However, the garnet from the leucogranite has a higher content of pyrope (Mg end member) whilst the one from the granodiorite has higher content of spessartine (Mn end member) (Fig. 27). These compositional differences suggest the garnet from the granodiorite is not igneous.

A possible origin for the garnet may be metamorphic, which commonly occurs in amphibolite facies from 500°C, but it also can appear in upper greenschist facies. Whether the garnet in the granodiorite is metamorphic, the Sn foliation in the granitoids may be metamorphic as well. Further evidence of metamorphism at Peteca is the biotite metatonaline occurrence. Its recrystallized matrix and the presence of non-reactive contact between biotite and plagioclase can support its metamorphic classification (Fig. 13M).

5.2. HYDROTHERMAL SYSTEMS

The following two images (Fig. 39, 40) show the hydrothermal systems on geologic section and drill cores. They represent the main hydrothermal alteration that affects each portion of the rocks. Whether there are more than one predominant alteration stage, then its portion is represented by two or more colors.

Both of the hydrothermal systems occur in the drill cores PT-8, PT-22, PT-12 and PT-15 (Fig. 39). However, the PT-30 was less affected by the shear-hydrothermal system once it does not present mylonites, phyllonites (Fig. 40). Furthermore, its mineralized vein is hosted by the biotite metatonalite, which differs from the other drill cores.

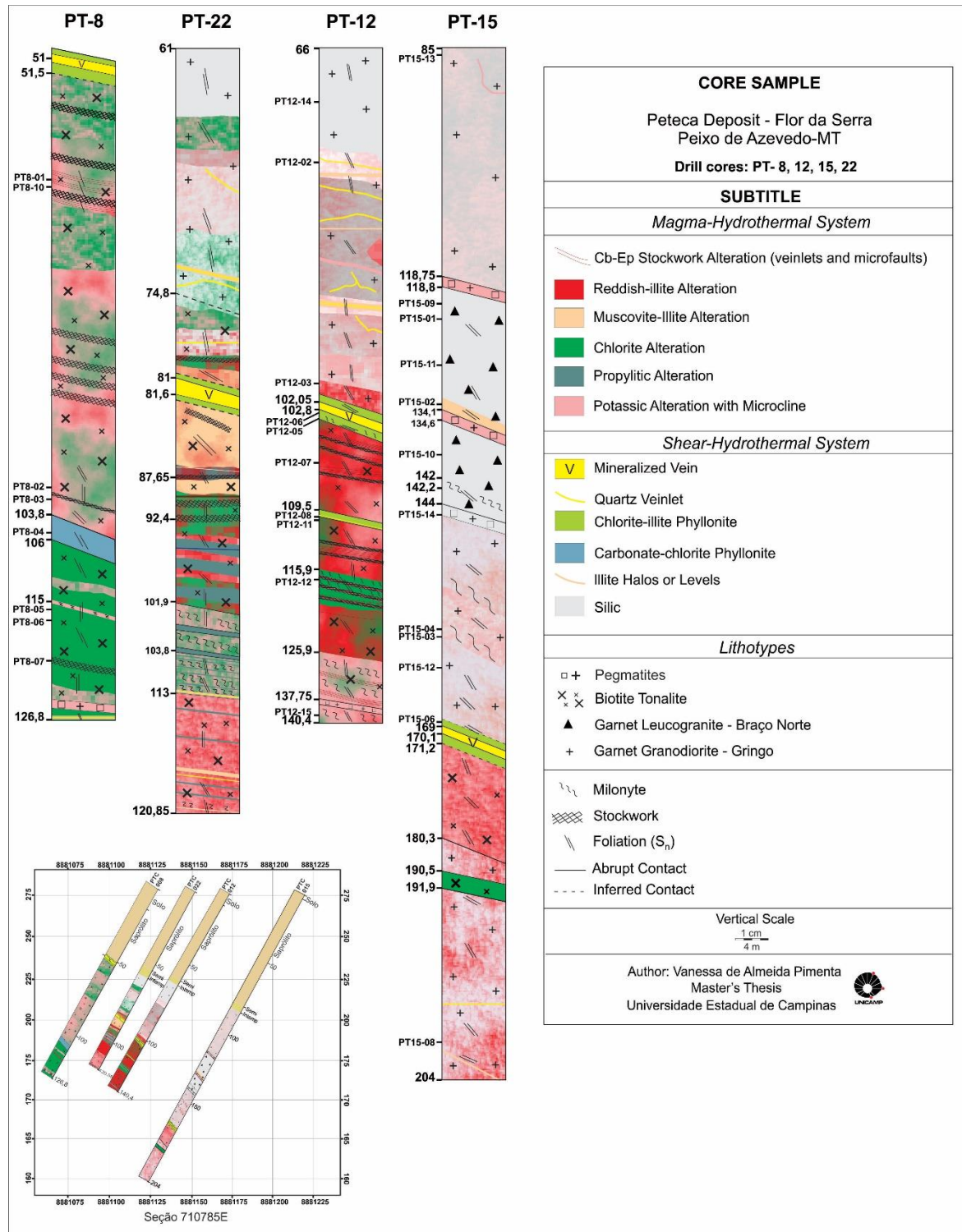


Figure 39 - Geologic section of oriented drill cores (PT-8, PT-22, PT-12, PT-15) display their lithotypes and both of the shear- and magmatic-hydrothermal systems distributions. The color mix in some portions indicate predominance of more than one hydrothermal alteration.

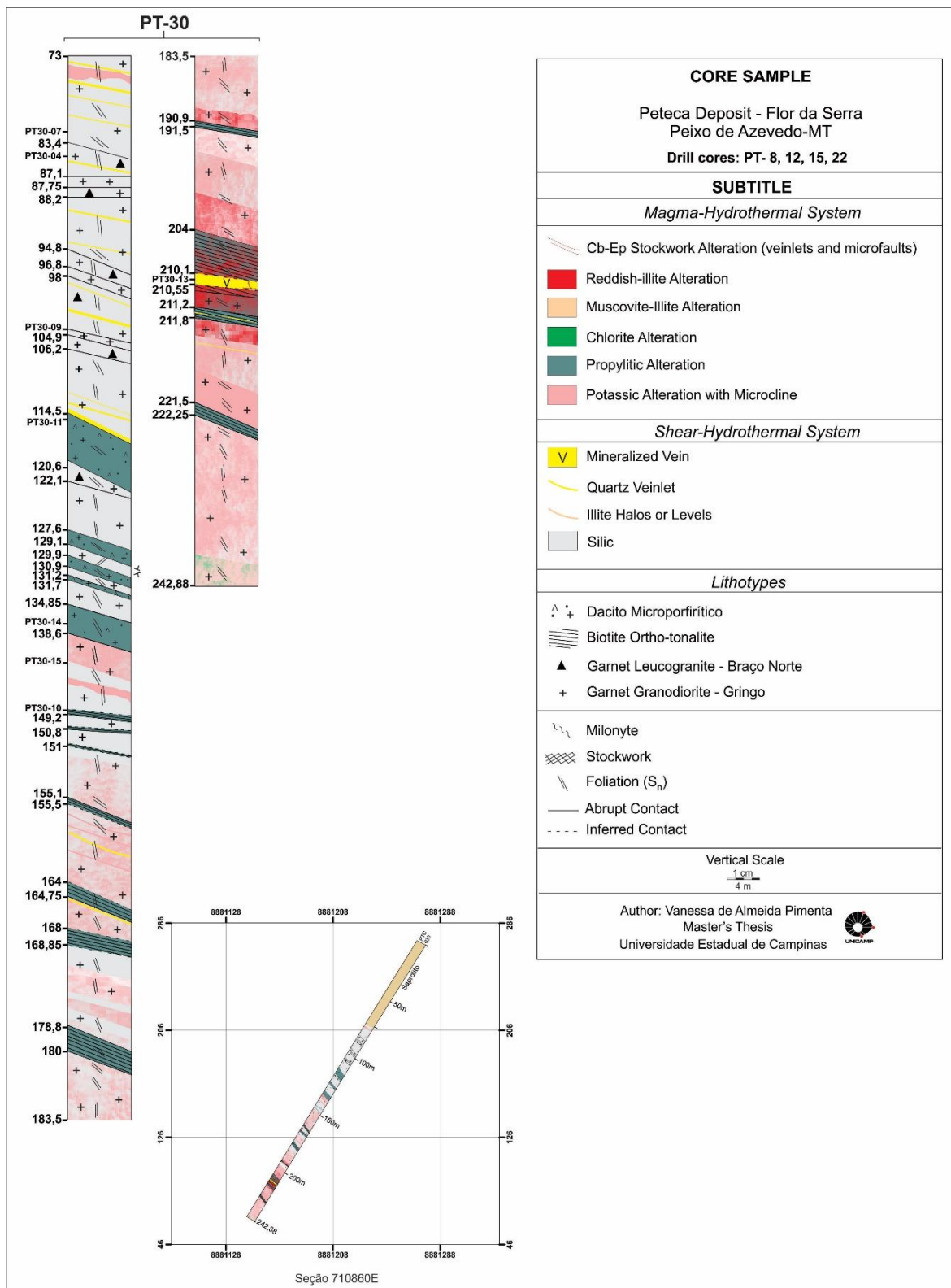


Figure 40 - Geologic section of oriented drill core (PT-30) displays its lithotypes and both of the shear- and magmatic-hydrothermal systems distributions. The color mix in some portions indicate predominance of more than one hydrothermal alteration.

5.2.1. Shear-hydrothermal System

Microstructures of deformation in feldspars appears in the granitoids toward the protomylonite and the garnet quartz mylonite. Flame perthite (Fig. 13G, 15C) and myrmekite (Fig. 15C) in the granitoids are products of softening reaction, which occurs in response to concentration of tension in grains, and contributes to volume reduction of the feldspar crystals (Pryer & Robbin, 1996; Hippert, 1998). Flame perthites occur from grain boundaries, sub parallel to the direction of maximum compression, orthogonal to the Sn foliation (Hippert, 1998). They present a temperature range of 300°-500°C (Pryer, 1993) or of 400°-500°C (Passchier & Trouw, 2005). Myrmekites are intergrowths between quartz and plagioclase that substitute part of the feldspar by removing K from feldspar, and Na e Ca from plagioclase (Vernon, 2004; Menegon et al., 2006).

Microcline twinning found in the feldspar boundaries (Fig. 13I) occur due to the transition from monoclinic to triclinic system of K-feldspar to reduce the local strain (Putnis, 1992). Microfractures in K-feldspar appears in the granodiorite, leucogranite and biotite tonalite. Fracturing mechanism is important to the rock weakening once it facilitates fluid flow, and is precursor of continuous shear zone (Hippert, 1998; Macktwlow & Pennacchioni, 2005; Fusseis & Handy, 2008).

Microstructures of deformation found in quartz indicate metamorphic conditions up to upper greenschist facies. Undulose extinction is possible between 250° and 400°C (Passchier & Trouw, 2005). Quartz boundaries present bulges (Fig. 13D) as a dynamic recrystallization through grain boundary migration, which appears in temperature ranging from 400° to 500°C. Steep et al. (2002) defined a range of 280°-400°C for BLG recrystallization.

The chlorite crystallization temperature in the chlorite-illite phyllonite ranges from 356° to 379°C, with geometric mean of 369° (Inoue et al., 2009; Fig. 36). Through the same method, the chlorite 1 related to the phyllonite formation at Paraiba deposit presents a slight higher temperature ranging from 374° to 434°C with a geometric mean of 396° (Poggi, *in prep*). From the illite granodiorite mylonite to the chlorite-illite phyllonite, the illite crystallization temperature rises from 288° to 304°C (Battaglia, 2004; Fig. 37). These temperatures ranges equals to greenschist metamorphic conditions.

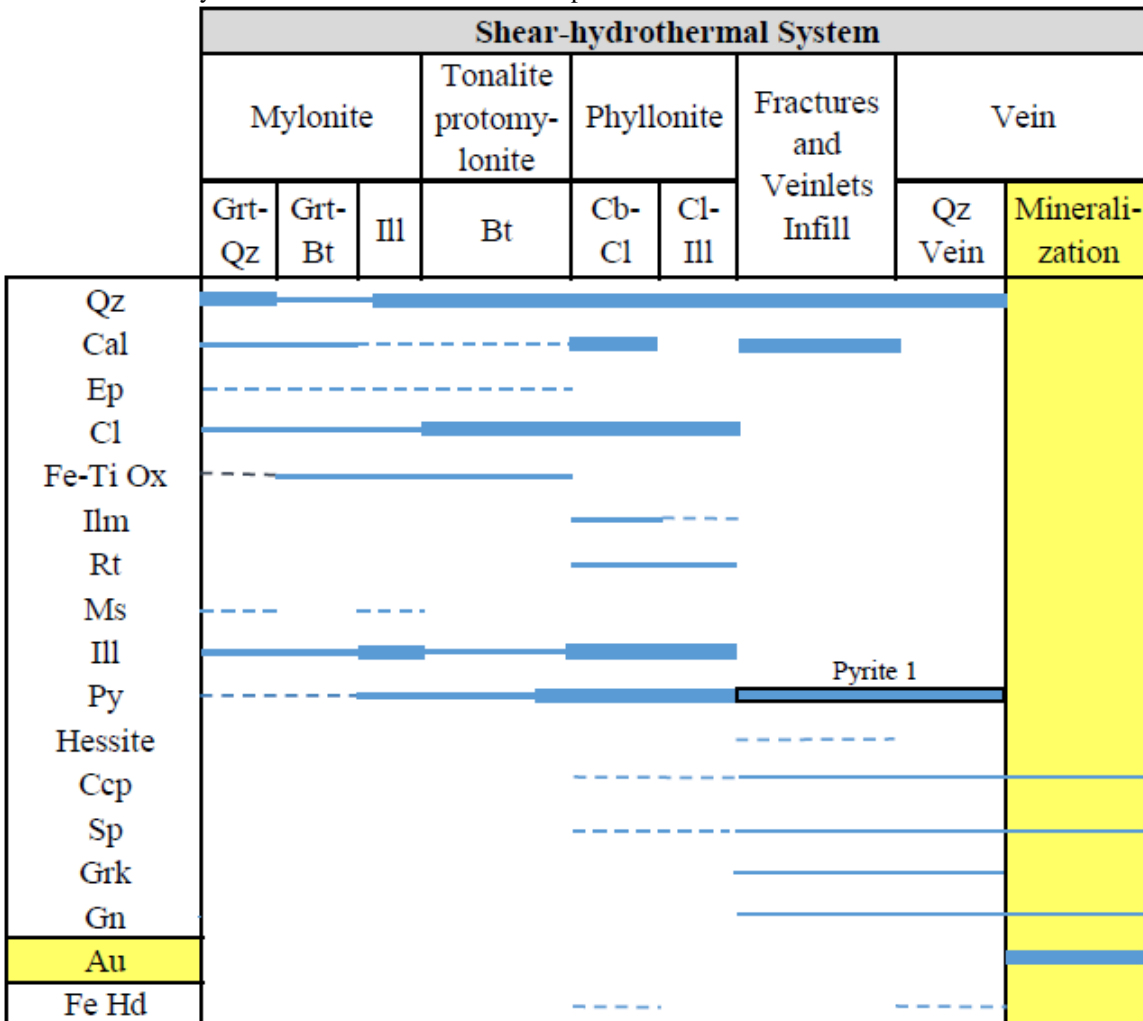
Toward the protomylonite and mylonites to the phyllonites, there are several evidences of the deformation and fluid flow. These include:

1. Grain-size reduction of matrix minerals and porphyroclasts (Platt & Beher, 2011; Platt, 2015) mainly occurred by: (a) dynamic recrystallization in quartz, (b) fracturing in feldspars and garnet, (c) core-and-mantle structure in porphyroclasts. According to Gapais (1989), these processes can occur in temperatures conditions related to greenschist facie.
2. Globular quartz. One of the possible mechanisms for its origin is through silica dissolution and reprecipitation due to pressure solution (Mesquita et al., 2006). It only appears in the foliated granitoids that exhibit flame perthite and microcline twinning formation, which corroborates for being a product of deformation.
3. The increasing amount of quartz ribbons in the mylonites demonstrates the rising of water flow, which intensified the ductile deformation in quartz by a process called hydrolytic weakening (Grigg, 1974; Tullis & Yund, 1980; Mesquita et al., 2013).
4. In addition to a probable external source, the amount of silica as a releasing product of several process caused the increasing of pervasive silica toward the mylonites. These processes are (a) myrmekite formation (Menegon et al., 2006), (b) breakdown of feldspars, plagioclase and garnet, (c) flame perthite generation (Hippert, 1998), (d) microcline twinning generation (Putnis, 1992). The sites opened after grain-size reduction may allow silica precipitation.
5. The mylonites are a deformational evolution with reduction of K-feldspar, plagioclase, garnet, epidote, and increase amount of chlorite and white mica. Feldspar and garnets present a brittle behaviour with fracturing. Plagioclase also presents fracturing and microfaults, but its porphyroclasts show core-and-mantle structure. Fractures on these minerals are dilatant sites for chlorite and white mica precipitation (Cruz et al., 2005). Furthermore, the exchanging $K \rightarrow Na$ for flame perthite generation may supply the potassium demand for illite formation in the plagioclase (Mesquita et al., 2013).
6. The presence of phyllonites is the main evidence of the huge fluid flow in the shear zone once it induced hydrothermal segregations that concentrated phyllosilicates and quartz toward the mineralized vein (Cruz et al., 2005; Jefferies et al., 2006; Mesquita et al., 2013). From the illite granodiorite mylonite toward the phyllonite and mineralized vein, the evolution demonstrates progressive increasing of flow/rock ratio.

The carbonate-chlorite phyllonite takes part of the shear-hydrothermal system, but it does not present relation to the evolution toward the mineralization (Tab. 5). Its origin remains with open questions once it is away from the mineralized vein, besides its protolith

may be the biotite tonalite protomylonite, but no clear evidence as a contact between them was denoted.

Tabela 5 - Shear-hydrothermal evolution at Peteca deposit.



After the phyllonites, the next stage corresponds to the veinlets infill that affect the illite granodiorite mylonite and the chlorite-illite phyllonite (Fig. 17; Tab. 5). They are 30°-70° or 90° in relation to the Sn foliation, and correspond to stages where the shear stress increases, generating the local fracturing. Then, as the flow ratio increases there is hydrothermal alteration. Afterwards, the shear stress increase again and a new cycle starts. All these processes correspond to the mechanism called as fault valve behavior (Sibson et al., 1975) or pump valve (Sibson, 1981). At Peteca, a prior cycle was richer in CO₂ fluids filling the veinlets with calcite (Fig. 17A), and the latter was richer in SiO₂ and S precipitating quartz and sulphides (Fig. 17B-E). Among these sulphides, pyrite 1 presents rare inclusion of hessite

(Ag_2Te ; Tab. 5). This mineral also appears as inclusion in pyrite in the proximal deposit Paraíba, a vein-type gold deposit (Trevisan, 2015).

The microstructural domain 1 in the quartz vein, which presents syntax quartz crystals (Fig. 18A), suggests that the vein opened by brittle process in a first stage (Bons et al., 2012). The mineral assemblage of the quartz vein is similar to the quartz veinlet discussed above, which indicate concomitant generation. It corresponds to quartz, pyrite 1, sphalerite, greenockite, chalcopyrite, and galena (Tab. 5). The ZnS-Cd-S system present hydrothermal solid solution inferior to 400°C (Tombros et al., 2005). In hydrothermal deposits, greenockite occur mainly in Pb-Zn deposits, but it occurs in orogenic gold deposits (Kreuzer, 2006), Cu skarn (Liu & Zhang, 2017), and epithermal Ag-Au-Te, as the Francisco deposit (Assis, 2011; Tombros et al., 2015). These authors and references within affirm that Cd can replace Zn according to the temperature, pH, $f\text{O}_2$, $a\text{Cl}^-$, and Cu ratio in the flow. The rutile, ilmenite and pyrite increasing from the chlorite-illite phyllonite indicate a redox flow toward the mineralized vein.

Although the ore mineral assemblage might appears in the quartz veinlets, the Table 5 presents the ore stage related to the quartz vein. The ore mineral assemblage comprises pyrite 1, sphalerite, chalcopyrite, gold and galena. Gold occurs in microfractures or microcavities within pyrite 1, and its size ranges from 0,07 to 01 mm, is composed of up to 19% of Ag, and the Ag:Au is at 0,16-0,25.

5.2.2. Magmatic-hydrothermal system

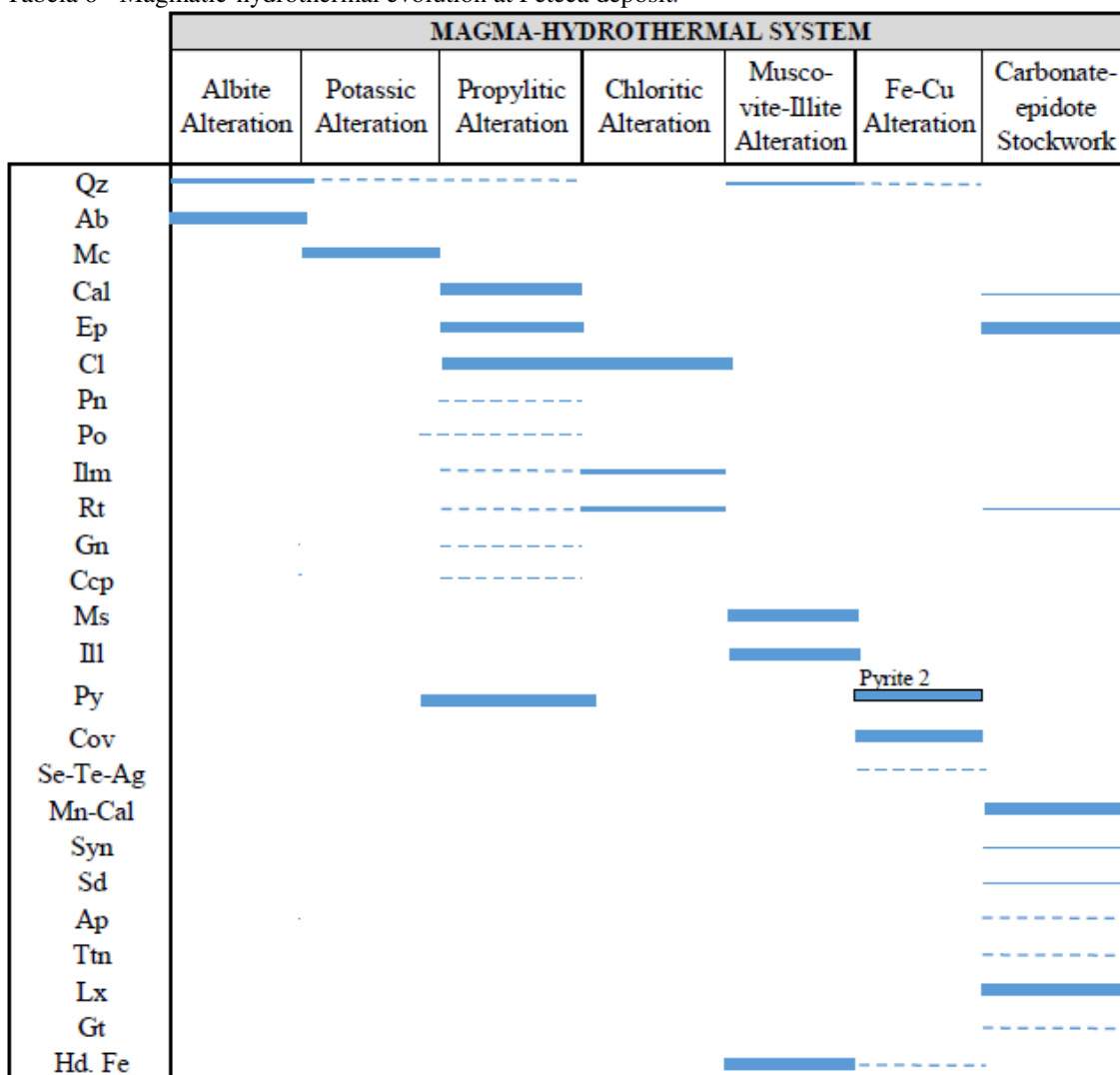
Albitization (Fig. 20A, B; Tab. 6) correspond to the replacement of alkali or plagioclase feldspar by coupled exchange from $\text{Ca}^{2+} + \text{Al}^{3+}$ to $\text{Na}^+ + \text{Si}^{4+}$ (Engvik et al., 2008; Hövelmann et al., 2010). It occurs in several types of rocks and tectonic regimes, including hydrothermal alteration in granites (Plümper & Putnis, 2009) and tonalites (Engvik et al., 2008). It happens on regional or on mineral grains scales (Engvik et al., 2008). Pollard (1983) relates the formation of hydrothermal albite to the entrance of Na^+ from magmatic fluids under temperature range of 400°-600 ° C. Munz et al. (1994) considered the temperature range of 300°-450°C for albitization based on the lower greenschist facies mineral.

At the eastern sector of AFGP, albitization occurs at Pezão and Pé Quente Au ± Cu disseminated deposits (Assis, 2011; Assis et al., 2014). Fluid inclusions studies carried out at Pé Quente show an aqueous-carbonic system in coexistence with aqueous fluids biphasic, suggestive of an immiscibility process that would have occurred at high temperatures and deep crustal levels.

Potassic alteration (Fig. 20C-F; Tab. 6) is well known as an important feature in porphyry mineralising systems, indicating needed temperatures up to 700°C (Pirajno, 2009; Sinclair, 2007; Seedorf et al., 2005; Seedorf et al., 2008; Sillitoe, 2010). Microcline alteration increases in more felsic, granodioritic rocks in porphyry systems (Sillitoe, 2010). At Peteca, the previous releasing of K^+ because of the albitization contributed to an increase of $a\text{K}^+$, which is needed for the potassic alteration.

In the biotite tonalite protomylonite at Peteca, two possible different groups of biotite were analyzed. The first correspond to the igneous origin that appears as major lamellae distributed in the matrix. The second is a fine-grained group present in the recrystallized bands, which suggested a hydrothermal origin related to the potassic alteration. The results of mineral chemistry (Fig. 27, 28) show that all biotite from this rock is Fe richer compared to the other granitoids, including the igneous group. However, there is no chemical difference between these two biotite groups found in the protomylonite, which may indicate there is no hydrothermal biotite. Despite this absence of major chemical differences between the two groups, the occurrence of the fine-grained lamellae tightly restricted to the recrystallized bands can point a metamorphic origin for them, which request further studies.

Tabela 6 - Magmatic-hydrothermal evolution at Peteca deposit.



The propylitic alteration (Fig. 20G-J; Tab. 6) mainly comprises chlorite, epidote, pyrite, calcite, indicating $\text{CO}_2\text{-H}_2\text{S}$ -rich flow. Chlorite presence indicates high $a(\text{Fe}, \text{Mg})^{2+}/a\text{H}^+$ ratio. Propilitization occurs at pH near neutral, at low fluid/rock ratio, and at 200°-350°C (Robb, 2004). In the filling style, the mineral assemblage is chlorite, mangano-calcite, allanite, galena, pyrrhotite, ilmenite, rutile. The probable source of manganese is from the hydrolysis of garnet, while the titanium present in ilmenite and rutile, from the hydrolysis of biotite.

The mineral chemistry data (Fig. 29) classified the chlorite from the propylitic alteration as ripidolite (Foster, 1962) or Fe-Al clinochlore (Ciesielczuk, 2012). According to the Bourdelle et al. (2013) geothermometer, its crystallization temperature was above 350°C, which matches with the geometric mean at 394°C by Inoue et al. (2009) geothermometer (Fig.

35, 36). A comparison among these data to the same in chlorite from the shear-hydrothermal system indicates there was a temperature increase toward the magmatic-hydrothermal system.

The next stage at Peteca is the chloritic alteration (Fig. 21A; Tab 7). Its chlorite product correspond to ripidolite to brunsvigite (Foster, 1962) or Fe-Al clinochlore to Mg chamosite (Ciesielczuk, 2012) classification (Fig. 29). Elements such as Fe and Mg released from de biotite and garnet indicate high $a(\text{Fe}, \text{Mg})^{2+}/a\text{H}^+$ ratio in the flow.

Comparing the mineral chemistry results of the chloritization in the granodiorite, leucogranite, biotite tonalite, and biotite tonalite protomylonite, the last one present higher $\text{Fe}/(\text{Fe}+\text{Mg})$ ratio content than the other ones. These results reflects the same higher ratio content of the biotite in the protomylonite, once the chlorite alters this mica.

Besides biotite alteration, chlorite also affects garnet crystals in the granodiorite and the leucogranite. Although both of the garnet correspond to almandine, this mineral can present slight higher content of Fe in the leucogranite (Fig. 26). It can explain the higher $\text{Fe}/(\text{Fe}+\text{Mg})$ ratio of its chloritization compared to the granodiorite (Fig. 29B).

Concerning the chlorite crystallization temperature in the chloritic alteration, the geometric mean keeps at 394°C, but its minimum temperature reached 156°C regarding the garnet granodiorite, while most of the temperature data are above 300°C (Fig. 35, 36). Nevertheless, biotite replacements to chlorite in granites (Parneix et al., 1985), in granodiorites and dacitic to riodacitic volcanic rocks (Yamni et al., 2017), occur under temperature range of 117°-350°C, with prevalence of 200°-250°C temperatures.

The mineral data of the oxides associated to the chloritic alteration corresponds to hematite-ilmenite. The total absence of magnetite points to a more redox conditions of the flow.

The muscovite-illite alteration (Fig. 21 B-D) indicates high concentration of K, but there is a reduction of the ratio $a\text{K}^+ / a\text{H}^+$, since a more acidic environment is required for precipitation. The mineral chemistry results show that either the illite or the muscovite corresponds to phengite, and the muscovite present slight higher content of Mg compared to illite (Fig. 30A, B). The muscovite appears only in lithotypes containing garnet, whereas illite is the most common alteration at Peteca. It is a product of alteration of garnet, biotite, chlorite, potassium feldspar, and plagioclase.

This alteration occurs in temperatures close to 200° C (Chatelineau, 1988; Merriman & Ferry, 1999). However, the geometric mean results for both of the illite and muscovite crystallization temperatures are about 300°C (Fig. 37, 38). Furthermore, regarding

the geometric mean data of illite and muscovite, the muscovite shows slight tendency to lower crystallization temperatures (Fig. 37, 38).

In the biotite tonalite, this alteration in plagioclase generates intense reddish color (Fig. 21B), which can be a result of porosity produced in hydrothermal albite, once albitization occurs in the same rock at Peteca. Engvik et al. (2008) discuss about albitized tonalite and albitite in the Bamble sector of paleoproterozoic to mesoproterozoic rocks in the Scandinavia. They affirm that the volume and the crystallographic orientation of parental plagioclase crystals keep invariable, but the reaction produces porous on the hydrothermal albite. The porosity is important in the reaction interface where there is re-equilibration of solids through fluid infiltration (Putnis & Putnis, 2007). These pores may present very fine-grained Fe oxide that generate the red color (Engvik et al., 2008; Hövelmann et al., 2010; Morad et al., 2010). At Peteca, the strip where albitization appears is whitish, but there are tiny reddish fractures where Fe oxide was transported along.

The hydrothermal zone of Fe-Cu is associated with the microstructural domain 3 (Fig. 18, 21E-G; Tab 6), being an alteration of fissural filling. The reddish fractures of domain 3 affect the coarse pyrite (Py 1) and the dark cavities composed of pyrite and sphalerite. Thus, the fine pyrite associated with the Fe-Cu zone is considered posterior to Py 1 and, therefore, denominated as Pyrite 2 (Py 2). Intragranular fractures in Py 1 in sub-horizontal veinlet (Fig. 17F) are filled by covellite, which corroborates for the Fe-Cu zone to be posterior to the generation of Py 1.

Covellite and hematite were reported in the Paraíba and Pezão deposits as products of chalcopyrite alteration in the mineralization stage, indicating a relative increase of fO_2 (Trevisan, 2015). The presence of Fe hydroxides, possibly goethite, which generate the reddish appearance of fractures and faults associated to the Fe-Cu alteration at Peteca, correspond to an increase of fO_2 . Romberger & Barnes (1970) demonstrates that covellite transport and precipitation is favored at neutral pH to slightly alkaline at 200° C, besides reductions in temperature or pH contribute to CuS supersaturation.

The covellite presents Se (< 2.45%) and is associated with minor Ag, Te mineral phases. Ilmen et al. (2015) affirm that in the Cu-Au vein-type deposit in the Talat n'Imjjad shear zone in Morocco, the Bi-Se-Te minerals formed after the Cu-Au mineralization. Ciobanu et al (2010) suggest that Bi, Te, Ag and Cu in hydrothermal fluids occurs in temperature range of 200°-400°C for the formation of these mineral assemblages. Several of the Au(Ag)-tellurides deposits correspond to gold epithermal systems, and presents spatial relation to Cu, Mo or Cu-Mo porphyry (Ciobanu et al., 2006). According to Ciobanu et al.

(2005), Te-rich melt precipitates from oxidized fluids. This correlation occurs at Peteca, once the microfractures associated to the Fe-Cu alteration are reddish due to oxidation.

The last hydrothermal stage at Peteca deposit comprises carbonate-epidote stockwork (Fig. 22; Tab. 6). It appears in veinlets, stockworks, microfractures, fractures, which indicate shallow crustal environment. At Paraíba deposit, hydrothermal breccias of epidote, calcite and gold mineralized hematite (Mesquita et al., 2018). The assemblage presents calcite, mangano-calcite, epitote, rutile, leucoxene, goethite, titanite, synchisite, monazite, apatite, siderite, quartz. It indicates addition of CO_2 , PO_4^{3-} under neutral to alkaline pH conditions. Rutile, leucoxene and siderite point to high $a\text{Fe}_t$. The increase of $f\text{O}_2$ may indicate the contribution of oxidant magmatic fluids. The concentration of heavy rare earths in synchisite and monazite increases as the environment becomes more acidic (Mikhald, 1989). The oxidation associated with the stockworks and hydrothermal breccias may indicate a shallower environment for the development of this zone.

Although the content phase of REE as carbonate and phosphate, and of Ti as rutile and leucoxene were classified as part of the carbonate-epidote stockwork, it may request further studies. Baker (1985) discussed the REE mobility during albitization in peraluminous granite in Sweden. The author states depletion of Fe^{2+} , Fe^{3+} , Mn, K, Sc, Ba, Pb, U, F, REE, while Ti, Al, P and Y are immobile. On the other hand, Hövelmann et al. (2010) affirm there are Ti and Y releasing. The Mn releasing would explain the minor Mn amount in calcite. Ca^{2+} released contributes to the formation of epidote, titanite, calcite, monazite and synchisite, meanwhile Al^{3+} to the epidote formation. Al is immobile at most geologic settings, unless there is a hot and alkaline fluid source (Mark, 1998).

The behaviour of REE in hydrothermal systems remains clearly incomplete, but phosphate and carbonate adding to the fluid are the most effective means of REE mineral deposition (Migdisonva et al., 2016). Middleton et al. (2013) report synchisite, monazite and xenotime as alteration product from titanite. Xenotime is absent at Peteca, but appears at Paraiba and Pezão Au ± Cu vein type deposits.

Moreover, the Ti phase present as rutile and ilmenite occurs in some albitized tonalite (e.g. Engvik et al., 2008). The Ti mobility Engvik et al. (2008) reports rutile forming in the albitization as product of alteration of ilmenite. Some studies show that the higher Na-Al-silicate dissolved the greater Ti solubility (Antignano & Manning, 2008; Haidden & Manning, 2011).

5.3. SYNTHESIS OF DISCUSSIONS

The evidences for metamorphism at Peteca rely on the presence of the biotite metatonalite, the medium- to high-grade metamorphic conditions of microstructures found in the country rocks, and the possibility of the garnet be metamorphic. The latter can suggest that Sn foliation has a metamorphic origin once the garnet marks it.

In the same rocks, the presence of microstructures of deformation of lower metamorphic conditions indicate there was a temperature decreasing. It could be result of a retrometamorphism, but the clear evidences of deformation-fluid interaction from the country rocks toward the mineralized vein point for the shear-hydrothermal system presence.

Metamorphism implies in mineral assemblage changing due to the new conditions of pressure and temperature, while hydrothermal alterations are result of pressure, temperature, and chemical changes between the protolith and the product mineral assemblage, indicating a fluid presence (Barnes, 1997; Putnis & Austrheim, 2010). According to that, several features at Peteca demonstrate the ratio fluid/deformation increasement, such as the phyllonite and quartz vein formation toward the shear zone centre.

The metamorphic event was prior to the shear-hydrothermal system mainly because there was a temperature decreasing figured out by the microstructures resulted by fluid-deformation interaction in the shear system. This system generated the shear rocks as the protomylonite, mylonites and phyllonites, besides the veinlets and main quartz vein. All these structures are parallel to the Sn foliation in the country rocks. As long as the shear rocks and the quartz vein are result of the shear system, their related foliation is denominated S_{n+1} as a product of later deformation process that generated the shear zone.

Other fluid evidence on this system is the presence of veinlets filled by two different composition groups such as carbonate, and quartz with sulphide. It indicates the cyclic feature of the shear-hydrothermal system, in which shear stress rate and fluid rate alternate the predominance. The veinlets can be filled when the flow ratio is greater than the local shear stress.

Although the shear system is later than metamorphism, the four drill cores PT-8, PT-12, PT-15 and PT-22 present shear rocks and the chlorite-illite phyllonite is the host rock of the mineralized vein, meanwhile the PT-30 do not present shear products and the metatonalite hosts the vein. These different features lead to question whether the vein in the PT-30 is not the same one found in the other drill cores.

Concerning the main quartz vein structure, syntax quartz crystals developed in the vein at first, followed by a second flow direction, which precipitated coarse quartz crystals orthogonal to the first ones. Pyrite 1 (Py 1) tends to be parallel to the second microstructure domain suggesting the composition flow was rich in Si and S. It also filled the veinlets in the chlorite-illite phyllonite once they have the same mineral assemblage: quartz, Py 1, sphalerite, greenockite, chalcopyrite, and galena. Regarding the similar sulphide assemblage in the cavities found in the vein, such as pyrite and sphalerite, the cavities belong to the shear hydrothermal system.

Concerning the ore mineral assemblage that occur in fractures or microcavities in the pyrite 1, the gold precipitated later than this sulphide generation. Furthermore, the ore restriction to the main quartz vein allow to consider the Peteca as a vein-type gold deposit.

The chlorite and illite crystallization temperatures in the chlorite-illite phyllonite from the shear-hydrothermal system presented geometric mean at 369° and 304°C, respectively. In addition, the greenockite presence suggest temperatures lower than 400°C (Tombros et al., 2005). Albition and potassification with microline indicate magmatic fluid source and a suggested temperature of up to 700°C (Sinclair, 2007; Seedorf et al., 2005; Seedorf et al., 2008; Sillitoe, 2010). This temperature increase allow to state that the magmatic-hydrothermal system is later than the shear- hydrothermal system at Peteca. Likewise, the geothermometry results for chlorite and illite in the magmatic system show an increase of 14°C on average compared to the data obtained for the shear system. In addition, the characteristic absence of orientation of the hydrothermal alterations related to the magmatic is the main difference between the two systems.

Within the magmatic system, its hydrothermal evolution presents a temperature decrease from albition to the Fe-Cu alteration and carbonate-epidote stockworks, once the covellite precipitation points to temperature of up to 200°C (Romberger & Barnes, 1970). The suggested temperature for covellite, the association to fractures of the Fe-Cu alteration, and the stockworks presence indicate a shallower crustal level during the last two stages of development of the Peteca deposit.

6. CONCLUSIONS

The petrologic and mineral chemistry studies allowed the characterization of the country rocks at Peteca deposit, its hydrothermal systems and their respective deformation microstructures and hydrothermal alterations.

The country rocks comprise foliated granitoids (garnet granodiorite, garnet leucogranite, biotite tonalite), the biotite metatonalite, and dykes of microporphyritic dacite and pegmatites.

The medium- to high-grade metamorphic conditions of microstructures in feldspar and quartz found in the granitoids, besides the different compositions of garnet in these rocks corroborate to a metamorphic origin of the Sn foliation. The presence of the metatonalite give support to this evidence.

The shear-hydrothermal system generated low- to medium-grade metamorphic conditions of microstructures in feldspar, plagioclase, and quartz found in the granitoids. In addition to these features, the deformation-fluid interaction produced (a) shear rocks (biotite tonalite protomylonite, carbonate-chlorite phyllonite, garnet-quartz mylonite, garnet-biotite granodiorite mylonite, illite granodiorite mylonite, chlorite-illite phyllonite), (b) their foliation denominated as S_{n+1} , which is parallel to Sn, (c) quartz, carbonate veinlets with 70°-90° in relation to S_n or S_{n+1} , (d) main quartz vein, and (e) mineralization. The foliations S_n , S_{n+1} are parallel to the mineralized vein (N70-80W/60-80NE).

The granodiorite, garnet-biotite granodiorite mylonite, illite-granodiorite mylonite, the chlorite-illite phyllonite, and quartz veinlets correspond to an evolution toward the quartz vein and mineralization. The chlorite-illite phyllonite is the main host rock of the mineralized vein, although the biotite metatonalite hosts it as well.

The quartz vein present three microstructural domains classified as: (1) quartz crystal with syntax growth, (2) medium-grained quartz crystals (sub)-parallel to the vein orientation, and (3) fine-grained quartz crystals associated to microfractures and microfaults parallel to the vein orientation. In this vein, the mineralization occurs in fractures or microcavities within coarse-grained pyrite classified as pyrite 1.

The magmatic-hydrothermal system is post-mineralization and comprises seven hydrothermal alteration stages: (a) albite alteration, (b) potassic alteration with microline, (c) propylitic alteration, (d) chloritic alteration, (e) muscovite-illite alteration, (f) Fe-Cu alteration, and (g) carbonate-epidote stockwork. These hydrothermal alterations are with no

preferential orientation and do not comprise foliation. Fine-grained pyrite correlated to the Fe-Cu alteration is denominated as pyrite 2, and do not present gold ore.

The geothermometry results for chlorite crystallization temperature show an average of $350^\circ \pm 20^\circ\text{C}$. However, from the shear-hydrothermal system to the magmatic-hydrothermal system the temperature change up from 369°C to $394^\circ \pm 20^\circ\text{C}$. A similar slight increase of temperature occurs for the illite crystallization temperature. Its results change up from $288^\circ\text{-}304^\circ\text{C}$ in the shear-hydrothermal system to $295^\circ\text{-}314^\circ\text{C}$ in the magmatic-hydrothermal system. In agreement with this last range of temperatures in the magmatic system, the muscovite crystallization temperatures are between 275° and 314°C .

In conclusion, the development of Peteca deposit is a result of three different main stages in temporal order: metamorphism, the shear-hydrothermal system that mark a temperature decrease and embraces the ore mineralization process, and the magmatic-hydrothermal system marked by the temperature increase as a consequence of a magmatic external source.

Furthermore, the new geologic framework at Peteca enhance the comprehension of evolution of the $\text{Au} \pm \text{Cu}$ vein-type deposits in the Peixoto de Azevedo region at Alta Floresta Gold Province.

REFERENCES

- Almeida F.F.M. 1977. *Tectonic map of South América*, 1:5.000.000 - Explanatory note. Trabalho elaborado em parceria com CGMW e UNESCO. Brasília: DNPM, 23 p.
- Amaral G. 1974. Geologia Pré-Cambriana da região amazônica. Tese de Livre Docência, Instituto de Geociências, Universidade de São Paulo, São Paulo, 212p.
- Antignano A. & Manning C.E. 2008. Rutile solubility in H_2O , H_2O-SiO_2 , and $H_2O-NaAlSi_3O_8$ fluids at 0.7–2.0 GPa and 700–1000°C: Implications for mobility of nominally insoluble elements. *Chemical Geology*, **255**: 283–293.
- Assis R. R. 2008. Contexto geológico e associação paragenética das mineralizações auríferas de União do Norte, região de Peixoto de Azevedo, Província de Alta Floresta (MT). Trabalho de Conclusão de Curso, Instituto de Geociências, Universidade Estadual de Campinas, 77p.
- Assis R.R. 2011. Depósitos auríferos associados ao magmatismo granítico do setor leste da Província de Alta Floresta (MT), Craton Amazônico: tipologia das mineralizações, modelos genéticos e implicações prospectivas. Dissertação de Mestrado, Instituto de Geociências, Universidade Estadual de Campinas, 462p.
- Assis, R.R., Xavier, R.P., Trevisan, V.G., Creaser, R., Paes de Barros, A.J. 2014. Re-Os sulfide ages for the Paleoproterozoic disseminated Au-porphyry from the Alta Floresta Gold Province: Amazon Craton (Mato Grosso). In: 47º Congresso Brasileiro de Geologia, Salvador.
- Assis R.R. 2015. Depósitos auríferos associados ao magmatismo felsico da Província de Alta Floresta (MT), Cráton Amazônico: litogeochimica, idade das mineralizações e fonte dos fluidos. Tese de Doutorado, Instituto de Geociências, Universidade Estadual de Campinas, 363p.
- Assis R.R., Xavier R.P., Creaser R.A. 2017. Linking the Timing of Disseminated Granite-Hosted Gold-Rich Deposits to Paleoproterozoic Felsic Magmatism at Alta Floresta Gold Province, Amazon Craton, Brazil: Insights from Pyrite and Molybdenite Re-Os Geochronology. *Economic Geology*, **112**: 1937–1957.
- Baker J.H. 1985. Rare earth and other trace element mobility accompanying albitization in a Proterozoic granite, W. Bergslagen, Sweden. *Mineralogical Magazine*, **49**: 107-15.
- Barnes, H. L. 1997. *Geochemistry of Hydrothermal Ore Deposits*. John Wiley and Sons (ed.), Inc. New York., 798p.
- Barros A.J.P. 2007. Granitos da região de Peixoto de Azevedo – Novo Mundo e mineralizações auríferas relacionadas – Província Aurífera Alta Floresta (MT). Tese de Doutorado, Instituto de Geociências, Universidade Estadual de Campinas, Campinas, 154p.
- Battaglia S. 2004. Variations in the chemical composition of illite from five geothermal fields: a possible geothermometer. *Clay Minerals*, **39**: 501–510.
- Blenkinsop T.G., Oliver N.H.S., Dirks P.G.H.M., Nugus M., Tripp G., Saniskav I. (no prelo). 2018. Structural geology applied to the evaluation of hydrothermal gold deposits. (Aceito ainda sem data de publicação).
- Bourdelle F. & Cathelineau M. 2015. Low-temperature chlorite geochemistry: a graphical representation based on a T-R2 + - Si diagram. *Eur. J. Miner.*, **27**: 617- 626.
- Bons P.D., Elburg M.A., Gomez-Rivas, E. 2012. A review of the formation of tectonic veins and their microstructures. *Journal of Structural Geology*, **43**:33–62, doi:10.1016/j.jsg.2012 .07.00
- Ciesielczuk J. 2012. Chlorite of hydrothermal origin in the Strzelin and Borów granites (Fore-Sudetic Block, Poland). *Geological Quarterly*, **56**(2): 333-344.

- Ciobanu C.L., Cook N.J., Spry P.G. 2006. Preface – Special Issue: Telluride and selenide minerals in gold deposits – how and why? *Mineralogy and Petrology*, **87**: 163–169.
- Costa J.B.S. & Hasui, Y. 1997. Evolução geológica da Amazônia. In: Costa, M. L. da; Angélica, R. S. Contribuições à geologia da Amazônia. Belém: SBG-NO, 15-90.
- Cruz Filho B.E., Conceição H., Rosa M.L.S., Rios D.C., Marinho M.M. 2005. Química mineral e condições de colocação do batólito trondjemítico Nordestina, Núcleo Serrinha, Bahia. *Revista Brasileira de Geociências*, **35(4)**: 83-92.
- Deer W.A., Howie R.A., Zussman J. 1992. *An introduction to rock-forming minerals*. 2nd Ed., Essex. Longman Scientific & Technical. 696p.
- Dezula S.E.M., Barros M.A.S.Ab. Santos J. J.O. Rafael Rodrigues Assis R.R.. Granito Aragão — Suíte intrusiva Nhandú — um granito oxidado, tipo A2, de 1967 a 1964 Ma na Província Aurífera Alta Floresta — Cráton Amazônico. *Revista do Instituto de Geociências (USP)*, **(18)**: 3-20.
- Drake H., Tullborg E., Annersten H. 2008. Red-staining of the wall rock and its influence on the reducing capacity around water conducting fractures. *Applied Geochemistry*, **23**:1898-1920.
- Einaudi, M.T., Hedenquist, J.W., Inan, E.E. 2003. Sulfidation state of fluids in active and extinct hydrothermal systems: transitions from porphyry to epithermal environments. *Society of Economic Geologist and Geochemical Society, Special Publication 10*. In press: Guggenbach Volume.
- Engvik A. K., Putnis A., Gerald J.D.F., Austrheim H. 2008. Albitization of granitic rocks: the mechanism of replacement of oligoclase by albite. *The Canadian Mineralogist*, **46**:1401-1415.
- Fossen H. & Cavalcante G.C.G. 2017. Shear zones – A review. *Earth-Science Reviews*, **171**: 434-455.
- Foster M.D. 1960. Layer charge relations in the dioctahedral and trioctahedral micas. *The American Mineralogist*, **45**: 383-398.
- Foster M.D. (Ed.) 1962. Interpretation of the Composition of Trioctahedral Micas. In: Foster M.D. (Ed.) *Shorter contributions to general geology*. Geological Survey Professional Paper **354B**: 11-48.
- Fusseis F. & Handy M.R. 2008. Micromechanisms of shear zone propagation at the brittle–viscous transition. *Journal of Structural Geology*, **30**: 1242–1253.
- Gapais, D. 1989. Shear structures within deformed granites: mechanical and thermal indicators. *Geology*, **17**: 1144–1147.
- Goldfarb RJ, Baker T, Dube B, Groves DI, Hart CJR, Gosselin P. 2005. Distribution, character, and genesis of gold deposits in metamorphic terranes: *Econ Geol 100th Anniv*:407-450
- Groves DI, Goldfarb RJ, Gebre-Mariam M, Hagemann SG, Robert F. 1998. Orogenic gold deposits: a proposed classification in the context of their crustal distribution and relationship to other gold deposit types. *Ore Geol Rev*, **13**:7–27.
- Guidotti C.V., Cheney J.T., Henry D.J. 1988. Compositional variation of biotite as a function of metamorphic reactions and mineral assemblage in the pelitic schists of western maine. *American Journal of Science*, **288A**: 270-292.
- Guidotti C.V., Cheney J.T. 1975. Interrelationship between Mg/Fe Ratio and Octahedral Al₁ content in Biotite. *The American Mineralogist*, **60**: 849-853.
- Hartman S.M., Paterson S.R., Holk G.J., Kirkpatrick J.D. 2018. Structural and hydrothermal evolution of a strike-slip shear zone during a ductile-brittle transition, Sierra Nevada, CA. *Journal of Structural Geology*, **113**: 134-154.

- Hasui Y., Haralyi N.L., Schobbenhaus C. 1984. Elementos geofísicos e geológicos da região Amazônica: subsídios para o modelo geotectônico. In: Simpósio de Geologia da Amazonia, Manaus, SBG, p. 129-147.
- Hayden L.A. & Manning C.E. 2011. Rutile solubility in supercritical NaAlSi₃O₈-H₂O fluids. *Chemical Geology*, **284**: 74-81.
- Hippert J. F. 1998. Breakdown of feldspar, volume gain and lateral mass transfer during mylonitization of granitoid in a low metamorphic shear zone. *Journal of Structural Geology*, **20**:175-193.
- Hedenquist J. 2003. Sulfidation state of hydrothermal fluids: The porphyry-epithermal transition and beyond. Special publication 10, *Society of Economic Geologists and Geochemical Society*, **15**: 1-50.
- Hövelmann J., Putnis A., Geisler T., Schmidt B.C., Golla-Schindler U. 2010. The replacement of plagioclase feldspars by albite: observations from hydrothermal experiments. *Contrib. Mineral Petrol.*, **159**: 43–59.
- Ilmen S., Alansari A., Bajddi A., Maacha L. 2015. Cu-Au vein mineralization related to the Talat n'Imjjad shear zone (western High Atlas, Morocco): geological setting, ore mineralogy, and geochemical evolution. *Arab J Geosci.*, **8**:5039-5056.
- Inoue A., Meunier A., Patrier-Mas P., Rigault C., Beaufort D., Vieillard P. 2009. Application of chemical geothermometry to low-temperature trioctahedral chlorites. *Clays and Clay Minerals*, **57(3)**: 371–382.
- Jaket Y. & Schmalholz S.M. 2018. Spontaneous ductile crustal shear zone formation by thermal softening and related stress, temperature and strain rate evolution. *Tectonophysics*, **746**: 384-397.
- Jefferies S.P., Holdsworth R.E., Wibberley C.A.J., Shimamoto T., Spiers C.J., Niemeijer A.R., Lloyd G.E. 2006. The nature and importance of phyllonite development in crustal-scale fault cores: an example from the Median Tectonic Line, Japan. *Journal of Structural Geology*, **28**: 220–235.
- JICA/MMAJ. 2000. Metal Mining Agency of Japan/Japan International Cooperation Agency. Report on the Mineral Exploration in the Alta Floresta Area, Brazil, Final Report, Projeto Alta Floresta - MT, Japan, March, 137p.
- Kreuzer O. P. 2006. Textures, paragenesis and wall-roch alteration of lode-gold deposits in the Charters Towers district, north Queensland: implications for the conditions of ore formation. *Mineralium Deposita* 40:639-663.
- Dilles J.H. & Einaudi M.T. 1992. Wall-Rock Alteration and Hydrothermal Flow Paths about the Ann-Mason Porphyry Copper Deposit, Nevada--A 6-Kin Vertical Reconstruction. *Economic Geology*, **87**: 1963-2001.
- Kruhl J.H. 1996. Prism- and basal-plane parallel subgrain boundaries in quartz: a microstructural geothermobarometer. *Journal Metamorphic Geol.*, **14**:581-589.
- Lang J.R. & Baker T. 2001. Intrusion-related gold systems: The present level of understanding. *Mineralium Deposita*, **36**: 477-489.
- Lexa J., Stohl J., Konecný V. 1999. The Banská Štiavnica ore district: relationship between metallogenetic processes and the geological evolution of a stratovolcano. *Mineralium Deposita*, **34**: 639-654.
- Lee A.L., Torvela T., Lloyd G.E., Walker A.M. 2018. Melt organisation and strain partitioning in the lower crust. *Journal of Structural Geology*, **113**: 188-199.
- Leite J.A.D. & Saes G.S. 2003. Geocronologia Pb/Pb de zircões detriticos e análise estratigráfica das coberturas sedimentares proterozóicas do Sudoeste do Cráton Amazônico. *Geologia USP: Série Científica*, **3(1)**:113-127.

- Mancktelowa N.S. & Pennacchioni G. 2004. The influence of grain boundary fluids on the microstructure of quartz-feldspar mylonites. *Journal of Structural Geology*, **26**: 47–69.
- Mancktelowa N.S. & Pennacchioni G. 2005. The control of precursor brittle fracture and fluid–rock interaction on the development of single and paired ductile shear zones. *Journal of Structural Geology*, **27**: 645–661.
- Mark G. 1998. Albite formation by selective pervasive sodic alteration of tonalite plutons in the Cloncurry district, Queensland. *Australian Journal of Earth Sciences*, **45**: 765-774.
- Meinert L.D. 1992. Skarns and Skarn Deposits. *Geoscience Canada*, **19(4)**: 145-162.
- Menegon L., Pennacchioni G., Stünitz H. 2006. Nucleation and growth of myrmekite during ductile shear deformation in metagranites. *Journal Metamorphic Geol.*, **24**:553-568.
- Mesquita, M. J., Hartmann, L. A., Fyfe, W. S., Picanço, J. L., Castro, A. B. 2006. Alteração metamórfico-hidrotermal nos depósitos de ouro tipo-veio da Província de Porto Nacional, TO, Brasil: evidências de química mineral e microestruturas. *Revista Brasileira de Geociências*, **36**:34–50.
- Mesquita, M. J.; Bitencourt, M. F. ; Picanço, J. L. ; Vasconcellos, E. M. G. ; Moretto, A. L. 2013. Evolução Microestrutural do Granito Água Comprida e formação de filonitos, Antiforme Setuva, Paraná. *Geociências (São Paulo. Online)*, **32**: 269-285.
- Mesquita M.J, Quispe P. C., Xavier R., Geraldes M., Matos J. H., Moreira I., Gaidukas G. 2017. Geology, Geochemistry and U-Pb Geochronology of Arc-Related Granitoids of the Alta Floresta Gold Province and implications to the Orosian gold metallogeny of SW Amazon craton, Brazil. In: 14th SGA Biennial Meeting, 2017, Quebec. Proceedings of the 14th SGA Biennial Meeting, Québec City, Canada, 1628p. *Quebec: Society for Geology Applied to Mineral Deposits*, **1**:175-178.
- Miller C.F., Stoddard E.F., Bradfish L.J., Dollase W.A. 1981. Composition of plutonic muscovite: genetic implications. *Can. Mineral.*, **19**:25-34.
- Mikhail A. 1989. Rare Earth element systematics in hydrothermal fluids. *Geochemica et Cosmochimica Acta*, **53**:745-750.
- Middleton A.W, Förster A.J., Uysal I.T., Golding S.D., Rhede D. 2013. Accessory phases from the Soultz monzogranite, Soultz-sous-Forêts, France: Implications for titanite destabilisation and differential REE, Y and Th mobility in hydrothermal systems. *Chemical Geology*, **335**: 105-117.
- Migdisonva A., Williams-Jones A.E., Brugger J., Caporuscio F.A. 2016. Hydrothermal transport, deposition, and fractionation of the REE: Experimental data and thermodynamic calculations. *Chemical Geology*, **439**: 13-42.
- Miguel Jr E. 2011. Controle Estrutural das mineralizações auríferas e idades U-Pb das rochas encaixantes ao longo do Lineamento Peru-Trairão: Província Aurífera de Alta Floresta, Mato Grosso. Dissertação de Mestrado, Universidade Estadual de Campinas, 86p.
- Moreton L.C. & Martins E.G. 2005. Geologia e Recursos Minerais de Alta Floresta. Vila Guarita. Escala 1:250.000. Brasília, Serviço Geológico do Brasil, CPRM, 68 p.
- Morad S., El-Ghali M.A.K., Caja M.A., Sirat M., Al-Ramadan K., Mansurbeg H. 2010. Hydrothermal alteration of plagioclase in granitic rocks from Proterozoic basement of SE Sweden. *Geol. J.*, **45**: 105–116.
- Moura M.A. 1998. O Maciço Granítico Matupá e o Depósito de Ouro Serrinha (MT): Petrologia, Alteração Hidrotermal e Metalogenia. Tese de Doutorado, Instituto de Geociências, Universidade de Brasília, 238p.
- Munz I.A., Wayne D., Austrheim H. 1994. Retrograde fluid infiltration in the high-grade Modum Complex, South Norway: evidence for age, source and REE mobility. *Contrib. Mineral Petrol.*, **116**: 32-46.

- Nachit H., Ibhi A., Abia E. H., Ohoud B. 2005. Discrimination between Primary Magmatic Biotites, Reequilibrated Biotites and Neoformed Biotites. *Comptes Rendus Geoscience*, **337(16)**: 1415-1420.
- Parneix J.C., Beaufort D., Dudoignon P., Meunier A. 1985. Biotite chloritization process in hydrothermally altered granites. *Chemical Geology*, **51**:89-101.
- Passchier C.W. & Trouw R.A. 2005. *Microtectonics*. 2nd ed., Springer, Berlin, 366pp.
- Pirajno, F. 2009. *Hydrothermal processes and mineral systems*. Geological Survey of Western Australia, Perth, 1250 pp.
- Pümpel O. & Putnis A. 2009. The complex hydrothermal history of granitic rocks: multiple feldspar replacement reactions under subsolidus conditions. *Journal of Petrology*, **50**:967-987.
- Poggi L. (in preparation). 2019. O depósito de Au-Cu-Mo Paraíba (MT): integração de técnicas espectrais e convencionais para a exploração mineral. Tese de Mestrado, Instituto de Geociências, Universidade Estadual de Campinas (UNICAMP), 93p.
- Pryer L.L. 1993. Microstructures in feldspars from a major crustal thrust zone: the Grenville Front, Ontario, Canada. *J Struct Geol.*, **15**:21-36
- Pryer L.L. & Robin P.Y.F. 1996. Differential stress control on the growth and orientation of flame perthite: a paleostress-direction indicator. *Journal of Structural Geology*, **18**:1151-1166.
- Putnis A. & Putnis C.V. 2007. The mechanism of reequilibration of solids in the presence of a fluid phase. *Journal of Solid State Chemistry*, **180**:1783–1786.
- Putnis, A. & Austrheim, H. 2010. Fluid-induced processes: measomatism and metamorphism. *Geofluids*, **10**:254-269.
- Quispe, P.E. 2016. Geologia, geoquímica e geocronologia dos granitoides foliados e rochas subvulcânicas da região de Peixoto de Azevedo, setor leste da AFGP, MT, IG-Unicamp. Dissertação de Mestrado.
- Ramos G.S. 2011. Características geoquímicas de plútôns graníticos auríferos e estéreis da Província Aurífera de Alta Floresta (MT). Trabalho de Conclusão de Curso, Instituto de Geociências, Universidade Estadual de Campinas, 82p.
- Robb L. 2004. *Introduction to ore-forming processes*. Blackwell, Oxford, 386 pp.
- Rodrigues R.M. 2012. Caracterização geológica e metalogenética do Depósito X1 – Província Aurífera de Alta Floresta, Região de Matupá (MT). Dissertação de Mestrado, Instituto de Geociências, Universidade Estadual de Campinas, 70p.
- Rosenberg C.L. & Stünitz H. 2003. Deformation and recrystallisation of plagioclase along 707 a temperature gradient: an example from the Bergell tonalite. *J. Struct. Geol.*, **25**:389-408.
- Seedorff E., Dilles J.H., Proffett Jr J.M., Einaudi M.T., Zurcher L., Stavast W.J.A., Johnson D.A., Barton M.D. 2005. Porphyry deposits: characteristics and origin of hypogene features. *Economic Geology 110th Anniversary*, 251-298.
- Santos J.O.S. 2000. Os terrenos Paleoproterozóicos da Província do Tapajós e as mineralizações de ouro associadas. Tese de Doutorado, Instituto de Geociências, Universidade Federal do Rio Grande do Sul, 208p.
- Santos J.O.S., Hartmann L.A., Gaudette H.E., Groves D.I., McNaughton N.J., Fletcher I.R. 2000. A New understand of the provinces of the Amazon Craton based on integration of field mapping and U-Pb and Sm-Nd geochronology. *Gondw. Res.*, **3(4)**:453-488.
- Sibson R.H., Moore J.M., Rankin A.H. 1975. Seismic pumping: A hydrothermal fluid transport mechanism: *Journal of the Geological Society*, **131**:653–659.
- Sibson R.H. 1981. Fluid flow structure faulting: field evidence and models. *Earthquake Prediction: an international review. Maurice Ewing Series*, **4**:593-603.

- Sillitoe R.H. 2010. Porphyry Copper Systems. *Economic Geology*, **105**:3–41.
- Silva, F.R. 2014. Geoquímica e geocronologia U-Pb (SHRIMP) de granitos da região de Peixoto de Azevedo – Província Aurífera de Alta Floresta – MT. Dissertação de Mestrado, Instituto de Ciências Exatas e da Terra, Universidade Federal de Mato Grosso, 80p.
- Silva M.G. & Abram M.B. 2008. Projeto metalogenia da Província Aurífera Juruena-Teles Pires, Mato Grosso. Goiânia, Serviço Geológico Brasileiro, CPRM, 212p.
- Sinclair W.D. 2007. Porphyry deposits, in Goodfellow, W.D., ed., Mineral Deposits of Canada: A Synthesis of Major Deposit-Types, District Metallogeny, the Evolution of Geological Provinces, and Exploration Methods: Geological Association of Canada, Mineral Deposits Division, Special Publication, **5**:223-243.
- Souza J.P., Frasca A.A.S., Oliveira C.C. 2005. Geologia e Recursos Minerais da Província Mineral de Alta Floresta. Relatório Integrado. Brasília, Serviço Geológico Brasileiro, CPRM, 164p.
- Tamizel I., Mehmet A., Emel A.Y., Cem Y. 2014. Mineral chemistry and thermobarometry of Eocene monzogabbroic stocks from the Bafra (Samsun) area in Turkey: implications for disequilibrium crystallization and emplacement conditions. *International Geology Review*, **56(10)**:1226-1245.
- Tappert M. C., Rivard B., Giles D., Tappert R., Mauger A.J. 2013. The mineral chemistry, near-infrared, and mid-infrared reflectance spectroscopy of phengite from the Olympic Dam IOCG deposit, South Australia. *Ore Geology Reviews*, **53**:26-38.
- Tassinari C.C.G. & Macambira M.J.B. 1999. Geochronological Provinces of the Amazonian Craton. *Episodes*, **22(3)**:174-182.
- Teixeira R.V. 2015. Rochas hospedeiras e controle estrutural da mineralização aurífera do depósito Peteca, região de Flor da Serra – MT, na província Aurífera de Alta Floresta. Trabalho de Conclusão de Curso, Instituto de Geociências, Universidade Estadual de Campinas, 107p.
- Tullis J., & Yund R.A. 1980. Hydrolitic weakening of experimentally deformed Westerly granite and hale albite rock. *Journal of Structural Geology*, **2**:439-452.
- Thompson A.J.B. & Thompson J.F.H. 1996. *Atlas of alteration: a field and petrographic guide to hydrothermal alteration minerals*. Geological Association of Canada, Mineral Deposits Division, 119 pp.
- Velde B. 1985. Possible chemical control illite/smectite composition during diagenesis. *Mineral Magazine*, **49**:387–391.
- Vitório J.A. 2010. A suíte granítica Teles Pires da Província Aurífera de Alta Floresta: Características petrográficas, geoquímicas e implicações metalogenéticas. Instituto de Geociências, Universidade Estadual de Campinas, Relatório PIBIC/ CNPq, 20p.
- Whitney D.L. & Bernard W.E. 2010. Abbreviations for names of rock-forming minerals. *American Mineralogist*, **95**:185-187.
- Zhu Y., An F., Tan J. 2011. Geochemistry of hydrothermal gold deposits: A review. *Geoscience Frontiers*, **2(3)**:367–374.

APPENDIX B

Coordinates for location of the Peteca deposit and drill cores analyzed.

	X	Y	Final Depth
Peteca Deposit Location	710748	8881153	
Drill Cores	Drill Cores Location		
PT-8	710771,69	8881107,20	127
PT-12	710759,36	8881150,63	140,4
PT-15	710764,50	8881200,63	204
PT-22	710771,69	8881133,48	120,85
PT-30	710665,50	8881244,55	242,88

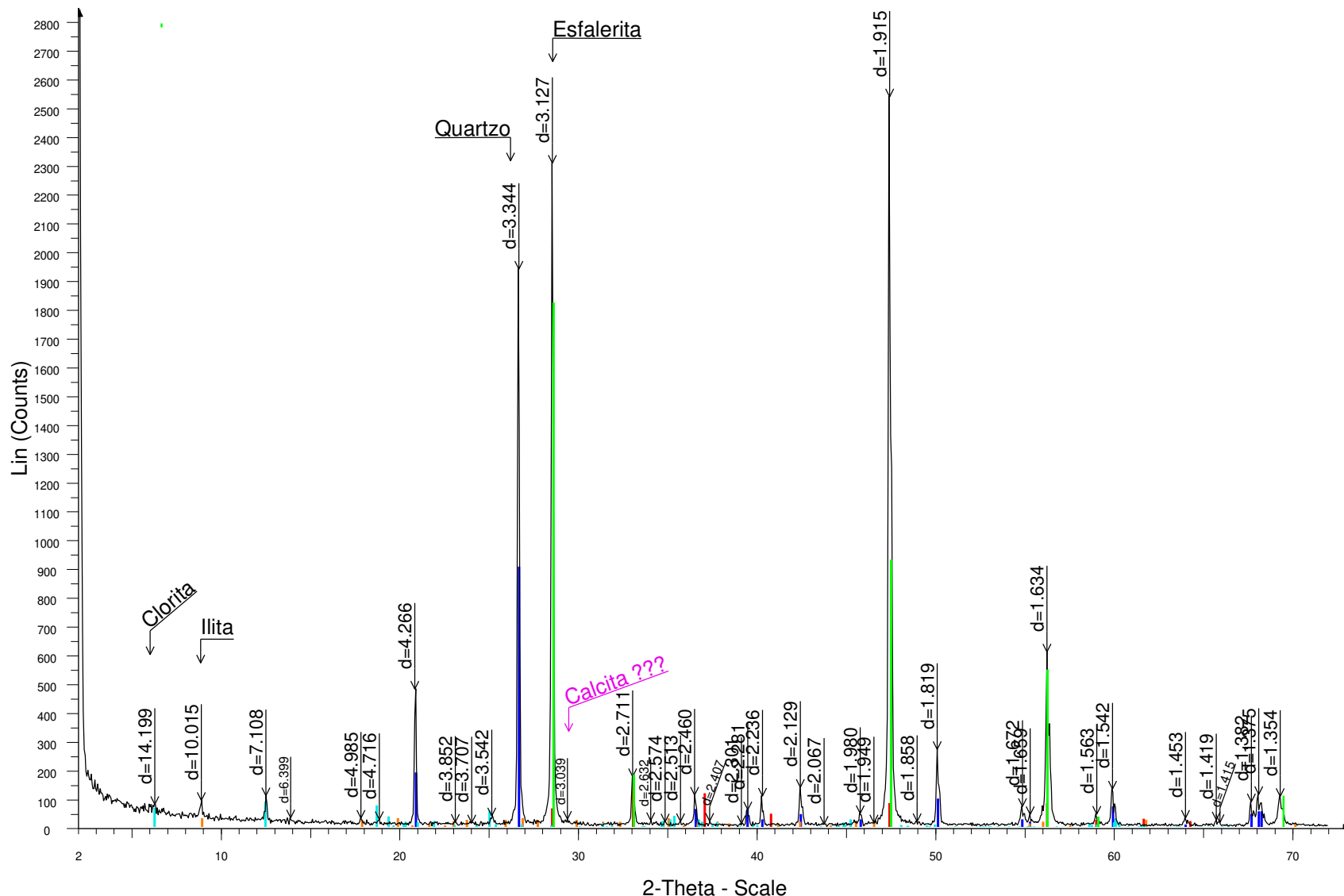
APPENDIX C

Modal compositions of the lythotypes and shear rocks.

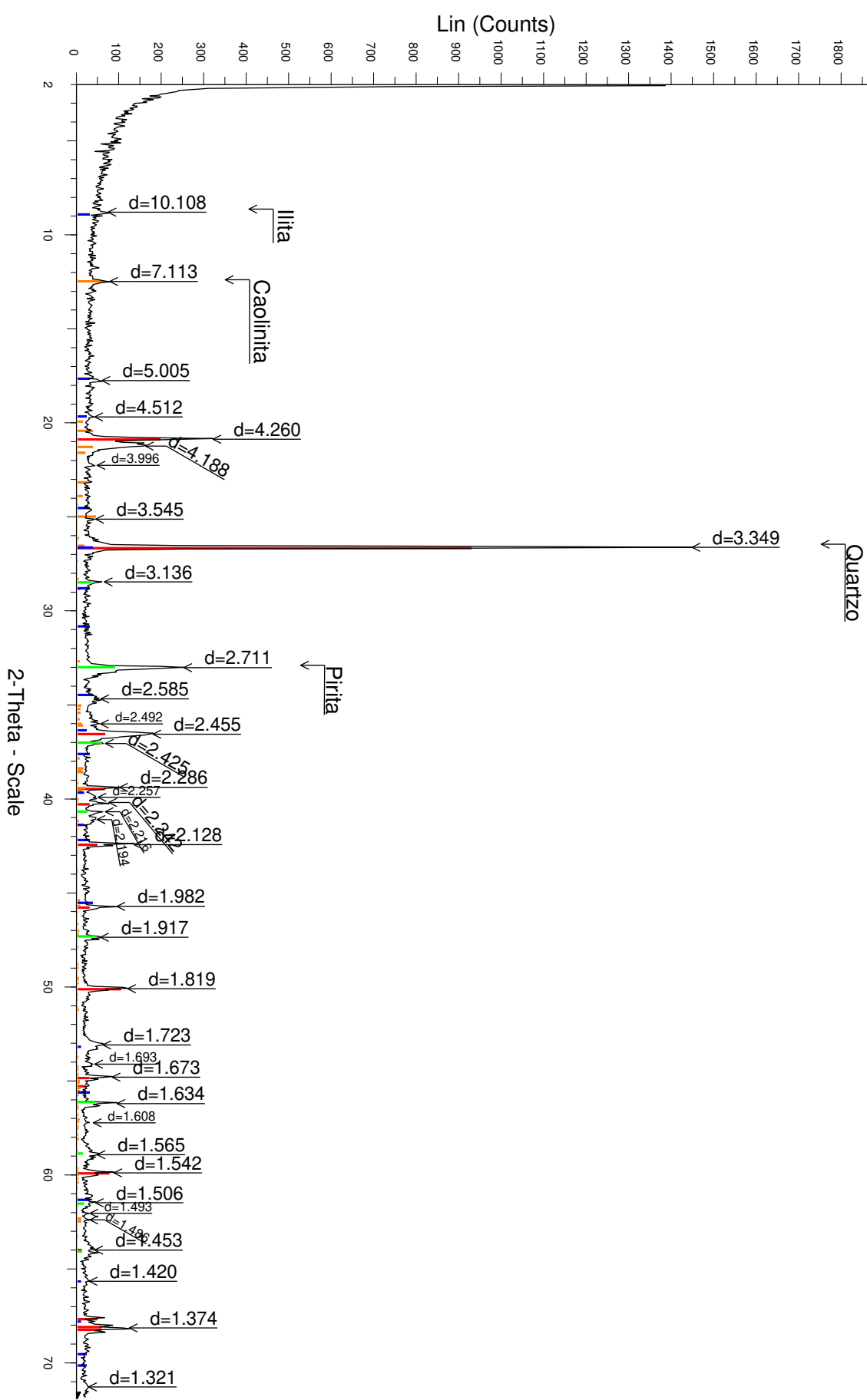
	Qz	Pl	Kfs	Bt	Grt	Chl	Ilm	Ms	Cal	Ep	Py	Ccp	Fe-Ti oxide	IIm	Rt	Fe hydroxide	
Foliated Granites	Garnet granodiorite	20 to 27	18 to 27	10 to 13,5	7,5 to 15	3 to 8	4 to 6	9 to 15	4 to 9	0,5 to 2,5	0,5	1	x	1 to 8	x	x	
	Garnet leucogranite	30	11 to 25	5 to 25	3 to 8	≤2	3 to 10	13	10	2 to 5	≤1	traces	x	4	x	x	
	Biotite orthotonalite	29	16	7	17	x	8	10	x	3	4	3	x	0,5-3	x	x	
	Biotite tonalite	10 to 38	27 to 35	≤8	12 to 15	x	5 to 16	5 to 10	x	≤3	1 to 5	≤3	x	traces	x	x	
Dyke	Microporphyrhetic dacite dyke	25 to 35	20-25	x	x	x	7 to 8	8 to 18	x	10	1 to 8	≤0,5	x	2	x	x	
Shear-hydrothermal System	Bt tonalite protomylonite	20	17	27	12	x	8	7	x	traces	1	2	x	6	x	x	
	Grt-Qz mylonite	34 to 47	10 to 13	20 to 21		1 to 3	3	6 to 9	5 to 8	10,5 to 5	1,5	traces	x	≤2	x	x	
	Grt-bt granodiorite mylonite	22	6	traces	20	0,5	15	27	x	4	traces	0,5	x	5	x	x	
	Ilite granodiorite mylonite	28 to 31	15 to 22	6	x	x	5 to 7	32 to 38	5 to 10	≤2	1	2	x	6	x	x	
	Cb-chl phyllonite	14	x	x	x	x	40	20	x	13	x	5	traces	x	4	3	
	Chl-ilm phyllonite	12 to 20	x	x	x	x	30 to 31	40	x		x	8 to 9	traces	x	≤2	3 to 8	x

APPENDIX D

Representative XRD Diffractograms for the cavities in the quartz vein. Sphalerite is the main sulphide, but it also can contain pyrite [Sample PTC5-1].



[Sample PTC4-3]



APPENDIX E

Representative major element analyses of plagioclase.

Analyses	Garnet Granodiorite															Sample PT15-08						
	Sample PT15-13																					
	fsp1	fsp2	fsp9	fsp10	fsp11	fsp12	fsp13	fsp14	fsp5	fsp6-1c	fsp6-2b	fsp7-1c	fsp7-2b	fsp8-1c	fsp8-2b	fsp1-1c	fsp1-2b	fsp2	fsp3	fsp4	fsp5	fsp6
SiO ₂	64.17	64.43	64.35	63.99	64.39	64.12	65.02	64.49	64.32	66.01	67.22	64.39	68.64	69.28	68.60	62.71	64.65	62.64	62.69	62.82	68.36	62.63
TiO ₂	0.01	0.01	0.00	0.03	0.02	0.01	0.00	0.02	0.00	0.02	0.02	0.02	0.02	0.00	0.00	0.00	0.01	0.03	0.02	0.02	0.00	0.05
Al ₂ O ₃	22.91	22.75	22.90	23.01	22.96	22.95	20.62	22.10	22.62	21.39	20.87	22.66	19.66	19.62	20.15	24.03	23.15	23.72	23.81	23.75	20.70	23.66
Cr ₂ O ₃	0.01	0.02	0.00	0.00	0.00	0.00	0.00	0.01	0.01	0.02	0.00	0.00	0.00	0.00	0.00	0.00	0.00	0.00	0.00	0.00	0.00	0.00
Fe ₂ O ₃	0.03	0.02	0.06	0.01	0.03	0.00	0.01	0.04	0.00	0.24	0.39	0.10	0.04	0.11	0.00	0.00	0.00	0.06	0.09	0.01	0.00	0.00
FeO	0.00	0.00	0.00	0.00	0.00	0.00	0.00	0.00	0.00	0.00	0.00	0.00	0.00	0.00	0.00	0.00	0.00	0.00	0.00	0.00	0.00	0.00
MnO	0.01	0.04	0.02	0.00	0.01	0.02	0.00	0.03	0.00	0.05	0.00	0.02	0.00	0.00	0.00	0.00	0.00	0.03	0.00	0.00	0.00	0.00
MgO	0.00	0.00	0.01	0.01	0.00	0.01	0.01	0.01	0.00	0.09	0.05	0.01	0.01	0.01	0.00	0.00	0.00	0.00	0.00	0.00	0.00	0.01
CaO	4.05	4.26	4.30	4.33	4.14	4.28	2.38	3.37	4.03	2.25	2.34	4.21	0.86	0.54	1.83	5.10	3.37	4.84	4.91	4.92	1.03	4.92
Na ₂ O	9.16	9.39	9.42	9.21	9.29	9.46	6.25	7.67	9.62	9.80	10.35	9.37	11.21	11.58	10.90	8.70	9.74	8.89	8.75	8.92	10.50	8.84
K ₂ O	0.28	0.06	0.10	0.12	0.18	0.07	6.11	3.19	0.04	0.43	0.08	0.09	0.08	0.06	0.06	0.11	0.04	0.10	0.27	0.07	0.59	0.09
Totals	100.63	101.18	101.16	100.71	101.02	100.92	100.40	101.12	100.84	100.30	101.32	100.87	100.52	101.20	101.54	100.65	100.96	100.31	100.54	100.51	101.18	100.20
Si	2.82	2.82	2.81	2.81	2.82	2.81	2.91	2.84	2.83	2.89	2.92	2.82	2.99	2.99	2.96	2.76	2.82	2.77	2.76	2.77	2.96	2.77
Ti	0.00	0.00	0.00	0.00	0.00	0.00	0.00	0.00	0.00	0.00	0.00	0.00	0.00	0.00	0.00	0.00	0.00	0.00	0.00	0.00	0.00	0.00
Al	1.19	1.17	1.18	1.19	1.18	1.19	1.09	1.15	1.17	1.11	1.07	1.17	1.01	1.00	1.03	1.25	1.19	1.23	1.24	1.23	1.06	1.23
Cr	0.00	0.00	0.00	0.00	0.00	0.00	0.00	0.00	0.00	0.00	0.00	0.00	0.00	0.00	0.00	0.00	0.00	0.00	0.00	0.00	0.00	0.00
Fe ₃	0.00	0.00	0.00	0.00	0.00	0.00	0.00	0.00	0.00	0.01	0.01	0.00	0.00	0.00	0.00	0.00	0.00	0.00	0.00	0.00	0.00	0.00
Fe ₂	0.00	0.00	0.00	0.00	0.00	0.00	0.00	0.00	0.00	0.00	0.00	0.00	0.00	0.00	0.00	0.00	0.00	0.00	0.00	0.00	0.00	0.00
Mn	0.00	0.00	0.00	0.00	0.00	0.00	0.00	0.00	0.00	0.00	0.00	0.00	0.00	0.00	0.00	0.00	0.00	0.00	0.00	0.00	0.00	0.00
Mg	0.00	0.00	0.00	0.00	0.00	0.00	0.00	0.00	0.00	0.01	0.00	0.00	0.00	0.00	0.00	0.00	0.00	0.00	0.00	0.00	0.00	0.00
Ca	0.19	0.20	0.20	0.20	0.19	0.20	0.11	0.17	0.19	0.11	0.11	0.20	0.04	0.03	0.09	0.24	0.16	0.23	0.23	0.23	0.05	0.23
Na	0.78	0.81	0.80	0.78	0.79	0.80	0.54	0.66	0.82	0.83	0.87	0.80	0.95	0.97	0.91	0.74	0.82	0.76	0.75	0.76	0.88	0.76
K	0.02	0.00	0.01	0.01	0.01	0.00	0.35	0.18	0.00	0.02	0.00	0.01	0.00	0.00	0.00	0.01	0.00	0.01	0.02	0.00	0.03	0.01
Sum	4.99	5.01	5.00	4.99	4.99	5.00	5.00	5.00	5.00	4.98	4.98	4.99	4.99	4.99	4.99	4.99	5.00	5.00	5.00	5.00	4.97	5.00
XOr	0.02	0.00	0.01	0.01	0.01	0.00	0.35	0.18	0.00	0.02	0.00	0.01	0.00	0.00	0.00	0.01	0.00	0.01	0.02	0.00	0.03	0.01
XAb	0.79	0.80	0.79	0.79	0.80	0.54	0.65	0.81	0.87	0.89	0.80	0.96	0.97	0.91	0.75	0.84	0.76	0.75	0.76	0.92	0.76	
XAn	0.19	0.20	0.20	0.21	0.20	0.20	0.11	0.17	0.19	0.11	0.11	0.20	0.04	0.03	0.09	0.24	0.16	0.23	0.23	0.23	0.05	0.23

Analyses	Garnet Granodiorite																				
	Sample PT15-08																				
	fsp8	fsp9	fsp10	fsp11	fsp12-2	fsp13	fsp14	fsp18	fsp19-1c	fsp19-2b	fsp20-1	fsp20-2	fsp21-1c	fsp21-2b	fsp22-1c	fsp22-2b	fsp25-1c	fsp25-2b	fsp23-1c	fsp23-2b	fsp24-1c
SiO ₂	62.90	62.28	62.97	62.45	61.90	62.36	62.22	64.96	66.08	65.25	64.40	62.45	62.92	63.09	62.90	63.81	66.33	67.90	62.32	62.58	66.61
TiO ₂	0.03	0.03	0.02	0.01	0.01	0.02	0.00	0.00	0.00	0.00	0.01	0.03	0.02	0.01	0.01	0.01	0.00	0.02	0.01	0.00	0.03
Al ₂ O ₃	23.72	24.02	23.93	23.92	24.22	23.98	24.15	22.64	22.15	22.16	22.86	23.80	23.66	23.63	23.76	23.21	21.75	21.02	23.68	23.79	21.37
Cr ₂ O ₃	0.00	0.00	0.00	0.00	0.00	0.00	0.00	0.00	0.00	0.00	0.00	0.00	0.00	0.00	0.00	0.00	0.00	0.00	0.00	0.00	0.00
Fe ₂ O ₃	0.00	0.00	0.08	0.04	0.06	0.02	0.05	0.01	0.03	0.00	0.02	0.00	0.09	0.00	0.03	0.00	0.01	0.02	0.01	0.14	0.24
FeO	0.00	0.00	0.00	0.00	0.00	0.00	0.00	0.00	0.00	0.00	0.00	0.00	0.00	0.00	0.00	0.00	0.00	0.00	0.00	0.00	0.00
MnO	0.00	0.01	0.00	0.00	0.04	0.00	0.00	0.03	0.04	0.02	0.05	0.01	0.03	0.02	0.00	0.00	0.01	0.00	0.02	0.00	0.02
MgO	0.01	0.00	0.01	0.00	0.02	0.00	0.00	0.02	0.00	0.00	0.00	0.01	0.00	0.01	0.00	0.02	0.00	0.00	0.00	0.00	0.00
CaO	4.87	4.89	4.78	5.04	5.03	5.01	5.28	3.03	2.28	2.77	3.42	4.85	4.76	4.63	4.73	4.15	1.79	1.08	4.76	4.79	1.53
Na ₂ O	8.79	8.66	8.91	8.75	8.73	8.73	8.61	9.77	10.33	10.09	9.76	8.84	8.85	9.09	9.22	9.26	10.72	10.65	8.96	8.93	10.75
K ₂ O	0.09	0.17	0.14	0.08	0.09	0.07	0.07	0.21	0.06	0.08	0.07	0.06	0.05	0.07	0.06	0.08	0.08	0.05	0.10	0.11	0.13
Totals	100.41	100.06	100.84	100.29	100.10	100.19	100.38	100.67	100.97	100.37	100.59	100.04	100.39	100.54	100.72	100.52	100.70	100.75	99.84	100.36	100.68
Si	2.77	2.76	2.76	2.76	2.74	2.76	2.75	2.84	2.88	2.86	2.82	2.76	2.77	2.78	2.77	2.80	2.89	2.94	2.76	2.762	2.904
Ti	0.00	0.00	0.00	0.00	0.00	0.00	0.00	0.00	0.00	0.00	0.00	0.00	0.00	0.00	0.00	0.00	0.00	0.00	0.00	0.000	0.001
Al	1.23	1.25	1.24	1.25	1.26	1.25	1.26	1.17	1.14	1.15	1.18	1.24	1.23	1.23	1.23	1.20	1.12	1.07	1.24	1.238	1.098
Cr	0.00	0.00	0.00	0.00	0.00	0.00	0.00	0.00	0.00	0.00	0.00	0.00	0.00	0.00	0.00	0.00	0.00	0.00	0.00	0.000	0.000
Fe ₃	0.00	0.00	0.00	0.00	0.00	0.00	0.00	0.00	0.00	0.00	0.00	0.00	0.00	0.00	0.00	0.00	0.00	0.00	0.00	0.005	0.008
Fe ₂	0.00	0.00	0.00	0.00	0.00	0.00	0.00	0.00	0.00	0.00	0.00	0.00	0.00	0.00	0.00	0.00	0.00	0.00	0.00	0.000	0.000
Mn	0.00	0.00	0.00	0.00	0.00	0.00	0.00	0.00	0.00	0.00	0.00	0.00	0.00	0.00	0.00	0.00	0.00	0.00	0.00	0.001	0.001
Mg	0.00	0.00	0.00	0.00	0.00	0.00	0.00	0.00	0.00	0.00	0.00	0.00	0.00	0.00	0.00	0.00	0.00	0.00	0.00	0.000	0.000
Ca	0.23	0.23	0.23	0.24	0.24	0.24	0.25	0.14	0.11	0.13	0.16	0.23	0.23	0.22	0.22	0.20	0.08	0.05	0.23	0.227	0.071
Na	0.75	0.74	0.76	0.75	0.75	0.75	0.74	0.87	0.86	0.83	0.76	0.76	0.78	0.79	0.91	0.90	0.77	0.764	0.909		
K	0.01	0.01	0.01	0.01	0.00	0.00	0.01	0.00	0.00	0.00	0.00	0.00	0.00	0.00	0.00	0.00	0.01	0.006	0.007		
Sum	4.99	4.99	5.00	5.00	5.00	5.00	5.00	4.99	5.00	5.00	5.00	4.99	5.00	5.01	4.99	5.01	4.97	5.01	5.002	5.000	
XOr	0.01	0.01	0.01	0.01	0.01	0.00	0.00	0.01	0.00	0.00	0.00	0.00	0.00	0.00	0.00	0.00	0.01	0.01	0.01	0.01	
XAb	0.76	0.75	0.76	0.76	0.75	0.76	0.74	0.84	0.89	0.86	0.83	0.76	0.77	0.78	0.78	0.80	0.91	0.94	0.77	0.77	0.92
XAn	0.23	0.24	0.23	0.24	0.24	0.24	0.25	0.14	0.11	0.13	0.16	0.23	0.23	0.22	0.22	0.20	0.08	0.05	0.23	0.23	0.07

Analyses	Garnet Granodiorite					Garnet Granodiorite - phenocrysts					Garnet Leucogranite									
	Sample PT15-08										Sample PT30-04									
	fsp24-2b	fsp26-1c	fsp26-2c	fsp27-1c	fsp27-2c	fsp15	fsp16	fsp17	fsp28-1	fsp28-2	fsp28-3	fsp1-1c	fsp1-2b	fsp2-1c	fsp2-2b	fsp3-1	fsp3-2	fsp4-1c	fsp4-2b	fsp8-2b
SiO ₂	67.76	66.79	66.07	67.35	68.60	62.10	62.57	62.16	61.22	61.80	62.39	68.86	68.16	68.23	68.48	63.50	63.66	68.43	66.18	64.74
TiO ₂	0.01	0.03	0.02	0.02	0.01	0.03	0.02	0.02	0.01	0.00	0.02	0.02	0.01	0.01	0.00	0.01	0.01	0.00	0.00	0.01
Al ₂ O ₃	20.82	21.31	21.86	20.97	20.17	23.99	24.03	24.11	24.10	24.36	23.63	19.77	19.68	20.22	19.73	23.05	22.89	19.72	21.19	22.94
Cr ₂ O ₃	0.00	0.00	0.00	0.00	0.00	0.00	0.00	0.00	0.00	0.00	0.00	0.00	0.00	0.00	0.00	0.00	0.00	0.00	0.00	0.00
Fe ₂ O ₃	0.06	0.05	0.03	0.01	0.10	0.05	0.07	0.08	0.08	0.02	0.06	0.04	0.03	0.00	0.01	0.02	0.02	0.01	0.04	0.02
FeO	0.00	0.00	0.00	0.00	0.00	0.00	0.00	0.00	0.00	0.00	0.00	0.00	0.00	0.00	0.00	0.00	0.00	0.00	0.00	0.00
MnO	0.02	0.00	0.00	0.00	0.00	0.00	0.00	0.00	0.00	0.00	0.02	0.00	0.01	0.00	0.05	0.00	0.00	0.00	0.04	0.00
MgO	0.00	0.00	0.00	0.00	0.00	0.02	0.01	0.00	0.00	0.00	0.00	0.02	0.01	0.01	0.00	0.01	0.00	0.00	0.00	0.01
CaO	0.88	1.57	2.12	1.20	0.35	5.27	5.00	5.25	5.79	5.54	5.07	0.36	0.45	0.91	0.48	4.40	4.37	0.58	2.01	3.87
Na ₂ O	10.99	10.91	10.35	11.14	11.27	8.67	8.55	8.56	8.40	8.25	8.56	11.61	11.62	11.30	11.55	9.34	9.41	11.74	10.70	9.52
K ₂ O	0.07	0.06	0.09	0.07	0.07	0.08	0.14	0.08	0.14	0.14	0.39	0.16	0.09	0.06	0.07	0.06	0.09	0.06	0.17	0.04
Totals	100.61	100.72	100.54	100.76	100.57	100.21	100.39	100.26	99.74	100.11	100.34	100.84	100.06	100.74	100.37	100.38	100.46	100.54	100.33	101.15
Si	2.945	2.909	2.885	2.929	2.977	2.747	2.758	2.747	2.727	2.736	2.765	2.985	2.980	2.963	2.983	2.797	2.803	2.979	2.900	2.822
Ti	0.000	0.001	0.001	0.001	0.000	0.001	0.001	0.001	0.000	0.000	0.001	0.001	0.000	0.000	0.000	0.000	0.000	0.000	0.000	0.000
Al	1.067	1.094	1.125	1.075	1.092	1.251	1.249	1.256	1.266	1.271	1.231	1.010	1.014	1.035	1.013	1.197	1.188	1.012	1.095	1.179
Cr	0.000	0.000	0.000	0.000	0.000	0.000	0.000	0.000	0.000	0.000	0.000	0.000	0.000	0.000	0.000	0.000	0.000	0.000	0.000	0.000
Fe ₃	0.002	0.002	0.001	0.000	0.003	0.002	0.002	0.003	0.003	0.001	0.002	0.001	0.001	0.000	0.000	0.001	0.001	0.000	0.001	0.001
Fe ₂	0.000	0.000	0.000	0.000	0.000	0.000	0.000	0.000	0.000	0.000	0.000	0.000	0.000	0.000	0.000	0.000	0.000	0.000	0.000	0.000
Mn	0.001	0.000	0.000	0.000	0.000	0.000	0.000	0.000	0.000	0.000	0.001	0.000	0.000	0.000	0.002	0.000	0.000	0.000	0.001	0.000
Mg	0.000	0.000	0.000	0.000	0.000	0.001	0.001	0.000	0.000	0.000	0.000	0.001	0.001	0.001	0.000	0.000	0.001	0.000	0.000	0.001
Ca	0.041	0.073	0.099	0.056	0.016	0.250	0.236	0.249	0.276	0.263	0.240	0.017	0.021	0.042	0.022	0.208	0.206	0.027	0.094	0.181
Na	0.926	0.921	0.876	0.939	0.948	0.744	0.731	0.733	0.726	0.708	0.733	0.976	0.985	0.952	0.976	0.798	0.803	0.991	0.909	0.805
K	0.004	0.003	0.005	0.004	0.004	0.005	0.008	0.005	0.008	0.008	0.022	0.009	0.005	0.003	0.004	0.003	0.005	0.003	0.010	0.002
Sum	4.986	5.004	4.992	5.004	4.981	5.000	4.985	4.992	5.005	4.986	4.995	5.001	5.007	4.996	5.000	5.004	5.007	5.012	5.011	4.991
XOr	0.00	0.00	0.01	0.00	0.00	0.01	0.01	0.01	0.01	0.01	0.02	0.01	0.00	0.00	0.00	0.00	0.00	0.00	0.01	0.00
XAb	0.95	0.92	0.89	0.94	0.98	0.74	0.75	0.74	0.72	0.72	0.74	0.97	0.97	0.95	0.97	0.79	0.79	0.97	0.90	0.81
XAn	0.04	0.07	0.10	0.06	0.02	0.25	0.24	0.25	0.27	0.27	0.24	0.02	0.02	0.04	0.02	0.21	0.20	0.03	0.09	0.18

Analyses	Biotite Tonalite Promylonite											Biotite Tonalite Protomylonite - perhites			
	Sample PTB-05											Sample PTB-05			
	fsp1	fsp2	fsp3	fsp4	fsp5	fsp6	fsp7	fsp8	fsp9	fsp10	fsp15	fsp1-1	fsp2-1	fsp2-2	fsp2-4
SiO ₂	67.56	68.20	62.69	62.43	62.52	63.14	63.36	68.31	62.91	63.28	66.24	68.85	69.01	67.09	69.64
TiO ₂	0.00	0.01	0.02	0.03	0.03	0.00	0.01	0.02	0.02	0.00	0.02	0.02	0.01	0.01	0.03
Al ₂ O ₃	20.70	20.25	23.72	23.79	23.73	23.36	23.32	20.17	23.50	23.54	20.12	20.11	19.84	19.57	19.80
Cr ₂ O ₃	0.00	0.00	0.00	0.00	0.00	0.00	0.00	0.00	0.00	0.00	0.00	0.00	0.00	0.00	0.00
Fe ₂ O ₃	0.01	0.02	0.10	0.07	0.11	0.07	0.02	0.08	0.01	0.07	0.00	0.04	0.06	0.03	0.02
FeO	0.00	0.00	0.00	0.00	0.00	0.02	0.00	0.00	0.00	0.00	0.00	0.00	0.00	0.00	0.00
MnO	0.01	0.00	0.00	0.01	0.01	0.00	0.00	0.00	0.01	0.00	0.03	0.00	0.03	0.02	0.00
MgO	1.40	0.78	5.09	5.37	5.36	5.27	4.93	1.00	5.24	5.28	0.66	0.01	0.00	0.00	0.00
CaO	10.88	10.96	8.59	8.51	8.50	8.77	9.01	11.17	8.57	8.69	8.70	0.29	0.42	0.14	0.19
Na ₂ O	0.05	0.06	0.10	0.08	0.18	0.08	0.01	0.02	0.02	0.00	3.43	11.18	11.12	8.66	11.11
K ₂ O	0.00	0.00	0.00	0.00	0.00	0.00	0.00	0.00	0.00	0.00	0.00	0.11	0.26	4.77	0.17
Totals	100.61	100.28	100.31	100.29	100.44	100.71	100.66	100.77	100.28	100.86	99.20	100.61	100.75	100.29	100.96
Si	2.913	2.946	2.720	2.710	2.712	2.730	2.740	2.940	2.729	2.730	2.905	2.984	2.991	2.974	3.004
Ti	0.000	0.000	0.001	0.001	0.001	0.000	0.000	0.001	0.001	0.000	0.001	0.001	0.000	0.000	0.001
Al	1.052	1.031	1.213	1.218	1.213	1.191	1.189	1.023	1.202	1.197	1.040	1.030	1.010	1.020	1.010
Cr	0.000	0.000	0.000	0.000	0.000	0.000	0.000	0.000	0.000	0.000	0.000	0.000	0.000	0.000	0.000
Fe ₃	0.000	0.001	0.003	0.002	0.004	0.002	0.001	0.003	0.000	0.002	0.019	0.001	0.002	0.001	0.001
Fe ₂	0.000	0.000	0.000	0.000	0.000	0.001	0.000	0.000	0.000	0.000	0.001	0.000	0.000	0.000	0.000
Mn	0.000	0.000	0.000	0.000	0.000	0.000	0.000	0.000	0.000	0.000	0.001	0.000	0.001	0.001	0.000
Mg	0.090	0.050	0.329	0.347	0.346	0.340	0.318	0.064	0.339	0.339	0.043	0.001	0.000	0.000	0.000
Ca	0.503	0.507	0.399	0.396	0.395	0.406	0.417	0.513	0.398	0.402	0.409	0.013	0.020	0.007	0.009
Na	0.004	0.005	0.008	0.007	0.015	0.007	0.001	0.002	0.002	0.000	0.292	0.940	0.934	0.744	0.929
K	0.000	0.000	0.000	0.000	0.000	0.000	0.000	0.000	0.000	0.000	0.000	0.006	0.014	0.270	0.009
Sum	4.563	4.540	4.675	4.682	4.687	4.677	4.666	4.547	4.670	4.671	4.708	4.974	4.976	5.021	4.960
XOr	0.00	0.00	0.00	0.00	0.00	0.00	0.00	0.00	0.00	0.00	0.00	0.01	0.01	0.26	0.01
XAb	0.01	0.01	0.02	0.02	0.04	0.02	0.00	0.00	0.01	0.00	0.42	0.98	0.96	0.73	0.98
XAn	0.99	0.99	0.98	0.98	0.96	0.98	1.00	1.00	1.00	1.00	0.58	0.01	0.02	0.01	0.01

Representative major element analyses of K-feldspar.

Analyses	Garnet Granodiorite						Garnet Leucogranite					Biotite Tonalite Mylonite								
	Sample PT15-08			Sample PT15-13			Sample PT30-04					Sample PT8-3								
	Kfs1	Kfs2	Kfs3	Kfs5	Kfs2	Kfs3	Kfs1	Kfs2	Kfs3	Kfs4	Kfs5	Kfs4-1	Kfs4-2	Ksf6	Ksf7	Ksf8	Ksf9-1	Ksf9-2	Ksf10-1	Ksf10-2
SiO ₂	64.08	64.01	63.57	63.61	65.03	65.25	64.33	64.57	64.78	64.8	64.31	65.11	65.38	65.49	65.06	65.47	65.44	65.4	65.49	65.24
TiO ₂	0.02	0.000	0.01	0.04	0.04	0.01	0.31	0.04	0.03	0.03	0.03	0.04	0.01	0.01	0.03	0.02	0.03	0.03	0.000	0.02
Al ₂ O ₃	18.67	18.52	18.84	18.52	18.11	18.33	18.31	18.39	18.4	18.63	18.36	18.24	18.01	17.99	18.09	18.09	18.07	18.24	18.12	18.3
Cr ₂ O ₃	0.00	0.00	0.00	0.00	0.00	0.00	0.00	0.00	0.00	0.00	0.00	0.00	0.00	0.00	0.00	0.00	0.00	0.00	0.00	0.00
Fe ₂ O ₃	0.06	0.00	0.00	0.04	0.00	0.00	0.02	0.00	0.01	0.00	0.01	0.00	0.04	0.00	0.00	0.01	0.03	0.00	0.09	0.06
FeO	0.00	0.00	0.00	0.00	0.00	0.00	0.00	0.00	0.00	0.00	0.00	0.00	0.00	0.00	0.00	0.00	0.00	0.00	0.00	0.00
MnO	0.00	0.00	0.00	0.00	0.00	0.00	0.00	0.00	0.04	0.00	0.00	0.00	0.00	0.03	0.00	0.00	0.00	0.02	0.05	0.00
MgO	0.00	0.00	0.00	0.00	0.00	0.01	0.00	0.00	0.01	0.00	0.00	0.01	0.00	0.01	0.00	0.00	0.00	0.00	0.00	0.00
CaO	0.01	0.00	0.02	0.07	0.04	0.00	0.04	0.00	0.00	0.11	0.09	0.00	0.00	0.03	0.02	0.01	0.04	0.02	0.00	0.01
Na ₂ O	0.71	0.49	0.55	0.51	0.41	0.48	0.41	0.76	0.48	0.53	0.54	0.48	0.47	0.91	0.48	0.80	0.40	0.43	0.47	0.54
K ₂ O	15.33	15.83	15.70	15.84	15.91	15.83	16.10	15.83	16.02	15.90	15.84	15.96	15.99	15.38	15.90	15.42	16.06	15.83	15.90	15.69
Totals	98.88	98.85	98.69	98.63	99.54	99.93	99.52	99.61	99.77	100	99.18	99.84	100.1	99.85	99.58	99.82	100.07	99.99	100.12	99.86
Si	2.99	2.99	2.97	2.98	3.01	3.01	2.99	2.99	3.00	2.99	2.99	3.01	3.02	3.02	3.01	3.02	3.02	3.01	3.02	3.01
Ti	0.00	0.00	0.00	0.00	0.00	0.00	0.01	0.00	0.00	0.00	0.00	0.00	0.00	0.00	0.00	0.00	0.00	0.00	0.00	0.00
Al	1.03	1.02	1.04	1.02	0.99	1.00	1.00	1.01	1.00	1.01	1.01	0.99	0.98	0.98	0.99	0.98	0.98	0.99	0.98	1.00
Cr	0.00	0.00	0.00	0.00	0.00	0.00	0.00	0.00	0.00	0.00	0.00	0.00	0.00	0.00	0.00	0.00	0.00	0.00	0.00	0.00
Fe ₃	0.00	0.00	0.00	0.00	0.00	0.00	0.00	0.00	0.00	0.00	0.00	0.00	0.00	0.00	0.00	0.00	0.00	0.00	0.00	0.00
Fe ₂	0.00	0.00	0.00	0.00	0.00	0.00	0.00	0.00	0.00	0.00	0.00	0.00	0.00	0.00	0.00	0.00	0.00	0.00	0.00	0.00
Mn	0.00	0.00	0.00	0.00	0.00	0.00	0.00	0.00	0.00	0.00	0.00	0.00	0.00	0.00	0.00	0.00	0.00	0.00	0.00	0.00
Mg	0.00	0.00	0.00	0.00	0.00	0.00	0.00	0.00	0.00	0.00	0.00	0.00	0.00	0.00	0.00	0.00	0.00	0.00	0.00	0.00
Ca	0.00	0.00	0.00	0.00	0.00	0.00	0.00	0.00	0.00	0.01	0.00	0.00	0.00	0.00	0.00	0.00	0.00	0.00	0.00	0.00
Na	0.06	0.04	0.05	0.05	0.04	0.04	0.04	0.07	0.04	0.05	0.05	0.04	0.04	0.04	0.08	0.04	0.07	0.04	0.04	0.05
K	0.91	0.94	0.94	0.95	0.94	0.93	0.95	0.94	0.95	0.94	0.94	0.94	0.94	0.90	0.94	0.91	0.94	0.93	0.93	0.92
Sum	4.99	5.00	5.00	5.00	4.98	4.98	5.00	5.00	5.00	4.99	5.00	4.99	4.98	4.99	4.98	4.98	4.98	4.98	4.98	4.98

Analyses	Garnet Granodiorite					Biotite Tonalite Mylonite										
	Sample PT13-08					Sample PT8-5										
	Phenocryst					Porphyroblast										
Analyses	Kfs6-3	Kfs6-4	Kfs6-5	Kfs7-1	Kfs7-2	Kfs1-1	Kfs1-2	Kfs1-3	Kfs1-4	Kfs1-5	Kfs1-6	Kfs2-1	Kfs2-2	Kfs2-3	Kfs2-4	Kfs2-6
SiO ₂	64.72	64.17	64.02	64.19	64.33	63.34	64.69	64.47	63.24	63.22	64.69	64.63	64.99	63.47	63.23	63.77
TiO ₂	0.02	0.03	0.01	0.04	0.02	0.03	0.00	0.03	0.03	0.01	0.03	0.01	0.07	0.02	0.01	0.03
Al ₂ O ₃	18.41	18.38	18.46	18.80	18.35	19.23	18.36	18.40	18.37	18.61	18.42	18.16	18.19	18.39	18.39	18.46
Cr ₂ O ₃	0.00	0.00	0.00	0.00	0.00	0.00	0.00	0.00	0.00	0.00	0.00	0.00	0.00	0.00	0.00	0.00
Fe ₂ O ₃	0.00	0.00	0.08	0.00	0.03	0.01	0.00	0.06	0.07	0.03	0.08	0.00	0.04	0.06	0.02	0.00
FeO	0.00	0.00	0.00	0.00	0.00	0.00	0.00	0.00	0.00	0.00	0.00	0.00	0.00	0.00	0.00	0.00
MnO	0.00	0.02	0.00	0.00	0.02	0.00	0.00	0.00	0.00	0.00	0.00	0.00	0.00	0.01	0.00	0.00
MgO	0.00	0.00	0.00	0.00	0.00	0.00	0.00	0.02	0.00	0.00	0.00	0.00	0.00	0.00	0.00	0.00
CaO	0.00	0.02	0.00	0.00	0.00	0.25	0.09	0.06	0.00	0.00	0.00	0.00	0.00	0.02	0.00	0.03
Na ₂ O	0.47	0.43	0.43	0.63	0.37	2.77	1.42	0.52	0.42	1.21	0.40	0.40	0.69	2.59	1.30	2.44
K ₂ O	16.02	16.08	15.98	15.34	15.83	13.10	14.64	15.94	16.28	15.18	16.06	16.00	15.74	13.09	14.74	12.87
Totals	99.64	99.13	99.00	99.20	99.37	100.73	99.20	99.30	100.41	100.26	99.68	99.22	99.72	99.85	99.69	99.60
Si	3.00	2.99	2.99	2.98	2.99	2.97	3.00	2.99	3.00	2.99	3.00	3.01	3.01	3.00	3.01	3.01
Ti	0.00	0.00	0.00	0.00	0.00	0.00	0.00	0.00	0.00	0.00	0.00	0.00	0.00	0.00	0.00	0.00
Al	1.01	1.01	1.02	1.03	1.01	1.03	1.00	1.01	1.00	1.01	1.01	1.00	0.99	1.00	1.00	1.00
Cr	0.00	0.00	0.00	0.00	0.00	0.00	0.00	0.00	0.00	0.00	0.00	0.00	0.00	0.00	0.00	0.00
Fe ₃	0.00	0.00	0.00	0.00	0.00	0.00	0.00	0.00	0.00	0.00	0.00	0.00	0.00	0.00	0.00	0.00
Fe ₂	0.00	0.00	0.00	0.00	0.00	0.00	0.00	0.00	0.00	0.00	0.00	0.00	0.00	0.00	0.00	0.00
Mn	0.00	0.00	0.00	0.00	0.00	0.00	0.00	0.00	0.00	0.00	0.00	0.00	0.00	0.00	0.00	0.00
Mg	0.00	0.00	0.00	0.00	0.00	0.00	0.00	0.00	0.00	0.00	0.00	0.00	0.00	0.00	0.00	0.00
Ca	0.00	0.00	0.00	0.00	0.00	0.01	0.00	0.00	0.00	0.00	0.00	0.00	0.00	0.00	0.00	0.00
Na	0.04	0.04	0.04	0.06	0.03	0.24	0.13	0.05	0.04	0.11	0.04	0.04	0.06	0.13	0.12	0.11
K	0.95	0.96	0.95	0.92	0.94	0.76	0.87	0.94	0.96	0.89	0.95	0.95	0.93	0.76	0.87	0.75
Sum	4.99	5.00	5.00	4.99	4.99	5.02	5.00	5.00	4.99	5.00	4.99	4.99	5.00	4.99	4.97	

Representative major element analyses of garnet.

Representative major element analyses of biotite.

Analyses	Garnet Granodiorite												Biotite Tonalite					
	Sample PT15-13							Sample PT15-08					Sample PT8-6					
	bi1	bi2-2	bi2-3	bi2-4	bi3	bi4-1	bi4-2	bi5-1	bi5-4	bi5-5	bi5-6	bi6-1	bi1	bi2	bi3	bi4	bi5	bi6
SiO ₂	31.83	34.37	34.05	34.43	33.80	34.55	32.93	33.95	34.05	34.54	34.50	33.29	33.30	35.06	35.01	34.07	34.21	33.95
TiO ₂	0.17	1.38	1.48	1.64	0.07	0.10	0.10	2.21	2.47	2.23	2.22	2.29	2.01	2.51	2.32	1.19	2.17	2.13
Al ₂ O ₃	19.13	18.30	17.84	17.96	19.10	19.44	19.17	16.63	16.62	16.42	16.25	16.62	15.78	16.00	16.17	16.24	16.28	15.94
Cr ₂ O ₃	0.02	0.06	0.06	0.07	0.06	0.02	0.02	0.00	0.00	0.04	0.02	0.00	0.01	0.00	0.06	0.00	0.01	0.04
Fe ₂ O ₃	4.24	0.00	2.04	1.39	3.48	2.56	4.12	0.06	0.00	0.17	1.88	1.37	4.30	0.00	1.29	4.01	2.49	4.03
FeO	21.62	21.79	20.46	20.87	20.24	20.41	21.01	22.20	22.74	22.43	21.22	22.01	21.91	22.19	22.85	20.46	22.27	20.64
MnO	0.46	0.31	0.36	0.35	0.45	0.36	0.52	0.36	0.42	0.39	0.41	0.37	0.31	0.22	0.25	0.21	0.29	0.27
MgO	9.62	8.24	8.52	8.58	7.93	8.05	8.29	8.39	8.10	8.48	8.77	8.13	9.13	8.06	8.31	8.88	8.06	8.67
CaO	0.10	0.00	0.05	0.05	0.05	0.03	0.01	0.03	0.13	0.13	0.06	0.00	0.01	0.00	0.02	0.15	0.00	0.02
Na ₂ O	0.06	0.06	0.05	0.05	0.10	0.05	0.05	0.02	0.07	0.03	0.08	0.01	0.01	0.01	0.05	0.04	0.05	0.05
K ₂ O	6.07	9.91	8.86	8.89	9.08	8.88	8.15	9.39	9.11	9.13	8.84	9.48	7.26	9.60	9.01	8.05	9.00	8.61
Totals	93.31	94.62	93.76	94.28	94.36	94.46	94.37	93.24	93.71	93.99	94.25	93.57	94.05	93.65	93.34	93.30	94.83	94.37
Si	2.512	2.687	2.673	2.685	2.645	2.683	2.583	2.704	2.701	2.750	2.708	2.656	2.630	2.773	2.728	2.696	2.689	2.670
Ti	0.010	0.093	0.087	0.096	0.004	0.006	0.006	0.132	0.147	0.132	0.131	0.137	0.119	0.149	0.136	0.071	0.128	0.126
Al IV	1.488	1.313	1.327	1.315	1.355	1.317	1.417	1.296	1.299	1.250	1.292	1.344	1.370	1.227	1.272	1.304	1.311	1.330
Cr	0.001	0.004	0.004	0.004	0.004	0.001	0.001	0.000	0.000	0.002	0.001	0.000	0.001	0.000	0.004	0.000	0.001	0.002
Al VI	0.292	0.374	0.324	0.336	0.407	0.463	0.356	0.263	0.253	0.277	0.211	0.219	0.099	0.263	0.214	0.211	0.197	0.148
Fe ₃	0.252	0.000	0.120	0.081	0.205	0.150	0.243	0.004	0.000	0.010	0.111	0.082	0.255	0.000	0.076	0.239	0.147	0.240
Fe ₂	1.427	1.425	1.343	1.361	1.325	1.326	1.379	1.478	1.509	1.480	1.393	1.469	1.447	1.468	1.489	1.354	1.463	1.357
Mn	0.031	0.021	0.024	0.023	0.030	0.024	0.035	0.024	0.028	0.026	0.027	0.025	0.021	0.015	0.017	0.014	0.019	0.018
Mg	1.131	0.960	0.997	0.997	0.925	0.932	0.969	0.996	0.958	0.997	1.026	0.967	1.077	0.950	0.965	1.047	0.944	1.016
Ca	0.008	0.000	0.004	0.004	0.004	0.002	0.001	0.003	0.011	0.011	0.005	0.000	0.001	0.000	0.002	0.013	0.000	0.002
Na	0.009	0.009	0.008	0.008	0.015	0.008	0.008	0.003	0.011	0.005	0.012	0.002	0.002	0.002	0.008	0.006	0.008	0.008
K	0.611	0.988	0.887	0.885	0.907	0.880	0.816	0.954	0.922	0.919	0.885	0.965	0.732	0.969	0.896	0.813	0.902	0.864
Sum	7.772	7.874	7.800	7.797	7.827	7.790	7.814	7.860	7.841	7.833	7.803	7.867	7.755	7.818	7.806	7.767	7.811	7.781

Analyses	Biotite Tonalite Protomylonite																			
	Sample PT8-06					Sample PT8-05														
	bi7	bi9	bi10-1	bi10-2	bi11	bi1-1	bi1-2	bi1-3	bi1-4	bi2-1	bi2-2	bi2-3	bi3-1	bi3-2	bi3-3	bi4-1	bi4-2	bi5-1	bi6-1	bi6-2
SiO ₂	33.36	33.27	34.06	34.34	34.49	33.98	34.51	33.88	33.06	34.52	34.48	32.76	35.19	34.78	34.05	32.88	32.58	34.53	34.47	34.28
TiO ₂	2.07	2.39	2.69	1.93	2.17	2.46	2.39	2.35	2.43	2.36	2.48	1.81	2.93	2.53	2.35	2.44	2.49	2.60	3.23	3.00
Al ₂ O ₃	16.39	16.10	15.28	16.13	14.96	15.60	15.36	15.91	15.79	15.64	15.36	15.79	16.68	16.45	16.28	16.41	15.91	16.71	15.36	15.29
Cr ₂ O ₃	0.00	0.00	0.00	0.00	0.01	0.04	0.03	0.01	0.04	0.03	0.02	0.01	0.00	0.00	0.02	0.03	0.00	0.00	0.00	0.01
Fe ₂ O ₃	1.93	0.74	0.10	0.36	0.97	0.00	0.00	4.57	4.34	1.63	0.00	4.73	0.00	0.00	0.00	3.06	4.38	0.00	0.00	0.00
FeO	21.98	23.54	24.35	23.55	24.49	25.76	26.12	23.30	22.14	24.48	25.67	24.11	23.83	24.57	24.27	22.58	22.31	23.84	26.05	26.17
MnO	0.23	0.18	0.19	0.23	0.28	0.18	0.22	0.19	0.24	0.23	0.17	0.17	0.21	0.18	0.21	0.22	0.20	0.22	0.16	0.22
MgO	7.99	7.50	7.58	7.91	7.50	6.36	6.51	6.92	7.95	7.15	6.83	6.97	6.53	6.46	6.52	6.99	7.07	6.33	6.28	6.12
CaO	0.04	0.00	0.00	0.01	0.00	0.11	0.11	0.05	0.05	0.10	0.09	0.02	0.05	0.07	0.09	0.07	0.03	0.14	0.01	0.09
Na ₂ O	0.03	0.05	0.08	0.04	0.03	0.10	0.07	0.07	0.09	0.03	0.05	0.08	0.04	0.06	0.04	0.02	0.08	0.05	0.04	0.12
K ₂ O	9.14	9.30	9.24	9.51	9.40	9.14	9.16	8.30	7.54	8.78	9.04	7.00	9.64	9.47	9.18	8.44	8.01	9.16	9.36	8.97
Totals	93.18	93.27	93.57	94.01	94.30	93.73	94.68	95.55	93.68	94.94	94.19	93.45	95.10	94.57	93.01	93.15	93.06	93.58	94.96	94.27
Si	2.671	2.676	2.733	2.731	2.755	2.738	2.753	2.662	2.632	2.728	2.757	2.635	2.758	2.753	2.741	2.642	2.624	2.750	2.742	2.747
Ti	0.125	0.160	0.160	0.120	0.130	0.150	0.155	0.140	0.150	0.140	0.150	0.110	0.170	0.150	0.140	0.150	0.150	0.150	0.190	0.180
Al _{IV}	1.329	1.324	1.267	1.269	1.245	1.262	1.247	1.338	1.368	1.272	1.243	1.365	1.242	1.247	1.259	1.358	1.376	1.250	1.238	1.253
Cr	0.000	0.000	0.000	0.000	0.001	0.003	0.002	0.001	0.003	0.002	0.001	0.001	0.000	0.000	0.001	0.002	0.000	0.000	0.000	0.001
Al _{VI}	0.218	0.203	0.178	0.243	0.164	0.220	0.198	0.136	0.114	0.185	0.205	0.132	0.299	0.288	0.286	0.196	0.135	0.319	0.183	0.192
Fe ₃	0.117	0.045	0.006	0.021	0.058	0.000	0.000	0.270	0.260	0.097	0.000	0.286	0.000	0.000	0.000	0.185	0.265	0.000	0.000	0.000
Fe ₂	1.472	1.584	1.634	1.566	1.636	1.736	1.743	1.531	1.474	1.618	1.716	1.622	1.562	1.627	1.634	1.517	1.503	1.588	1.733	1.754
Mn	0.016	0.012	0.013	0.015	0.019	0.012	0.015	0.013	0.016	0.015	0.012	0.012	0.014	0.012	0.014	0.015	0.014	0.015	0.011	0.013
Mg	0.933	0.899	0.906	0.938	0.893	0.764	0.774	0.810	0.943	0.842	0.814	0.835	0.763	0.762	0.782	0.837	0.849	0.751	0.745	0.731
Ca	0.003	0.000	0.000	0.001	0.000	0.009	0.009	0.004	0.004	0.008	0.008	0.002	0.004	0.006	0.008	0.006	0.003	0.012	0.001	0.008
Na	0.005	0.008	0.012	0.006	0.005	0.016	0.011	0.011	0.014	0.005	0.008	0.012	0.006	0.009	0.006	0.003	0.012	0.008	0.006	0.019
K	0.934	0.954	0.946	0.965	0.958	0.940	0.932	0.832	0.766	0.885	0.922	0.718	0.964	0.956	0.943	0.865	0.823	0.931	0.950	0.917
Sum	7.842	7.863	7.859	7.873	7.863	7.849	7.840	7.748	7.740	7.799	7.835	7.730	7.785	7.812	7.818	7.775	7.755	7.780	7.823	7.818

Analyses	Biotite Tonalite Protomylonite								
	Sample PT8-05								
	bi7-1	bi7-2	bi8-1	bi8-2	bi9-1	bi9-2	bi10	bi11-1	bi11-2
SiO ₂	34.58	34.48	34.73	33.16	34.64	34.53	34.72	34.52	34.60
TiO ₂	2.66	2.75	2.86	2.74	2.52	2.60	2.58	2.56	2.60
Al ₂ O ₃	16.35	15.96	15.84	15.65	16.24	15.95	16.02	16.05	16.36
Cr ₂ O ₃	0.00	0.03	0.02	0.00	0.02	0.01	0.01	0.01	0.00
Fe ₂ O ₃	0.00	0.00	0.00	4.39	0.00	0.00	0.00	0.00	0.00
FeO	25.30	25.50	25.06	22.40	24.51	25.33	25.23	24.95	25.04
MnO	0.19	0.20	0.20	0.29	0.21	0.23	0.16	0.25	0.21
MgO	6.57	6.54	6.47	7.60	6.89	6.80	6.90	6.62	6.32
CaO	0.00	0.00	0.01	0.05	0.00	0.00	0.00	0.00	0.00
Na ₂ O	0.03	0.06	0.07	0.03	0.01	0.04	0.03	0.03	0.05
K ₂ O	9.63	9.70	9.62	7.79	9.72	9.63	9.32	9.33	9.63
Totals	95.33	95.22	94.88	94.10	94.76	95.14	94.97	94.52	94.83
Si	2.729	2.732	2.733	2.635	2.742	2.735	2.745	2.745	2.742
Ti	0.160	0.160	0.170	0.160	0.150	0.160	0.150	0.150	0.150
Al IV	1.271	1.268	1.247	1.365	1.258	1.265	1.255	1.255	1.256
Cr	0.000	0.002	0.001	0.000	0.001	0.001	0.001	0.001	0.000
Al VI	0.250	0.223	0.233	0.101	0.257	0.224	0.238	0.296	0.271
Fe ₃	0.000	0.000	0.000	0.263	0.000	0.000	0.000	0.000	0.000
Fe ₂	1.670	1.690	1.661	1.488	1.623	1.678	1.668	1.659	1.660
Mn	0.013	0.013	0.013	0.020	0.014	0.015	0.011	0.017	0.014
Mg	0.773	0.772	0.764	0.900	0.813	0.803	0.813	0.784	0.747
Ca	0.000	0.000	0.001	0.004	0.000	0.000	0.000	0.000	0.000
Na	0.005	0.009	0.011	0.005	0.002	0.006	0.005	0.005	0.006
K	0.972	0.980	0.973	0.790	0.982	0.975	0.940	0.967	0.976
Sum	7.841	7.854	7.828	7.735	7.842	7.857	7.828	7.836	7.831

Representative major element analyses of chlorite.

Analyses	Garnet Granodiorite												Garnet Leucogranite				Biotite Tonalite				
	Sample PT15-08								Sample PT15-13				Sample PT30-04				Sample PT8-06				
	Propylitic alteration		Selective alteration of biotite						Selective alteration of garnet and biotite						Propylitic alteration	Selective alteration of biotite					
	Chl1-3	Chl1-4	Chl2-1	Chl2-2	Chl2-3	Chl2-4	Chl3-1	Chl3-2	Chl3-3	Chl4	Chl5	Chl6	Chl7	Chl8-1	Chl8-2	Chl8-3	Chl8	Chl1	Chl2	Chl3	Chl4
SiO ₂	24.45	24.90	25.44	25.63	26.49	25.41	27.04	26.65	28.51	25.73	26.16	26.38	24.41	24.28	26.84	24.25	23.72	24.47	24.79	24.51	24.71
TiO ₂	0.16	0.05	0.05	0.07	0.52	0.12	0.47	0.08	0.77	0.07	0.19	0.06	0.04	0.04	0.08	0.02	0.03	0.06	0.10	0.10	0.07
Al ₂ O ₃	19.25	19.81	18.46	17.87	17.68	19.12	17.60	17.37	15.74	19.90	17.98	19.21	19.44	21.14	24.89	21.72	18.73	19.85	19.75	19.85	18.22
Cr ₂ O ₃	0.03	0.02	0.01	0.00	0.00	0.00	0.00	0.00	0.02	0.05	0.03	0.02	0.03	0.00	0.00	0.03	0.00	0.00	0.00	0.00	0.01
Fe ₂ O ₃	0.00	0.00	0.73	1.33	0.31	0.60	0.00	0.00	0.00	0.00	0.00	0.00	0.00	0.00	0.00	0.00	1.47	0.55	0.20	0.29	0.42
FeO	28.22	28.22	29.93	28.25	29.29	28.63	27.97	29.75	29.04	29.39	29.02	28.04	30.41	30.67	25.85	30.58	31.01	29.65	30.05	30.33	29.87
MnO	0.76	0.77	0.70	0.72	0.58	0.75	0.53	0.66	0.52	0.59	0.64	0.66	0.74	0.72	0.54	0.62	0.48	0.48	0.47	0.44	0.49
MgO	11.98	12.51	12.08	13.12	12.01	12.82	11.23	12.66	11.53	11.33	11.93	11.80	9.97	10.41	8.68	10.39	10.03	11.65	11.69	11.33	11.50
CaO	0.20	0.06	0.04	0.02	0.03	0.02	0.10	0.07	0.10	0.14	0.06	0.17	0.15	0.04	0.04	0.05	0.03	0.04	0.03	0.03	0.00
Na ₂ O	0.01	0.02	0.01	0.04	0.02	0.00	0.00	0.03	0.04	0.03	0.00	0.05	0.05	0.01	0.04	0.00	0.02	0.00	0.00	0.03	0.00
K ₂ O	0.06	0.01	0.03	0.02	0.90	0.10	1.04	0.09	1.19	0.48	0.54	0.50	0.32	0.06	1.91	0.05	0.00	0.04	0.06	0.00	0.02
Totals	85.12	86.37	87.47	87.07	87.83	87.57	85.98	87.36	87.46	87.71	86.55	87.09	85.56	87.37	88.87	87.71	85.53	86.80	87.14	86.91	85.31
Si	2.726	2.725	2.780	2.796	2.877	2.752	2.975	2.901	3.098	2.787	2.874	2.876	2.742	2.658	2.802	2.639	2.686	2.689	2.713	2.696	2.772
Ti	0.013	0.004	0.004	0.006	0.042	0.010	0.039	0.007	0.063	0.006	0.016	0.005	0.003	0.003	0.006	0.002	0.003	0.005	0.008	0.008	0.006
Al _{IV}	1.274	1.275	1.220	1.204	1.123	1.248	1.025	1.099	0.902	1.213	1.126	1.124	1.258	1.342	1.198	1.361	1.314	1.311	1.287	1.304	1.228
Cr	0.003	0.002	0.001	0.000	0.000	0.000	0.000	0.000	0.002	0.004	0.003	0.002	0.003	0.000	0.000	0.003	0.000	0.000	0.000	0.000	0.001
Al _{VI}	1.271	1.273	1.219	1.204	1.123	1.248	1.025	1.099	0.900	1.209	1.123	1.122	1.255	1.342	1.198	1.358	1.187	1.261	1.262	1.270	1.182
Fe ₃	0.000	0.000	0.060	0.110	0.025	0.049	0.000	0.000	0.000	0.000	0.000	0.000	0.000	0.000	0.000	0.000	0.126	0.046	0.016	0.024	0.035
Fe ₂	2.631	2.583	2.735	2.577	2.661	2.594	2.573	2.708	2.639	2.662	2.666	2.537	2.857	2.808	2.257	2.783	2.938	2.725	2.751	2.790	2.800
Mn	0.072	0.071	0.065	0.067	0.053	0.069	0.049	0.061	0.048	0.054	0.060	0.060	0.070	0.067	0.048	0.057	0.046	0.045	0.044	0.041	0.047
Mg _o	1.990	2.040	1.967	2.133	1.944	2.069	1.841	2.054	1.867	1.829	1.953	1.903	1.669	1.699	1.350	1.685	1.693	1.908	1.907	1.857	1.923
Ca	0.024	0.007	0.005	0.002	0.003	0.002	0.012	0.008	0.012	0.016	0.007	0.020	0.018	0.005	0.004	0.006	0.004	0.005	0.004	0.004	0.000
Na	0.002	0.004	0.002	0.008	0.004	0.000	0.000	0.006	0.008	0.006	0.000	0.010	0.011	0.002	0.008	0.000	0.004	0.000	0.000	0.006	0.000
K	0.009	0.001	0.004	0.003	0.125	0.014	0.146	0.012	0.163	0.066	0.076	0.069	0.046	0.008	0.254	0.007	0.000	0.006	0.008	0.000	0.003
Sum	9.999	9.995	10.000	10.000	10.000	10.000	9.918	9.987	9.917	9.971	9.983	9.933	9.994	9.979	9.792	9.968	10.000	10.000	10.000	10.000	10.000

Analyses	Biotite Tonalite			Biotite Tonalite Protomylonite										Chlorite-Illite Phyllonite				
	Sample PT8-06		Sample PT12-08	Sample PT8-05										Sample RPT-2				
	Selective alteration of biotite			Selective alteration of biotite														
Analyses	ChI5-1	ChI5-2	ChI6	ChI1-1	ChI1-2	ChI1-3	ChI2	ChI3-1	ChI3-2	ChI4-1	ChI4-2	ChI5-1	ChI5-2	ChI1	ChI2	ChI3	ChI4	ChI5
SiO ₂	24.33	23.96	25.58	23.42	24.00	24.50	24.94	25.68	27.01	24.31	24.46	23.81	25.21	24.84	25.07	24.67	24.87	24.52
TiO ₂	0.19	0.12	0.07	0.13	0.11	0.16	0.12	0.86	0.38	0.11	0.11	0.07	0.07	0.05	0.04	0.06	0.02	0.01
Al ₂ O ₃	19.98	19.89	19.36	20.03	19.11	20.35	18.91	16.97	16.44	19.19	19.13	19.98	17.36	20.38	20.51	19.84	20.13	20.03
Cr ₂ O ₃	0.00	0.02	0.00	0.03	0.03	0.00	0.02	0.01	0.03	0.00	0.00	0.03	0.01	0.00	0.01	0.00	0.00	0.00
Fe ₂ O ₃	0.00	0.50	0.00	0.94	0.51	0.00	0.27	0.00	0.00	1.21	0.77	0.00	0.82	0.00	0.00	0.00	0.00	0.00
FeO	30.17	29.76	28.33	30.99	32.58	32.76	32.79	32.52	33.84	33.09	33.27	33.44	32.63	27.07	27.61	28.16	27.46	27.51
MnO	0.41	0.44	0.68	0.46	0.40	0.35	0.37	0.35	0.30	0.45	0.40	0.46	0.41	2.34	2.25	2.36	2.32	2.12
MgO	11.37	11.17	12.82	9.58	9.31	9.38	10.09	9.49	9.95	9.64	9.60	8.83	10.26	11.89	11.88	11.27	11.67	11.13
CaO	0.05	0.04	0.01	0.27	0.03	0.05	0.06	0.53	0.10	0.01	0.04	0.03	0.05	0.04	0.01	0.02	0.03	0.05
Na ₂ O	0.00	0.00	0.00	0.06	0.03	0.01	0.05	0.00	0.00	0.01	0.00	0.00	0.03	0.03	0.04	0.00	0.02	0.00
K ₂ O	0.00	0.03	0.05	0.08	0.08	0.06	0.04	0.77	0.60	0.00	0.03	0.01	0.02	0.05	0.03	0.03	0.02	0.02
Totals	86.50	85.93	86.90	85.98	86.19	87.82	87.67	87.18	88.65	88.02	87.81	86.66	86.87	86.69	87.45	86.41	86.34	85.39
Si	2.685	2.666	2.778	2.633	2.707	2.694	2.755	2.868	2.964	2.690	2.711	2.674	2.819	2.712	2.715	2.722	2.725	2.726
Ti	0.016	0.010	0.006	0.011	0.009	0.013	0.010	0.072	0.031	0.009	0.009	0.006	0.006	0.004	0.003	0.005	0.002	0.001
Al IV	1.315	1.334	1.222	1.367	1.293	1.306	1.245	1.132	1.036	1.310	1.289	1.326	1.181	1.288	1.285	1.278	1.275	1.274
Cr	0.000	0.002	0.000	0.003	0.003	0.000	0.002	0.001	0.003	0.000	0.000	0.003	0.001	0.000	0.001	0.000	0.000	0.000
Al VI	1.285	1.275	1.257	1.288	1.248	1.332	1.217	1.102	1.091	1.193	1.211	1.348	1.638	1.335	1.334	1.302	1.326	1.351
Fe ₃	0.000	0.042	0.000	0.079	0.043	0.000	0.023	0.000	0.000	0.101	0.064	0.000	0.069	0.000	0.000	0.000	0.000	0.000
Fe ₂	2.785	2.769	2.573	2.913	3.073	3.013	3.029	3.037	3.106	3.062	3.084	3.141	3.052	2.472	2.501	2.598	2.517	2.558
Mn	0.038	0.041	0.063	0.044	0.038	0.033	0.035	0.033	0.028	0.042	0.038	0.044	0.039	0.216	0.206	0.221	0.213	0.200
Mg	1.870	1.852	2.075	1.605	1.565	1.570	1.661	1.579	1.627	1.590	1.586	1.478	1.710	1.934	1.918	1.853	1.906	1.844
Ca	0.006	0.005	0.001	0.033	0.004	0.006	0.007	0.063	0.012	0.001	0.005	0.004	0.006	0.005	0.001	0.002	0.004	0.006
Na	0.000	0.000	0.000	0.013	0.007	0.002	0.011	0.000	0.000	0.002	0.000	0.000	0.007	0.006	0.008	0.000	0.004	0.000
K	0.000	0.004	0.007	0.011	0.012	0.008	0.006	0.110	0.084	0.000	0.004	0.001	0.003	0.007	0.004	0.004	0.003	0.003
Sum	9.999	10.000	9.981	10.000	10.000	9.978	10.000	9.998	9.982	10.000	10.000	9.996	10.000	9.979	9.978	9.985	9.976	9.962

Representative major elements analyses of illite.

Analysis	Garnet Granodiorite																Garnet Leucogranite			
	Sample PT13-13				Sample PT15-08												Sample PT30-04			
	Selective alteration of feldspars and micas																	Selective alteration of garnet		
	mu1	mu2-1	mu2-2	mu3	mu4-1	mu4-2	mu4-3	mu4-4	mu4-5	mu4-6	mu5-1	mu5-2	mu5-3	mu5-4	mu5-6	mu5-7	mu5-8	mu6-1	mu6-2	mu7-1
SiO ₂	43.64	44.97	46.18	44.49	41.19	42.07	43.39	43.38	44.26	44.12	46.49	46.62	46.26	44.37	43.56	44.44	43.57	44.74	46.36	44.68
TiO ₂	0.03	0.02	0.03	1.00	0.77	0.73	1.42	0.62	0.39	0.59	0.24	0.22	0.25	1.26	1.03	0.06	1.29	0.09	0.12	0.04
Al ₂ O ₃	31.89	31.41	32.11	30.13	31.93	32.32	31.62	32.48	32.01	31.87	30.97	31.19	31.13	30.21	31.64	31.65	31.50	34.19	33.76	32.27
Cr ₂ O ₃	0.01	0.02	0.00	0.02	0.01	0.00	0.00	0.01	0.04	0.00	0.00	0.01	0.00	0.00	0.02	0.00	0.01	0.00	0.00	0.02
Fe ₂ O ₃	0.31	3.47	0.00	2.95	3.43	3.61	2.75	3.57	3.30	3.04	1.26	0.01	1.30	1.53	3.35	2.59	2.23	2.17	0.69	2.61
FeO	3.00	1.34	2.61	1.62	1.32	1.39	1.77	1.38	1.27	1.79	2.90	3.38	2.68	3.07	1.66	1.69	1.78	0.84	1.90	1.53
MnO	0.16	0.18	0.06	0.07	0.05	0.01	0.05	0.05	0.00	0.04	0.04	0.04	0.02	0.03	0.00	0.00	0.03	0.05	0.05	0.07
MgO	1.22	1.70	1.12	1.75	1.19	1.11	1.06	1.09	1.09	1.10	1.48	1.40	1.42	1.27	1.10	1.28	1.23	1.67	1.36	1.39
CaO	0.00	0.04	0.00	0.04	0.04	0.00	0.00	0.03	0.03	0.00	0.00	0.00	0.00	0.01	0.02	0.00	0.00	0.01	0.00	0.01
Na ₂ O	0.16	0.16	0.18	0.18	0.32	0.42	0.25	0.39	0.29	0.31	0.25	0.29	0.22	0.22	0.35	0.22	0.13	0.24	0.18	0.19
K ₂ O	11.34	10.93	11.19	10.76	10.47	10.34	10.55	10.36	10.00	10.77	10.99	10.92	10.83	10.82	10.55	10.83	10.76	10.62	11.23	11.29
Totals	93.76	94.24	93.48	93.02	90.72	92.00	92.86	93.36	92.68	93.62	94.63	94.08	94.11	92.78	93.28	92.76	92.52	94.62	93.83	94.10
Si	3.139	3.083	3.167	3.093	2.945	2.961	3.021	3.001	3.065	3.047	3.167	3.186	3.162	3.101	3.022	3.088	3.040	3.023	3.108	3.067
Ti	0.002	0.001	0.002	0.052	0.041	0.039	0.074	0.032	0.020	0.031	0.012	0.011	0.013	0.066	0.054	0.003	0.068	0.005	0.006	0.002
Al _{IV}	0.861	0.917	0.833	0.907	1.053	1.039	0.979	0.999	0.935	0.933	0.833	0.814	0.838	0.899	0.978	0.912	0.960	0.977	0.892	0.933
Cr	0.001	0.001	0.000	0.001	0.001	0.000	0.000	0.001	0.002	0.000	0.000	0.001	0.000	0.000	0.001	0.000	0.001	0.000	0.000	0.001
Al _{VII}	1.725	1.622	1.763	1.562	1.637	1.643	1.616	1.650	1.678	1.642	1.655	1.699	1.671	1.590	1.610	1.681	1.631	1.747	1.765	1.678
Fe ₃	0.016	0.179	0.000	0.155	0.185	0.191	0.144	0.186	0.172	0.158	0.065	0.000	0.067	0.080	0.175	0.135	0.117	0.110	0.035	0.135
Fe ₂	0.173	0.077	0.150	0.094	0.079	0.082	0.103	0.080	0.074	0.103	0.165	0.193	0.153	0.179	0.096	0.098	0.104	0.047	0.106	0.088
Mn	0.009	0.010	0.003	0.004	0.003	0.001	0.003	0.003	0.000	0.002	0.002	0.002	0.001	0.002	0.000	0.000	0.002	0.003	0.003	0.004
Mg	0.125	0.174	0.114	0.181	0.127	0.116	0.110	0.112	0.112	0.113	0.150	0.143	0.145	0.132	0.114	0.133	0.128	0.168	0.135	0.142
Ca	0.000	0.003	0.000	0.003	0.003	0.000	0.000	0.002	0.002	0.000	0.000	0.000	0.000	0.001	0.001	0.000	0.001	0.001	0.000	0.001
Na	0.021	0.021	0.024	0.024	0.044	0.057	0.034	0.052	0.039	0.042	0.033	0.038	0.029	0.030	0.047	0.030	0.018	0.031	0.023	0.025
K	0.995	0.956	0.979	0.954	0.955	0.928	0.937	0.914	0.883	0.949	0.955	0.952	0.945	0.965	0.934	0.960	0.958	0.916	0.956	0.989
Sum	7.067	7.045	7.036	7.032	7.075	7.058	7.021	7.033	6.983	7.041	7.039	7.041	7.024	7.026	7.033	7.040	7.026	7.029	7.030	7.065

Analyses	Garnet Leucogranite							Biotite Tonalite												
	Sample PT30-04			Sample PT12-08																
	Selective alteration of garnet		Selective alteration of feldspar and mica							Infilling alteration										
	mu7-2	mu7-3	mu1	mu2	mu3	mu4	mu5	mu6	mu7	mu8	mu9	mu10	mu11-1	mu11-2	mu11-3	mu12-1	mu12-2	mu12-3	mu12-4	mu13
SiO ₂	47.09	46.92	47.52	47.32	46.31	46.66	48.16	46.26	47.46	47.16	47.26	45.25	46.73	46.47	46.80	46.11	46.06	46.23	46.50	50.15
TiO ₂	0.04	0.01	0.22	0.25	0.30	0.33	0.18	0.34	0.43	0.20	0.21	0.18	0.18	0.18	0.15	0.34	0.08	0.32	0.10	0.10
Al ₂ O ₃	31.39	33.05	31.21	29.37	29.74	30.29	28.54	29.87	30.42	31.69	30.30	30.71	30.41	29.83	30.75	30.10	30.85	31.29	30.84	28.89
Cr ₂ O ₃	0.05	0.06	0.01	0.01	0.01	0.00	0.00	0.04	0.00	0.00	0.00	0.01	0.00	0.01	0.00	0.02	0.00	0.00	0.02	0.00
Fe ₂ O ₃	0.00	1.62	0.31	0.00	2.40	1.02	0.69	0.97	0.00	0.00	1.48	1.55	2.48	1.82	2.44	2.39	1.02	2.21	0.00	0.00
FeO	3.02	1.82	2.10	2.62	2.02	2.58	3.18	2.92	3.20	1.92	2.62	2.16	2.49	2.19	2.23	1.85	1.98	2.55	1.87	3.23
MnO	0.10	0.06	0.02	0.07	0.06	0.02	0.08	0.04	0.02	0.00	0.04	0.04	0.02	0.08	0.02	0.05	0.01	0.00	0.04	0.03
MgO	1.35	1.44	2.12	2.22	1.93	1.82	2.17	1.72	1.57	1.73	2.04	1.64	1.87	1.93	1.77	1.88	1.63	1.60	1.79	1.33
CaO	0.02	0.02	0.01	0.00	0.09	0.08	0.05	0.01	0.03	0.02	0.08	0.05	0.01	0.00	0.00	0.13	0.10	0.07	0.03	0.08
Na ₂ O	0.17	0.17	0.18	0.15	0.14	0.10	0.09	0.10	0.11	0.19	0.11	0.14	0.14	0.17	0.10	0.11	0.12	0.13	0.10	2.16
K ₂ O	11.16	11.17	10.92	10.68	10.69	10.81	10.70	10.98	10.76	10.79	10.77	10.88	11.14	11.06	11.04	10.65	10.79	11.02	10.97	9.24
Totals	94.39	96.34	94.62	92.69	93.69	93.71	93.84	93.25	94.00	93.70	93.43	92.54	94.54	94.40	94.68	93.67	94.01	94.23	94.47	95.21
Si	3.196	3.124	3.207	3.264	3.183	3.198	3.295	3.197	3.235	3.204	3.234	3.147	3.185	3.180	3.179	3.167	3.153	3.155	3.165	3.357
Ti	0.002	0.001	0.011	0.013	0.016	0.017	0.009	0.018	0.022	0.010	0.011	0.009	0.009	0.009	0.008	0.018	0.004	0.016	0.005	0.005
Al IV	0.804	0.876	0.793	0.736	0.817	0.802	0.703	0.803	0.765	0.796	0.766	0.853	0.815	0.820	0.821	0.833	0.847	0.845	0.835	0.643
Cr	0.003	0.003	0.001	0.001	0.001	0.000	0.000	0.002	0.000	0.000	0.000	0.001	0.000	0.000	0.001	0.000	0.000	0.000	0.001	0.000
Al VI	1.723	1.718	1.690	1.652	1.593	1.645	1.597	1.631	1.679	1.742	1.678	1.665	1.629	1.586	1.642	1.604	1.643	1.673	1.640	1.637
Fe ₃	0.000	0.081	0.016	0.000	0.124	0.053	0.036	0.050	0.000	0.000	0.000	0.077	0.079	0.128	0.093	0.126	0.123	0.052	0.113	0.000
Fe ₂	0.171	0.101	0.119	0.151	0.116	0.148	0.182	0.169	0.182	0.109	0.150	0.126	0.142	0.125	0.127	0.106	0.113	0.146	0.107	0.181
Mn	0.006	0.003	0.001	0.004	0.003	0.001	0.005	0.002	0.001	0.000	0.002	0.002	0.001	0.005	0.001	0.003	0.001	0.000	0.002	0.002
Mg	0.137	0.143	0.213	0.228	0.198	0.186	0.221	0.177	0.159	0.175	0.208	0.170	0.190	0.197	0.179	0.192	0.166	0.163	0.182	0.133
Ca	0.001	0.001	0.001	0.000	0.007	0.006	0.004	0.001	0.002	0.001	0.006	0.004	0.001	0.000	0.000	0.010	0.007	0.005	0.002	0.006
Na	0.022	0.022	0.024	0.020	0.019	0.013	0.012	0.013	0.015	0.025	0.015	0.019	0.019	0.023	0.013	0.015	0.016	0.017	0.013	0.280
K	0.966	0.949	0.940	0.940	0.937	0.945	0.934	0.968	0.936	0.935	0.940	0.965	0.965	0.957	0.933	0.942	0.960	0.953	0.789	
Sum	7.032	7.023	7.013	7.009	7.013	7.015	7.000	7.033	6.997	6.998	7.011	7.039	7.039	7.039	7.021	7.008	7.016	7.033	7.019	7.033

Analyses	Biotite Tonalite												Illite Granodiorite Mylonite											
	Sample PT12-08												Sample PT2-05											
	Infilling alteration																							
	mu14-1	mu14-2	mu15	mu16-1	mu16-2	mu16-3	mu16-4	mu16-5	mu17-1	mu17-2	mu17-3	mu1-1	mu1-2	mu1-3	mu2-1	mu2-2	mu2-3	mu2-4	mu3-1	mu3-2				
SiO ₂	45.68	46.15	45.08	44.95	46.36	46.04	46.44	47.11	44.46	45.01	44.70	46.71	46.80	48.13	46.65	47.34	46.87	46.56	46.32	47.41				
TiO ₂	0.33	0.44	1.11	0.04	0.07	0.80	0.01	0.09	0.10	0.11	0.01	0.23	0.06	0.09	0.12	0.07	0.07	0.07	0.21	0.10				
Al ₂ O ₃	32.38	30.79	31.64	31.48	32.47	30.59	31.49	29.14	31.17	31.99	31.86	31.10	30.72	31.18	31.11	30.56	29.76	30.95	31.72	31.10				
Cr ₂ O ₃	0.03	0.00	0.01	0.00	0.02	0.03	0.01	0.00	0.01	0.00	0.02	0.00	0.02	0.01	0.01	0.00	0.00	0.00	0.00	0.00				
Fe ₂ O ₃	1.30	2.45	0.59	3.73	0.72	2.91	1.94	3.83	4.26	2.40	2.31	0.92	2.54	0.00	0.35	0.20	0.93	0.83	1.30	0.00				
FeO	2.28	1.88	3.00	1.44	2.78	1.90	2.41	1.68	1.64	1.55	1.34	2.71	1.35	2.92	2.88	3.32	2.89	2.84	2.41	3.34				
MnO	0.05	0.04	0.05	0.00	0.00	0.04	0.02	0.05	0.05	0.02	0.02	0.01	0.04	0.07	0.06	0.00	0.03	0.02	0.05	0.02				
MgO	1.11	1.69	1.12	1.32	1.12	1.74	1.33	2.27	1.47	1.31	1.17	1.58	1.83	1.69	1.61	1.65	1.74	1.58	1.36	1.40				
CaO	0.00	0.00	0.00	0.05	0.00	0.00	0.03	0.00	0.00	0.00	0.00	0.01	0.05	0.00	0.01	0.02	0.01	0.13	0.01	0.00				
Na ₂ O	0.14	0.12	0.20	0.24	0.17	0.13	0.24	0.15	0.18	0.23	0.22	0.10	0.18	0.15	0.18	0.18	0.08	0.15	0.18	0.16				
K ₂ O	10.86	10.89	10.85	10.64	11.01	11.01	10.74	11.09	10.81	10.70	10.82	11.04	10.31	10.99	11.04	10.89	10.80	10.87	10.86	10.86				
Totals	94.16	94.46	93.65	93.89	94.72	95.19	94.65	95.40	94.15	93.32	93.47	94.41	93.90	95.23	94.01	94.43	93.18	94.00	94.82	94.39				
Si	3.115	3.146	3.103	3.089	3.143	3.125	3.155	3.194	3.063	3.099	3.070	3.180	3.186	3.234	3.188	3.231	3.232	3.184	3.152	3.220				
Ti	0.017	0.023	0.057	0.002	0.004	0.041	0.001	0.005	0.005	0.006	0.001	0.012	0.003	0.005	0.006	0.004	0.004	0.004	0.011	0.003				
Al IV	0.885	0.854	0.897	0.911	0.857	0.875	0.845	0.806	0.937	0.901	0.930	0.820	0.814	0.766	0.812	0.769	0.768	0.816	0.848	0.780				
Cr	0.002	0.000	0.001	0.000	0.001	0.002	0.001	0.000	0.001	0.000	0.001	0.000	0.001	0.001	0.000	0.000	0.000	0.000	0.000	0.000				
Al VI	1.719	1.620	1.671	1.639	1.738	1.573	1.677	1.523	1.394	1.695	1.731	1.676	1.651	1.704	1.694	1.680	1.651	1.679	1.686	1.710				
Fe ₃	0.067	0.126	0.031	0.193	0.037	0.149	0.099	0.195	0.221	0.124	0.119	0.047	0.130	0.000	0.018	0.010	0.048	0.043	0.077	0.000				
Fe ₂	0.130	0.107	0.172	0.083	0.158	0.108	0.137	0.095	0.095	0.089	0.077	0.154	0.077	0.164	0.164	0.189	0.167	0.162	0.137	0.190				
Mn	0.003	0.002	0.003	0.000	0.000	0.002	0.001	0.003	0.003	0.001	0.001	0.001	0.002	0.004	0.003	0.000	0.002	0.001	0.003	0.001				
Mg	0.113	0.172	0.115	0.135	0.113	0.176	0.135	0.229	0.151	0.134	0.120	0.160	0.186	0.169	0.164	0.167	0.179	0.161	0.137	0.142				
Ca	0.000	0.000	0.000	0.004	0.000	0.000	0.002	0.000	0.000	0.000	0.000	0.001	0.004	0.000	0.001	0.001	0.001	0.010	0.001	0.000				
Na	0.019	0.016	0.027	0.032	0.022	0.017	0.032	0.020	0.024	0.031	0.029	0.013	0.024	0.020	0.024	0.024	0.011	0.020	0.024	0.021				
K	0.945	0.947	0.953	0.933	0.952	0.953	0.931	0.959	0.950	0.940	0.948	0.959	0.895	0.942	0.962	0.944	0.950	0.948	0.939	0.941				
Sum	7.014	7.014	7.030	7.021	7.025	7.020	7.015	7.030	7.044	7.021	7.028	7.023	6.973	7.008	7.038	7.020	7.012	7.028	7.014	7.011				

Chlorite-Illite Phyllonite			
Sample RPT-2			
Analyses	mu5	mu6	mu7
SiO ₂	48.83	46.68	45.05
TiO ₂	0.05	0.04	0.05
Al ₂ O ₃	28.35	29.78	31.73
Cr ₂ O ₃	0.00	0.00	0.00
Fe ₂ O ₃	0.00	0.17	1.72
FeO	2.87	2.50	1.91
MnO	0.07	0.09	0.09
MgO	2.55	2.18	1.27
CaO	0.00	0.01	0.01
Na ₂ O	0.13	0.13	0.10
K ₂ O	10.81	10.99	10.86
Totals	93.66	92.57	92.79
Si	3.333	3.233	3.120
Ti	0.003	0.002	0.003
Al IV	0.667	0.767	0.880
Cr	0.000	0.000	0.000
Al VI	1.614	1.664	1.711
Fe3	0.000	0.009	0.090
Fe2	0.164	0.143	0.111
Mn	0.004	0.005	0.005
Mg	0.259	0.225	0.131
Ca	0.000	0.001	0.001
Na	0.017	0.017	0.013
K	0.941	0.971	0.960
Sum	7.004	7.040	7.024

Analyses	Illite granodiorite mylonite															Chlorite-Illite Phyllonite					
	Sample PT12-05															Sample RPT-2					
	mu3-3	mu4-1	mu4-2	mu4-3	mu5-1	mu5-2	mu5-3	mu5-4	mu6	mu7-1	mu7-2	mu7-3	mu8-1	mu8-2	mu9-1	mu9-2	mu10	mu1	mu2	mu3	mu4
SiO ₂	47.20	48.21	46.68	49.16	47.30	46.78	51.65	47.40	50.59	50.77	47.33	46.65	46.36	46.46	49.66	48.14	49.79	48.20	47.58	45.86	47.20
TiO ₂	0.05	0.20	0.15	0.25	0.31	0.50	0.37	0.23	0.17	0.09	0.07	0.08	0.09	0.06	0.01	0.06	0.10	0.13	0.21	0.11	0.10
Al ₂ O ₃	30.79	29.76	30.77	29.01	30.50	29.60	27.70	29.64	28.40	27.63	30.03	30.05	30.10	30.22	32.23	30.79	29.63	29.76	30.43	29.62	30.59
Cr ₂ O ₃	0.00	0.00	0.00	0.00	0.00	0.03	0.00	0.01	0.00	0.00	0.01	0.00	0.00	0.00	0.00	0.01	0.00	0.00	0.00	0.00	0.00
Fe ₂ O ₃	0.00	0.33	3.00	0.00	0.00	0.00	0.00	0.42	0.00	0.00	0.00	2.89	2.11	2.30	0.00	0.00	0.00	0.00	0.32	3.81	0.01
FeO	3.13	3.25	1.33	3.27	3.32	3.40	3.37	3.47	2.62	3.83	3.61	2.13	2.38	2.37	1.50	2.14	3.28	2.83	2.23	1.49	3.00
MnO	0.03	0.06	0.03	0.00	0.04	0.04	0.05	0.02	0.01	0.00	0.03	0.03	0.02	0.08	0.02	0.00	0.04	0.07	0.02	0.15	0.02
MgO	1.23	1.82	1.79	1.58	1.67	1.84	1.50	1.66	1.34	1.78	1.70	1.88	1.89	1.74	1.21	1.43	1.59	1.96	2.23	1.92	1.74
CaO	0.04	0.04	0.05	0.03	0.00	0.04	0.01	0.00	0.07	0.06	0.07	0.02	0.01	0.06	0.04	0.07	0.07	0.00	0.00	0.00	0.00
Na ₂ O	0.51	0.07	0.15	0.11	0.13	0.13	0.11	0.14	0.76	0.14	0.16	0.15	0.14	0.20	0.16	0.26	0.20	0.12	0.17	0.11	0.12
K ₂ O	10.71	10.70	10.43	10.66	11.08	10.94	10.27	10.73	8.40	10.34	11.05	11.09	11.16	10.93	10.88	9.73	10.25	11.01	10.83	11.02	10.90
Totals	93.69	94.44	94.40	94.07	94.35	93.30	95.03	93.71	92.36	94.64	94.06	94.97	94.46	94.42	93.71	92.63	94.93	94.08	94.02	94.09	93.68
Si	3.229	3.271	3.168	3.338	3.222	3.227	3.452	3.250	3.435	3.422	3.239	3.174	3.182	3.176	3.280	3.283	3.338	3.279	3.232	3.154	3.228
Ti	0.003	0.010	0.008	0.013	0.016	0.026	0.019	0.012	0.009	0.005	0.004	0.004	0.005	0.003	0.000	0.003	0.005	0.007	0.011	0.006	0.005
Al _{IV}	0.771	0.729	0.832	0.662	0.778	0.773	0.548	0.750	0.365	0.378	0.761	0.826	0.818	0.824	0.720	0.717	0.662	0.721	0.768	0.846	0.772
Cr	0.000	0.000	0.000	0.000	0.002	0.000	0.001	0.000	0.000	0.001	0.000	0.000	0.000	0.000	0.000	0.001	0.000	0.000	0.000	0.000	0.000
Al _{VI}	1.713	1.651	1.630	1.660	1.671	1.634	1.634	1.646	1.708	1.618	1.662	1.584	1.607	1.611	1.790	1.759	1.680	1.666	1.669	1.556	1.694
Fe ₃	0.000	0.017	0.153	0.000	0.000	0.000	0.000	0.021	0.000	0.000	0.000	0.148	0.109	0.118	0.000	0.000	0.000	0.000	0.016	0.197	0.001
Fe ₂	0.179	0.185	0.073	0.186	0.189	0.196	0.188	0.199	0.149	0.216	0.207	0.121	0.136	0.136	0.083	0.122	0.184	0.161	0.127	0.086	0.171
Mn	0.002	0.003	0.002	0.000	0.002	0.002	0.003	0.001	0.001	0.000	0.002	0.002	0.001	0.005	0.001	0.000	0.002	0.004	0.001	0.009	0.001
Mg	0.125	0.184	0.181	0.160	0.170	0.189	0.149	0.170	0.136	0.179	0.173	0.191	0.192	0.177	0.119	0.145	0.159	0.199	0.226	0.197	0.177
Ca	0.003	0.003	0.004	0.002	0.000	0.003	0.001	0.000	0.005	0.004	0.005	0.001	0.001	0.004	0.003	0.005	0.005	0.000	0.000	0.000	0.000
Na	0.068	0.009	0.020	0.014	0.017	0.017	0.014	0.019	0.100	0.018	0.021	0.020	0.019	0.027	0.020	0.034	0.026	0.016	0.022	0.015	0.016
K	0.935	0.926	0.905	0.923	0.963	0.963	0.876	0.939	0.728	0.889	0.965	0.963	0.973	0.953	0.917	0.847	0.877	0.955	0.939	0.967	0.951
Sum	7.028	6.989	6.979	6.958	7.028	7.033	6.884	7.008	6.834	6.930	7.039	7.035	7.043	7.035	6.934	6.917	6.938	7.008	7.012	7.032	7.018

Representative major element analyses of muscovite.

Garnet Leucogranite			
	Sample PT30-04		
	Disseminated alteration as coarse muscovite		
Analyses	mu11-3	mu11-4	mu11-5
SiO ₂	43.29	43.84	43.86
TiO ₂	0.17	0.14	0.20
Al ₂ O ₃	36.13	35.71	36.51
Cr ₂ O ₃	0.01	0.00	0.02
Fe ₂ O ₃	0.00	0.00	0.00
FeO	1.64	1.54	1.58
MnO	0.00	0.03	0.00
MgO	0.61	0.62	0.55
CaO	0.01	0.00	0.00
Na ₂ O	0.43	0.56	0.54
K ₂ O	10.81	10.89	10.69
Totals	95.12	95.33	95.93
Si	3.031	3.060	3.037
Ti	0.009	0.007	0.01
Al/IV	0.969	0.940	0.963
Cr	0.001	0.000	0.001
Al/VI	1.882	1.871	1.888
Fe3	0.000	0.000	0.000
Fe2	0.092	0.086	0.088
Mn	0.000	0.002	0.000
Mg	0.061	0.062	0.054
Ca	0.001	0.000	0.000
Na	0.058	0.072	0.069
K	0.923	0.928	0.903
Sum	7.026	7.028	7.014

Analyses	Garnet Granodiorite								Garnet Leucogranite													
	Sample PT15-13								Sample PT30-04													
	Selective alteration of garnet												Disseminated alteration as coarse muscovite									
Analyses	mu1-1	mu1-2	mu2-1	mu2-2	mu3	mu4	mu5	mu6	mu7-1	mu7-2	mu8-2	mu9-1	mu9-2	mu9-3	mu10-1	mu10-2	mu10-3	mu10-4	mu10-5	mu10-6	mu11-1	mu11-2
SiO ₂	45.37	45.56	44.81	45.35	44.58	45.35	45.04	45.49	44.88	45.19	46.29	45.26	46.72	46.30	45.36	46.40	45.38	45.35	45.83	45.83	46.05	45.89
TiO ₂	0.04	0.00	0.00	0.04	0.03	0.04	0.00	0.00	0.03	0.02	0.05	0.02	0.00	0.05	0.05	0.02	0.02	0.00	0.05	0.02	0.19	0.29
Al ₂ O ₃	34.27	33.74	33.92	32.80	34.37	32.81	35.76	36.06	36.66	35.55	35.66	36.70	35.14	36.01	36.63	35.79	36.09	36.51	36.35	36.29	35.78	35.75
Cr ₂ O ₃	0.03	0.04	0.04	0.03	0.03	0.03	0.00	0.02	0.03	0.01	0.01	0.00	0.00	0.00	0.00	0.04	0.00	0.00	0.01	0.01	0.00	0.00
Fe ₂ O ₃	0.00	0.00	0.00	0.00	0.00	0.00	0.00	0.00	1.22	0.00	0.00	1.38	0.00	0.37	0.00	0.00	0.00	0.00	0.00	0.00	0.00	0.00
FeO	2.26	2.59	2.20	2.76	2.48	2.60	1.93	1.87	0.92	1.90	1.84	0.65	1.91	1.59	1.55	1.56	1.62	1.67	1.58	1.50	1.68	1.55
MnO	0.04	0.06	0.00	0.02	0.00	0.04	0.00	0.00	0.01	0.03	0.00	0.00	0.02	0.01	0.03	0.03	0.02	0.00	0.04	0.02	0.03	0.04
MgO	0.55	0.83	0.73	0.91	0.69	0.88	0.56	0.56	0.72	0.48	0.67	0.71	0.75	0.68	0.59	0.76	0.62	0.64	0.69	0.70	0.60	0.60
CaO	0.00	0.00	0.00	0.01	0.03	0.00	0.02	0.00	0.00	0.08	0.00	0.03	0.04	0.05	0.02	0.00	0.00	0.00	0.00	0.00	0.00	0.01
Na ₂ O	0.35	0.38	0.48	0.22	0.34	0.23	0.59	0.50	0.37	0.33	0.42	0.57	0.40	0.38	0.48	0.47	0.53	0.53	0.34	0.33	0.30	0.48
K ₂ O	11.14	11.14	10.90	11.30	11.14	11.15	10.79	11.00	11.05	10.60	10.54	10.33	10.58	10.46	10.79	11.01	10.89	11.01	11.15	10.77	11.10	10.89
Totals	94.05	94.34	93.08	93.64	93.69	93.13	94.69	95.30	95.91	94.19	95.48	95.63	95.36	95.90	95.70	96.08	95.37	95.91	96.04	95.67	95.73	95.50
Si	3.088	3.098	3.081	3.125	3.054	3.124	3.035	3.039	2.986	3.054	3.079	3.003	3.105	3.064	3.027	3.073	3.043	3.027	3.040	3.045	3.063	3.058
Ti	0.002	0.00	0.00	0.00	0.00	0.00	0.00	0.00	0.00	0.00	0.00	0.00	0.00	0.00	0.002	0.001	0.001	0.00	0.002	0.001	0.01	0.015
Al IV	0.912	0.902	0.919	0.875	0.946	0.876	0.965	0.961	1.014	0.946	0.921	0.997	0.895	0.936	0.973	0.927	0.957	0.973	0.960	0.955	0.937	0.942
Cr	0.002	0.002	0.002	0.002	0.002	0.002	0.000	0.001	0.003	0.001	0.001	0.000	0.000	0.000	0.000	0.002	0.000	0.000	0.001	0.001	0.000	0.000
Al VI	1.838	1.803	1.830	1.778	1.829	1.788	1.876	1.879	1.862	1.886	1.875	1.874	1.859	1.874	1.897	1.867	1.884	1.887	1.882	1.887	1.869	1.866
Fe ₃	0.000	0.000	0.000	0.000	0.000	0.000	0.000	0.000	0.061	0.000	0.000	0.069	0.000	0.018	0.000	0.000	0.000	0.000	0.000	0.000	0.000	0.000
Fe ₂	0.129	0.147	0.126	0.158	0.142	0.130	0.109	0.104	0.051	0.107	0.102	0.036	0.106	0.088	0.086	0.086	0.090	0.093	0.088	0.083	0.093	0.086
Mn	0.002	0.003	0.000	0.001	0.000	0.002	0.000	0.000	0.001	0.002	0.000	0.000	0.001	0.001	0.002	0.002	0.001	0.000	0.002	0.001	0.002	0.002
Mg	0.056	0.084	0.075	0.093	0.070	0.090	0.056	0.056	0.071	0.048	0.066	0.070	0.074	0.067	0.058	0.075	0.062	0.063	0.068	0.069	0.059	0.060
Ca	0.000	0.000	0.000	0.001	0.002	0.000	0.001	0.000	0.000	0.006	0.000	0.002	0.003	0.004	0.001	0.000	0.000	0.000	0.000	0.000	0.000	0.001
Na	0.046	0.050	0.064	0.029	0.045	0.033	0.077	0.065	0.048	0.043	0.054	0.073	0.052	0.049	0.062	0.060	0.069	0.068	0.044	0.068	0.039	0.062
K	0.967	0.966	0.956	0.989	0.974	0.980	0.928	0.937	0.938	0.914	0.894	0.874	0.897	0.883	0.913	0.930	0.928	0.933	0.943	0.913	0.942	0.926
Sum	7.042	7.057	7.054	7.055	7.066	7.048	7.048	7.043	7.036	7.008	6.995	7.001	6.993	6.986	7.024	7.024	7.034	7.045	7.031	7.024	7.015	7.018

Representative major elements analyses of Fe-Ti oxides.

Analyses	Biotite Tonalite Protomylonite															
	Sample PT8-05															
	Medium grains with mica															
Analyses	iilhem1-1	iilhem1-4	iilhem1-5	iilhem1-6	iilhem1-7	iilhem2-1	iilhem2-2	iilhem2-3	iilhem2-4	iilhem2-5	iilhem2-6	iilhem2-7	iilhem2-8	iilhem3-1	iilhem3-2	iilhem4-1
SiO ₂	0.04	0.00	0.06	0.16	0.02	0.00	0.03	0.01	0.04	0.05	0.00	0.04	0.00	0.01	0.05	0.04
TiO ₂	54.37	0.07	0.05	0.10	0.11	0.04	0.03	0.09	0.05	49.76	49.30	50.03	53.91	0.04	0.02	0.06
Al ₂ O ₃	0.00	0.03	0.00	0.02	0.00	0.01	0.00	0.00	0.00	0.00	0.00	0.00	0.00	0.00	0.04	0.00
Cr ₂ O ₃	0.02	0.05	0.00	0.09	0.05	0.03	0.05	0.06	0.02	0.00	0.01	0.02	0.01	0.05	0.04	0.08
Fe ₂ O ₃	0.00	102.48	97.92	98.53	102.44	99.24	102.18	103.15	99.43	5.05	5.07	3.87	0.01	102.83	102.53	101.84
FeO	34.75	0.93	0.89	0.90	0.93	0.90	0.93	0.94	0.90	39.42	39.01	39.89	36.18	0.93	0.93	0.93
MnO	4.22	0.04	0.00	0.00	0.00	0.04	0.01	0.05	0.00	5.05	5.21	5.00	6.22	0.00	0.06	0.01
MgO	0.03	0.00	0.00	0.03	0.04	0.01	0.00	0.00	0.00	0.04	0.00	0.02	0.01	0.00	0.01	0.00
CaO	0.06	0.02	0.01	0.02	0.00	0.00	0.00	0.02	0.00	0.01	0.00	0.00	0.02	0.00	0.00	0.00
Na ₂ O	0.02	0.00	0.05	0.00	0.00	0.00	0.02	0.03	0.00	0.04	0.01	0.01	0.00	0.01	0.00	0.00
K ₂ O	0.00	0.00	0.00	0.00	0.00	0.00	0.00	0.00	0.00	0.00	0.00	0.00	0.00	0.00	0.00	0.00
Totals	93.51	103.62	98.98	99.84	103.59	100.27	103.25	104.34	100.46	99.43	98.61	98.88	96.36	103.87	103.68	102.95
Si	0.001	0.000	0.002	0.004	0.001	0.000	0.001	0.000	0.001	0.001	0.000	0.001	0.000	0.000	0.001	0.001
Ti	1.070	0.001	0.001	0.002	0.002	0.001	0.001	0.002	0.001	0.951	0.951	0.962	1.042	0.001	0.000	0.001
Al	0.000	0.001	0.000	0.001	0.000	0.000	0.000	0.000	0.000	0.000	0.000	0.000	0.000	0.000	0.001	0.000
Cr	0.000	0.001	0.000	0.002	0.001	0.001	0.001	0.001	0.000	0.000	0.000	0.000	0.000	0.001	0.001	0.002
Fe ₃	0.000	1.982	1.982	1.975	1.981	1.984	1.983	1.981	1.983	0.097	0.098	0.074	0.000	1.984	1.981	1.982
Fe ₂	0.760	0.020	0.020	0.020	0.020	0.020	0.020	0.020	0.020	0.838	0.837	0.853	0.778	0.020	0.020	0.020
Mn	0.094	0.001	0.000	0.000	0.000	0.001	0.000	0.001	0.000	0.109	0.113	0.108	0.135	0.000	0.001	0.000
Mg	0.001	0.000	0.000	0.001	0.002	0.000	0.000	0.000	0.000	0.002	0.000	0.001	0.000	0.000	0.000	0.000
Ca	0.002	0.001	0.000	0.001	0.000	0.000	0.000	0.001	0.000	0.000	0.000	0.000	0.001	0.000	0.000	0.000
Na	0.001	0.000	0.003	0.000	0.000	0.000	0.001	0.001	0.000	0.002	0.000	0.000	0.000	0.000	0.000	0.000
K	0.000	0.000	0.000	0.000	0.000	0.000	0.000	0.000	0.000	0.000	0.000	0.000	0.000	0.000	0.000	0.000
Sum	1.929	2.007	2.008	2.005	2.006	2.007	2.007	2.008	2.006	2.000	2.000	2.000	1.957	2.007	2.007	2.006

Biotite Tonalite Mylonite													
Sample PT8-05													
Analyses	Medium grains with rims							Along cleavage planes and melt boundaries			Intra-grain exsolution		
	iilhem4-2	iilhem4-3	iilhem4-4	iilhem4-5	iilhem5-1	iilhem5-2	iilhem5-3	iilhem6-2	iilhem9-1	iilhem9-3	iilhem7-1	iilhem7-2	iilhem7-3
SiO ₂	0.00	0.03	0.04	0.00	0.03	0.03	0.06	0.00	0.14	0.08	0.05	0.04	0.02
TiO ₂	0.06	0.13	0.04	0.06	0.02	0.03	0.04	33.55	49.08	49.68	0.02	0.04	0.09
Al ₂ O ₃	0.00	0.00	0.00	0.03	0.00	0.00	0.00	0.00	0.03	0.00	0.00	0.00	0.02
Cr ₂ O ₃	0.08	0.08	0.07	0.05	0.04	0.06	0.06	0.00	0.00	0.02	0.06	0.09	0.07
Fe ₂ O ₃	102.86	102.92	102.45	102.49	103.18	102.44	98.77	0.00	3.92	3.55	101.79	102.21	101.76
FeO	0.93	0.94	0.93	0.93	0.94	0.93	0.90	33.71	30.57	32.76	0.93	0.93	0.92
MnO	0.00	0.02	0.03	0.04	0.01	0.01	0.00	3.87	12.58	11.04	0.01	0.04	0.03
MgO	0.00	0.00	0.00	0.02	0.01	0.00	0.00	0.02	0.04	0.08	0.01	0.01	0.00
CaO	0.00	0.00	0.03	0.00	0.00	0.00	0.00	0.19	0.62	0.03	0.00	0.01	0.01
Na ₂ O	0.00	0.03	0.00	0.00	0.00	0.00	0.03	0.00	0.00	0.04	0.01	0.03	0.01
K ₂ O	0.00	0.02	0.00	0.02	0.00	0.00	0.00	0.01	0.04	0.15	0.01	0.00	0.00
Totals	103.94	104.16	103.39	103.64	104.23	103.50	99.86	93.35	97.02	97.44	102.89	103.40	102.93
Si	0.000	0.001	0.001	0.000	0.001	0.001	0.002	0.000	0.004	0.002	0.001	0.001	0.001
Ti	0.001	0.002	0.001	0.001	0.000	0.001	0.001	1.045	0.958	0.967	0.000	0.001	0.002
Al	0.000	0.000	0.000	0.001	0.000	0.000	0.000	0.000	0.001	0.000	0.000	0.000	0.001
Cr	0.002	0.002	0.001	0.001	0.001	0.001	0.001	0.000	0.000	0.000	0.001	0.002	0.001
Fe ₃	1.983	1.980	1.982	1.982	1.984	1.983	1.982	0.000	0.077	0.069	1.982	1.981	1.981
Fe ₂	0.020	0.020	0.020	0.020	0.020	0.020	0.020	0.775	0.664	0.709	0.020	0.020	0.020
Mn	0.000	0.000	0.001	0.001	0.000	0.000	0.000	0.129	0.277	0.242	0.000	0.001	0.001
Mg	0.000	0.000	0.000	0.001	0.000	0.000	0.000	0.001	0.002	0.003	0.000	0.000	0.000
Ca	0.000	0.000	0.001	0.000	0.000	0.000	0.000	0.005	0.017	0.001	0.000	0.000	0.000
Na	0.000	0.001	0.000	0.000	0.000	0.000	0.002	0.000	0.000	0.002	0.001	0.001	0.001
K	0.000	0.001	0.000	0.001	0.000	0.000	0.000	0.000	0.001	0.003	0.000	0.000	0.000
Sum	2.006	2.007	2.007	2.007	2.006	2.006	2.007	1.955	2.000	2.000	2.007	2.008	2.007

Analyses	Biotite Tonalite Mylonite												Chlorite-Illite Phyllonite		
	Sample PT8-05												Sample RPT-2		
	Intra-grain exsolution					Exsolution with titanite							Rutile as part of intra-grain exsolution	Rutile	
	ilhem7-4	ilhem7-5	ilhem7-6	ilhem7-7	ilhem8	ilhem10-1	ilhem10-2	ilhem10-3	ilhem10-4	ilhem10-5	ilhem10-6	Rt2	Rt1-1	Rt1-2	
SiO ₂	0.06	0.04	0.02	0.03	0.02	0.01	0.03	0.05	0.00	0.01	0.01	0.46	0.43	0.61	
TiO ₂	0.09	0.03	49.48	0.04	48.63	0.02	0.03	0.08	0.01	0.01	0.03	93.43	96.10	95.68	
Al ₂ O ₃	0.00	0.01	0.00	0.00	0.00	0.00	0.00	0.02	0.01	0.00	0.00	0.06	0.18	0.14	
Cr ₂ O ₃	0.06	0.04	0.00	0.05	0.01	0.06	0.06	0.02	0.09	0.07	0.09	0.00	0.00	0.00	
Fe ₂ O ₃	102.27	102.35	4.90	102.37	6.81	102.23	102.27	102.13	102.56	102.43	102.34	0.00	0.00	0.00	
FeO	0.93	0.93	40.83	0.93	39.65	0.93	0.93	0.93	0.93	0.93	0.93	3.90	0.87	0.77	
MnO	0.05	0.00	3.57	0.02	3.91	0.03	0.01	0.02	0.00	0.03	0.03	0.01	0.03	0.00	
MgO	0.00	0.01	0.04	0.00	0.01	0.02	0.01	0.00	0.00	0.00	0.01	0.00	0.13	0.03	
CaO	0.01	0.00	0.00	0.04	0.03	0.01	0.00	0.00	0.00	0.01	0.00	0.22	0.05	0.37	
Na ₂ O	0.00	0.02	0.00	0.00	0.02	0.00	0.00	0.03	0.00	0.03	0.00	0.02	0.04	0.03	
K ₂ O	0.01	0.00	0.00	0.00	0.00	0.02	0.00	0.00	0.00	0.00	0.00	0.00	0.12	0.14	
Totals	103.48	103.43	98.84	103.48	99.08	103.33	103.34	103.28	103.61	103.52	103.44	98.11	97.16	97.65	
Si	0.002	0.001	0.001	0.001	0.001	0.000	0.001	0.001	0.000	0.000	0.000	0.006	0.006	0.008	
Ti	0.002	0.001	0.952	0.001	0.934	0.000	0.001	0.002	0.000	0.000	0.001	0.969	0.984	0.982	
Al	0.000	0.000	0.000	0.000	0.000	0.000	0.000	0.001	0.000	0.000	0.000	0.001	0.001	0.001	
Cr	0.001	0.001	0.000	0.001	0.000	0.001	0.001	0.000	0.002	0.001	0.002	0.00	0.00	0.00	
Fe ₃	1.980	1.983	0.094	1.983	0.131	1.983	1.983	1.981	1.984	1.983	1.983	0.001	0.001	0.001	
Fe ₂	0.020	0.020	0.874	0.020	0.847	0.020	0.020	0.020	0.020	0.020	0.020	0.043	0.010	0.009	
Mn	0.001	0.000	0.077	0.000	0.085	0.001	0.000	0.000	0.000	0.001	0.001	0.001	0.001	0.001	
Mg	0.000	0.000	0.002	0.000	0.000	0.001	0.000	0.000	0.000	0.000	0.000	0.001	0.001	0.001	
Ca	0.000	0.000	0.000	0.001	0.001	0.000	0.000	0.000	0.000	0.000	0.000	0.003	0.001	0.005	
Na	0.000	0.001	0.000	0.000	0.001	0.000	0.000	0.001	0.000	0.001	0.000	0.001	0.001	0.001	
K	0.000	0.000	0.000	0.000	0.000	0.001	0.000	0.000	0.000	0.000	0.000	0.001	0.001	0.001	
Sum	2.006	2.007	2.000	2.007	2.000	2.007	2.006	2.007	2.007	2.007	2.008	2.007	2.020	1.000	1.004

APPENDIX F

Chlorite crystallization temperature results according to Inoue et al., 2009.

Lithotype	Sample	System	Alteration type	Analyses	Temp (°C)	Geometric mean (°C)	
Garnet Granodiorite	PT13-08	Magmatic hydrothermal	Propylitic	Chl1-3	372		
	PT13-08			Chl1-4	383	377	
	PT13-08		Selective alteration of biotite	Chl2-1	390		
	PT13-08			Chl2-2	409		
	PT13-08			Chl2-3	278		
	PT13-08			Chl2-4	395	291	
	PT13-13			Chl3-1	193		
	PT13-13			Chl3-2	318		
	PT13-13			Chl3-3	164		
	PT30-04		Selective alteration of garnet and biotite	Chl4	293		
Garnet Leucogranite	PT30-04			Chl5	283		
PT30-04	Chl6			246	287		
PT30-04	Chl7			327			
PT30-06	Chloritization			Chl8-1	380		
Biotite Tonsite				PT30-06	Chl8-2	156	282
PT30-06				Chl8-3	379		
PT30-06	Selective alteration of biotite	Chl1	409				
PT30-06		Chl2	392				
PT30-06		Chl3	400	401			
PT30-06		Chl4	388				
PT30-06		Chl5-1	401				
PT30-06		Chl5-2	416				
PT30-06	Propylitic	Chl6	360	360			
PT30-06		Chl8	430	430			
Biotite Tonsite Promylonite	PT30-05	Chloritization	Selective alteration of biotite	Chl1-1	397		
	PT30-05			Chl1-2	384		
	PT30-05			Chl1-3	364		
	PT30-05			Chl2	366		
	PT30-05			Chl3-1	257		
	PT30-05			Chl3-2	254	353	
	PT30-05			Chl4-1	423		
	PT30-05			Chl4-2	400		
	PT30-05			Chl5-1	388		
	PT30-05			Chl5-2	369		
Chlorite-Illite Phyllonite	RPT-2	Shear + hydrothermal	Ch-Hill phyllonite	Chl1	371		
	RPT-2			Chl2	371		
	RPT-2			Chl3	379		
	RPT-2			Chl4	368		
	RPT-2			Chl5	356		

Illite crystallization temperature results according to Battaglia, 2004.

Lithotype	Sample	System	Alteration type	Analyses	Fe / Mg	K + Fe - Mg	Temp (°C)	Geometric mean (°C)
Garnet Granodiorite	PT1513		Selective alteration of feldspar and micas	mu1	0.064	1.059	315	
				mu2-1	0.082	1.038	310	
				mu2-2	0.036	1.015	303	
				mu3	0.068	1.022	305	
				mu4-1	0.137	1.092	324	
				mu4-2	0.157	1.085	322	
				mu4-3	0.137	1.074	319	
				mu4-4	0.154	1.068	318	
				mu4-5	0.134	1.017	304	314
				mu4-6	0.148	1.097	325	
				mu5-1	0.08	1.035	309	
				mu5-2	0.03	1.002	300	
				mu5-3	0.073	1.020	305	
				mu5-4	0.127	1.092	324	
				mu5-5	0.157	1.091	324	
				mu5-6	0.1	1.060	316	
				mu5-7	0.1	1.060	316	
				mu5-8	0.093	1.031	313	
Garnet Leucogranite	PT3004		Selective alteration of garnet	mu6-1	-0.011	0.927	280	
				mu6-2	0.006	0.962	289	
				mu7-1	0.081	1.070	318	296
				mu7-2	0.034	1.000	299	
				mu7-3	0.039	0.988	296	
Biotite Tonalite	PT12-08	Magma-hydrothermal	Selective alteration of feldspar and mica	mu1	-0.078	1.018	304	
				mu2	-0.077	1.017	304	
				mu3	0.042	0.979	294	295
				mu4	0.015	0.960	289	
				mu5	-0.003	0.937	283	
			Infilling alteration	mu6	0.042	1.010	302	
				mu7	0.023	0.959	288	
				mu8	-0.066	1.001	300	
				mu9	-0.038	0.998	299	
				mu10	0.033	0.998	299	
				mu11-1	0.031	1.000	299	
				mu11-2	0.036	1.021	305	
				mu11-3	0.041	0.998	299	
				mu12-1	0.04	0.973	292	
				mu12-2	0.07	1.012	303	
				mu12-3	0.033	0.995	298	
				mu12-4	0.038	0.991	297	302
				mu13	0.048	0.837	236	
				mu14-1	0.084	1.029	307	
				mu14-2	0.061	1.008	302	
				mu15	0.088	1.041	310	
				mu16-1	0.141	1.074	319	
				mu16-2	0.082	1.034	309	
				mu16-3	0.081	1.034	309	
				mu16-4	0.101	1.032	308	
				mu16-5	0.061	1.020	305	
				mu17-1	0.163	1.115	330	
				mu17-2	0.079	1.019	309	
				mu17-3	0.076	1.024	306	

Muscovite crystallization temperature results according to Battaglia, 2004.

Lithotype	Sample	System	Alteration type	Analyses	Fe - Mg	K + Fe - Mg	Temp (°C)	Geometric mean (°C)
Garnet Granodiorite	PT 15-13			mu1-1 mu1-2 mu2-1 mu2-2 mu3 mu4	0.073 0.063 0.051 0.065 0.072 0.060	1.040 1.029 1.007 1.054 1.046 1.040	310 307 301 314 312 310	310
			Selective of garnet	mu5 mu6 mu7-1 mu7-2 mu8-2 mu9-1 mu9-2 mu9-3	0.053 0.048 0.041 0.059 0.036 0.035 0.032 0.039	0.981 0.985 0.979 0.973 0.930 0.909 0.929 0.922	294 295 294 292 281 275 280 279	286
Ganet Leucogranite	PT 30-04	Magma-Hydrothermal	Disseminated as coarse muscovite	mu10-1 mu10-2 mu10-3 mu10-4 mu10-5 mu10-6 mu11-1 mu11-2 mu11-3 mu11-4 mu11-5	0.028 0.011 0.028 0.030 0.020 0.014 0.034 0.026 0.031 0.024 0.034	0.943 0.941 0.956 0.963 0.963 0.927 0.976 0.952 0.954 0.952 0.937	284 284 288 290 290 280 293 287 287 287 283	286